Materials Radioassay for the XENON1T Dark Matter Experiment, and Development of a Time Projection Chamber for the Study of Low-energy Nuclear Recoils in Liquid Xenon

Dissertation
zur
Erlangung der naturwissenschaftlichen Doktorwürde
(Dr. sc. nat.)

vorgelegt der
Mathematisch-naturwissenschaftlichen Fakultät
der
Universität Zürich

von
Francesco Piastra
aus
Italien

Promotionskommission

Prof. Dr. Laura Baudis (Vorsitz)
Prof. Dr. Benjamin Kilminster
Dr. Alexander Kish

Zürich, 2017

ZUSAMMENFASSUNG

Astrophysikalische und kosmologische Beobachtungen geben starke Hinweise darauf, dass nur 5 % des Universums aus normaler Materie und Strahlung bestehen, während etwa 27 % aus kalter, nicht leuchtender Materiebestehen, deren Wesen noch unbekannt ist. Die anderen 68 % liegen in Form von Dunkler Energie vor, die für die beschleunigte Expansion des Universums verantwortlich ist.

Da die Dunkle Materie laut Vorhersagen nur sehr schwach mit der gewöhnlichen Materie wechselwirken soll, wird ihre Anwesenheit durch Gravitationswechselwirkungen mit grossen Objekten wie Galaxien, Galaxienhaufen und Superhaufen von Galaxien abgeleitet. Auch ist bekannt, dass sie eine entscheidende Rolle bei der Entstehung dieser Strukturen gespielt hat. Theorien jenseits des Standardmodells der Teilchenphysik sagen voraus, dass Dunkle Materie in Form eines neuen, stabilen oder langlebigen Teilchens vorliegt, das beim Urknall erzeugt wurde. Seine unbekannte Natur ist der Grund für die bestehenden intensiven experimentellen Bemühungen, diese neue Art von Teilchen zu identifizieren und schliesslich ihre Eigenschaften zu untersuchen.

Mehrere Detektoren zur direkten Beobachtung der Streuung solcher Teilchen an Atomkernen wurden in den letzten Jahrzehnten gebaut und in Betrieb genommen, und es wurden keine schlüssigen Nachweise für die Detektion Dunkler Materie erbracht. XENON1T, ein Detektor der neuen Generation, wurde Ende 2015 bei den Laboratori Nazionali del Gran Sasso (LNGS) in Italien installiert und ist seit Anfang 2016 in Betrieb. Nach einer anfänglichen Anlaufphase wurde im November 2016 der erste wissenschaftliche Durchlauf gestartet und setzte mit $\sim$ 34 Tagen Lebensdauer die höchste Ausschlussobergrenze für die Wechselwirkung von schwach wechselwirkenden massereichen Teilchen (WIMPs) mit normaler Materie. Für die nächsten zwei Jahre der Datenerfassung wird eine Verbesserung der Empfindlichkeit gegenüber dem WIMP-Nukleonquerschnitt auf $1.6 \times 10^{-47}\,\mathrm{cm}^2$ erwartet, etwa 2 Grössenordnungen weniger als bei seinem Vorgänger XENON100. Die Arbeiten, die zu dieser Abhandlung beigetragen haben, umfassen drei wesentliche Forschungsschwerpunkte: die Radioassay-Kampagne von XENON1T, die Untersuchung der kosmogenen Produktion von Radionukliden in natürlich vorkommenden Xenon-Gas durch atmosphärische kosmische Strahlung und die Entwicklung einer kleinen flüssigen Xenon-Spurendriftkammer zur Untersuchung der Xenon-Reaktion für neutroneninduzierte nukleare Rückstösse mit Energien unter 10 keV.

Die radioaktive Kontamination der Konstruktionsmaterialien des Detektors ist eine der gefährlichsten Hintergrundquellen, die die experimentelle Endempfindlichkeit beeinträchtigen könnte. Aus diesem Grund wurde eine Radioassay-Kampagne zur Auswahl der Detektorkomponenten mit Strahlungsspektrometertechnik aus hochreinem Germanium mit geringer Hintergrundstrahlung (HP-Ge) durchgeführt, mit der radioaktive Kontaminationen in Materialien bis auf $10^{-17}\,\mathrm{g/g}$ bei ^{238}U und $10^{-10}\,\mathrm{g/g}$ bei ^{232}Th nachgewiesen werden konnten. Im Rahmen der Radioassay-Kampagne wurden die neuen hochreinen Hamamatsu R11410-11 Photomultiplikatoren, die als Photosensoren in XENON1T eingesetzt werden, entwickelt, so dass der Lichtsensor die bisher höchste Strahlungsreinheit pro sensitivem Bereich aufweist. Die Vorhersage der auf Radioessay-Messungen

basierenden Hintergrundstrahlung zeigt, dass der Strahlenhintergrund bei den gewählten Materialien voraussichtlich weniger als 5 % der gesamten Hintergrundstrahlung ausmacht und die aus radiogenen Neutronen bestehende Hintergrundstrahlung auf ~ 1.2 Ereignisse/a geschätzt wird. Daraus kann die Schlussfolgerung gezogen werden, dass das Experiment in der Lage sein wird, WIMP-Wechselwirkungen mit Nukleonen bis zu einem Querschnitt von für eine WIMP-Masse von $50\,\mathrm{GeV/c^2}$ bei einer Exposition von $\sim 2\,\mathrm{t\,a}$ zu untersuchen.

Es wird hier die erste spezifische experimentelle Untersuchung der von der kosmischen Strahlung induzierten Aktivierung einer natürlichen Xenonprobe, gemeinsam mit der Aktivierung einer sauerstofffreien Kupferprobe mit hoher Leitfähigkeit zur Vergleichskontrolle vorgestellt. Die für beide Proben erzielten Ergebnisse werden mit den Vorhersagen verglichen, die mit Hilfe der verfügbaren Programme Activia und Cosmo erhalten wurden, und im Falle von Kupfer auch mit der einzigen in der Literatur vorhandenen experimentellen Untersuchung zu seiner kosmogenen Aktivierung. Es wurde festgestellt, dass, während die Berechnungen für das Kupfer Werte in erheblicher Übereinstimmung mit der Messung vorhersagen, im Falle von Xenon die Ausbeuten vieler beobachteter kosmogener Radionuklide stark unterschätzt wurden. Dies ist wahrscheinlich auf die schlechte Kenntnis der Querschnitte der Kernprozesse für die Xenon-Isotope zurückzuführen. Unter den fünf untersuchten kosmogenen Radionukliden stimmt die Produktionsrate von ^{127}Xe mit dem gemessenen niederenergetischen Hintergrund des LUX-Experiments für die Dunkle Materie überein. Aufgrund der relativ kurzen Halbwertszeit wird es jedoch kein Problem für die Versuche zum Nachweis von Dunkler Materie mit flüssigem Xenon darstellen. Zwei weitere kosmogene Produkte, die Isotope ^{101}Rh und ^{125}Sb, haben eine ausreichend lange Halbwertszeit, um für die nächste Generation flüssiger Xenon-Detektoren für Dunkle Materie auf der Multitonnenskala wie XENONnT, LZ und DARWIN in Frage zu kommen. Ersteres würde jedoch den gesamten Hintergrund in einem Energiebereich erzeugen, der für die Suche unter Einsatz von Xenon nicht relevant ist, während Letzteres eine zu grosse Produktionsrate aufweist, um mit dem LUX-Hintergrund konsistent zu sein. Es wird daher der Schluss gezogen, dass entweder die reale Produktionsrate nahe am unteren Rand des angegebenen Messunsicherheits-Intervalls liegt, oder dass sie aufgrund ihrer Elektronegativität von den Xenon-Filtersystemen effizient entfernt wird, oder dass sie von den Oberflächen der internen Komponenten des Detektors abgeschirmt wird.

Es wurde eine kleine Zeitprojektionskammer Xurich II für die Untersuchung von niederenergetischen Kernrückstössen entwickelt, die durch Neutronenwechselwirkungen mit den Xenon-Kernen ausgelöst werden, und zur Beurteilung und Analyse der Kommission vorgestellt. Da bei einer WIMP-Wechselwirkung in flüssigem Xenon von einem niederenergetischen Kernrückstoss ausgegangen wird, sind diese Messungen von besonderer Bedeutung für die korrekte Interpretation der Dunkle Materie-Messungen. Das Design des Detektors wurde optimiert, um die wenigen Photonen des Szintillationslichts beim flüssigen Xenon und die wenigen aus der Ionisation entstehenden Elektronen zu detektieren, die durch nukleare Rückstösse mit Energien von wenigen keV entstehen. Die Detektorleistungen wurden mittels Kalibrierungen mit dem metastabilen Edelgasisomer bestimmt. Eine detaillierte Untersuchung des absoluten Licht- und Ladungsverhaltens des Detektors sowie Messungen der Elektronendriftgeschwindigkeit als Funktion des elektrischen Feldes werden hier vorgestellt. Es wurde nachgewiesen, dass der Detektor eine Lichtausbeute von ~ 9 Photoelektronen/keV für Elektronenrückstösse mit einer

Energie von 32.15 keV und einem elektrischen Feld von 1 kV / cm aufweist. Die Auswertung zeigt, dass es keine systematischen Effekte gibt, die die Genauigkeit der geplanten Untersuchungen beeinträchtigen können, und es wird der Schluss gezogen, dass die aktuelle Leistung des Detektors die Messung der Reaktion am flüssigen Xenon für nukleare Rückstösse bis zu einer Energie von 2.5 keV möglich macht.

ABSTRACT

There is strong evidence from astrophysical and cosmological observations, that only 5 % of the Universe is made out of ordinary matter and radiation, while about 27 % is in a form of cold, non-luminous matter, whose intrinsic nature is still unknown. The other 68 % in form of dark energy, that is responsible for the accelerated expansion of the Universe.

Since dark matter is predicted to interact only very weakly with ordinary matter, its presence is inferred by the gravitational effects on large scale objects such as galaxies, clusters and super-clusters of galaxies, and it played a fundamental role in the formation of these structures. Theories beyond the Standard Model of particle physics predict that dark matter is in form of a new, stable or long-lived particle, produced in the hot Big Bang. Their unknown nature motivates the strong existing experimental efforts to detect these new kind of particles and eventually to study their properties.

Several detectors, to directly observe the scattering of such particles with atomic nuclei, have been built and operated during the last decades, and no conclusive evidence of dark matter detection has been reported. The new generation XENON1T detector has been installed at the Laboratori Nazionali del Gran Sasso (LNGS) in Italy at the end of 2015, and is operating since the start of 2016. After an initial commissioning phase it started the first scientific run in November 2016, and with ~ 34 days of lifetime, it placed the strongest exclusion upper limit on the interaction of weakly massive particles (WIMPs) with ordinary matter. In the next two years of data acquisition it is expected to improve the sensitivity to WIMP-nucleon cross section to $1.6 \times 10^{-47}\,\mathrm{cm}^2$, about 2 orders of magnitude lower compared to its predecessor XENON100.

The work that lead to this thesis comprises three main studies: the radioassay campaign of XENON1T, the study of the cosmogenic production of radionuclides in natural xenon by atmospheric cosmic rays, and the development of a small liquid xenon time-projection chamber for study of the liquid xenon response to neutron-induced nuclear recoils with energies below 10 keV.

The radioactive contamination of the detector construction materials is one of the most dangerous background sources that might compromise the final detection sensitivity of the experiment. For this reason, a radioassay campaign for the selection of detector components was performed with the low-background, high-purity germanium (HP-Ge) γ-ray spectrometry technique, which allowed to detect radioactive contaminations in materials down to $10^{-17}\,\mathrm{g/g}$ of ^{238}U and $10^{-10}\,\mathrm{g/g}$ of ^{232}Th. Within the radioassay campaign the new highly radio-pure Hamamatsu R11410-11 photomultipliers, employed as the photosensors in XENON1T, have been developed, resulting in the light sensor with highest radio-purity per sensitive area available to date. The prediction of the background based on the radioassay measurements are discussed, showing that γ-ray background from the selected materials is expected to contribute less than 5 % of the total background, and the background from radiogenic neutrons is estimated to be ~ 1.2 events/y. It is concluded that the experiment will be able to probe WIMP interactions with nucleons down to a cross section of $\sim 1.6 \times 10^{-47}\,\mathrm{cm}^2$ for a WIMP mass of $\sim 50\,\mathrm{GeV/c}^2$ with an exposure of $\sim 2\,\mathrm{t\,y}$.

The first dedicated experimental study of the cosmic ray induced activation of a natural xenon sample, together with the activation of an oxygen-free high conductivity copper sample for benchmark control, is presented. The results achieved for both samples are compared with the predictions performed with the available codes, Activia and Cosmo, and in the case of copper also with the only existing experimental study of cosmogenic activation found in the literature. It was found that while for the copper the calculations predict values in substantial agreement with the measurement, in the case of xenon the predictions strongly underestimate the production yields of many observed cosmogenic radionuclei. This is most likely due to the poor knowledge of the cross sections of the nuclear processes for the xenon isotopes. Among the five observed cosmogenic radionuclei, the ^{127}Xe production rate is found to be consistent with the measured low-energy background published by the LUX dark matter experiment. Because of the relatively short half-life it will however not be a concern for liquid xenon dark matter search experiments. Other two cosmogenic products, the ^{101}Rh and the ^{125}Sb isotopes, have half-lives long enough to be of concern for next generation multi-tonne scale liquid xenon dark matter detectors such as XENONnT, LZ and DARWIN. However, the former will produce all the background in an energy region not relevant for liquid xenon based searches, while for the latter is observed with a production rate too high to be consistent with the LUX background. It is concluded therefore, that either the real production rate is close to the lower edge of the quoted uncertainty interval, or because of its electronegativity it is efficiently removed by the xenon purification systems, or it plates out the surfaces of the internal components of the detector.

A small-scale time-projection chamber Xurich II for the study of low-energy nuclear recoils induced by neutron interactions with the xenon nuclei has been developed and the analysis of its commission are presentented. As a WIMP interaction in liquid xenon is expected to produce a low-energy nuclear recoil, these measurements are of particular importance for the correct interpretation of the dark matter data. The design of the detector has been optimised to detect few photons of liquid xenon scintillation light and few electrons of ionisation arising from nuclear recoils with energies of few keV. The detector performances have been characterised by means of calibrations performed with the metastable noble gas isomer ^{83m}Kr . A detailed study of the absolute light and charge response of the detector is presented here, as well as measurements of the electron drift velocity as a function of the electric field. It is found that the detector features a light yield of ~ 9 photoelectrons/keV for electron recoils of energy of 32.15 keV and with an electric field of 1 kV/cm. The analysis shows that there are no systematic effects that can compromise the precision and the accuracy the planned studies, and it is concluded that the current performance of the detector will allow measurement of the liquid xenon response to nuclear recoils down to an energy of ~ 2.5 keV.

CONTENTS

ABBREVIATIONS

$\beta\beta$ decay	Double beta decay
BR	Branching ratio
BSM	Beyond the standard model
CI	Credibility interval
CL	Confidence level
CMB	Cosmic microwave background
CNNS	Coherent neutrino-nucleus scattering
CR	Cosmic rays
DM	Dark Matter
ER	Electron Recoil
FV	Fiducial volume
FWHM	Full width at half maximum
GD-MS	Glow discharge mass spectrometry
HE	High energy
HPGe	High-purity germanium
ICP-MS	Inductively coupled plasma mass spectrometry
LXe	Liquid xenon
mwe	Meter of water equivalent
MC	Monte Carlo
MCMC	Monte Carlo Markov Chain
MIP	Minimum ionizing particle
MS	Mass spectrometry
NME	Nuclear matrix element
NR	Nuclear recoil
PMT	Photo-multiplier tube
ppm	Part per million
ppb	Part per billion
ppt	Part per trillion
QE	Quantum efficiency
Q_{v}	Q value
RMS	Root mean square
ROI	Region of interest
SM	Standard model of particle physics
WIMP	Weakly interacting massive particle

INTRODUCTION

The first hints of a non-luminous component in the Universe is dated back to the 1933, when the Swiss astronomer Zwicky observed that the velocity dispersion of several galaxies and nebulae at the edges of the Coma cluster was too high to be explained by the mass of the luminous objects contained in the cluster alone. In later decades, the astronomical and cosmological observations confirmed with increasing accuracy and precision that most of the matter of the Universe is dominated by an unknown form of non-luminous matter, called *dark matter*, that played a central role in the formation of large scale structures such as galaxies, galaxy clusters and superclusters. Despite the fact that the content of the dark matter and its distribution in the Universe are known with a relatively high accuracy through its gravitational effects, no other interactions - provided they exist - with ordinary matter have been ever directly or indirectly observed, and thus the nature of this form of matter remains unknown. If the dark matter consists of elementary stable particles, strong arguments show that the standard model of particles does not predict them. Hence, understanding their nature and the properties of their interactions with ordinary matter is currently one of the most important and long-standing open problems in physics, whose solution would open a window on new physics beyond the Standard Model of particle physics. Such a challenge motivated over the last 3 decades an increasing number of theoretical and experimental efforts to explain and detect these elusive particles. Despite all the efforts no convincing signals compatible with dark matter detection has yet been found and worldwide the scientific community is increasing the experimental efforts to detect the faint signals from the interaction of dark matter particles with the ordinary matter.

Among several experimental efforts, the XENON dark matter project is one of the leading experimental programs that provided so far the most stringent limits on the interaction cross section between the ordinary matter class of dark matter candidates, the weakly interacting massive particles (WIMP). The program is now in its third phase, where a tonne scale liquid xenon detector, XENON1T, has been built at the underground laboratory of Laboratory Nazionali del Gran Sasso (LNGS), where it is being operated since early 2016. The XENON1T detector will run for about 2 years and is designed and expected to probe the WIMP-nucleon cross section with unprecedented sensitivity with strong discovery potentiality.

The aim of this thesis is to provide a summary of three main topics of the ~ 4.5 years long PhD program. The first of the topics is about the contribution to the radioassay campaign for the material screening and selection of the XENON1T detector material components.

A second theme still linked to dark matter searches based on LXe detectors consists in the first dedicated experimental study of the activation of natural xenon due to the atmospheric cosmic rays. This is mainly a study concerning the next generations dark matter detectors that will search for dark matter interactions using LXe target masses of several tonnes.

The final main topic is the development of a small liquid xenon detector for studies of the low-energy neutron-induced nuclear recoils. The aim of this R&D project, entirely

developed at the University of Zurich, is to measure the LXe response to the low-energy nuclear recoils, as are expected from WIMP interactions in LXe.

The thesis is structured as follows. In chapter 1 some main aspects of the standard cosmological framework, are briefly reviewed. It is followed by a bibliographic research with the aim to outline some of the most important evidences for the presence of dark matter that have been accumulated in the last $\sim$ 80 years. The chapter ends with an enumeration of some of the current most compelling dark matter particle candidates, the QCD axions, the axion like particles (ALP), and the WIMPs, where their main theoretical motivations behind these candidates are briefly reviewed.

The experimental methods for dark matter searches are introduced in chapter 2, where a strong emphasis is put on the direct searches, which are the central theme of this work. The main experimental challenges and a very brief review of some of the most recent direct search experiments are given, following the traditional literature. The last part of the chapter deals with liquid xenon based detectors and the related physics on particle interactions. Here the main advantages in using this detection medium for WIMP searches are highlighted. Finally the detection technique based on the dual phase (liquid-gas) time projection chamber is introduced, highlighting the benefits that this technique offers for the development of ultra-low background experiments for rare event searches.

The XENON1T experiment, its scientific goal and the main fatures for its detection sensitivity are introduced in the first two sections of chapter 3. The rest of the chapter is dedicated to the description of the technique based on high-purity germanium (HP-Ge) γ-ray spectrometry, for the materials radioassay and selection of the XENON1T detector components. In this part the radioassay results of the most critical components are reported and discussed together with the work performed to develop the radio pure photomultipliers for the XENON1T detector. The chapter ends presenting the expected sensitivity of the experiment, based on the results of the material radioassay.

Chapter 4 deals with an experimental study - the first - dedicated to the study of the cosmogenic activation of natural xenon. This study is motivated by the poor predictive power of the existing codes, and by the fact that eventual long-lived activation products in xenon might represent significant background in future, multi-tonne experiments. In addition the second experimental study of cosmogenic activation of a high-purity copper sample, used as benchmark, is presented and the results are compared with the existing literature.

Chapter 5, is dedicated to the development of a small liquid xenon detector for the study of low-energy ($<$ 10 keV) nuclear recoils. In the first part of the chapter the principle of the measurement and the detector layout are presented, emphasising the efforts made to reach a low-energy threshold and an experimental setup aimed at the minimisation of systematic uncertainties. Afterwards the hardware description the raw data processor developed and upgraded over $\sim$ 3 years is presented, where only the most important features of last version are shown omitting on the issues found during several versions and the solutions adopted at each step. The final part of the chapter is dedicated to the characterisation of the detector with the ^{83m}Kr radioactive source. The detector response in terms of the scintillation and ionisation yield are presented together with the development of the analysis strategies to build the energy scale based on the combination of the absolute number of emitted photons and of extracted ionisation electrons. The identified systematics and their sources are discussed. As the event-

by-event fluctuations of the light and charge signals produced by the interaction of a particle with LXe are strictly connected to some intrinsic properties of this detection material, a probabilistic model tailored to the description of these fluctuations and their relation to those coming from the detector has been developed. Its main features and its comparison with the data are closing the discussion of the chapter.

1

DARK MATTER IN THE UNIVERSE

1.1 THE STANDARD COSMOLOGICAL MODEL OF THE UNIVERSE

1.1.1 *The expansion of the Universe*

The visible Universe, observed on scales larger than $\sim 50\,\mathrm{Mpc}$, appears isotropic as thoroughly reviewed in [1]. Later observations, such as the Sloan Digital Sky Survey [2], also provide evidence about a homogeneous distribution of galaxies over such scales which implies an isotropic Universe, as seen from any galaxy. The photons of the cosmic microwave background, which travelled across the Universe for about 15 billion years, are observed with an isotropy level of $\sim 10^5$, that further supports the hypothesis of a homogeneous Universe [3]. The *cosmological principle*, that follows from all these observations, states that over large enough scales at any epoch the Universe assumes the same aspect, namely it looks isotropic and homogeneous from any free-fall reference frame. This principle is implemented in the metric of the space-time, by requiring that the geodesic of each "cosmological particle" (e.g. a galaxy or a cluster of galaxies), whose peculiar velocity is negligible compared to the speed of light, is at any time perpendicular to a class of space-like hypersurfaces. This is equivalent saying that the *comoving coordinates* of each matter "cosmological particle" are constant over the time. Hence in such a Universe the proper space-time interval $\mathrm{d}\,s$ between two infinitesimally close events has the form $\mathrm{d}\,s^2 = (c\,\mathrm{d}\,t)^2 + g_{ik}\,\mathrm{d}\,x^i\,\mathrm{d}\,x^k$, the indexes i and k run over the spatial coordinates. Finally, the only class of metrics that can satisfy the requirement of isotropy and homogeneity of the space like hypersurfaces are the Friedmann-Lemaitre-Robertson-Walker metrics (FLRW):

$$\mathrm{d}\,s^2 = g_{\mu\nu}\,\mathrm{d}\,x^\mu\,\mathrm{d}\,x^\nu = \mathrm{d}\,t^2 - a^2(t)\left[\frac{\mathrm{d}\,r^2}{1-Kr^2} + r^2\,\mathrm{d}\,\Omega^2\right], \tag{1.1}$$

where r is the comoving radial distance from the observer, and $\mathrm{d}\,\Omega^2 = \mathrm{d}\,\theta^2 + (\sin(\theta)\,\mathrm{d}\,\phi)^2$. The scale factor $a(t)$ represents the isotropic expansion of the Universe and is related to the cosmological redshift z by:

$$1 + z = a_0/a(t)\,, \tag{1.2}$$

where a_0 is the scale factor at present epoch.

The parameter K represents the square of the scalar curvature of the space, and distinguish three main classes of the FLRW Universes. The class of Universes with $K > 0$ are closed and finite (3-sphere metric); Universes with $K = 0$ are flat and

infinite (euclidean metric); and Universes with $K < 0$ are open and infinite (hyperbolic metric). In central coordinates the metric tensor $g_{\mu\nu}$ assumes the diagonal form:

$$g_{00} = 1, \quad g_{rr} = \frac{-a(t)^2}{1 - Kr^2}, \quad g_{\theta\theta} = -a(t)^2 r^2, \quad g_{\phi\phi} = -a(t)^2 r^2 \sin^2(\theta)\,. \tag{1.3}$$

The dynamic of the space-time evolution is determined by the Einstein's field equation, that relates the geometry to the matter-energy content of the Universe, represented by the energy-momentum tensor $T^{\mu\nu}$:

$$R^{\mu\nu} = 8\pi G \left(T^{\mu\nu} - \frac{1}{2} g^{\mu\nu} T \right) - \Lambda g^{\mu\nu}\,, \tag{1.4}$$

where $R^{\mu\nu}$ is the Ricci tensor, $T = T^{\mu}_{\ \mu}$, and Λ is the *c*osmological constant which represents a possible generalisation of the field equations. This constant was historically introduced by Einstein to make a static Universe (non-expanding), that however was in tension with the observations of the redshift of light from the galaxies strictly correlated with their distance. Recently, several cosmological and astrophysical observations support the presence of this constant and thus it is part of the current cosmological model. According to the cosmological principle the matter-energy content of the Universe behaves as an isotropic and homogeneous perfect fluid at rest, and thus the energy-momentum tensor $T^{\mu\nu} = \mathrm{diag}(\rho, -p, -p, -p)$, where ρ is the energy density of the matter and p its pressure: The only independent field equations that determine the dynamics of the universe are for the R^{00} and R^{11} components (here the index 1 represents the radial coordinate r), called Friedmann's equations:

$$H^2(t) = \frac{8\pi G}{3}(a^2\rho) - \frac{K}{a^2} + \frac{\Lambda}{3}a^2\,, \tag{1.5}$$

$$\frac{\ddot{a}}{a} = -\frac{8\pi G}{3}\left(\rho + 3p - 2\rho_\Lambda\right), \tag{1.6}$$

where $H(t) = \dot{a}/a$ is the Hubble expansion parameter and $\rho\Lambda = \Lambda/8\pi G$.

There are two interesting cases for the energy density ρ:

- **Non-relativistic matter**: This kind of matter is featured by zero pressure, and thus its density ρ_{M} represents actually the mass density. This is also called dust approximation, which provides a sufficient first description of the energy-momentum tensor for the galaxies (seen over large scale as a gas of very massive particles), for the diffused gas in plasma state between the galaxies and for the cold dark matter which will be introduced in the next section. From the conservation law, it follows that the density of non-relativistic matter scales as $\rho_{\mathrm{M}} \propto a^{-3}$.

- **Radiation**: The radiation represent all those species which are relativistic and their equation of state can be well approximated by $\rho_{\mathrm{R}} = 3p_{\mathrm{R}}$. In the present Universe the radiation is almost entirely given by the CMB, that contribute not significantly to the total energy density of the Universe. However, since $\rho_{\mathrm{R}} \propto a^{-4}$ the radiation dominated the dynamics of the Universe evolution in the primordial Universe.

It is worth noting that the Λ term enters in the field equations like a fluid with constant energy $\rho_\Lambda = \Lambda/8\pi G$ and a negative pressure $p_\Lambda = -\rho_\Lambda$. This term dominates

the evolution of the Universe at large scales, when all the other energy contributions become negligible. Interpreted as a form of vacuum energy (*dark energy*), its origin is perhaps more mysterious than the nature of the dark matter, and the only knowledge about is the inferred value of Λ from cosmological observations.

The equation 1.5 allows linking the topology of the Universe with the total mean energy density at the present epoch (indicated by the 0 index):

$$\Omega_{K_0} + \Omega_{\mathrm{R}_0} + \Omega_{\mathrm{M}_0} + \Omega_{\Lambda_0} = 1\,, \tag{1.7}$$

where $\Omega_{\mathrm{R}_0} = \rho_{\mathrm{R}_0}/\rho_{\mathrm{cr}_0}$, $\Omega_{\mathrm{M}_0} = \rho_{\mathrm{M}_0}/\rho_{\mathrm{cr}_0}$, $\Omega_{\Lambda_0} = \rho_{\Lambda_0}/\rho_{\mathrm{cr}_0}$, $\Omega_{K_0} = -K/(H_0 a_0)^2$, and $\rho_{\mathrm{cr}} = 3H^2(t)/8\pi G$ is the critical density of the Universe.

The expansion of the Universe as a function of the redshift and of the matter-energy content at present epoch is:

$$H^2(z) = H_0^2 \left[\Omega_{\mathrm{R}_0}\,(1+z)^4 + \Omega_{\mathrm{M}_0}\,(1+z)^3 + \Omega_{K_0}\,(1+z)^2 + \Omega_{\Lambda_0}\right]\,. \tag{1.8}$$

If H_0 indicates the current status of the expansion velocity of the Universe, it does not provide informations about the status of the acceleration. This information is however encoded into the deceleration parameter $q_0 = -a(t_0)\ddot{a}(t_0)/\dot{a}^2(t_0)$, that by using the 1.6 can be expressed in terms of the energy and pressure content of the Universe:

$$q_0 = \Omega_{\mathrm{R}_0} + \Omega_{\mathrm{M}_0}/2 - \Omega_{\Lambda_0} + \sum_x (1+3w_x)\,\Omega_{x0}\,, \tag{1.9}$$

where x denotes all the other species (for instance neutrinos) which have an equation of state $p_x = w_x \rho_x$.

The parameters introduced in this section are fundamental to understand the future evolution of the Universe, and at the same time they can be determined by observing the Universe in the past. Those measurements are done by studying the brightness of distant standard candles of known absolute luminosity and more recently by the study of the CMB radiation. The most recent measurements of the cosmological parameters have been performed by the Plank space experiment [4], which is designed to probe and analyse the CMB radiation with unprecedented accuracy. As already inferred by previous missions such as COBE [5] and WMAP [6], the best model that fits the current Universe is the ΛCDM model, which is the most simple model, based on 6 fundamental parameters, with the presence of the cosmological constant and the presence of cold dark matter. In particular from the energy contents at present time inferred by the data is an almost flat expanding Universe, that is passing from a matter dominated phase to a dark energy domination, and thus to an indefinite acceleration of its expansion.

1.1.2 *Thermal relics of the early Universe*

In the previous section some features of the present Universe have been given, with more emphasis on the role played by the mass-energy content in the evolution of the Universe. When the Universe was in its early stages, it was much smaller and its constituents were approximately in thermal equilibrium. With the expansion different species departed from the equilibrium giving rise to thermal relics, thermodynamically decoupled from other species. This is called freeze-out mechanism, and is able to

explain many properties of the Universe, such as the origin of the CMB radiation and the primordial abundances of the lightest nuclei (BBN), with a remarkable accuracy. Beside these very well known processes it is widely believed that the same mechanism can explain other phenomena such as cosmic neutrino background, experimentally not yet observed, baryogenesis and, most important for the topics of the present thesis, the expected abundance of the weakly interacting massive particle (WIMPs), a compelling dark matter particle candidate class.

In what follows this mechanism is very briefly reviewed first for the case of the CMB in an approximate but accurate fashion, and later for more general cases were the kinetic theory is involved.

The CMB relic

The radiation, that is almost irrelevant for the dynamic of the Universe at present era, was the most relevant component determining the expansion of the very early Universe, when it was much smaller and hotter than now. The transition from a radiation- to matter- dominated universe, called matter-radiation equality era, corresponds to the time when the matter and radiation terms in equation 1.8 were giving the same contribution. This is usually expressed in terms of redshift, that relates the age to the relative size of the Universe:

$$z_{\rm eq} = (\Omega_{\rm M_0}/\Omega_{\rm R_0}) - 1 \simeq 3.4 \cdot 10^3 \,, \tag{1.10}$$

where $\Omega_{\rm R_0} = 4.14 \cdot 10^{-5} h^{-2}$ and $\Omega_{\rm M_0} = 0.142$ are assumed [4, 7].

At present time it is evident that the CMB photons are not in equilibrium with the rest of the matter in the Universe, but they stream across unimpeded, featured by an energy distribution corresponding to a black-body radiation temperature $T_{\rm CMB} \simeq 2.7\,{\rm K}$. Since the momentum of free massless particles scales with the inverse of the Universe scale ($p \propto a(t)^{-1}$), it can be shown that for a gas of non interacting particles with a thermal distribution, as in the case of the CMB, the effective temperature T also scales as the inverse of the Universe radius. Using the more convenient redshift parametrisation the temperature of the distribution evolves as:

$$T(z) = z\, T_{\rm CMB} \,. \tag{1.11}$$

Hence, at the matter-radiation equality era the temperature of the CMB photons was $T_{\rm eq} \simeq 9.2 \times 10^3\,{\rm K}$, enough to keep hydrogen and helium completely ionised.

Since photons do not interact with each other (at tree level), there was an era when they were in thermal equilibrium with other species, after which they decoupled and their energy distribution froze. As will be briefly shown, this occurred when the rate of energy exchange between the photons and the matter (mainly ionised electrons) dropped, because of the expansion of the Universe. Considering the ordinary primordial abundances of hydrogen ($\sim 76\,\%$) and helium ($\sim 24\,\%$), the ratio of the electron to the baryon (nucleons) density was $n_{\rm e}/n_{\rm B} \simeq 0.88$. At the age of radiation-matter equality the photons interaction rate, Λ_γ, with free (ionised) non-relativistic electrons can be estimated assuming that the radiation-matter interaction was governed by the Thomson

scattering process:

$$\Lambda_\gamma = 0.88\, n_{\rm B} \left(\frac{T}{T_{\rm CMB}}\right)^3 \sigma_{\rm T} c \simeq 1.97 \times 10^{-19} \times \Omega_{\rm B_0} h^2 \left(\frac{T}{T_{\rm CMB}}\right)^3 {\rm s}^{-1}\,, \tag{1.12}$$

where $\sigma_{\rm T} \simeq 6.7 \times 10^{-24} {\rm cm}^2$ is the Thomson cross section and $\Omega_{\rm B_0}$ is the density of the barionic matter normalised to the critical density at present era. The typical amount of energy that a photon transfers to a non relativistic electron in an interaction is of order $(K_B T)^2/m_{\rm e}c^2$, and the ratio $f_{\rm ex} = (K_B T)/m_{\rm e}c^2$ can be interpreted as the fraction of the photon energy that is exchanged. Hence the freeze-out time can be estimated as the time when the exchange rate of photon energy fraction, $\Gamma_\gamma = \Lambda_\gamma f_{\rm ex}$, becomes smaller than the Universe expansion rate H. In a radiation dominated Universe this is given by:

$$H_{\rm fo} \simeq H_0 \sqrt{\Omega_{\rm R_0}} \left(\frac{T_{\rm fo}}{T_{\rm CMB}}\right)^2 \simeq 2 \times 10^{-20} \left(\frac{T_{\rm fo}}{T_{\rm CMB}}\right)^2 {\rm s}^{-1}\,, \tag{1.13}$$

where the neutrinos and anti-neutrinos of the three families are included also inside the radiation term. Hence, the CMB freeze-out temperature can be estimated as:

$$T_{\rm fo} \simeq 1.5 \times 10^4 \left(\Omega_{\rm B_0} h^2\right)^{-1/2} {\rm K}\,. \tag{1.14}$$

It should be noted that at that time the interaction rate with electrons was still relatively high $\Lambda_\gamma \sim 10^5 H$, and the Universe was still opaque to the radiation. However, the energy exchanged in each interaction was not enough to significantly modify the photon spectrum and sustain the equilibrium with the electrons. Since then the photons have been thermodynamically decoupled from matter, and thus their energy distribution evolved with the same thermal shape as at the freeze-out, with an effective temperature scaling with the inverse of the Universe scale.

The Boltzmann equation

A more general description of the early Universe energy exchanges between the species is based on the general-relativistic version of the Boltzmann equation, which describes the evolution of the time-dependent single particle distribution function for the species s, $f_s(x^\mu, p^\mu)$, in the 6-dimensional phase-space and space-time described by the metric tensor $g_{\mu\,\nu}(x)$[1]. This is given by:

$$p^\alpha \frac{\partial}{\partial x^\alpha} f_s + \Gamma^\alpha_{\beta\,\gamma} p^\beta p^\gamma \frac{\partial}{\partial p^\alpha} f_s = \mathcal{C}[f_s]\,, \tag{1.15}$$

where $\Gamma^\alpha_{\beta\,\gamma}$ are the Christoffel symbols and $\mathcal{C}[f_s]$ is the collisional functional (Lorentz-invariant), replacing the non-relativistic Boltzmann equation collisional term, $(\partial f_s/\partial t)_c$. In this form the only present and unavoidable external force field is the gravitational field, represented in the equation by the metric connections Γ that constrain the motion of the matter content on the geodesics. Other fields can be introduced as well with terms

1 To avoid confusion with the previous section, in this section for the momentum of the particles the small letter p is used, while for the pressure term will be used the capital letter P. In addition, throughout this section the natural units $\hbar = c = K_{\rm B} = 1$ are assumed as they make the notation lighter.

$F^{\alpha\beta}p_\beta\,(\partial f_s/\partial p^\alpha)$ if needed in the description of the system. A great simplification of the equation, with an immediate physical interpretation, comes from the requirements of homogeneity and isotropy of the early Universe. This requires that single particle distribution function will actually depend only on the time t and on the 3-momentum module $|\mathbf{p}|$ or equivalently on the energy, and the use FRWL metric, which together lead to the form:

$$p^0\partial_t f_s = -H(t)|\mathbf{p}|f_s + \mathcal{C}[f_s]\,, \tag{1.16}$$

where $H(t)$ is the Hubble expansion rate as defined in the previous section.

The number of particles of the species n_s will thus be given by:

$$n_s(t) = \int \frac{\mathrm{d}^3p}{(2\pi)^3 f_s}\,. \tag{1.17}$$

Hence, its time evolution is given by:

$$\frac{\mathrm{d}}{\mathrm{d}t}n_s(t) = -3Hn_s + g_s\int \mathcal{C}[f_s]\frac{\mathrm{d}^3p}{(2\pi)^3E}\,, \tag{1.18}$$

where the first term on the right side represents the density dilution effect due to the Universe expansion, and g_s is the internal multiplicity of the species s. The collisional term provides the variation rate of f_s caused by the interaction with all the other species and eventually by self-interactions. Since it contains the cross sections of all the involved processes and the single particle distribution functions of all the species participating to the interaction with the species s, it is the term that couples the distributions of the species and describes the energy and momentum transfers among them. An exhaustive and detailed overview of the most general case, where an arbitrary number of species are involved in the collision term, can be found in [8, 9].

Here, it will be examined only for a simple process between two stable species of the type:

$$\chi\,\overline{\chi} \rightleftarrows \psi\,\overline{\psi}\,, \tag{1.19}$$

where only annihilation and inverse annihilation can change the particle number.

In this case, considering the evolution of the species χ, the collisional term is given by:

$$\begin{aligned}\int \frac{\mathrm{d}^3p_\chi}{(2\pi)^3E_\chi}\,\mathcal{C}[f_\psi] = -\int &\frac{\mathrm{d}^3p_\chi}{(2\pi)^3E_\chi}\frac{\mathrm{d}^3p_{\overline{\chi}}}{(2\pi)^3)E_{\overline{\chi}}}\frac{\mathrm{d}^3p_\psi}{(2\pi)^3E_\psi}\frac{\mathrm{d}^3p_{\overline{\psi}}}{(2\pi)^3E_{\overline{\psi}}}\\ &\times(2\pi)^4\delta^{(4)}(p_\chi + p_{\overline{\chi}} - p_\psi - p_{\overline{\psi}})\\ &\times\left[|\mathcal{M}|^2_{\chi\overline{\chi}\to\psi\overline{\psi}}\,f_\chi\,f_{\overline{\chi}} - |\mathcal{M}|^2_{\psi\overline{\psi}\to\chi\overline{\chi}}\,f_\psi\,f_{\overline{\psi}}\right]\,.\end{aligned} \tag{1.20}$$

Considering only interactions where CP violation is absent or can be neglected, it results in $|\mathcal{M}|^2_{\chi\overline{\chi}\to\psi\overline{\psi}} = |\mathcal{M}|^2_{\psi\overline{\psi}\to\chi\overline{\chi}} = |\mathcal{M}|^2$. Assuming a local thermodynamic equilibrium (LTE) of the species ψ and $\overline{\psi}$, their distribution on the momentum space can be approximated with a Maxwell-Boltzmann distribution with zero chemical potential.

Hence taking into account the energy conservation it results that

$$f_\psi\, f_{\overline{\psi}} = \exp\left[-\frac{E_\psi + E_{\overline{\psi}}}{T}\right] = \exp\left[-\frac{E_\chi + E_{\overline{\chi}}}{T}\right] = f_\chi^{(\mathrm{eq})}\, f_{\overline{\chi}}^{(\mathrm{eq})}\,, \tag{1.21}$$

where $f_\chi^{(\mathrm{eq})}$ and $f_{\overline{\chi}}^{(\mathrm{eq})}$ are the local equilibrium distributions of the χ and $\overline{\chi}$ species. Assuming further that there is no asymmetry between the species ψ and $\overline{\psi}$, the Boltzmann equation for the χ species can be written as:

$$\frac{\mathrm{d}\, n_\chi}{\mathrm{d}\, t} = -3Hn_\chi - \langle\sigma_{\chi\overline{\chi}\to\psi\overline{\psi}} v\rangle \left[n_\chi^2 - \left(n_\chi^{(\mathrm{eq})}\right)^2\right], \tag{1.22}$$

where $\langle\sigma_{\chi\overline{\chi}\to\psi\overline{\psi}} v\rangle$ is the thermally averaged product of the annihilation cross section by the relative velocity rate for the χ particle. The equilibrium distribution $n_\psi^{(\mathrm{eq})}$ is defined as

$$n^{(\mathrm{eq})} = \frac{g}{2\pi^2}\int_{m_\chi}^{\infty} \frac{(E^2 - m^2)^{1/2}}{\exp\left[(E-\mu)/T\right] \pm 1} E^2\, \mathrm{d}\, E, \tag{1.23}$$

where μ is the chemical potential (here assumed zero) and the $+$ $(-)$ sign is for Fermi-Dirac (Bose-Einstein) species χ.

As for interacting species the entropy of the particles at equilibrium in a comoving volume is conserved, it is convenient replacing the density number n_χ with the quantity $Y = n_\chi/s$, where s is the entropy density of the species in equilibrium, defined as:

$$s = \frac{\rho + P}{T} = \frac{2\pi}{45} g_{*s}(T) T^3, \tag{1.24}$$

where only the relativistic species in thermal equilibrium contribute to the entropy density[2]. The function $g_{*s}(T)$ represents the effective degree of freedom of the species contributing to s as a function of the photon temperature T:

$$g_{*s}(T) = \sum_{i\in\mathrm{bosons}} g_i \left(\frac{T_i}{T}\right)^3 + \frac{7}{8}\sum_{i\in\mathrm{fermions}} g_i \left(\frac{T_i}{T}\right)^3. \tag{1.25}$$

In the radiation-dominated Universe the expansion rate can be also defined in terms of the photon temperature:

$$H_{\mathrm{rad}}^2 = \frac{8\pi}{3M_{\mathrm{Pl}}} \sum \rho_i = \frac{8\pi^3}{90 M_{\mathrm{Pl}}} g_* T^4\,, \tag{1.26}$$

where g_* represents the effective multiplicity of all the relativistic species contributing to the expansion (also those not in equilibrium):

$$g_*(T) = \sum_{i\in\mathrm{bosons}} g_i \left(\frac{T_i}{T}\right)^4 + \frac{7}{8}\sum_{i\in\mathrm{fermions}} g_i \left(\frac{T_i}{T}\right)^4. \tag{1.27}$$

2 Technically all the species contribute, however for the non relativistic particles the contribution is negligible as it is suppressed by a term $e^{-m/T}$.

Another convenient variable change consists in replacing the time t with the ratio m_χ/T. With this change of variables the Boltzmann equation can be written as:

$$\frac{x}{Y_{\rm eq}}\frac{{\rm d}Y}{{\rm d}x} = -\frac{\Gamma_{\rm A}}{H}\left[\left(\frac{Y}{Y_{eq}}\right)^2 - 1\right], \tag{1.28}$$

where $\Gamma_{\rm A} = n_\chi^{(\rm eq)}\langle\sigma_{\rm A} v\rangle$ is the annihilation rate and $\sigma_{\rm A}$ the annihilation cross section.

In this form of the equation it is evident that the evolution is mainly determined by the ratio of the annihilation rate and the expansion rate, and hence by a measure of the deviation from the equilibrium. For general conditions this equation does not have a closed form and the solutions have to be obtained numerically. However, it is possible to study at lest qualitatively the two limits: the decoupling of a relativistic species ($T_{\rm fo} \gg m_\chi$) and the opposite limit of a completely non relativistic species($T_{\rm fo} \ll m_\chi$). In both cases the annihilation rate decreases with T, and the freeze-out is likely to occur for a "time" $x_{\rm f}$ when $\Gamma_{\rm A}$ roughly falls below H. Hence, below this critical value $Y(x)$ from its equilibrium value and the rate of interactions is not enough to efficiently dump the disequilibrium.

In the case that $x_{\rm f} \lesssim 1$ the species χ decouples from the when it is still relativistic, and it is called *hot relic*. It can be seen that Y_{eq} does not change significantly with time:

$$Y_{eq}^{\rm rel} \simeq 0.278 g_{\rm eff}/g_{*s}(T)\,, \tag{1.29}$$

where $g_{\rm eff} = g$ if the species χ is a boson and $g_{\rm eff} = 3g/4$. Hence, in this case the asymptotic value $Y_\infty = Y(x\to\infty) \simeq Y(x_{\rm f})$ and the relic density at present time can be estimated:

$$n_{\chi 0} \simeq s_0 Y_\infty \simeq 825\left[g_{\rm eff}/g_{*s}(x_{\rm f})\right]\,, \tag{1.30}$$

where s_0 is the entropy density at present era. This approximation can be applied to both the CMB and to the neutrinos which are expected to have decoupled from thermal equilibrium at a T of a few MeV.

In the case of *cold relics*, the freeze-out happened at a "time" $x_{\rm f} > 1$, and the description is more complex as now it depends more critically on the details of the freeze-out. An approximate method, able to predict the asymptotic relic abundances with a discrepancy lower than $\sim 10\,\%$ with respect to the numerical solution can be obtained by using the parametrisation $\langle\sigma_{\rm A} v\rangle \simeq \sigma_0 x^{-n}$. For non-relativistic species at the freeze-out time the equilibrium abundance decreases exponentially with x:

$$Y_{eq}^{\rm nrel} \simeq 0.145\frac{g_{\rm eff} x^{3/2}}{g_{*s}(x_{\rm f})} e^{-x}\,. \tag{1.31}$$

After some algebra, it can be shown that within this approximation the asymptotic abundance is given by

$$Y_\infty \simeq \frac{n+1}{\lambda} x_{\rm fo}^{n+1}\,, \tag{1.32}$$

where

$$\lambda = \left[\frac{xs\langle\sigma_{\rm A}v\rangle}{H}\right]_{x=1} = 0.264\left(\frac{g_{*s}}{\sqrt{g_*}}\right) M_{\rm Pl} m_\chi \sigma_0 \,. \tag{1.33}$$

The freeze-out "time" $x_{\rm fo}$ considering the condition where the deviation from the equilibrium is of order Y_{eq}:

$$Y(x_{\rm fo}) - Y_{eq}^{\rm nrel} = \alpha Y_{eq}^{\rm nrel} \,, \tag{1.34}$$

where α is a multiplicative constant of order unity and is chosen according to the specific process of annihilation (usually $\alpha(\alpha+2) = n+1$).

Finally, it is interesting to note that with this approximate method the predicted asymptotic abundance of the thermal relic results inversely proportional to the quantity $\langle\sigma_{\rm A}v\rangle$:

$$Y_\infty \simeq \frac{3.79(n+1)x_{\rm fo}\sqrt{g_*}}{M_{\rm Pl} m_\chi g_{*s}\langle\sigma_{\rm A}v\rangle} \,. \tag{1.35}$$

This result will be used in section 1.3 to get an estimation of the relic abundance for a specific class of cold thermal relic, that represents a compelling candidate for dark matter particles.

1.2 EVIDENCES FOR DARK MATTER

On the scale of single galaxies the most direct evidence of dark matter presence comes from the measurements of the galactic disk rotational velocity as a function of the radius (*rotation curves*) from the centre of the galaxy. The determination of the rotation curves of spiral galaxies is one of the most important tools for the measurements of the mass distribution of a galaxy. The velocity of a mass in circular orbital motion at radius r is well predicted for a galactic system by the Newton's law of gravitation:

$$v(r) = \sqrt{\frac{G\,M(r)}{r}} \,, \tag{1.36}$$

where G is the gravitational constant and $M(r)$ is the mass enclosed inside the radius r.

Approximately flat rotation curves were initially observed in the M31 (Andromeda nebula) and M33 spiral galaxies [10, 11]. However, given the limited precision offered by the photographic means at the time, it was pointed out that there was no evident discrepancy between the luminosity and mass distribution over the disk [12]. From the 1950s the rotation curves of many spiral galaxies were reconstructed by the study of the Doppler shift of the Hα and HI spectral lines at 656 nm and 21 cm, respectively, arising from the H clouds within the galaxies [13–19]. Thanks to improvements of the instrumentation for radio astronomy from the late 1970s, several observation surveys of spiral galaxies in the 21 cm line provided the strong evidence for flat rotation curves well beyond the photometric galactic disk [20–24]. Under the natural assumption that the Newtonian gravitational theory still holds over length scales as large as ~ 50 kpc,

these observations implied that galactic systems are embedded in a dark (non-luminous) matter halo with a density profile $\rho(r) \propto r^{-2}$. Particularly interesting cases are the low surface brightness (LSB) galaxies, which are small dark matter dominated galactic systems where the stellar and gas components are negligible for the dynamic determination at small radii ($\sim 1\,\mathrm{kpc}$). The mass density profiles of these galaxies, derived from high resolution observations of the 21 cm emitting zones, revealed the presence of large spherical dark matter halos, extending up to 10 times the maximum radius of the optical disk [25].

Self-gravitating systems such as galaxy clusters are a further source of evidence of the presence of large amount of dark matter over scales much larger than the galactic ones. The relatively rich phenomenology featuring these systems allowed over the past decades to independently compare the luminous mass and the total mass with different methods. Among them, the studies of the velocity dispersion of the galaxies, of the X-ray spectra of the hot intergalactic gases, and of the gravitational lensing are those that provided the strongest evidence for the presence of a large amount of non-luminous matter over intergalactic scales. Differently from a spiral galaxy, where the stars and the gas clouds forming the disk have circular Keplerian orbits, the trajectories of the galaxies constituting a cluster are in general not known and impossible to determine. However, the mean kinetic energy E_{K} and the mean potential energy U of a gravitationally bound system are governed by the virial theorem:

$$< E_{\mathrm{K}} >= -\frac{1}{2} < U > \ . \tag{1.37}$$

Hence, measuring the weighted dispersion of the radial velocity as $< v_r^2 >= \sum_i m_i v_i^2$ and the gravitational distance as $R_G = 2M_{\mathrm{T}}^2 \left(\sum_{i \neq k} m_i m_k / r_{ik} \right)^{-1}$ of the galaxies belonging to the bound system:

$$M_{\mathrm{T}} = \frac{R_{\mathrm{G}} v_r^2}{G} \, , \tag{1.38}$$

where the velocities are calculated with respect to the cluster reference system. It is assumed that the velocities of the galaxies v_{r_i} are isotropically distributed and uncorrelated with the positions, and thus $< v_i^2 >= 3 < v_{\mathrm{r}_i} >$, where v_{r_i} is the measured radial velocities. In 1933 Zwicky applied for the first time this method to the Coma cluster of galaxies, measuring gravitational mass being about 300 times larger than the expected mass from the luminosity of the galaxies [26], confirmed later by the studies of Smith [27] on the same system. For nearly all the groups and clusters of galaxies, observed and catalogued in the following decades [28, 29], the ratio M/L derived from the velocity dispersion is $\sim 300\,(M_\odot/L_\odot)$ [30]. Considering the mass-luminosity ratio for the galaxies, these studies imply that only $\sim 10\,\%$ of the total mass produces optical radiation.

The strongest extragalactic X-ray emission was initially detected from the directions of the Virgo [31], the Coma [32], and the Perseus [33] clusters by means of rocket-, balloon-, and air-borne experiments. The next X-ray surveys, performed by many satellite-based experiments with improved energy and angular resolution [34–41],

demonstrated that these sources are extended, with typical sizes from $\sim 0.5\,\mathrm{Mpc}$ to $\sim 3\,\mathrm{Mpc}$, and usually associated with groups or cluster of galaxies. The observations of X-ray spectra from the clusters indicate that the intra-cluster medium (ICM) is filled by hot ($T \sim 10^8\,\mathrm{K}$) low-density gas ($\rho \sim 10^{-3}\,\mathrm{cm}^{-3}$), in approximate equilibrium with the radiation, and thus in first approximation the temperature of the ICM gas can be directly inferred from the radiation spectra.

Although the angular resolution of these early X-ray surveys provided only information about the bulk temperature of the cluster, without being able to have highly space-resolved spectra, it was already possible to have first estimations of the ICM gas mass M_g of and the total mass M_T. The former was inferred from the spatial-distribution of the X-emission intensity, while the total mass was inferred from the ICM temperature of the clusters core, under the assumption that all the gravitational energy has been converted into heat during the gas collapse [41].

Important advances in X-ray surveys of galaxy clusters came primarily from the Chandra [42] and XMM-Newton [43] space missions, equipped with X-ray telescopes much improved in angular resolution and sensitivity, allowing for a temperature mapping of the ICM. The total mass and the gas mass distributions can be determined by the profiles of the temperature $T(r)$ and of the gas density $\rho_\mathrm{g}(r)$, assuming the hydrodynamic equilibrium and a spherical distribution of the total cluster mass within the radius r :

$$M(r) = -\frac{k_\mathrm{B} T \cdot r}{G\mu m_\mathrm{p}} \left(\frac{\mathrm{d}\log(\rho_\mathrm{g})}{\mathrm{d}\log(r)} + \frac{\mathrm{d}\log(T)}{\mathrm{d}\log(r)} \right) . \tag{1.39}$$

This technique applied to rich galaxy clusters, for which the assumption of a central distribution of the mass was possible, provided a much more accurate estimation of the ICM gas mass fraction: $f_\mathrm{gas} \sim 5 - 15\,\%$, depending on the specific galaxy cluster analysed and on its redshift index [44–47]. Further, the observed luminous matter is constrained to nearly negligible fraction of the entire clusters mass ($\sim 1 - 2\,\%$ [48]), namely a factor of ~ 6 less than the hot plasma mass filling the intra-cluster space [49, 50].

The gravitational field generated by the mass of a cluster can deflect the optical path of the light passing through it, acting thus as a gravitational optical lens. The study of the image distortion of the galaxies in the background of a cluster can provide a powerful tool to glean the total mass of the cluster and to map its distribution [51]. In particular, weak gravitational lensing allows determination of the projected mass density of a cluster without the need to make assumptions of spherical symmetry or hydrostatic equilibrium, which are valid only for well relaxed rich clusters. The cluster masses determined with gravitational lenses agree within a factor of 2 with those determined by the study of the X-ray temperature profiles, confirming thus the same amount of dark matter already estimated with the other methods.

In addition cluster mergers are an additional testing system where the presence of dark matter is commonly detected by the combined use of the gravitational lensing technique and the X-ray imaging of the cluster. One of the most studied cluster mergers is the so-called "bullet cluster" (object 1E0657-56) [52], shown in figure 1.1. The mass of this colliding system, determined by the weak gravitational lensing effects, is concentrated on two separated galaxy clusters with a relative velocity of $\sim 4500\,\mathrm{km/s}$. The galaxies are observed in correspondence of the two potential wells, exhibiting the behaviour of collisionless particles. On contrast from the X-ray emission of the intra-cluster plasma clouds it is possible to deduce that the gas clouds are experiencing ram

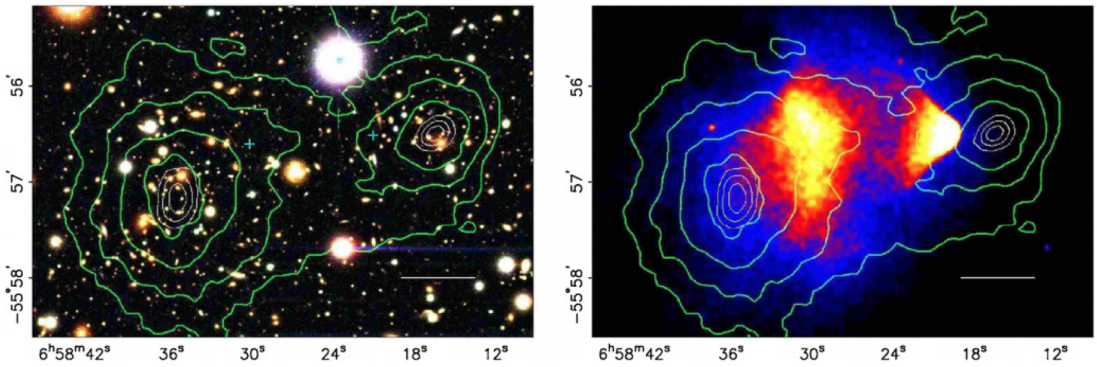

Figure 1.1.: (*Left*) Colour picture of the "bullet cluster". (*Right*) Image in false colours of the intra-cluster X-ray emission, as observed by the Chandra satellite. In both the figures the green contour lines represent the mass distributions as determined by weak gravitational lensing. The white internal contours represent the uncertainty region of the centre of the mass distribution at 68.3 %, at 95.5 % and at 99.7 % confidence levels. The white bar corresponds to 200 kpc transversal length at the distance of the cluster. Figure taken from [52].

pressure, induced by the electromagnetic interaction of the charged particles. As result of this fluid-like interaction the plasma clouds are delayed in their motion toward their parent clusters. In addition, studies of the gas lagging behind in clusters mergers constrain the dark matter self interaction to cross sections $\sigma/m \lesssim 1\,\mathrm{cm}^2/\mathrm{g}$, corresponding to $\sigma/m \lesssim 2 \cdot 10^{-24}\mathrm{cm}^2/(\mathrm{GeV/c}^2)$ [53, 54].

On cosmological scales the presence of non-baryonic dark matter is suggested by the studies of primordial nucleosynthesis of light elements and of the angular spectrum of the CMB anisotropies. These have been performed with increasing accuracy and spatial resolution by the COBE [5], WMAP [6] and Plank [55] satellite-based observatories.

Among the light nuclei synthesised during the BBN, the abundance of deuterium is perhaps the most sensitive one to the photon to baryon (nucleons) number density ratio η and thus to the baryon density Ω_{B_0}. Starting from the 1990s a large number of astrophysical observations tried to infer the primordial deuterium to hydrogen mass ratio y_{DP}, analysing spectroscopic properties of different interstellar gas samples. Among these, the most relevant studies were based on the observation of the interstellar medium [59, 60] and of the solar wind [61]. These early studies were followed by observations of the deuterium and hydrogen absorption lines in the emission spectra of distant quasars, due to absorption in primordial intergalactic gas clouds of large redshifts. Many of these observations are thoroughly discussed by Kirkman *et al.* [62], where the results from different observations are combined finding $\Omega_{\mathrm{B}_0}h^2 = (0.0021 \pm 0.002)$, in agreement with other results from the CMB studies.

Studies of the CMB anisotropy can directly measure the barionic density without inferring it from the light nuclei hashes. At the time of writing, the most recent measurement has been published by the Plank collaboration [4], resulting in $\Omega_{\mathrm{B}_0}h^2 = (0.02225 \pm 0.00023)$, represented by the vertical red band in figure 1.2. This is highly consistent with the BBN predictions (green band) from the astrophysical precision measurements of the primordial deuterium abundance y_{DP} [57, 58] (grey bands). Hence, the resulting picture from all these independent investigations is that barionic matter represents just a small fraction of the total energy content of the present Universe. The temperature power spectrum at high-l multipoles (30) is featured by a strong peak

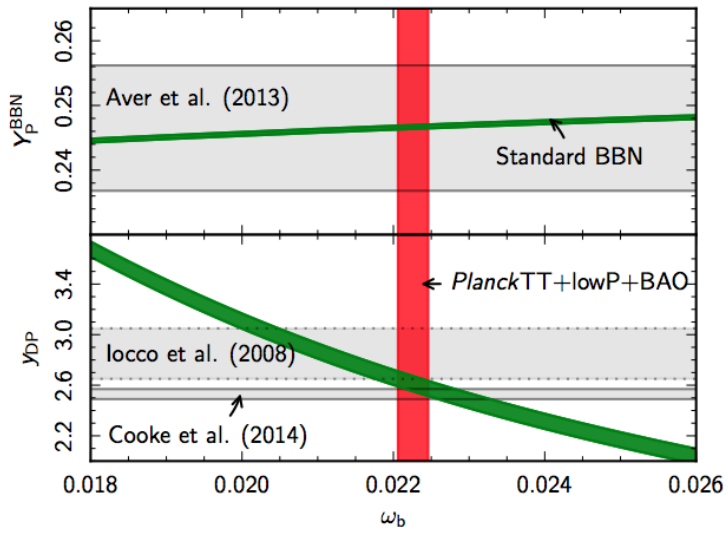

Figure 1.2.: Comparison of the ^{4}He (top panel) and D (bottom panel) primordial abundances as a function of the barionic energy content of the present Universe $\omega_b = \Omega_{B_0} h^2$. The red vertical band is the 68 % C.I. measurement of ω_b by Plank combining the temperature angular power spectrum (*PlankTT*) with the low-l multipole polarisation data (*lowP*) and with the astrophysical data on baryon acoustic oscillations (*BAO*). The horizontal bands are 68 % C.I. from astrophysical measurements of ^{4}He [56] and D [57, 58] primordial abundances. The green bands are the predictions of the two isotope abundances as computed from the standard BBN model. Their widths represent the 68 % C.I. coming mostly from the uncertainty on the neutron life time. The horizontal intervals between the grey bands and the green bands determine the best intervals of ω_b as obtained from the astrophysical observations. It is possible to observe the high degree of agreement between the ω_b inferred from abundance measurements and the interval measured by the Plank experiment. Figure taken from [4].

followed by higher harmonics as shown in figure 1.3. In the ΛCDM model this is understood as the oscillating sound waves of the baryon-photon plasma, driven by the dark matter gravitational perturbations. The main peak found at $l_{max} = 220.0 \pm 0.5$ is consistent with the presence of cold dark matter with an energy density $\Omega_{DM_0} h^2 = (0.1197 \pm 0.0022)$ [4], which constitutes about 84 % of the total non-relativistic content of the Universe.

1.3 DARK MATTER PARTICLE CANDIDATES

In the previous sections many convincing evidences for the presence of non-barionic dark matter from galactic to cosmological scales have been reviewed. However, beyond its presence, distribution, and abundance, there is no knowledge about its intrinsic nature, and not even whether it can be explained by particles.

At the moment the largest consensus is that dark matter should be explained by some class of particles, which, according to the astrophysical and cosmological observations, should be electrically neutral, collisionless, non-relativistic and with a lifetime of the same order as the age of the Universe or higher. It should be mentioned that non-particle explanations have been pursuit as well, such as modifications to the gravitational laws and massive compact halo objects (MACHOs).

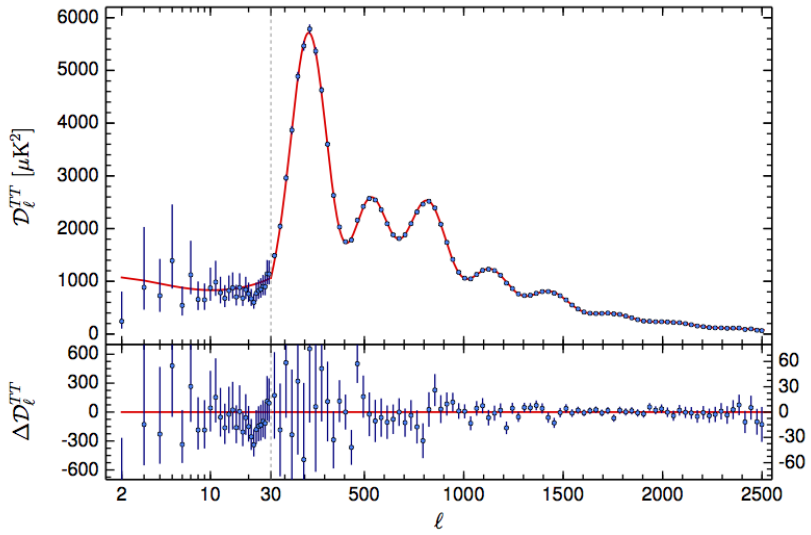

Figure 1.3.: Angular power spectrum of the CMB temperature map measured by the Plank experiment. The red line is the best fit of the ΛCDM model. For the description of the data the Plank experiment employs two different likelihood functions for the low multipole ($l \leq 29$) and for high multipole index ($l > 29$). The residuals of the fit are shown in the bottom panel. Figure taken from [4].

Modification to the Newton and Einstein laws of gravitation, aimed to explain the gravitational phenomena attributed to the dark matter, have been proposed since the first observations of inconsistencies at the galactic scales, and more recently introduced also to explain the cosmological observations [63, 64]. However, because of the strong success of the general relativity in describing with high accuracy the law of gravitation as well as the evolution of the Universe and some phenomena happened during its early times, there is not yet a shared consensus among the scientific community about these theories, for which there is still an open debate on their validity and the prediction power.

MACHOs, on the other hand are one hypothesis that tries to explain dark matter (or at least a significant part of it) in terms of baryonic matter, primarily for galactic systems.They consist of cold gas clouds of molecular hydrogen, planets, and non-luminous compact objects dispersed in the galactic haloes, such as brown and white dwarfs, and neutron stars, and also of black holes [65]. However, although these objects can explain up to 50 % of the baryonic matter content of such galaxy as the Milky Way, it was argued they hardly can explain the large mass of the galaxy dark halo [66, 67].

Beside the strong astrophysical motivations, there are also important arguments stemming from particle physics that ask for an answer, among which is the hierarchy problem and the strong CP problem. Unless accepting an highly un-natural fine-tuning of physical quantities, these problems lead to new physics beyond the Standard Model, and can as well provide good candidates for dark matter particles.

1.3.1 *Axions*

Axion has been originally proposed by Peccei and Quinn [68], to solve the problem originated from the so-called θ parameter in the QCD Lagrangian. As all the quarks

are massive, the θ parameter is expected to be non-zero, and it depends on the masses through the combination of another parameter $\overline{\theta} = \theta - \arg(\det M_{\rm q})$, where $M_{\rm q}$ is the quarks mass matrix. If $\overline{\theta} \neq 0$ the strong interaction would violate both CP and P, that has never been observed. Experiments on neutron electric dipole moment are compatible with zero constrains ($\overline{\theta} < 10^{-9}$), which seems to be a fine-tuning of the parameter θ with no explanations by the Standard Model. A solution consisted in introducing a global U(1) symmetry in the QCD Lagrangian, that its spontaneously broken below an energy scale $f_{\rm a}$ and thus would naturally (dynamically) bring the $\overline{\theta}$ parameter toward zero without requiring any unnatural fine tunings. The axion field, $a(x)$, is the resultant Nambu-Goldston boson associated to the spontaneous breaking of this approximate symmetry. Because of non-perturbative terms in the QCD Lagrangian the axion acquires a mass [69]:

$$m_{\rm a} \simeq 0.6\,{\rm eV}\frac{10^7\,GeV}{f_a}. \tag{1.40}$$

As any energy scale $f_{\rm a}$ is allowed for the solution of the strong CP problem, the axion mass is allowed to be in a wide interval that ranges from 10^{-12} eV to 1 MeV. Although the high energy details that can give origin to axions are not known, a low-energy effective model has been proposed by Georgi, Kaplan and Randall [70], which is valid between $\Lambda_{\rm QCD} \sim 1$ GeV and $E_{\rm EW}$ 250 GeV:

$$\mathcal{L}_a = \frac{1}{2}(\partial^\mu a)(\partial_\mu a) - \frac{a(x)}{f_{\rm a}}\frac{\alpha_{\rm s}}{8\pi}G^{\mu\nu}\widetilde{G}_{\mu\nu} - \frac{g_\gamma}{4}aF^{\mu\nu}\widetilde{F}_{\mu\nu} - \frac{\partial_\mu a}{2f_{\rm a}}\sum_f C_f\overline{\psi}_f\gamma_5\gamma^\mu\psi_f, \tag{1.41}$$

where G, F, $\widetilde{G}$, $\widetilde{F}$ are, respectively, the QCD and QED gauge fields and their duals. The index f runs over all the fermions of the Standard Model, and the g_γ, C_f coupling constants depend on the specific model [71, 72]. The axion lifetime can be estimated through the two-photons axion coupling:

$$\tau_{{\rm a}\to\gamma\gamma} = \frac{64\pi}{g_\gamma^2 m_{\rm a}^3}. \tag{1.42}$$

Assuming the coupling $g_\gamma \sim (0.1 - 1)$ they are expected to decay with lifetimes that can be many orders of magnitude higher than the age of the Universe.

As these particles couple to the electromagnetic field, strong experimental efforts have been undertaken to build detectors able to observe the conversion of cosmic axions into photons (or photon to axion conversion) in cavities with strong magnetic fields [73, 74]. Current searches constrain the axion mass between $\sim 1\mu$eV and 3 meV, that at first glance seems to be tiny for a cold dark matter candidate. However, since axions are expected to be produced in the very early Universe by a spontaneous symmetry breaking, and since their interaction with the Standard Model particles is extremely weak, axions did not undergo significant energy exchange with other species (thermalisation) and are expected to be non-thermal relics, most likely in a form of coherent motion particles.

Experiments that search for the axio-electric effect might eventually find any kind of pseuduscalar field that couples to the photons with a Lagrangian of the type:

$$\mathcal{L} = \frac{1}{4}g_\phi\phi F^{\mu\nu}\widetilde{F}_{\mu\nu}\,, \tag{1.43}$$

that clearly mimics the axion-photon interaction (see equation 1.41). Those hypothetical particles, called axion-like particles (ALP), arise in the low-energy spectrum of

several extensions to the Standard Model. They can be the pseudo Nambu-Goldston bosons of approximate continuous global symmetries, related to particle flavour [75], lepton number [76, 77] or to R-symmetry breaking in Supersymmetry [78–80]. Differently to the QCD axions, the ALP mass is not constrained by the energy scale of the symmetry breaking, and these particles might have masses several orders of magnitude higher than the QCD axions.

1.3.2 *Weakly Interacting Massive Particles*

Weakly interacting massive particles (WIMPs) is a compelling class of particles expected as thermal relic of the early Universe. According to the standard cosmological model, at times before the BBN and most likely also before the baryo- and lepto-genesis the Universe was in a state of dense hot plasma where the several species were in chemical equilibrium at $K_{\mathrm{B}}T > 1\,\mathrm{GeV}$. In such conditions, the process of creation-annihilation of dark matter particle pairs $\chi, \overline{\chi}$ from and to one or more species of the SM,

$$\chi + \overline{\chi} \rightleftarrows \psi_{\mathrm{SM}} + \overline{\psi}_{\mathrm{SM}}, W^+ + W^-, Z, 2\gamma, H,$$

might have been efficient enough to sustain the thermal equilibrium for a while during the expansion. As the creation of the DM pairs from the SM species is a threshold process, only the fraction of the high-energy tail of the energy distribution, above $m_\chi c^2$, participate in this process while the Universe expands. Hence, with the temperature drop, the production rate of the WIMP pairs decreased exponentially according to the Boltzmann distribution $e^{-m_\chi c^2/K_{\mathrm{B}}T}$. In addition, the expansion of the Universe further reduced both the annihilation and expansion rates as a result of the particle density drop (see section 1.1.2) and accordingly also the production and annihilation rates which are proportional to the particle densities.

This process is halted when the expansion rate of the Universe overcame the rate of annihilation and the dark matter particles decoupled from the plasma. After the decoupling the WIMP number did not significantly change, and their distribution froze at the last equilibrium distribution with an effective temperature that during the following Universe expansion scaled as $T_{\mathrm{eff}}(t) = T_{\mathrm{dec}}(a_{\mathrm{dec}}/a(t))$.

Using the results of section 1.1.2 it is possible to show that:

$$\frac{\mathrm{d}\,Y}{\mathrm{d}x} = \left(-\frac{\pi M_p^2}{45}\right)^{1/2} \frac{g_*^{1/2}(T)m}{x^2} \langle\sigma_{\mathrm{ann}}v\rangle \left(Y - Y_{\mathrm{eq}}\right), \tag{1.44}$$

where $M_p = \sqrt{\hbar c/G_{\mathrm{N}}}$ is the Plank mass (and G_{N} the gravitational constant), $\langle\sigma_{\mathrm{ann}}v\rangle$ is the product of the annihilation cross section times the relative velocity of the WIMPs averaged over their thermal distribution. The function $g_*(T)$ represents the temperature-dependent effective degree of freedom considering all the species participating in the energy exchanges. An accurate computation of this function can be found in [81], where also the QCD degrees of freedom are taken into account. In figure 1.4 the function $Y(x)$, obtained by numerical integration, is shown together with the equilibrium abundance $Y_{\mathrm{eq}}(T)$ for different values of $\langle\sigma_{\mathrm{ann}}v\rangle$ [82]. In the standard cosmological frame this scenario means that the WIMP density remains close to its equilibrium value, that is strongly suppressed with the drop of the temperature. As mentioned before, when the

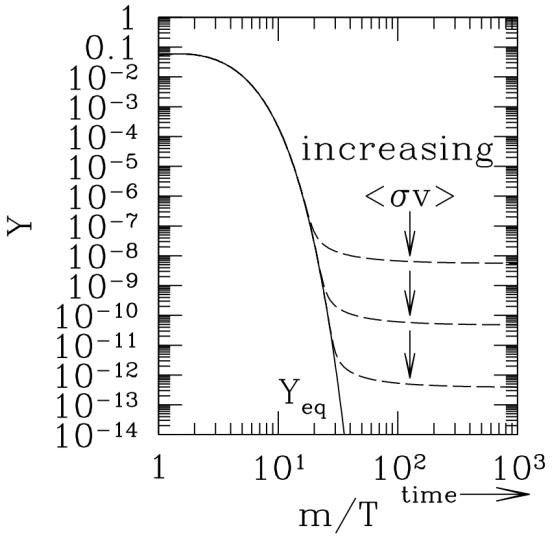

Figure 1.4.: Numerical solution to the equation 1.44 of the aboundance of a WIMP species initially in thermal and chemical equilibrium through the annihilation process with a SM species. The solution is shown for three different values of the mean annihilation rate $\langle \sigma_{\rm ann} v \rangle$, starting from a temperature $T_0 = m\chi c^2 / K_{\mathbf{B}}$. Figure from [82].

expansion rate of the Universe overcomes the annihilation rate, which corresponds to a WIMP mean free path close to the Universe scale, the WIMPs abundance departs from the equilibrium toward an almost constant relic density.

A rough estimation of the WIMPs relic abundance can be performed considering that $T_{\rm f.o.} \sim m_\chi c^2 / K_{\rm B}$ and thus:

$$\Omega_{\rm DM} h^2 \sim \frac{3 \times 10^{-27}\,{\rm cm^3 s^{-1}}}{\langle \sigma_{\rm ann} v \rangle}\,. \tag{1.45}$$

It is worth noting that for WIMPs with masses of the electroweak mass scale this approximate estimation would predict annihilation cross sections typical of the same energy scale. This is one of the strongest arguments that initially motivated the experimental efforts for WIMP searches.

Beyond the cosmological arguments, there are several proposals for the extensions of the SM that as byproduct predict new particles that can be good WIMP candidates. Among them the most compelling are the theory of supersymmetry, the Kaluza-Klein theories.

Supersymmetric theories represent a class of theories that extend the SM by associating to each bosonic and fermionic field of the Standard Model a fermionic and a bosonic supersymmetric partner (hereafter *sparticles*), respectively. As widely discussed this unification between force carriers (bosons) and matter fields (fermions) in supersymmetric multiplets has the advantage to be a very natural theory able to solve some specific open problems of the SM [83]. First, supersymmetry is able to stabilise the electroweak symmetry breaking of the SM (that is also known as the little hierarchy problem), curing the fine-tuning in the mass of the Higgs boson. Second, many of the R-parity conserving models predict a least stable particle (LSP) that is electrically neutral, massive and thus is an excellent cold dark matter candidate. Third, the introduction of the sparticles allows the unification of all the tree SM interactions above a specific energy scale, while in the SM the coupling constants of the three gauge fields

do not converge for a common energy. Although this theoretical framework can potentially provide solutions to important problems of the SM, the theory does not provide by itself the energy scale where the supersymmetry might show up, as well as for the sparticles masses. However, the little hierarchy problem arguments suggest that some of the predicted new particles might have masses down to 1 TeV, that is within the physics reach of the current colliders.

Kaluza-Klein theories is one of the extensions of the SM at the TeV energy scale, that would be able to provide a solution to the little hierarchy problem making use of hidden extra dimensions rather that supersymmetry. Early studies of extra dimensions were initially started by Kaluza [84] and later by Klein [85] in the 1920s in an attempt to unify the GR theory with the electromagnetism. In the 1980s the renaissance of the extra dimension physics came from the proposal of Arkani-Hamed, Dimopoulos, and Dvali (ADD) [86], which consists in lowering the energy scale of the quantum gravity, down to the TeV energies, by postulating the existence of n new warped extra dimensions, compactified into a volume of size R^n. Such a volume would therefore dilute the gravity strength from the natural scale Λ_{G} (for instance the TeV scale) to a much larger scale in the $3+1$ manifold of the SM, where the Plank mass would now be given by $M_{\mathrm{Planck}}c^2 = \Lambda_{\mathrm{G}}^{2+n} R^n$. As in the case of supersymmetry, there are a vast amount of extra-dimension models, and many of them are able to provide one or more stable or very long-lived electrically neutral particles at TeV scales, that on one hand provide a natural solution to some of the SM problems, and on the other hand provide good candidates for WIMP dark matter. More details about this kind of SM extensions and the most interesting extra-dimensions models for the WIMP searches are thoroughly reviewed in [87].

2

DARK MATTER SEARCHES

Investigation of dark matter interaction with SM particles is approached in three main classes of searches, which are sketched in figure 2.1: *indirect DM detection*, *collider DM particle production* and *direct DM detection*. Indirect DM detection consists in the searches for the signals of DM annihilation into SM particles from astrophysical objects, usually galactic centres. The signature of the production of a DM particle at the LHC, from high-energy proton-proton collisions, results in a lack of the measured energy in the final states, not compatible with the SM (for instance carried out by neutrinos). Direct DM detection consists in searches of signals from the scattering of cosmic relic DM particles off target nuclei. Since the three approaches are sensitive to different aspects of DM interactions with the SM particles, they provide the complementary information necessary to constrain the nature and properties of the DM particles.

2.1 INDIRECT SEARCHES

The annihilation of cosmic DM particles can produce stable SM particles such as γ-rays, electrons, neutrons, protons, neutrinos, or their antiparticles. However, most of these final states, especially those consisting of electrically charged particles, are also produced from several astrophysical processes in broad range of energies, which can constitute a strong and diffuse background for indirect DM searches. Among several channels, neutral particles and antiparticles are the most promising to look for DM annihilation signals.

Neutral particles such as γ-rays, neutrinos, and to some extent neutrons and antineutrons, are insensitive to the galactic and intergalactic magnetic fields, that in some specific regions can be very strong, and thus it is possible to trace back the direction and the location they originated from. As the dark matter is expected to reach the highest densities in the bulks of the galaxies, especially the spiral ones, this kind of final products are searched toward the Milky Way galactic centre. Hence, the signature of DM annihilation are localised signals featured by an energy spectrum that shows a peak corresponding to the mass of the DM particles. It should be mentioned that if on one hand this last requirement would provide a strong evidence in favour of DM detection, on the other side it would rule out all the annihilation channels where intermediate unstable SM particles mediate the process (for instance pions). An excess of $\sim 1 - 3\,\mathrm{GeV}$ γ-rays from the Galactic centre, observed by the Fermi-LAT telescope, has been interpreted by many authors as DM annihilation signature [88–91]. However, these claims have been weakened by the lack of detailed understanding of the astrophysical background and thus they are strongly debated. An unidentified spectral line at $3.5\,\mathrm{keV}$ has been very recently observed in the stacked XMM-Newton spectrum of

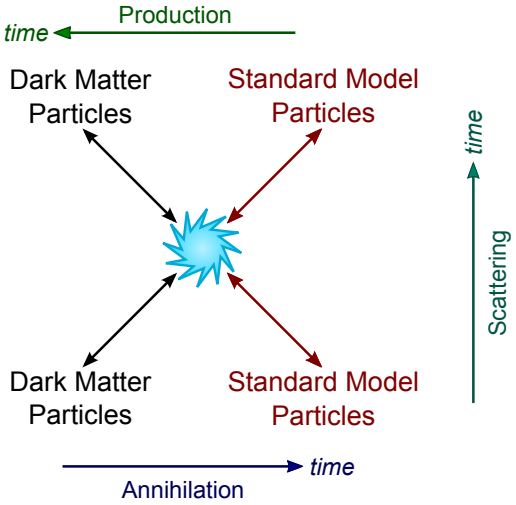

Figure 2.1.: The three different possible approaches for DM searches: indirect and direct detection, and production at particle collider.

73 galaxy clusters [92], and in the x-ray spectra of the Andromeda and Perseus galaxy cluster [93]. Although this signal would be consistent with ALP annihilation, no claims of DM detection have been yet put forward and analysis is still ongoing.

Searches for DM annihilation to antiprotons, positrons and antineutrons have the advantage of much lower background, as these particles are produced in astrophysical processes in much fewer abundances than the previously discussed classes of particles. However, they are expected (and observed) with a broad non-peaked spectrum, and thus a strong excess in some energy region of these particles would result in a very difficult interpretation as on evidence for DM annihilation, and the mass reconstruction would result strongly dependent on the model employed for the annihilation process. In addition, antiprotons and positrons are expected to be diffused by the random galactic magnetic fields, which makes it almost impossible to determine their production region. Further, their random walk trough the galaxy from the production location to the detector is expected to strongly modify their measured spectrum that would be hardly unfolded to determine their true spectrum. Claims of excesses of positrons consistent with DM annihilation results have recently been reported by the AMS collaboration, that confirmed previous PAMELA 2008 results [94], and provided a DM mass energy range between $\sim 700\,\mathrm{GeV/c^2}$ and $\sim 1\,\mathrm{TeV/c^2}$ [95]. However, there are alternative explanations of these excesses, as positrons can be produced from ordinary pulsar processes [96–98], and thus this claim is still debated among the scientific community.

2.2 DARK MATTER SEARCHES AT COLLIDERS

Dark matter can be produced at colliders from high-energy proton-proton collisions if the coupling to the SM matter is sufficiently large. A DM particle eventually produced in a collision of HE protonts would leave the detector without being detected, as it occurs for neutrinos. If final state of the DM particle was produced together with other detectable particles, such as γ-rays and/or charged light particles, it would be possible to infer their presence by observing a missing momentum in the visible particles.

There are two classes of events associated with DM production at colliders. The first consists of events where heavy short-lived particles are strongly coupled to DM particles, where the latter are produced together with the lighter visible products in the decay process of the massive state. The final states of this class of events are featured by multi-jets and by missing momentum in the visible states. The DM production rate in these states is weakly dependent on the mass of the DM particles, as it mostly depends on the production rate of the primary massive state.

The second class of candidate events for the collider-based DM searches are those where the DM particle is produced directly from the interaction with the partons participating to the collision. This class of events are featured by "mono-jets" and by missing momentum of the recoiled DM product. Since in this case the production of the DM particle does not rely on specific QCD properties of any additional heavy state, the results are less model dependent and they directly probe the interaction strength and the particle mass.

As dark matter particles are predicted in a very wide region of the parameter space, and no properties are known about their nature, with the exception of their electrical neutrality and substantial stability, it would be highly desirable to develop a detection approach as much as possible independent of the specific model of their interaction. This requirement is partially fulfilled by the Effective Field Theories (EFT) approach, which consists in the description of the DM-SM interaction with a minimal number of parameters. This is realised by mean of an effective Lagrangian of the type:

$$\mathcal{L}_{\text{int}} = C \left(\overline{\psi}_{\chi} \Gamma^{\chi} \psi_{\chi}\right) \left(\overline{\psi}_{\text{q}} \Gamma^{\text{q}} \psi_{\text{q}}\right), \tag{2.1}$$

where ψ_{χ} and ψ_{q} are the DM and quark (fermionic) fields, respectively. The operators $\Gamma^{\chi,\text{q}}$ are appropriate combinations of the sixteen 4×4 matrices $\{1, \gamma_5, \gamma^{\mu}, \gamma_5\gamma^{\mu}, \sigma^{\mu\nu}\}$, that all together represent a complete basis of spinor operators. Although this approach is explicitly independent on the heavier degrees of freedom of the specific UV microscopic theory that mediates the interaction, its range of validity depends on the mass m_{χ} and on the specific energy scale cutoff Λ, above which the model is not anymore unitary.

Recent analysis of the LHC data at 8 TeV and 13 TeV in the *pp* centre-of-mass, searching for the signatures of DM production in association with a top quark pair, reported no significant excess of events above SM predictions [99, 100]. The results of the 8 TeV and 13 TeV runs have been interpreted with a scalar EFT model and a scalar massive mediator, respectively. In figure 2.2 the limits on the coupling as a function of the dark matter particle mass are shown, together with the results from direct DM search experiments. From the 8 TeV data, cross sections larger than 20 to 55 fb are excluded at 90 % CL for DM masses from 1 GeV/c^2 to 1 TeV/c^2. The direct searches show much more stringent limits for masses below ~ 6 GeV/c^2.

2.3 DIRECT SEARCHES

As discussed in the previous sections, most of the masses of galaxies are constituted by dark matter, hence the Solar System and the Earth itself are likely to be immersed in a cloud of WIMPs. Assuming that in the early Universe these particles annihilated into SM particles, the cold cosmic WIMPs might have some very faint residual interaction rate with ordinary matter. As the most favoured WIMP candidates are expected to in-

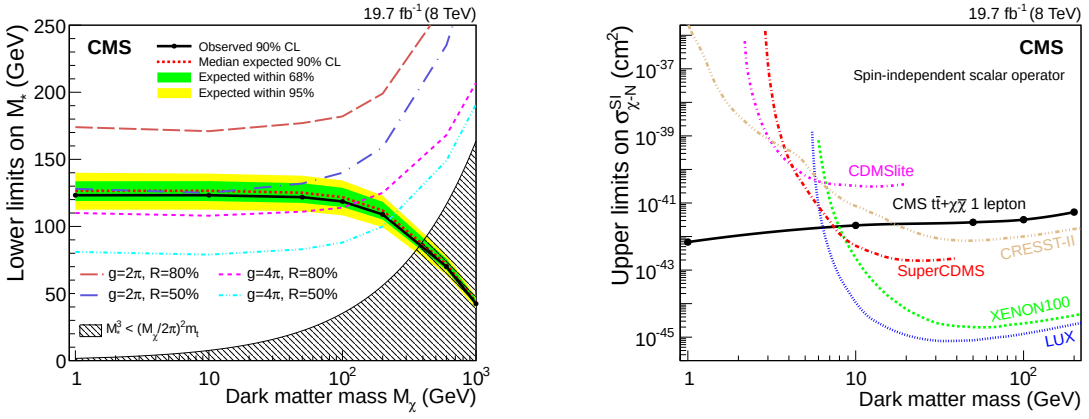

(a) **(b)**

Figure 2.2.: (a) Observed (black solid line) and expected (coloured bands) exclusion limits in the plane of the DM particle mass m_χ and the energy cutoff M_*, performed with the CMS experiment on the 8 TeV data. The region below the solid line is excluded at 90 % CL. The dashed red line is the median expectation from background only and the green and yellow zones the corresponding $\pm 1\sigma$ and $\pm 2\sigma$ CL bands, respectively. The shaded area represents the region where the minimal requirements for the EFT interpretation of the data are not satisfied.
(b) Corresponding upper limit, at 90 % CL, for the DM-nucleon spin-independent cross section as a function of the DM particle mass m_χ, compared with other direct DM searches. Figures from [99].

teract primarily with atomic nuclei, and since WIMPs are expected to be non-relativistic particles, these interactions are expected as elastic scattering nuclear recoils.

2.3.1 *Interaction differential rate*

As the Solar System in its journey around the Galaxy centre is believed to move through an almost uniform stationary DM halo, it is possible to estimate the interaction rate at the Earth if the local WIMP density, ρ_χ, and its velocity distribution (in the laboratory frame) $f_\chi(\mathbf{v})$ are known. With those ingredients it is possible to express the WIMP differential interaction rate per unitary target mass as:

$$\frac{\mathrm{d}\,R}{\mathrm{d}E_\mathrm{R}}(E_R) = \frac{\rho_\chi}{m_\mathrm{N} m_\chi} \int_{v_\mathrm{min}}^{v_\mathrm{esc}} v f(\mathbf{v}) \frac{\mathrm{d}\,\sigma}{\mathrm{d}E_\mathrm{R}}(E_\mathrm{R}, v) \mathrm{d}^3 v, \tag{2.2}$$

where $v_\mathrm{min} = \sqrt{E_\mathrm{R} m_\chi / 2\mu_{\chi N}^2}$ is the minimal WIMP velocity able to produce a recoil of energy E_R, $\mu_{\chi N}$ is the reduced mass of the WIPM-nucleon system, and v_esc is the escape velocity from the galactic gravitational well. As typical WIMP velocities are of the order $10^{-3}c$, the energy release in a collision with a nucleus can be approximated as:

$$E_\mathrm{R}^{(\mathrm{max})} = 2\frac{x}{(1+x)^2}\left(\frac{m_\mathrm{N} c^2}{\mathrm{GeV}}\right)\ \mathrm{keV}, \tag{2.3}$$

where $x = m_\chi / m_\mathrm{N}$. The unit for this quantity is the *differential rate unit* (hereafter *dru*) defined as $1\,\mathrm{dru} = 1\,\mathrm{events\,kg^{-1}d^{-1}keV^{-1}}$. Hence, typical nuclear recoil energy scale is in a range between few to tens of keV for WIMP masses between 1 GeV and

1 TeV. As will be shown in what follows, this might pose a strong challenge for some classes of detectors, which is related to their threshold-induced detection sensitivity. Given the low recoil energies expected from a WIMP-nucleus elastic scattering, an additional challenge is represented by the natural radioactivity and by the cosmic rays (CR) induced background, that can be higher than the expected signal rate by several orders of magnitude. Hence, special efforts are required in the design and construction phases of these detectors, aimed to control and limit the background to tolerable levels, based on the planned exposure and the aimed detection sensitivity. This topic will be detailed in chapter 3 for the case of the XENON1T detector.

The distribution of the velocities of the WIMPs in the dark halo rest frame, $\mathbf{v}'$, can be obtained from the stationary state of the Vlasov equation for a self-gravitating gas. This results in an isothermal sphere of density profile $\rho_\chi(r) \propto r^{-2}$, with Maxwellian velocity distribution. Considering the Earth relative velocity, $\mathbf{v}_\mathrm{E}$, with respect to the halo the WIMP velocity distribution function in the laboratory frame is given by:

$$f(\mathbf{v}) = k \exp\left[-\frac{(\mathbf{v}+\mathbf{v}_\mathrm{E})^2}{2\sigma_\mathrm{v}^2}\right], \tag{2.4}$$

where k is a normalisation factor that takes into account the truncation of the velocity distribution for $v' > v_\mathrm{esc}$, and σ_v is the dispersion velocity of the halo particles.

From astrophysical observations and detailed simulation for galactic haloes, a local WIMP density energy $\rho = 0.3\,\mathrm{GeV/cm^3}$ is widely accepted [101]. This local DM density value assumes a spherical dark halo, while it might be higher in case the Milky Way dark matter has also a dark disk. Although there are several observations converging toward the commonly used local DM density, the accuracy is not yet satisfactory and future satellite experiments are expected to strongly improve the accuracy as well as the precision. The accepted distance from the Solar system to the galactic centre is $r_\odot \simeq 8\,\mathrm{kpc}$, and recent studies find the Sun circular velocity $v_\mathrm{c} = (220 \pm 18)\,\mathrm{km/s}$ [102]. Considering the annual motion around the Sun the value is taken as the mean relative velocity of the Earth with respect to the galactic halo. The local escape velocity $v_\mathrm{esc} = \sqrt{2|\Phi(r)|}$ has been recently assayed at $v_\mathrm{esc} = 553^{+54}_{-41}\,\mathrm{km/s}$ by [103].

2.3.2 *Interaction types*

Another important ingredient that enters in the expected differential interaction rate calculation is the WIMP-nucleus cross section $\sigma(E_\mathrm{R}, v)$, where the nature of the searched particles and of their interactions with the SM matter are encoded (although not known yet). The differential cross section is generally represented as the sum of a *spin-independent* (SI) and *spin-dependent* (SD) components:

$$\frac{\mathrm{d}\,\sigma}{\mathrm{d}E_\mathrm{R}} = \frac{m_\mathrm{N}}{2\mu^2 v^2}\left[\sigma_0^\mathrm{SI} F_\mathrm{SI}^2(E_\mathrm{R}) + \sigma_0^\mathrm{SD} F_\mathrm{SD}^2(E_\mathrm{R})\right], \tag{2.5}$$

where the $\sigma_0^\mathrm{SI,SD}$ are the spin-independent and spin-dependent WIMP-nucleus cross sections at zero momentum transfer, and contain all the information on the specific interaction. The form factors $F_\mathrm{SI,SD}^2(E_\mathrm{R})$ depend on the nucleons distribution and thus on the nuclear energy spectrum of the specific target nuclei. In plane wave Born approximation the form factors correspond to the Fourier transform of the density

distribution of the nucleons (the "scattering centres"). As detailed in [104], in the assumption that the WIMP-SM effective interaction occurs with the quarks in the nucleons, the SI contribution arises from the scalar-scalar and vector-vector couplings for a Dirac WIMP candidate and from the scalar-scalar for a Majorana candidate. Scalar, self-conjugate (real) WIMP candidate fields can yield only SI interaction, while in the case of vector candidates the SI part comes from the scalar coupling to the quarks. All the other possible WIMP-quark couplings lead to SD cross sections.

At nuclear level the SI WIMP-nucleon cross section assumes the form:

$$\sigma_0^{\mathrm{SI}} = \frac{4\mu_{\chi\mathrm{n}}^2}{\pi}\left[Zf^{(\mathrm{p})} + (A-Z)f^{(\mathrm{n})}\right]^2, \tag{2.6}$$

where $\mu_{\chi\mathrm{N}}$ is the WIMP-nucleus reduced mass, A and Z are the mass and the atomic number of the target nucleus, respectively. The factors $f^{(\mathrm{p,n})} = \langle \mathrm{p,n}|m_{\mathrm{q}}\bar{q}q|\mathrm{p,n}\rangle/m_{\mathrm{p,n}}$ represent the contributions of the quarks to the proton (p) and neutron (n) masses, respectively, where in most cases the WIMP-nucleon couplings are very similar and thus $f^{(\mathrm{p})} \approx f^{(\mathrm{n})}$ is an acceptable approximation. Hence, for target nuclei where $Z \approx A/2$ the SI cross section is given by:

$$\left(\frac{\mathrm{d}\,\sigma}{\mathrm{d}E_{\mathrm{R}}}\right)_{\mathrm{SI}} \simeq \frac{2\mu_{\mathrm{N}}A^2\left(f^{(\mathrm{p})}\right)^2}{\pi v^2}F_{\mathrm{SI}}^2(E_{\mathrm{R}}), \tag{2.7}$$

hence, in general it is true that heavier target nuclei provide better detection sensitivity to SI WIMP interaction searches.

The SD interactions lead in general to nucleus matrix elements of the type:

$$\langle N|\overline{\psi_{\mathrm{q}}}\gamma_\mu\gamma_5\psi_{\mathrm{q}}|N\rangle = 2\lambda_{\mathrm{q}}^N\langle N|J_{\mathrm{N}}|N\rangle, \tag{2.8}$$

were J_{N} is the nuclear angular momentum, and λ_{q}^N are coefficients that express the contribution of the quarks to the angular momentum of the nucleons with terms as $\langle n,p|\overline{\psi_{\mathrm{q}}}\gamma\mu\gamma_5\psi_{\mathrm{q}}|n,p\rangle$. Therefore the SD cross section in the case of fermionic WIMP results [105]:

$$\left(\frac{\mathrm{d}\,\sigma}{\mathrm{d}E_{\mathrm{R}}}\right)_{\mathrm{SD}} \simeq \frac{16m_N}{\pi v^2}G_F^2\frac{J+1}{J}\left[a_{\mathrm{p}}\langle S_{\mathrm{p}}\rangle + a_{\mathrm{n}}\langle S_{\mathrm{n}}\rangle\right]^2 F_{\mathrm{SD}}^2(E_{\mathrm{R}}), \tag{2.9}$$

where $a_{\mathrm{p,n}}$ are effective WIMP-proton/neutron couplings, respectively, $\langle S_{\mathrm{p,n}}\rangle = \langle N|S_{\mathrm{p,n}}|N\rangle$ are the expected spin values of the proton and neutron groups in the nucleus, which can be estimated from nuclear magnetic moment measurements taking into account the model for a specific nucleus [106]. Since $\langle S_{\mathrm{p,n}}\rangle$ are zero for an even number of a nucleon groups, only odd-even and odd-odd target nuclei are sensitive to SD interactions, while no advantages are gained in using high A nuclei. Because of this considerations, it should be noted that the term $\left[a_{\mathrm{p}}\langle S_{\mathrm{p}}\rangle + a_{\mathrm{n}}\langle S_{\mathrm{n}}\rangle\right]^2 \sim J^2$, hence the actual enhanchment term in SD WIMP-nucleus cross section is $\propto J(J+1)$.

Since the nuclei are not point-like, the effects of nucleons distribution and their internal currents must be taken into account by means of the nuclear form factors, expressed as a function of the exchanged momentum in the interaction. In general, the form factors are significant as they are responsible for the differential interaction rate suppression

at higher energy recoils. Their calculations are based on the detailed knowledge of the excited nuclear energy properties and on the specific interaction type at quark level. Recent calculations based on chiral EFT have been published in [107, 108]

2.3.3 *Detector-induced effects*

The rate in equation 2.2 is the predicted WIMP interaction rate in the detector, however its response in general modifies both the rate and shape of the original differential spectrum. Among several effects that modify the rate, three are common to any class of detectors for direct DM searches: the energy-dependent detection efficiency, the energy resolution and the threshold cutoff. Other effects, less general and peculiar to each experiment, that also modify the observed spectrum, are those related to the specific hardware properties, performance and operational conditions, and those coming from the data manipulation in the analysis phase.

The detection efficiency is more common to detectors that are sensitive to the scintillation and to the ionisation produced by an energy deposit, while phonon based detectors suffer less from this effect. In this kind of detectors an energy deposit can produce a different amount of photons or electrons generated in the interaction, depending on whether the energy is deposited as an electronic or a nuclear recoil (hereafter ER and NR). This results in different reconstruction of the two energy scans based on the interaction type, that is mostly related to the intrinsic response properties to ionising radiation of the detection medium. Since the detector response can fluctuate during the operation, calibrations at regular intervals are performed. Usually it is more convenient to calibrate the ER energy response with γ emitters whose spectral lines will be recognised as prominent peaks in the differential rate spectrum.The calibration of the NR response is then performed by means of neutrons which however will be seen as a continuum, featureless spectrum. Because of this, dedicated studies are performed with R&D detectors in order to calibrate the ER and NR response of the detection medium, usually using an effective parameter defined as:

$$f_{\mathrm{n}}(E_{\mathrm{R}}) = E_{\mathrm{o}}/E_{\mathrm{R}}, \tag{2.10}$$

where E_{o} is the energy inferred from the measured scintillation and/or ionisation, based on the ER energy scale. In literature this energy-dependent factor is referred as NR *quenching factor*, and corresponds to the energy fraction of NR that does not contribute to the signal. Therefore, the observed differential rate R_{o} is related to the true rate by:

$$\frac{\mathrm{d}\,R_{\mathrm{o}}}{\mathrm{d}E_{\mathrm{o}}} = f_{\mathrm{n}}\left(1 + \frac{E_{\mathrm{R}}}{f_{\mathrm{n}}}\frac{\mathrm{d}\,f_{\mathrm{n}}}{\mathrm{d}E_{\mathrm{R}}}\right)\frac{\mathrm{d}\,R}{\mathrm{d}E_{\mathrm{R}}}. \tag{2.11}$$

Such a study is the central topic of chapter 5, where the development of a liquid xenon (LXe) detector for precision studies of low-energy NRs is detailed.

The finite energy resolution of the detector induces event by event random fluctuation of the observed energy E'_{o} around its true value E_{o}. This can be due to intrinsic random fluctuations of the amount of excitation in the interactions (photons, ionization, phonons), to efficiency-based processes (binomial process) and to the instrumental fluctuations (e.g. electronic noise). This process can be modelled by the convolution of the

rate $(\mathrm{d}\,R_\mathrm{o}/\mathrm{d}E_\mathrm{o})$ with a "smearing function", usually a zero mean normalised Gaussian with σ_{E_o} width:

$$\frac{\mathrm{d}\,R'_\mathrm{o}}{\mathrm{d}E_\mathrm{o}} = \frac{\mathrm{d}\,R_\mathrm{o}}{\mathrm{d}E_\mathrm{o}}(E_\mathrm{o}) * G(E_\mathrm{o}, \sigma_{E_\mathrm{o}}). \tag{2.12}$$

where the $*$ symbol represents the convolution operation.

The energy cut-off in a detector is due to threshold-based effects that suppress the relative response of a detector below a certain energy. This effect is usually modelled by a threshold efficiency function $T(E)$, which has the only requirements $T(0) = 0$ and $T(E_\mathrm{thr}) \simeq 1$, that is usually modelled by a sigmoid function such as a smooth step function or a Fermi-Dirac function, depending on the specific case. Threshold effects can be present at different levels in the conversion process from the true recoil energy E_R to the observed energy E_o, hence each of the differential rates above should be multiplied by its own $T(E)$. The threshold effect in the $(\mathrm{d}\,\sigma/\mathrm{d}E_\mathrm{R})$ rate should usually be negligible provided the detection mean is suitable for the energy range of interest. For the observed rate $(\mathrm{d}\,R/\mathrm{d}E_\mathrm{o})$ threshold effects can be recognised in the detection process of the measured quantity (for instance photons in a scintillation detector), that should be taken into account before the resolution is applied with a function $T_2(E_\mathrm{o})$, and the effects due to the active components (for instance a constant threshold discriminator for event triggering) should be applied to the observed spectrum after the resolution has been applied, using threshold function $T_3(E_\mathrm{o})$. It should be mentioned that these threshold cut-off efficiencies might play an important role not only in the observed differential rate interpretation for the dark matter search, but also when the NR energy detection efficiency of the target material is calibrated. In this case, if threshold effects are not properly considered, they might lead to a bias in the determination of the target material low-energy response, namely in an overestimation of the quenching factor f_n for the low-energy part. This can lead to an overestimation of the experimental sensitivity to WIMP-nucleus interaction, because of an inaccurate interpretation of the low-energy part of the observed differential rate in the scientific run for dark matter searches.

Considering only the listed detector-related effects, common to almost all low-energy particle detectors, the final observed rate to be used for a data analysis is given by:

$$\begin{aligned}\left(\frac{\mathrm{d}\,R}{\mathrm{d}E_\mathrm{o}}\right)_\mathrm{tot} = \Bigg\{\Bigg[\left(f_\mathrm{n} + E_\mathrm{R}\frac{\mathrm{d}\,f_\mathrm{n}}{\mathrm{d}E_\mathrm{R}}\right)\left(\frac{\mathrm{d}\,R}{\mathrm{d}E_\mathrm{R}}\right) T_1(E_\mathrm{R})\cdot \\ \cdot\, T_2(E_\mathrm{o})\Bigg] * G(E_\mathrm{o}, \sigma_{E_\mathrm{o}})\Bigg\} T_3(E_\mathrm{o})\,,\end{aligned} \tag{2.13}$$

where, as mentioned, for a properly chosen detection material $T_1 \simeq 1$ in the energy range of interest.

2.3.4 *Detection techniques*

There are a large variety of techniques that search for WIMP-nucleus interactions, and a thorough review of them can be found in [109], while here only a brief overview of the current generation detectors is given. The WIMP signal is searched in three main channels: as scintillation photons (light channel), as ionised electrons (charge channel), and as lattice vibrations (phonon/heat channel). There are several running dark matter experiments for each of these excitation channels. In addition, there are

several experiments that combine signals from the two excitation channels, that have the advantage of being able to discriminate ERs from NRs with high efficiency ($> 99\,\%$). This is possible because slow NRs produce ionisation less efficiently than ERs, while it is the opposite for the efficiency of phonon production. The ER discrimination allows therefore a strong suppression of the background from γ and β radiation, and at the moment dual-channel based experiments are those that set the most stringent limits on the WIMP-nucleon SI cross section, such as XENON100 [110], LUX [111], CREST II [112], PandaX [113] and the XENON1T experiment [114].

Cryogenic detectors that operate at the sub-Kelvin temperature are featured by a very low-energy threshold ($< 10\,\mathrm{keV}$) and a typical resolution better than $1\,\%$ at $10\,\mathrm{keV}$ [112, 115]. This good energy resolution is due to their use as bolometers, exploiting the T^3 thermal capacity dependence of ultracold detectors.

A relatively recent class of dark matter search detectors are superheated detectors [116–118], mainly based on the fluorine target, where the SD WIMP-nucleon cross-section sensitivity is enhanced up to a factor ~ 10 due to $^{19}\mathrm{F}$ that is the only isotope present in natural fluorine. They are based on the well established principle used for the bubble chambers, where in this case the metastable thermodynamic state of the liquid medium is broken when energy above a certain threshold is deposited as ER or NR. When the metastable state is broken, the bubble formation can be detected both optically and acoustically. As the pressure and temperature can be adjusted in order to allow the bubble formation only for NRs, these detectors are almost insensitive to ER from γ radiation. The remaining background is mostly due to the α decays of radon and its daughters, that however can be discriminated by means of the acoustic signals. Sensitivity studies have shown that the current generation superheated detectors are capable of probing SD WIMP-nucleus cross section down to $\sim 6 \times 10^{-39}\,\mathrm{cm}^2$.

Noble-gas detectors operated in dual phase (liquid-gas), read both the light and the charge signals produced by an interaction in liquid. This allows a very efficient ($> 99.5\,\%$) ER discrimination, with a good acceptance to NRs ($\sim 50\,\%$) and without a significant reduction of the detection sensitivity. At the moment of writing, the XENON1T experiment [114] is the one that set the most stringent limits to SI WIMP-nucleon cross section $\sigma_{\mathrm{SI}} < 7.7 \times 10^{-47}\,\mathrm{cm}^2$ ($90\,\%$ CL) for $m_\chi = 35\,\mathrm{GeV/c^2}$. Projection studies show that for WIMP masses from $5\,\mathrm{GeV/c^2}$ up to few $10\,\mathrm{TeV/c^2}$ the dual-phase xenon TPCs seem to be the most promising detectors to probe the WIMP-nucleon interactions down to SI cross sections of $\sigma_{\mathrm{SI}} \sim 10^{-49}\,\mathrm{cm}^2$ [119] (at $m_\chi \sim 50\,\mathrm{GeV/m^2}$), using LXe target masses $\sim 50\,\mathrm{tonne}$ and exposure time of $\sim 2\,\mathrm{y}$. For WIMP masses $\lesssim 5\,\mathrm{GeV/c^2}$, the *pp*-chain, $^7\mathrm{Be}$ and $^8\mathrm{B}$ solar neutrinos will be an irreducible background in the low-energy recoil spectrum that will limit the sensitivity of these detectors to $\sim 10^{-8}\,\mathrm{cm}^2$. For higher masses, NRs induced from atmospheric and diffuse supernovae neutrinos will limit the sensitivity to the ultimate value of $10^{-49}\,\mathrm{cm}^2$ [120–123]. In figure 2.3 the limits of recent experiments and projected sensitivities of planned experiments are shown, together with the ultimate sensitivity imposed by the neutrino backgrounds.

2.4 DIRECT WIMP DETECTION WITH LIQUID XENON

Among several target materials for particle detection, liquid xenon has some peculiar properties, that, since the start of its employ as detection medium it, it represented an

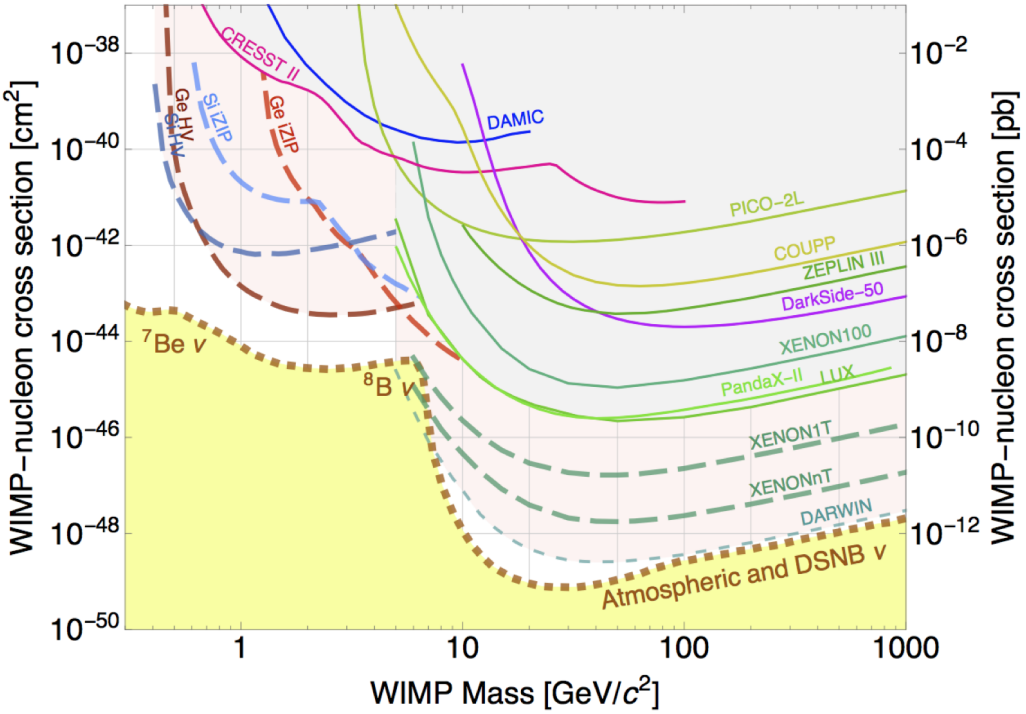

Figure 2.3.: Exclusion upper limits (90 % CL) for SI WIMP-nucleon cross section from several recent direct dark matter searches, and projected sensitivities for some dark matter experiments in design or commissioning phase. The dotted brown curve represents the ultimate sensitivity imposed by the irreducible neutrino backgrounds in the ER and NR spectrum.

attractive option for direct dark matter searches. Xenon is present in the atmosphere at concentrations of $\sim 10^{-7}$ g/g and is obtained as the byproduct of the air liquefaction when oxygen is separated from nitrogen. Because of this, it can be produced in relatively large quantities with reasonable costs, on the order of 1000 US dollars, and thus detectors with masses up to several ton can be achieved with joined efforts of multiple research institutions. In addition, as xenon liquefies at 165 K for standard conditions ($P = 1$ atm), large masses of xenon can be easily kept in liquid state with cryogenic systems with standard designs and standard instrumentation.

Natural xenon consists of eight stable isotopes (see table 4.2), and only one unstable isotope, the ^{136}Xe, that decays by double β emission to ^{136}Ba with a half-life of 2.165×10^{21} y [124], and thus can be also considered stable. In addition, the only relevant cosmogenically produced radioisotope is the metastable ^{127}Xe that decays by electron capture to ^{127}I ground state with a half-life of 36.3 d. As will be shown in chapter 4, this and other cosmogenic radioactive products of xenon do not pose any relevant background problems for the rare event searches.

As particle detection medium LXe features a relatively high scintillation yield, on the order of $\sim 10^7$ photons/keV for relativistic electrons [125], thus is suitable for the energy deposits expected from WIMP-nuclei interactions. Because of the mechanism of conversion of the atomic excitation to *vacuum-ultra-violet* (VUV) photons with $\lambda = 175$ nm, the LXe is transparent to its own scintillation light and can be efficiently instrumented with VUV-sensitive photon detectors. In addition, when a particle interacts with LXe, ionisation electrons are produced with a relatively high yeld, of the same order as photons. Because of the relatively high mobility of electrons in LXe they can be drifted

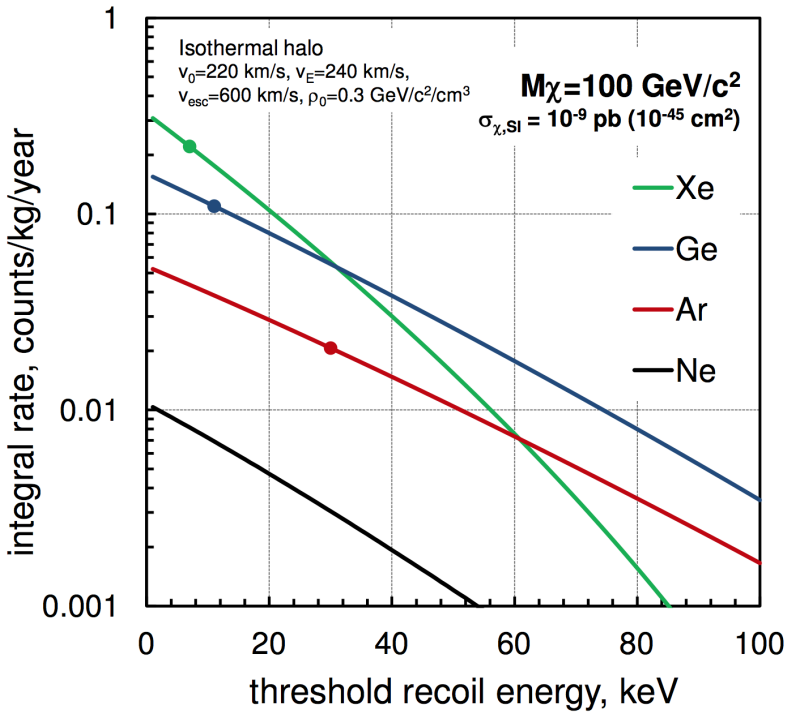

Figure 2.4.: Comparison of the expected WIMP rates for different detection media, assuming the WIMP mass of 100 GeV/c^2, galactic dark matter energy density $\rho_{\mathrm{DM}} = 0.3\,\mathrm{GeV/cm^3}$, and SI WIMP-nucleus cross section $\sigma_{\mathrm{SI}} = 10^{-45}\,\mathrm{cm}^2$. Figure from [126].

by an electric field, that allows for the simultaneous light and charge measurements of the interaction events. This allows discriminating electron recoils (ER), produced by the interaction of the γ- and β-radiation with the xenon atoms, from nuclear recoils (NR), that are expected to be produced by WIMP-nucleus interactions and by neutral radiation as in case of neutrons.

The high mass number A of xenon and the presence of the two naturally occurring isotopes ^{129}Xe and ^{131}Xe , featured by an unpaired neutron, makes this element one of the most favoured targets for direct WIMP searches. As seen in section 2.3, the former property allows for probing SI WIMP-nucleus cross sections with higher sensitivity compared to other targets employed for direct WIMP detection, while the latter allows to search for SD WIMP-nucleon interactions with sensitivity comparable to other targets. In figure 2.4 the expected WIMP interaction rates are shown as a function of the recoil energy, for a WIMP mass of 100 GeV/c^2 and a SI WIMP-nucleon cross section of $\sigma_{\mathrm{SI}} = 10^{-45}\,\mathrm{cm}^2$, now strongly excluded by several experiments. Including the weak nuclear form factors, it is evident that xenon offers an advantage in terms of sensitivity to low-energy NRs with respect to other noble gases and to germanium, that is among the most competitive cryogenic bolometer materials. A very rough estimate of the total WIMP-nucleus interaction rate for $\sigma_{\mathrm{SI}} \sim 10^{-47}\,\mathrm{cm}^2$ is of order $\sim 10^{-3}$events/kg yr, and about an order of magnitude lower for argon. The much steeper suppression of the expected rate with energy increase for xenon is due to its nuclear form factor, which becomes almost zero at energies of ~ 100 keV. However, because of this quasi-exponential recoil spectrum, the energy threshold is fundamental for the achievement of the aimed detection sensitivity.

2.4.1 *Energy absorption in LXe*

The energy loss of a particle in LXe occurs with three main mechanisms: elastic scattering with the xenon nuclei or with the atoms (*heat*), creation of excited xenon atoms (*direct excitation*), Xe^* (*excitons*), and through the production of electron-ion pairs (ionisation) [127]. Electrons (or β-rays), α-particles, X- and γ-rays interact primarily by inelastic collisions with the atomic electrons, producing mainly direct excitation and ionisation, while the energy losses through elastic scattering with xenon atoms are negligible. In addition, for electrons above 1 MeV the energy losses occur also by radiative emissions (*bremsstrahlung*), however their contribution becomes significant at energies much higher than those of interest for dark matter searches. Nonrelativistic heavy charged particles and neutrons lose a large fraction of their energy through elastic scattering with the Xe atoms (*heat*). Since only the energy that is released through the two types of electronic excitations can be measured in a LXe-based detector, this fraction will result in a quenching of the output signal, and for a correct energy reconstruction it must be characterised for the interactions of interest (e.g. for nuclear recoils).

Self-shielding of liquid xenon

For electrons with energies below ~ 1 MeV the LXe stopping power increases with the decrease of the energy, hence the electronic excitation along their tracks is expected to be stronger at the end than at the start. The opposite is true in the case of α particles and of nonrelativistic heavy ions. The relatively high stopping power featured by LXe for most of the charged particles is mainly due to the relatively high atomic number ($Z = 54$) and density ($\rho = 2.96\,\mathrm{g/cm^3}$), which this detection material provides. This is shown in figures 2.5 and 2.6, for fast electrons and α particles, respectively, where for both particles the contributions from different energy loss processes are also shown.

Similar properties are also valid for X- and γ-rays that are expected to be absorbed by LXe with a relatively high-efficiency. The interaction cross section for this kind of radiation is shown as a function of energy in figure 2.7, where the contribution of the different processes is separated. This radiation interacts with matter through photo-absorption, Compton and Rayleigh scattering, and by pair production. In liquid xenon the first process is the dominant one below ~ 200 keV, and the relative cross section decreases with the γ energy. The photo-absorption cross section is featured by some discontinuities at ~ 5 keV and ~ 32 keV, that correspond to the L- and K-shell edges, respectively. Namely, they are the threshold energies above which the atomic electrons of the two shells participate in the photo-absorption process, thus inducing an abrupt increase of the cross section. Gamma-rays in this low-energy region are strongly absorbed by liquid xenon with mean free-paths of a few mm. Above this energy Compton scattering starts to play a role becoming the dominant interaction process from ~ 300 keV to ~ 6 MeV, with typical mean free paths ranging from few cm up to ~ 10 cm. Pair production is a threshold process ($E_\gamma > 2m_e c^2 = 1.02$ MeV) and it becomes a dominant process in LXe only at energies above 5 MeV, that are however energies already much higher than the energies emitted from radioactive sources. All this phenomenology is deeply linked to the background expected in a liquid xenon detector for rare event searches, and it will be better detailed for the case of the XENON1T detector in the next chapter.

The listed absorption properties of liquid xenon for the ionising radiation provide to this detection medium a relatively strong self-shielding power against this kind of

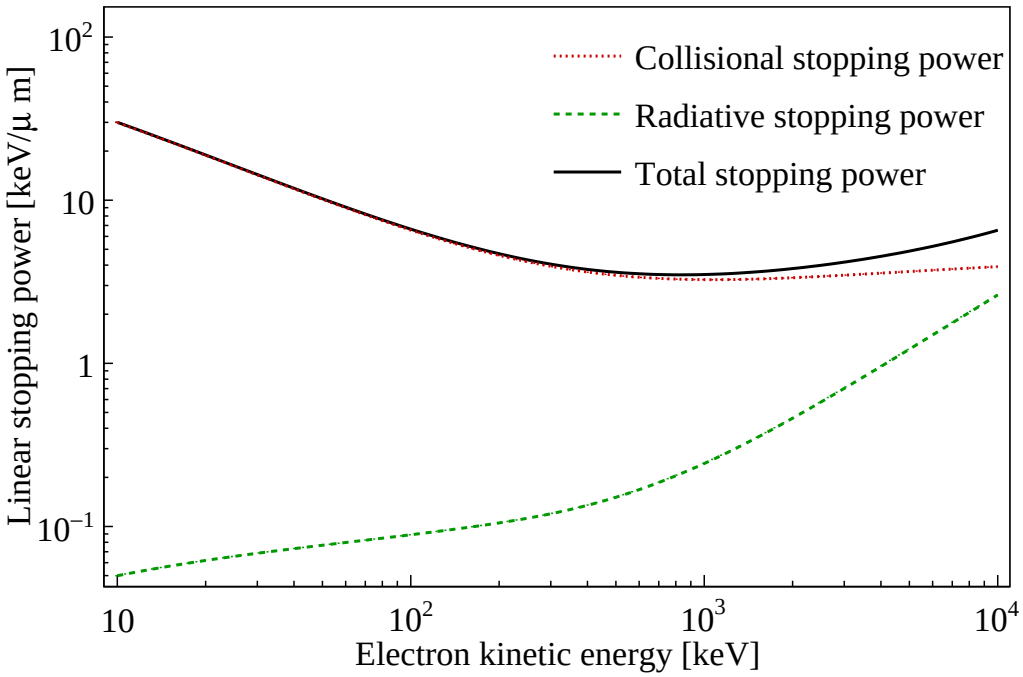

Figure 2.5.: Collisional and radiative linear stopping power of LXe for electrons with kinetic energies in the 10 keV−10 MeV range. This plot was produced with the data provided by the NIST-ESTAR program [128].

radiation. This is a very attractive feature for a low-background detector, as most of the background that would compromise the detection sensitivity to WIMP-nucleus interactions is confined in the outermost region of the active volume, leaving the most central region with a strongly suppressed background from ERs.

Neutron interactions

Neutrons interact in LXe primarily by elastic and inelastic collisions with the xenon nuclei depending on their energy. The neutron-nucleus cross section in the 1 keV-10 MeV energy range is shown in figure 2.8. At energies of the order of 100 keV neutrons scatter elastically off Xe nuclei with typical mean free-paths of $\sim$ 13 cm, where the produced NR is hardly measurable because of its low energy. Below $\sim$ 100 keV (*intermediate neutrons*) the elastic scattering is the dominant interaction, featured by strong resonances at neutron energies below 10 keV. For intermediate neutron in addition to elastic scattering, which is the dominant process, also the neutron capture process ${}^{A}\mathrm{Xe}\,(n,\gamma)^{A+1}\mathrm{Xe}$ followed by prompt γ emission (*radiative capture*) can occur. For fast neutrons ($>$ 1MeV) the inelastic interactions of type ${}^{A}\mathrm{Xe}\,(n,n')^{A*}\mathrm{Xe}$ can also occur, becoming as probable as elastic scattering for neutron energies of $\sim$ 3 MeV. At $\sim$ 10 MeV the neutrons mean free path increases up to $\sim$ 20 cm. Because of this penetrating power, fast neutrons can be efficiently used to calibrate NRs in large xenon chambers with almost uniform distribution. In addition, inelastic scattering off ${}^{129}\mathrm{Xe}$ and ${}^{131}\mathrm{Xe}$ nuclei can excite them to long-lived metastable energy levels, that decay by internal transition (γ emission) with half-lives of 8.9 d and 11.8 d, respectively. Because of their half-lives, after a NR

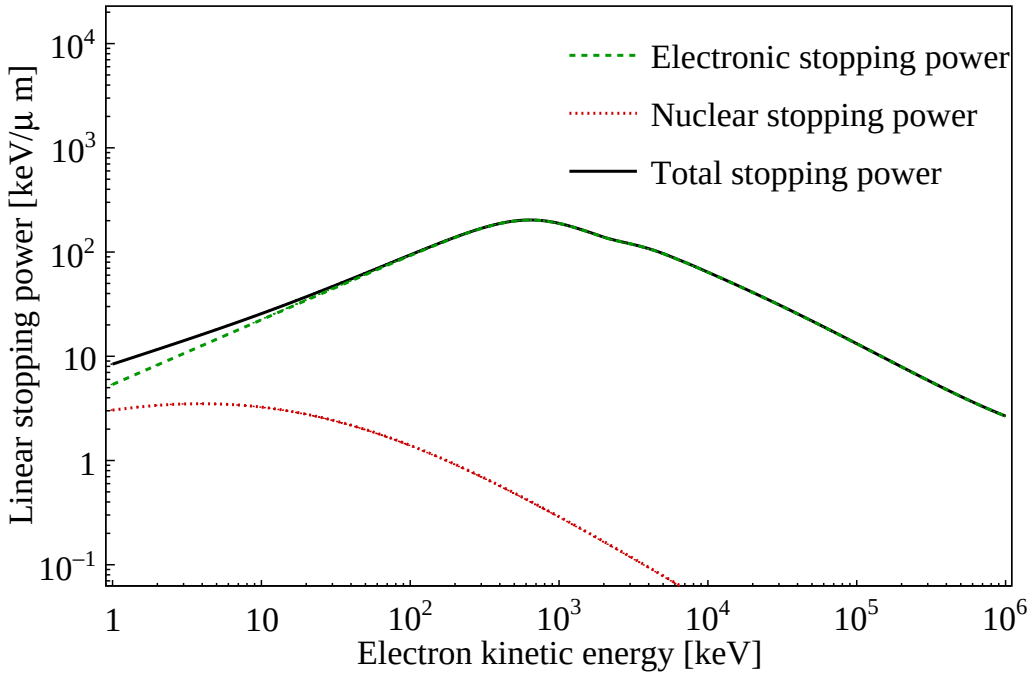

Figure 2.6.: Electronic and nuclear stopping power of xenon for α particles with kinetic energies in the 10 keV−10 MeV range. This plot was produced with the data provided by the NIST-ASTAR program [129].

calibration of the detector with neutrons, the de-excitations of these two isomers can be efficiently used as internal and uniformly distributed sources for the calibration of LXe response to ERs. However, as will be detailed in the next chapter, fast neutrons represent the most dangerous background source for direct WIMP searches.

2.4.2 *Scintillation and ionisation in LXe*

The energy that goes into initial excitation and ionisation is transformed into prompt scintillation signal, mediated by Xe_2^* excited molecules (*excimers*). These excimers are formed in the collision of the excitons with surrounding xenon atoms and decay with very short half-lives ($\lesssim 20$ ns) into two xenon atoms accompanied by the emission of a VUV photon. This is summarised in the following reactions:

$$\begin{aligned} Xe^* + Xe &\rightarrow Xe_2^* \\ Xe_2^* &\rightarrow 2Xe + h\nu \end{aligned} \tag{2.14}$$

The emitted scintillation photons are featured by an energy spectrum peaked at 175 nm, corresponding to a mean energy of $\sim$ 7 eV, and with a FWHM width of 10 nm [132]. The electronic excitation produces dimers in two states, the $^1\Sigma_u^+$ (singlet) and the $^3\Sigma_u^+$ (triplet). Both the states decay to the molecular ground level $^1\Sigma_g^+$ with short separation, where the potential is repulsive, and the almost immediate dissociation of the molecule occurs. The decay from the singlet state to the ground state occurs with an allowed radiative transition with a mean lifetime of $\sim$ 2.2 ns. The triplet

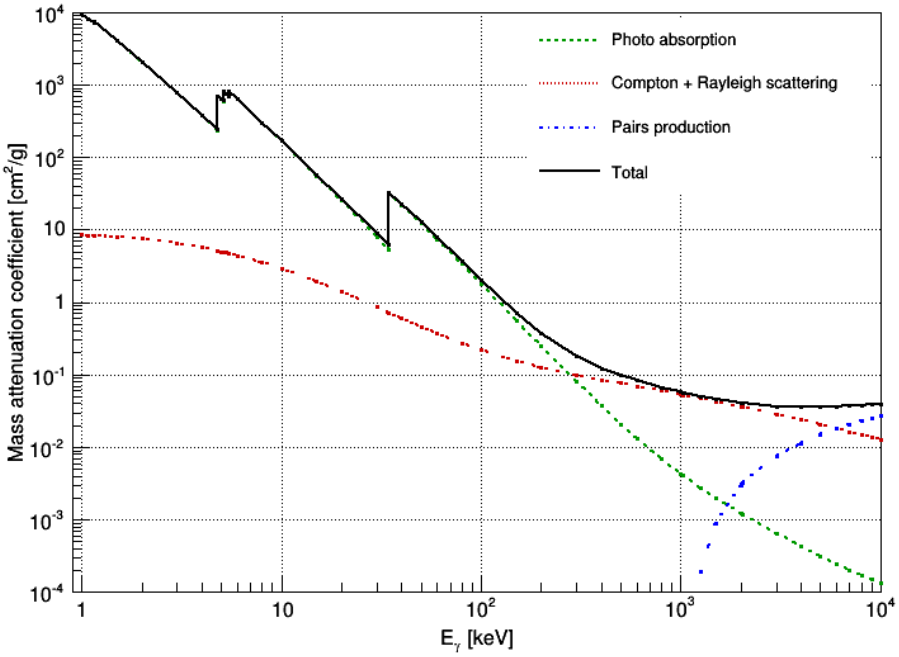

Figure 2.7.: Cross sections of the γ radiation in liquid xenon for the photo-absorption, Compton, Rayleigh scattering, and pair production processes in the 1 keV−10 MeV energy range. This plot was produced with the data provided by the NIST XCOM program [130].

state de-excites with a lifetime of 27 ns, much longer compared to the singlet lifetime. This is because the direct radiative transition to the ground state is forbidden by selection rules and the de-excitation is mediated by the mixing of the $^3\Sigma_u^+$ with the $^1\Pi_u$ state through spin-orbital coupling [133, 134].

Since the VUV photon is emitted from an excimer and not directly from an exciton, the LXe medium is transparent to the propagation of the scintillation light. This allows for the construction of LXe chambers with large volumes surrounded by the active light sensors, where eventual loss of light by absorption effects is negligible.

A reduction of the light output was observed, initially by Kubota *et al.* [135], when an electric field was applied to the detection medium. This was interpreted as a strong experimental evidence that part of the scintillation light comes from the recombination of the electrons with the xenon ions. It is now a well-established fact that the xenon ions form ionised dimers, Xe_2^+, in one of the numerous collisions with the surrounding xenon atoms, and the recombination occurs by forming an excimer which then produces a VUV photon. The recombination-induced excimer formation occurs with the following steps:

$$\begin{aligned} Xe^+ + Xe &\rightarrow Xe_2^+ \\ Xe_2^+ + e^- &\rightarrow Xe^{**} + Xe \\ Xe^{**} &\rightarrow Xe^* + \text{heat} \\ Xe^* + Xe &\rightarrow Xe_2^* \\ Xe_2^* &\rightarrow 2Xe + h\nu\,. \end{aligned} \tag{2.15}$$

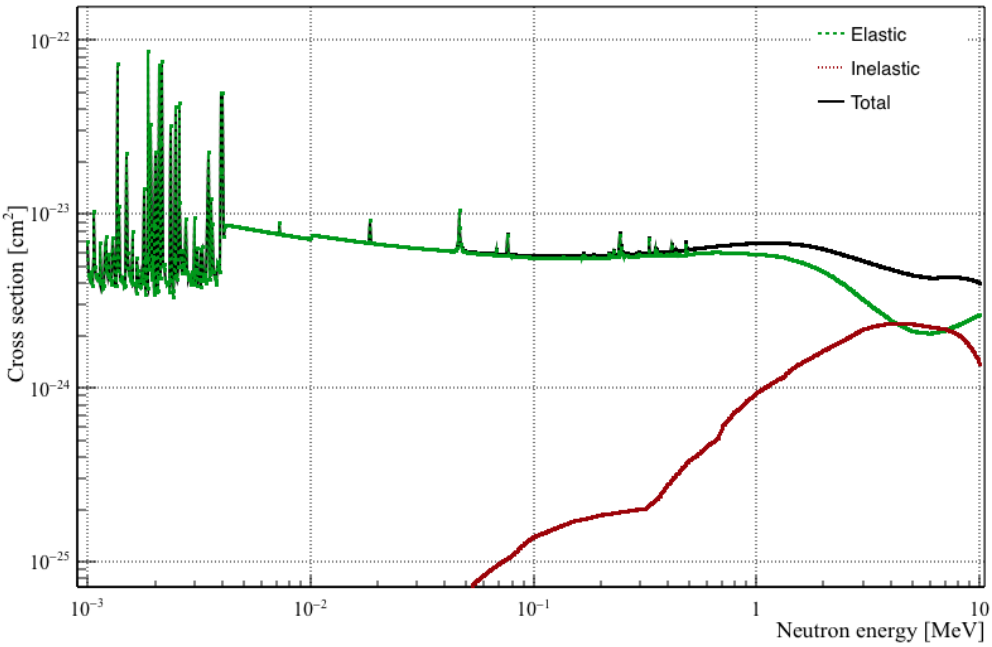

Figure 2.8.: Elastic and inelastic cross sections of neutron-LXe in the 10 keV - 10 MeV energy range. This plot was produced with the data provided by the ENsDF archive [131].

It should be mentioned that even without the application of an external field there is a fraction of ionisation electrons that thermalize with the medium relatively far from the ionisation track, and thus do not contribute to scintillation within the time scales of the prompt scintillation signal, produced by the direct excitation and the prompt recombination [136]. In addition, when the ionisation density is very high as in the case of nonrelativistic α particles or heavy ions, a reduction of scintillation light is observed [137]. It is believed that for those particles the energy loss in elastic collisions with xenon atoms (heat) is negligible, and thus the reduction (quenching) of the scintillation yield occurs most likely in an additional process in the electronic de-excitation chain. Since it was observed that the lifetime of the VUV emission did not depend on the ionisation density (or better on the stopping power $|\mathrm{d}\,E/\mathrm{d}x|$), it was suggested that the electronic quenching occurs prior to the formation of the excimers. The proposed mechanism to explain this reduction of scintillation, the *biexcitonic quenching*, consists of the non-radiative energy loss caused when two excitons interact [137]:

$$\mathrm{Xe}^* + \mathrm{Xe}^* \rightarrow \mathrm{Xe} + \mathrm{Xe}^+ + e^- + \mathrm{heat}\,. \tag{2.16}$$

Hence, this mechanism predicts only one VUV photon from two initial excitons. As the intensity of this process depends on the encountering probability of two excitons, it is relevant only when the electronic excitation density is high enough. This is not the case neither for neutron-induced (or WIMP) NRs nor for the γ- and β-induced ERs in LXe, which are responsible for most of the background in LXe based dark matter detectors. Therefore, within the rest of this chapter and in chapter 5, where low-energy ERs calibrations of an R&D LXe chamber are studied, this mechanism will be neglected.

Liquid xenon is not only an efficient low-threshold scintillator, but it is also featured by an efficient e^--Xe^+ production in response to the energy deposits. This is due to its electronic energy structure, that similarly to that of semiconductor materials, is featured by a valence and a conduction band separated by a large energy gap of 9.28 eV, that makes LXe a strong insulator [138]. The average energy to produce an electron-ion pair is 14.5 eV, about 50 % higher than the energy gap, which makes the LXe the liquefied noble gas with the highest ionisation yield. Additionally, LXe features an electron mobility $\mu_e > 100\,\mathrm{cm^2V^{-1}s^{-1}}$ that allows an efficient drift of charge. At relatively large electric fields ($E_d \gtrsim 100\,\mathrm{V/cm}$) the increase of the electron drift velocity is not anymore proportional to the increase of the drift field, as also shown in section 5.5.3, where the electron drift velocity as function of the electric field have been measured with the Xurich II detector. For fields higher than $\sim 5\,\mathrm{kV/cm}$ several measurements observed that the velocity flattens to a saturation value. Both the high electron mobility and the behaviour of the drift velocity at high fields have been explained, earlier by Shokley [139] and later extended by Cohen and Lekner [140], as being due to the relatively long energy-dependent scattering length (mean free path), λ, of the electrons in the conduction band with the LXe density fluctuations. The sub-linear increase of the electron velocity at higher fields is understood as a decrease of the λ parameter with the energy of electrons accelerated by the drift field (*hot electrons*) [141].

2.4.3 *Electron recoil energy scale*

As mentioned earlier, almost the entire energy deposited as ERs produces either direct excitation or ionisation. The following recombination process encoded into the electron-ion recombination probability, r, depends on the presence of an electric field and on its magnitude. Since the scintillation photons are emitted by both the relaxation of the initial xenon excitons and the recombined electrons, their number n_{ph} is given by:

$$n_{ph} = \alpha_{ex} \cdot N_{ex} + \alpha_i \cdot N_i\,, \tag{2.17}$$

where N_{ex} is the number of initial excitons, N_i the number of initial ions, and $\alpha_{ex,i}$ are, respectively, the probabilities that an exciton or a recombined electron yield a scintillation photon. As already motivated, those two parameters can be assumed unitary for the kind of interactions relevant to LXe-based detectors searching for WIMP signals. Therefore the extracted charge is given by:

$$n_e = (1 - r)\, N_i\,. \tag{2.18}$$

Since no electron quenching is assumed, it follows that $n_{ph} + n_e = N_{ex} + N_i$ and thus it is possible to define the W-value as the mean energy required to produce an electron excitation (a *quantum*):

$$W = \frac{E_r}{N_{ex} + N_i} = \frac{W_i}{1 + N_{ex}/N_i}\,, \tag{2.19}$$

where in the last step the relation $W_i = N_i/E_r$, which represents the mean energy per ionised electron, has been used. Within this work the value $W = (13.7 \pm 0.2)\,\mathrm{eV}$, measured in [142] and consistent with previous and later measurements, is adopted. Since the recombination probability r decreases with the increase of the electric field, the complementarity of the light and charge outputs, produced by an ER with a specific

energy, can be efficiently used to calibrate the light and charge signals in absolute units. This will be shown in chapter 5, where an absolute calibration of the Xurich II LXe chamber is performed by using the ^{83m}Kr de-excitation signals at 32 keV and at 41 keV. Another important parameter that influences the recombination process, and thus the calibration of the energy scales, is the exciton-to-ion ratio N_{ex}/N_i. From theoretical calculations based on absorption measurements and oscillator strengths in solid phase, this ratio is predicted to be 0.06 and is energy-independent [143]. Direct measurements aimed to determine this quantity are quite complicated, and there is not yet a general agreement on its actual value and whether it is indeed energy independent [144]. However, although the knowledge of the initial partition between excitons is important for a further understanding of the microphysics behind the recombination, it does not affect the ER energy reconstruction. This is because the equation 2.19 can be rewritten in an equivalent form with is independent from the N_{ex}/N_i value:

$$E = W\left(n_{ph} + n_e\right), \tag{2.20}$$

where the single $n_{ph,e}$ quantities are recombination- and field-dependent, but not their sum.

2.4.4 *Nuclear recoils*

Since recoiling nuclei interact with other atoms both elastically and inelastically, only part of their initial energy is transferred directly into electronic excitations, while the remainder is transferred into atomic motion. Although some of the secondary recoiling nuclei might have enough energy to produce further electronic excitation, most of their collisions occur with an energy transfer not sufficient to produce ionisation or direct excitation. The amount of energy that is lost as atomic motion was calculated by Lindhard for low-velocity ions ($v < c/137$) [145,146] in semiconductor detection media. The Lindhard factor (or *nuclear quenching*) is defined as the fraction, $\mathcal{L}$, of the total energy of the recoiling nucleus that does not yield electronic excitation:

$$E_{nr} = \frac{W\left(n_{ph} + n_e\right)}{\mathcal{L}}. \tag{2.21}$$

This is one of the motivations behind the development of a dedicated LXe time projection chamber that will be detailed in chapter 5. The Lindhard model developed to describe the energy loss leads to a complicated integral equation, which does not have closed solutions. Therefore some approximations are necessary, and the nuclear quenching parameter was parametrised as:

$$\mathcal{L} \simeq \frac{kg(\epsilon)}{1 + kg(\epsilon)}, \tag{2.22}$$

where:

$$\begin{aligned} \epsilon &= 11.5Z^{-7/3}\,\frac{E_{nr}}{\text{keV}}, \\ k &= 0.133Z^{2/3}A^{1/2}, \\ g(\epsilon) &= 3\epsilon^{0.15} + 0.7\epsilon^{0.6} + \epsilon, \end{aligned} \tag{2.23}$$

and where Z and A are, respectively the atomic number and the mass number, of both the recoiling nucleus and of atomic nuclei of the target medium. It was found that

this choice of parameters provides an accurate description of the nuclear quenching in semiconductors, specifically in germanium [147–149]. Recent measurements of low-energy nuclear recoils find a good agreement with a Lindhard model where the constant $k = (0.1735 \pm 0.0060)$ is determined by a fit to the data [150].

Since in general the nuclear quenching parameter is an energy-dependent parameter, as also observed experimentally, the nuclear recoil energy is not a linear function of the total quanta $n_{\rm ph} + n_{\rm e}$, as in the case of the electronic recoils. Since this parameter is fundamental to reconstruct the nuclear recoil energy scale, numerous experimental efforts have been dedicated to the characterisation of the LXe response to low-energy nuclear recoils.

Relative scintillation

For historical reasons and in order to compare experimental results obtained by single channel channel LXe detectors with those obtained with dual channel LXe detectors, the scintillation signal is commonly used to measure the energy of ERs and NRs. In addition, precision measurements of the absolute scintillation yield are in general quite complicated especially when the detector is sensitive only to light. Hence, for the nuclear quenching the relative scintillation efficiency, $\mathcal{L}_{\rm eff}$, has been defined as the ratio of the zero-field scintillation yield of NRs to the zero-field scintillation yield of a standard candle, usually the ^{57}Co spectral line at 122 keV:

$$\mathcal{L}_{\rm eff}(E_{\rm nr}) = \frac{Ly_{\rm nr}}{Ly_{\rm er}^{(0)}(E_{\rm er} = 122\,{\rm keV})} = \frac{Ly_{\rm nr}^{(0)}}{Ly_{\rm er}^{(0)}(E_{\rm er} = 122\,{\rm keV})}\left(\frac{S_{\rm er}}{S_{\rm nr}}\right), \tag{2.24}$$

where the subscripts "er" and "nr" indicate NR and ER related quantities, respectively; the superscript $^{(0)}$ indicates zero field quantities, and the field-dependent factor $S_{\rm nr}$ is the analogue of $S_{\rm er}$ for nuclear recoils. It should be emphasised that the two field quenching functions differ in that for nuclear recoil the ratio $N_{\rm ex}/N_{\rm i} \simeq 1$, and for a given initial number $N_{\rm i}$ the ionisation density is expected to be much higher compared to electron recoils.

2.4.5 *Discrimination*

Different low-energy recoiling particles produce in liquid xenon different ionisation densities along their tracks. In liquid xenon detectors, where both light and charge are measured, this feature can be used to discriminate interaction events of different particles. In higher density tracks, as in the case of nuclear recoils or α particles, the drift field is less efficient in drifting away the electrons from the most internal regions of the track. This is because of charge shielding effects that also occur in dense plasmas. As observed for the first time in [151], NRs showed a lower charge-to-light ratio compared to γ-induced ERs as a consequence of a higher recombination probability or equivalently a lower field quenching of the scintillation signal.

This is shown in figure 2.9 for the XENON100 detector (unpublished plot), where the y axis represents a monotonic function of the charge-to-light ratio and the x axis the light signal used in this case to reconstruct the ER energy scale. Two bands of events can be distinguished in the data. The upper band (blue points) with higher charge to light ratio is relative to ERs produced by the interactions of γ-rays with LXe, mainly

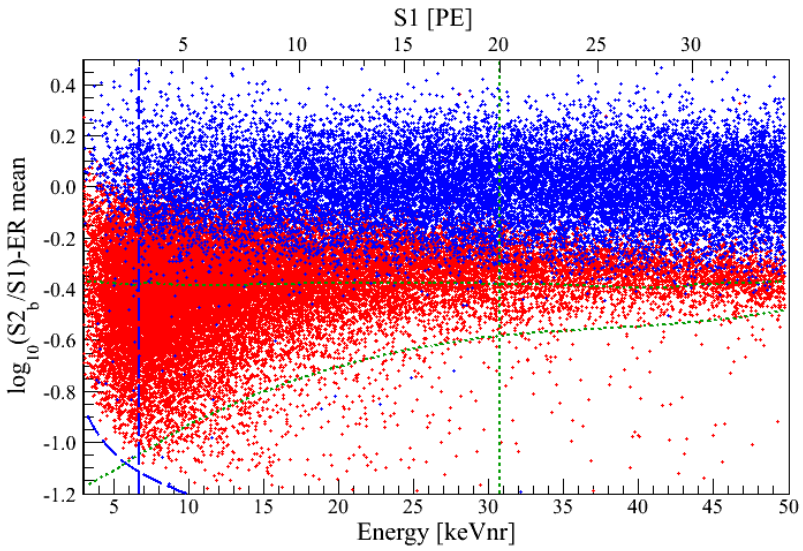

Figure 2.9.: Flattened electron (blue) and nuclear (red) recoil bands as measured with the XENON100 experiment. The ordinate is the logarithm of the charge-to light ratio as function by the mean of the scintillation light signal, used in this case to reconstruct the equivalent nuclear recoil energy. The flattening of the ER band is done by subtracting the energy-dependent mean value of the $\log(S2/S1)$ quantity, where as explained in section 2.4.6 S2 is the signal that measures the charge and S1 is the signal of the primary scintillation of LXe. The ERs events are induced by the penetrating γ-rays of the ^{60}Co and ^{228}Th calibration sources, while the NR are produced by neutrons from an AmBe calibration source. For completeness of information the blue dashed and green dashed vertical lines are, respectively, the lower and the upper limits of the benchmark WIMP search region. The region above the horizontal dotted green line is the 99.75 % ER rejection region (used only for benchmarking), while the bottom green dotted line represents the 97 % quantile of the NRs distribution. The dashed line at the bottom left of the plot defines the hardware trigger threshold of the experiment. More details can be found in [152]. Figure (not published) from the XENON collaboration.

by Compton scattering, which were emitted by ^{60}Co and ^{228}Th radioactive calibration sources. The bottom band (red points) is relative to NRs induced by the interaction of neutrons, from AmBe source, with LXe. As widely demonstrated [111, 152], in liquid xenon TPCs operated in dual phase, the ERs discrimination efficiency can be as high as 99.5%, while keeping a relatively high acceptance to NRs ($\simeq$ 50 %). Such a discrimination efficiency allows therefore for a strong suppression of the ER background, especially at low energies, which is fundamental for the detection sensitivities of WIMP searching experiments.

2.4.6 *Dual phase xenon time projection chambers*

The technique that takes better advantage of the high scintillation and ionisation yields featured by the liquid xenon is represented by dual-phase (liquid-gas) time-projection chambers. This technique allows for the simultaneous detection of the light and charge signals produced by a particle interaction in LXe, and offers several advantages compared to other LXe techniques, that will be briefly reviewed along this section.

The working principle, sketched in figure 2.10, consists in reading the prompt scintillation signal and the extracted charge with arrays of light detectors, usually photomul-

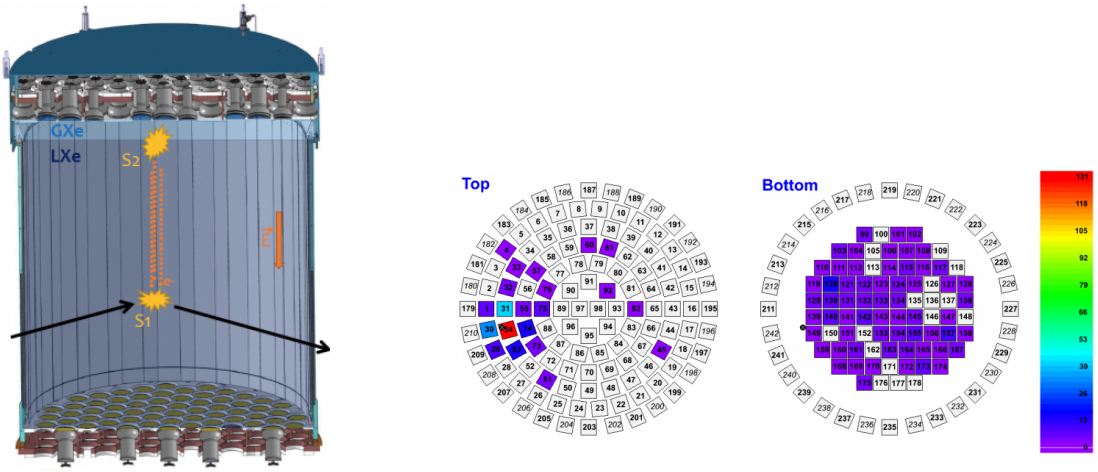

(a) (b)

Figure 2.10.: (a) Working principle of a liquid xenon time projection chamber operated in dual-phase (liquid-gas). The light sensors are arranged in two arrays, above the anode and below the cathode. In small detectors for R&D studies it is possible that the only one light sensor in the gas phase (top) and one in the liquid phase (bottom) are used. Figure from the XENON collaboration.
(b) Light pattern on the top and bottom PMT arrays of an S2 signal measured in the XENON100 experiment. The localised pattern on the top array allows for the x-y position reconstruction of the interaction vertex, that is indicated with a black spot. The same is not possible using the light pattern in the bottom array PMTs as their illumination is more uniform and featureless. Figure from [153].

tipliers sensitive to the xenon VUV light. The dual-phase TPC consists of a chamber containing the liquid xenon target, usually surrounded at the sides by cylindrical VUV reflecting wall. A metallic cathode mesh, biased at negative voltages, and gate mesh, usually kept at ground potential, define the lower and the upper borders of the LXe chamber. The electric field between these two electrodes will then extract and drift toward the gate the charge produced by a particle interaction with LXe. Few mm above the gate, in the gas phase, another electrode mesh, the anode, is biased at high positive potential generating an electric field much higher (about an order of magnitude) than the drift field between the gate and the cathode.

The gas-liquid separation surface falls between the anode and the gate, and because of the discontinuity of the electric permeabilities across the separation surface, a discontinuity in the electric field is produced. The charge drifted to the gate will be drifted by the higher field above the gate up to the surface level, where it will be extracted from the liquid phase and accelerated in the gas phase towards the anode electrode. For sufficiently large electric fields a secondary proportional scintillation is produced by the electrons drifting in the gas between the liquid surface and the anode (*electroluminescence* light).

In the most common configurations, the light sensors view the chamber from above the anode and from below the cathode, although other configurations have also been employed. Hence, each interaction event is featured by a first prompt luminescence signal, called S1 signal, followed in time by a second electroluminescence signal, called S2 or charge signal. The drift time between the two signals allows for the reconstruction of the z coordinate (the depth) of the interaction vertex (z coordinate). When the TPC

is instrumented with an array of several PMTs in the gas phase, from the S2 signal distribution pattern on the top array, the reconstruction of the x and y coordinates is possible. This is because the S2 scintillation occurs few mm below optical window of the PMTs, that makes the intensity pattern among the sensor array very localised. Among several techniques for the reconstruction of the horizontal position the most promising are based on the neural network algorithms [154] and support vector machines [153]. Both the techniques require prior training of the algorithms, which is usually performed with Monte Carlo simulations of the electroluminescence light propagation from known initial positions.

The ability of the 3D position reconstruction in a LXe time-projection chamber is the feature that takes better advantage of the strong self-shielding properties of the detection medium for background suppression purposes. As mentioned earlier, the β-radiation and most of the γ-rays, with not too large energies, are expected to produce ERs in the outer region of the LXe sensitive volume. Hence, the 3D position reconstruction allows to reject in the dark matter analysis phase all the events outside a virtual central volume (*fiducal volume* - FV), where the background rate is strongly suppressed.

Electron extraction

Since the dielectric constant is higher in the xenon liquid phase than in the gas phase, the electrons in the vicinity of the liquid surface experience a repulsive virtual potential that does not allow their free passage to the gas phase. The repulsive potential, shown in figure 2.11, is a sum of the three components: the energy of the electron in the conduction band ($-V_0$), the repulsive potential of a virtual charge placed in the gas phase and the potential of a homogeneous electric field [155]. Electrons with a momentum component normal to the surface which is high enough can overcome the potential barrier and get captured by the field in the gas phase. This usually does not happen for electrons in thermal equilibrium with the liquid phase, because of the too low probability of having a momentum value sufficient to overcome the potential barrier at the liquid-gas separation boundary. However, when the field in the liquid phase increases the thermal equilibrium of the drifted electrons and the liquid phase is broken, and the momentum distribution becomes strongly anisotropic toward the liquid surface. This mechanism is commonly called "hot" electron emission as when the electric field in the liquid phase is large enough ($E_\mathrm{d} \gtrsim 1\,\mathrm{kV/cm}$) the mean energy of the electrons is much higher than the thermal energy of the equilibrium. It should be noted that also at moderate fields ($\sim 10\,\mathrm{V/cm}$) is possible that some electrons in upper energy tail of the thermal distribution can be emitted. This is usually referred as "cold" emission. Measurements show that for electric fields in liquid phase above $\sim 5\,\mathrm{kV/cm}$ (above $\sim 10\,\mathrm{kV/cm}$) the emission electron extraction efficiency is almost 100 % and no increase of S2 signal size is observed at higher fields [155, 156].

S2 signal formation

The electron extracted from the liquid phase and accelerated in the gas phase produce light by the electroluminescence mechanism. Compared to direct charge measurements by means of capacitor coupled preamplifiers, the secondary has the strong advantage that an order of 10^2 VUV photons can be produced for a single extracted electron. As shown in [157] this strong amplification allows to observe signals from single extracted

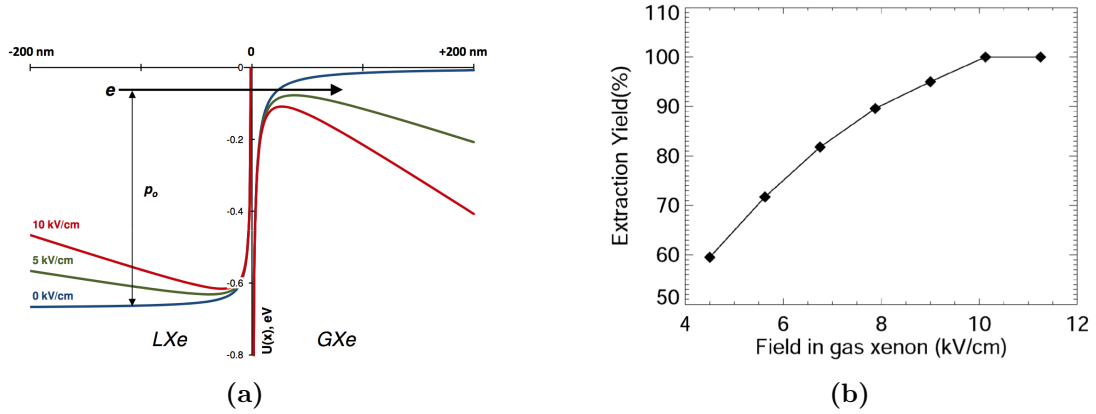

(a) (b)

Figure 2.11.: (a) Emission process of electrons from the xenon liquid phase to the gas phase. The Potential energy experienced by the electrons in the liquid phase is shown for different electric fields. Figure taken from [126].
(b) Extraction efficiency as function of field. The efficiency is inferred by the size of the S2 signals from the photo-absorption peak relative to the 570 keV spectral line of the ^{207}Bi. Figure from [156].

electrons, hence absolute calibrations of the detector response to charge can be done with high accuracy. An additional advantage of the secondary scintillation charge measurement, compared to electronic means, consists in a very large signal to noise ratio (SNR) already for single electrons signals. This mechanism of secondary scintillation in the xenon gas is a well established and explained process [158]. The impact of fast electron with the gas atoms excite with highest probability one of the $^3P_2$, $^3P_1$, $^3P_0$ and $^1P_0$ excited states of xenon. When the gas pressure is high enough as in double phase detectors, the atomic collisions are frequent enough to form the Xe_2^* dimers before radiative transitions, such as $^3P_1 \rightarrow^1 S_0$ and $^1P_1 \rightarrow^1 S_0$, occur. The emission spectrum from the excimers in gas phase, was measured by Takahashi *et al.* [159], who observed the emission peak at 171 nm with a FWHM of 12 nm. The slightly higher energy with respect to the same emissions in liquid phase was explained by a downward energy shift of the excimers level in the liquid phase.

The number of emitted photons in the electroluminescence mechanism is dependent on the the reduced field E_g/n_g, where E_g and n_g are the electric field and the xenon gas density, and it is proportional to the electrons drift length in gas. Empirically it is found that the number of photons generated per unit length is:

$$\frac{\mathrm{d}\,N_{\mathrm{ph}}}{\mathrm{d}x} = \alpha\left(\frac{E_g}{n_g} - \beta\right) n_g\,, \tag{2.25}$$

where α and β parameters are parameters which depend on the gas and are empirically found from model matching [160, 161].

3

RADIOASSAY OF THE XENON1T DETECTOR MATERIALS

In this chapter I will present the radioassay campaign of the XENON1T detector construction components, with particular emphasis on the results obtained by the γ-ray spectrometry technique. In section 3.2 I will briefly review the main background sources from materials (*radiogenic*), that are one of the primary concerns for the realization of any low-background experiment and in particular those for direct DM searches. In section 3.3 I will show and discuss the performance and the data analysis for the Gator γ-ray spectrometer, with is a screening facility entirely dedicated to the radioassay campaigns of the XENONDM searching program. The results of the most important components of the XENON1T experiment are presented and discussed in section 3.4 and subsections. In section 3.5 I will review the development of the new PMTs for the XENON1T detector, with improved radio-purity with respect to the photosensors used in the detectors of the previous generation. Finally the predictions of the ER and NR radiogenic background for the XENON1T detector are briefly reviewed in section 3.6.

3.1 THE XENON1T EXPERIMENT

The XENON dark matter project searches for signals from the scattering of WIMPs off xenon nuclei using LXe based on dual phase (liquid-gas) time projection chambers. The XENON1T experiment, the third phase of the XENON dark matter search program, is being operated at the Gran Sasso National Laboratories (LNGS) under at average rock depth of $\sim 1400\,\mathrm{m}$ that provides the shielding from the cosmic radiation (equivalent to $\sim 3600\,\mathrm{m}$ of water depth). With $\sim 3200\,\mathrm{kg}$ of ultra pure LXe the XENON1T detector, is the first tonne scale dual phase (liquid-gas) xenon TPC realised to date. The TPC is filled with $2200\,\mathrm{kg}$ of LXe, for a target mass of $1\,\mathrm{t}$, enclosed in a $1\,\mathrm{m}$ long, and $1\,\mathrm{m}$ wide cylinder. The LXe chamber is instrumented with 248 total 3 inch Hamamatsu R11410-21 PMTs with high quantum efficiency to VUV light ($\sim 36\%$ on average) [162], placed in two arrays, as shown in figure 3.1. The bottom PMT array is directly immersed in LXe and consists of 121 in a compact hexagonal structure, in order to maximise the light collection efficiency.

The top PMT array consists of 127 units, arranged in concentric rings in order to improve the accuracy of the position reconstruction. In order to improve the light collection efficiency to the primary scintillation signal (S1) the enclosure of the LXe chamber is made out of 24 interlocking PFTE panels, featured a reflectivity to VUV light higher than 90 %. The interlocking structure of PTFE panels is sustained from the outside region by PTFE pillars. Additional PTFE and copper disks provide the support for the two PMT arrays. The electrodes generating the electric field consist of

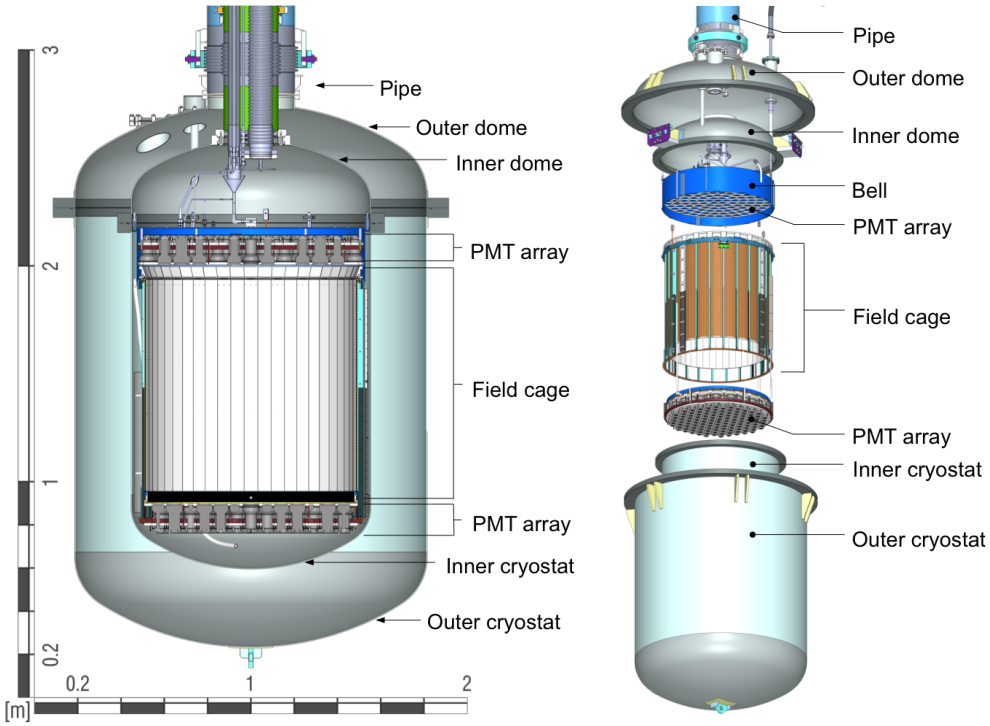

Figure 3.1.: (*Left*) Technical rendered drawing of the XENON1T TPC inside the double wall cryostat. (*Right*) Exploded view of the XENON1T internal components subgroups. Figures from [163].

stainless steel meshes or in the case of the cathode wires stretched onto stainless steel rings.

The grounded gate mesh, slightly below the LXe level, and the anode mesh is 5 mm above the gate, in the gas phase, define the proportional scintillation region. Both the meshes consist of 0.2 mm thick stainless steel hexagonal etched meshes. Above the anode and below the cathode other two grounded 0.2 mm thick stainless steel hexagonal etched meshes, screen the PMTs optical windows from the strong electric field generated by high voltage biased electrodes. All the 5 electrodes have been realized with an high geometrical transparency: 96 % for the cathode, 93 % for the anode and gate meshes and 94.5 % for the two screening meshes.

The cylindrical structure is surrounded by 74 copper field shaping rings that provide the necessary uniformity to the drift field inside the LXe chamber. Two chains of 75 resistors provide the electrical connection from the cathode and the anode to the field shaping rings, where the resistance values are chosen based on the optimal voltage value of each ring, determined on the base of electric field simulations.

A stainless steel bell partially immersed in the LXe provides the support to the top PMT array and to rest of the field cage, and allows the adjustment of the liquid level between the gate and the anode meshes. The liquid level adjustment is done by regulating the overpressure of the xenon gas inside the bell, where the xenon is reinjected after its chemical purification cycle.

The entire TPC is enclose in an internal stainless steel vessel, which is enclosed inside a second stainless steel vessel. The two vessels define the cryostat and are separated by a vacuum jacket, which provides the proper thermal insulation from the outer environment. also thermally insulated by the same vacuum beween The top of the inner vessel

consists in a dome that provides the connection to the pipes, used to transport all the necessary cabling to the instrumentation of the TPC, and to

The cryostat is immersed in a $\sim 10\,\mathrm{m}$ high $\sim 10\,\mathrm{m}$ wide water tank which provides the necessary shielding of the experiment to the external γ radiation and neutron radiation. In addition the water tank is instrumented as Cherenkov muon veto with 84 8 inch Hamamatsu R5912 phototube, and provides an efficient suppression of the muon-induced neutron background [164].

All the cabling for the internal instrumentation is transported from the facility building, next to the water tank, to the TPC through a stainless steel pipe connected to internal cryostat dome. Other pipes also connected to the same dome are used for the xenon recirculation through the hot metal (zirconium) getters, located in the facility building, and allow for the transportation of the liquid xenon, which is condensed by a cryocooler system, also located in the facility building. All the service pipes are enclosed in a larger pipe connected to the dome of the external cryostat. The same vacuum between the cryostat vessels provides also the thermal insulation between the service pipes an the eternal pipe.

The XENON1T experiment has been designed in order to probe the SI WIMP-nucleon cross section at the unprecedented level of $\sim 2 \times 10^{-47}\,\mathrm{cm}^2$ at WIMP mass of $\sim 50\,\mathrm{GeV/c}^2$ with an exposure of $\sim 2\,\mathrm{ton\,y}$. In order to reach this detection sensitivity, the background rate $< 0.5\,\mathrm{events/y}$ in the 1 ton FV and in the recoil energy range relevant for WIMP searches. Such low background levels require radioactive contaminations of materials at the sub mBq/kg level, which motivates the intensive radioassay campaign for the screening and selection of the materials for the XENON1T components.

3.2 TYPES OF BACKGROUND IN XENON1T EXPERIMENT

The relevant background, that might be a concerning for the detection sensitivity of a LXe particle detector for rare event searches, such as XENON1T, comes in two well-distinguished NR and ER interaction produced by neutron and γ radiation.

The ER single scatters are produced mainly by the γ-rays and β-rays , that are emitted in the decays of unstable nuclides which contaminate the materials (*radiogenic* sources) and from the unstable isotopes dissolved in the LXe (*intrinsic* sources). The energies of the γ-rays emitted by the radionuclides span over three orders of magnitude, from some keV to a few MeV. Within such a wide energy spectrum there are several interaction mechanisms between the γ radiation and the LXe that can lead to ER background. For a LXe detector like XENON1T, where the most concerning background events are those that produce a single interaction inside the internal FV,γ-rays with energies of $E_\gamma \gtrsim 1\,\mathrm{MeV}$ might pose a serious problem to the detection sensitivity. This is due to their relatively long mean free path in LXe of $\gtrsim 6\,\mathrm{cm}$, as shown in figure 2.7, allowing them into the most internal volume with a significant probability. In addition the cross section at those energies is dominated by the Compton mechanism, which produces a continuous ER background spectrum that extends down to the WIMP search energy region. In contrast γ-rays with energy $E_\gamma \lesssim 200\,\mathrm{keV}$ are mostly absorbed by the LXe within a few mm, which provides a strong self-shielding against radiogenic γ-rays.

The typical spectra of the β radiation extend up to the Q_v of the nuclear decay, that for the most common β-emitters present in nature does not exceed 10 MeV. The

electron stopping power for β particles in LXe in the 10 keV−10 MeV energy range is shown in figure 2.5. The corresponding electron ranges are of $10\,\mu$m and of at most $\sim$ 1 mm for electrons with initial energies of 100 keV and 1 MeV, respectively. Furthermore, the fraction of electron energy losses expected from the radiative processes (*bremsstrahlung*) is largely subdominant compared to the energy losses due to Coulomb collisions. Hence the β emissions in the detector materials do not constitute a concerning for the XENON1T background. However, when a β-emitter contaminates the LXe, the low-energy tail of the induced ER background spectrum might pose a serious limit to the detection sensitivity of the experiment.

The ER background is also produced by the interactions of residual HE muons (minimum ionization particles - MIP), which survived the rock shielding of the UG laboratory, with the Xe atomic electron. However, this kind of radiation is expected to release in the matter $\sim 2\,\mathrm{MeV\,cm^2\,g^{-1}}$, corresponding to $\sim 450\,\mathrm{keV\,mm^{-1}}$ in LXe, which is several orders of magnitude higher than the typical WIMP search energy region. Hence also the direct muon-LXe interaction can be neglected in the account of the XENON1T ER background.

In XENON1T experiment the background from NRs is the major threat, as the signal produced from these kind of interactions can mimic the signal of a WIMP-nucleus scattering. This background is mainly produced by neutrons, which come from the self-fission of heavy nuclei, the (α,n) reactions in the detector materials (*radiogenic* neutrons) and from the nuclear interactions of the residual HE muons, from cosmic rays (CR), with the nuclei of either the detector or the rock surrounding the experimental area. Additionally, although in a dual-phase Xe TPC ERs can be discriminated with high efficiency ($> 99.5\,\%$) with relatively high NR acceptance ($\gtrsim 50\,\%$) [152, 165, 166], the small fraction of ERs that statistically leak into the NR signal region must be accounted in the background budget.

Hence in the XENON1T radioassay campaign, besides the identification of all the radioactive contamination and the selection of the most radio-pure materials, a special effort was put into the selection of the materials with the lowest neutron yields. The construction materials were selected based on the background predictions from detailed Monte Carlo simulations.

3.2.1 *Background sources*

The radioactive nuclides that can contaminate the materials can be divided in three main categories according to their origin: *primordial*, *cosmogenic* and those produced by human activities (*anthropogenic*).

The primordial radionuclides with life times $> 10^9$ y, such as the isotopes belonging to the ^{238}U, ^{235}U and ^{232}Th decay chains, and ^{40}K, are present in nature in the soil, in the rock, in the water and in the air with variable concentrations, hence most materials are expected to be contaminated by them. However, for a given material the concentration of primordials can be very different, as it depends on the original contamination of the raw minerals and ores, and on the chemical processes occurring during the manufacturing process.

Cosmogenic radioactive isotopes are the result of nuclear interactions of the HE protons and neutrons of the atmospheric CR with the atomic nuclei in the materials. The most common long-lived radionuclides, relevant for the XENON1T experiment, are

$^{56-60}$Co, ^{54}Mn, ^{46}Sc and ^{8}Be. However, since these radio-nuclides are produced mainly by spallation and fragmentation of the target stable nuclei, their presence and their abundance strongly depends on the chemical composition of materials and on their time exposure to the CR.

Long-lived anthropogenic radioisotopes are mainly produced in nuclear power plants as wastes, in the nuclear-fuel reprocessing, in several accidents occurred in the last 40 y, and in the thousands of military tests performed in the last $\sim$ 50 y. Among many radionuclides of interest for the XENON1T background, that are commonly found to contaminate the materials are ^{137}Cs, ^{108m,110m}Ag. Their concentration is variable and depends on the place of origin of the raw materials. The ^{85}Kr is another very important radionuclide, continuously released from nuclear power plants, which is found in the air.

Primordial decay chains

The radionuclides of the ^{238}U , ^{235}U and ^{232}Th series, shown in figures 3.2 and 3.3, decay by α and β emissions, frequently associated to one or more prompt γ emissions. All the radiogenic neutrons are produced by the radionuclides belonging to these chains, either by their self-fission or by the (α,n) reactions in materials. In particular the latter mechanism is the dominant process for neutron emission in materials which are composed of elements with low atomic numbers, while for the target nuclei with higher atomic numbers the electrostatic potential barrier reduces the efficiency of the (α,n) reaction, that becomes negligible for target nuclei with Z$\gtrsim$ 29 (copper) [167]. Both the mechanisms produce neutrons with a continuous and featureless energy spectrum that extends up to $\sim$ 10 MeV. In figure 2.8 is shown that the typical cross-section as a function of neutron energy in this range, for elastic and inelastic scattering with natural Xe is $\sim$ 5 barns, which in LXe correspond to mean free path of $\sim$ 15 cm. Therefore radiogenic neutrons can easily penetrate and induce NR interactions in the most internal region of the LXe target, hence this background source is one of the most serious threats for dark matter detection. In addition, since the final states of the α and β decays of these series are frequently excited nuclear states, the subsequent de-excitation is usually associated with the emission of one or more γ-rays in cascade.

When the radionuclides of the same chain are in *secular equilibrium*, these all share the same activity of the progenitor of the chain. However, because of the different chemical properties of the elements belonging to the chain, the equilibrium is often broken in raw samples mined on the earth surface, while this is not the case for samples coming from the depths of the Earth crust. In addition, the chemical processes that occur during the manufacture of a specific material can induce an accumulation or a depletion of some specific radionuclides of a chain, and hence induce a disequilibrium. However, when a disequilibrium between two radionuclides happens, it is exponentially suppressed with the time t and depends only on the lifetime of the daughter isotope τ_{d}:

$$\Delta A(t) = \Delta A_0 \cdot e^{-(t-t_0)/\tau_{\mathrm{d}}}\,, \tag{3.1}$$

where A_0 is the activity difference at the time t_0. Therefore disequilibrium in a decay chain is usually observed in correspondence of long-lived radionuclides.

Different parts of the same decay chain might produce neutrons with different yields and with different energy spectra, that in turn might lead to different background estimations than if the equilibrium was assumed. As for neutrons, also the spectrum and

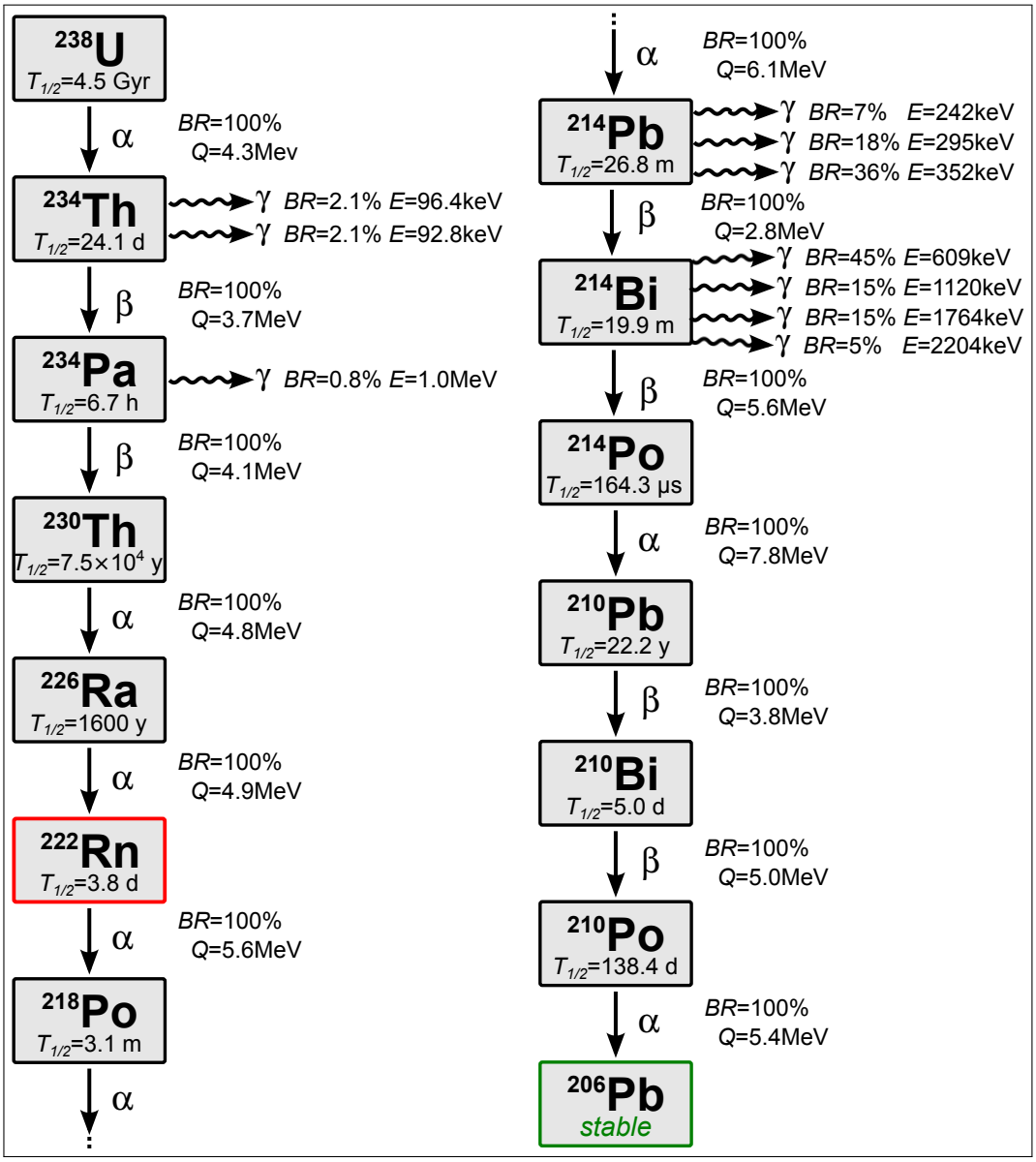

Figure 3.2.: Decay chain scheme of the ^{238}U.

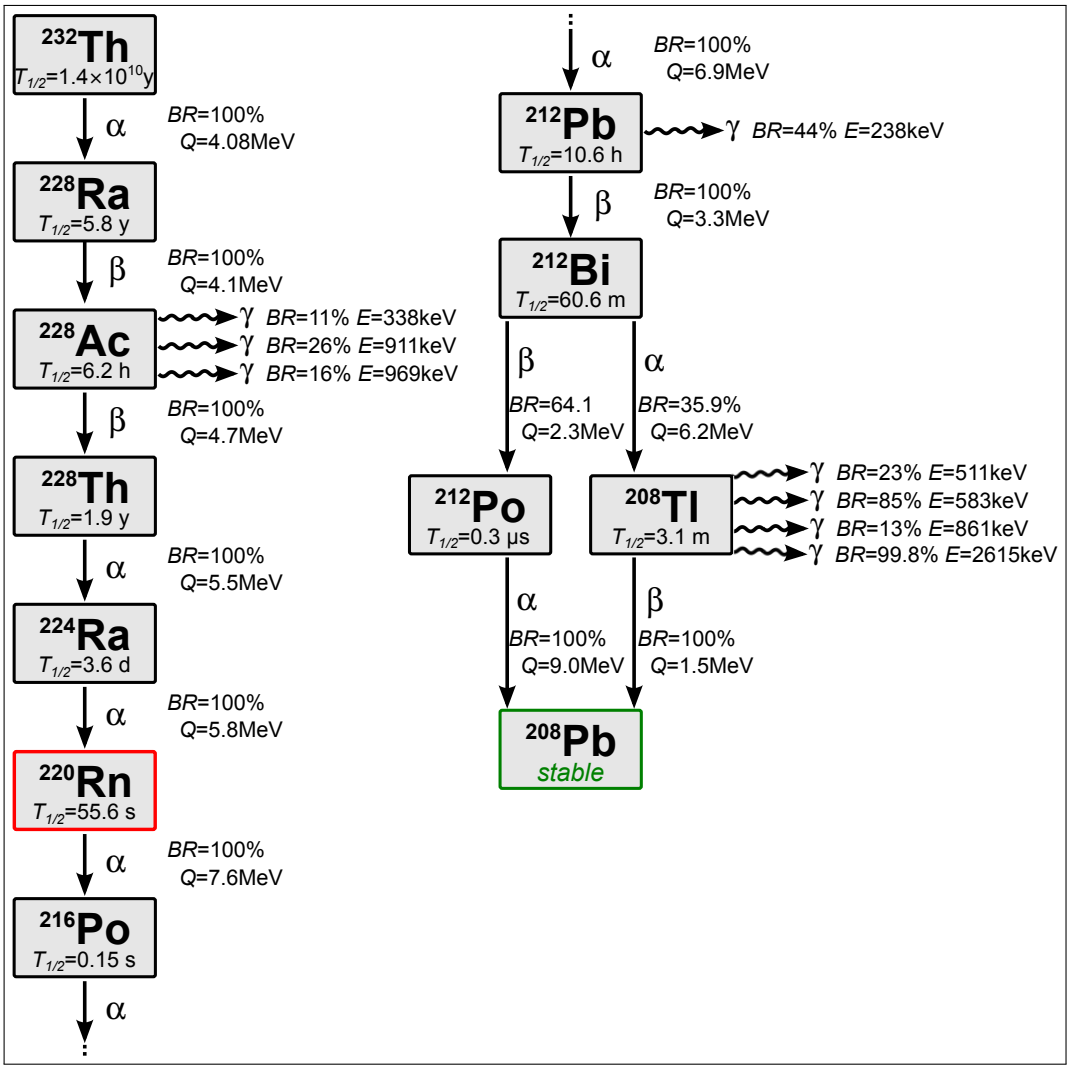

Figure 3.3.: Decay chain scheme of the ^{232}Th.

the total intensity of the γ background can be very different when a disequilibrium in the decay chain is considered. For these reasons the XENON1T radioassay campaign was carried on utilising different screening techniques, in order to understand whether the primordial chains that contaminate a specific sample are in equilibrium or not. Hence, all the screening results reported in section 3.4 and in the tables of the appendix A are given for the sub-chains.

The ^{238}U isotope decays by α emission to ^{234}Th with a half-life of $\sim 4.5 \times 10^9$ y, and with a branching ratio (BR) of $\sim 6 \cdot 10^{-7}$ the decay happens by spontaneous fission, associated with the emission of one or more neutrons. The uranium abundance in the earth crust is $\sim 2.5 \times 10^{-6}$ g/g, although in some specific places uranium ores can contain concentrations higher that 1 % in mass [168, 169]. Almost all the natural uranium is ^{238}U , while only a fracton of ~ 0.72 % is constituted by ^{235}U [170, 171]. The ^{235}U isotope also decays by α emission with a half-life of 7×10^8 y, and with a branching ratio of $\sim 7 \cdot 10^{-11}$ by spontaneous fission.

The disequilibrium of the ^{238}U chain is usually observed in correspondence of the long-lived ^{226}Ra ($T_{1/2} = 1.6 \times 10^3$ y) and of the ^{210}Pb ($T_{1/2} = 22.2$ y) radionuclides. Technically the breaking of the secular equilibrium might also occur in correspondence of ^{230}Th ($T_{1/2} = 7.5 \times 10^5$ y), however the chemical properties of all the heavy metals in actinides group are very similar and thus the first radionuclide that might be significantly out of equilibrium is ^{226}Ra . The upper ^{238}U chain is featured by the largest neutron yield from spontaneous fission, mostly due to ^{238}U . The only relevant γ emissions are the spectral lines from ^{234}Th at 96.4 keV and 92.8 keV, both with a branching ratio of 2.1 %, and a very weak spectral line at 1.0 MeV from the decay of ^{234m}Pa with a branching ratio of 0.8 %. Hence, the γ background from the ^{238}U $-^{230}$Th sub-chain can be usually neglected for LXe detectors.

Radium is featured by a strong chemical reactivity (standard redox potential $\simeq -2.92$ V), and despite it is the heaviest element in the alkaline-earth group it is the most volatile. As all the elements of the second group, radium has a relatively high reactivity to oxidation and is efficiently dissolved as Ra^{2+} in water. Due to this property it can be efficiently transported away from the ores, which might be the most natural process that can produce the breaking of the secular equilibrium by ^{226}Ra depletion. Among the 33 known radium isotopes ^{226}Ra is the longest lived one, and therefore almost all the natural radium consists of it. In the rock it is found with the same concentration of ^{238}U, however, because of the higher water solubility it can also be found in water at concentrations of $\sim 10^{-13}$ g/g [168, 169].

The neutron emission by the ^{226}Ra $-^{214}$Po sub-chain is generated from (α,n) reactions, while spontaneous fission happens only in ^{226}Ra with a branching ratio too small for any significant contribution to the neutron flux [168]. As studied in [154, 167], for materials consisting of light and medium elements ($Z \lesssim 30$), the contamination from ^{226}Ra might be among the most important neutron sources. In addition, as shown in the diagram of figure 3.2, the ^{226}Ra sub-chain contains two strong short-lived γ emitters, ^{214}Pb ($T_{1/2} = 26.8$ m) and ^{214}Bi ($T_{1/2} = 26.8$ m), which can give a significant contribution to the low-energy ER background. The ^{214}Pb isotope decays by β emission to ^{214}Bi, usually followed by prominent γ emissions at 242 keV (BR = 7 %), 295 keV (BR = 18 %) and 352 keV (BR = 36 %). The ^{214}Bi radionuclide decays primarily by β-emission to ^{214}Po, followed by prominent γ emissions at 609 keV (BR = 45 %), 1120 keV (BR = 15 %), 1764 keV (BR = 15 %), and 2204 keV (BR = 5 %). This γ radiation

can significantly penetrate into the most internal regions of the active volume, where low-energy ERs, produced by Compton scattering interactions with LXe, can constitute background contribution for the XENON1T experiment.

The ^{210}Pb nuclide usually accumulates on lead and plates out the surfaces of materials exposed to the environment radioactivity. In particular, since lead is the most efficient shielding material to γ radiation, it is widely used in low-background experiments and facilities. This radionuclide decays to ^{210}Bi by the emission of an electron with a maximum energy of 63.5 keV, and in only 4% of the cases a 46.5 keV γ-ray follows the β emission. This radiation hardly escapes from the materials' bulk, and in LXe both the radiations are entirely absorbed within a fraction of mm. However, the α decays of the ^{210}Po can be an additional source of radiogenic neutrons, especially when the contaminated material is composed of light elements. Hence, all the materials closer to the active volume were also screened for their content in ^{210}Pb.

The ^{232}Th isotope decays by α emission to ^{228}Ra with a half-life of $1.4 \times 10^{10} y$, without any γ emission relevant for the background of a LXe detector. This radionuclide decays by spontaneous fission with a branching ratio of $\sim 10^{-11}$, several orders of magnitude lower in comparison to ^{235,238}U. In the ^{232}Th chain the equilibrium breaking happens usually in correspondence of the ^{228}Ra ($T_{1/2} = 5.8$ y) and of the ^{228}Th ($T_{1/2} = 1.9$ y). Thorium is found in the environment, mainly in the rocks and silicates, at an average concentration of $\sim 8 \cdot 10^{-6}$ g/g, about 3 times higher than that of ^{238}U, which reflects the longer lifetime of ^{232}Th. Both the ^{228}Ra and the ^{228}Th sub-chains are featured by strong γ emitters. In the ^{228}Ra sub-chain ^{228}Ac ($T_{1/2} = 6.2$ h) is the most relevant γ emitter with prominent spectral lines at 338 keV (BR = 11 %), 911 keV (BR = 26 %), and 969 keV (BR = 16 %). The strongest γ emitters in the ^{228}Th sub-chains are ^{212}Pb ($T_{1/2} = 10.6$ h) and ^{208}Tl ($T_{1/2} = 3$ m). The first radionuclide decays to ^{212}Bi ($T_{1/2} = 61$ m) by β emission, that with a BR = 44 % is associated to a γ emission at 238 keV. The ^{208}Tl β decay to the stable ^{208}Pb is followed by prominent γ emissions at 511 keV (BR = 23 %), 583 keV (BR = 85 %), 861 keV (BR = 13 %), and at 2615 keV (BR = 99.8 %). As can be understod from the plot of figure 2.7, the predominant interaction of the γ-emissions from the upper and lower ^{232}Th sub-chains with the xenon atoms is by Compton scattering. Hence, although the energies of all these γ lines are well above the typical energies expected from a WIMP signal, the lower tail of the energy continuum produced by the Compton mechanism overlaps with the WIMP search region.

Radon

Within the ^{226}Ra and ^{228}Th series an important role is played by ^{222}Rn ($T_{1/2} = 3.82$ d) and ^{220}Rn ($T_{1/2} = 56$ s), which are produced by the α decays of ^{226}Ra and ^{224}Ra ($T_{1/2} = 3.63$ d), respectively. Since radon is a chemically inert gas with no stable isotopes, its ability to diffuse in the environment, through the soil, the rock cracks, and water makes it the main cause of the natural radioactivity. The ^{222}Rn natural concentration in air ranges from some tens of Bq/m^3 on the earth surface to some hundred of Bq/m^3 in closed underground environments such as in caves, mines or also in the buildings basements when the concrete and the other building materials have large concentrations of radium. The contribution of ^{220}Rn to the natural radioactivity is usually negligible because of the relatively short half-life of this isotope, although it strongly depends on the level of ^{228}Th contamination of a specific place. The ^{222}Rn environmental

level at the LNGS underground laboratory is $\mathrm{Bq/m^3}$ in the hall B (the XENON1T location), where an efficient ventilation system provides external fresh air with lower ^{222}Rn contamination, and $\sim 370\,\mathrm{Bq/m^3}$ in correspondence of the XENON100 experiment location, where the ventilation system is less efficient. In XENON1T the background from environmental radon is efficiently shielded to negligible levels by the water tank. However, radon can still diffuse through any leak of the gas system that would lead to intrinsic contamination of the xenon and thus might be a potentially strong source of intrinsic ER background. Hence, the sealing of the cryostats and of the gas system components was carefully tested using the Ne gas to $< 5 \times 10^{-9}\,\mathrm{mbar}\,l/\mathrm{s}$. Despite all the efforts taken to prevent the radon induced background, both the isotopes are continuously emanated into the xenon by the internal components of the detector, of the gas recirculation and purification systems. This is due to the ^{224,226}Ra disintegrations that take place either on the surface of a detector component in contact with the xenon or a few μm deep in the bulk. Because of the relatively high initial kinetic energy of the ^{220,222}Rn nuclei, soon after the α decay of the radium nuclides, at $\sim 5.7\,\mathrm{MeV}$ and $\sim 4.8\,\mathrm{MeV}$, respectively, the two radon nuclei have a significant chances to diffuse out of the material surface into the xenon. Besides the intrinsic ^{224,226}Ra contamination of the material, the rate of ^{222}Rn emanation depends critically on the surface properties such as the roughness, the microscopic structure of its porosity and on the applied chemical and physical treatments of the surfaces prior to the installation, as was thoroughly studied in [172]. Because of the 3.82 d half-life, even if emanated in remote places of the detector gas system, ^{222}Rn would be able to diffuse almost uniformly into the XENON1T sensitive volume, being thus a threat for the background. The same is not true for the ^{220}Rn that is expected to contribute to the background only if emanated by the components in the proximity of the sensitive volume. Considering all the ^{222}Rn daughters down to ^{210}Pb, the most concerning mechanism which can produce ERs in the WIMP searching region is ^{214}Pb β decay to the ground level of ^{214}Bi , that happens with a probability of $\simeq 11\,\%$. All the other β emissions to the excited states of ^{214}Bi are followed by prompt γ-rays ($\mathrm{T_{1/2}} < 1\,\mathrm{ns}$) shifting the reconstructed energy of those events by pile-up well above the WIMP search region. The main contribution to the background of the ^{214}Bi comes from the β emission to the ground level of ^{214}Po, which happens with a branching ratio of $\simeq 19\,\%$. However, as proved for the XENON100 experiment, the background from these events can be mitigated by the detection of the α decays of ^{214}Po, which has a relatively short half-life of $164\,\mu$s (*delayed coincidence tagging*) [173]. For the background from intrinsic ^{220}Rn contamination, only the low-energy tail of the ^{212}Pb β emission to the ^{212}Bi ground state (BR = 11 %) can significantly contribute to the single site ER background in the WIMP search region. As observed in the XENON100 experiment, the intrinsic ^{222}Rn contamination of xenon contributed 50 % of the total single ER background in the 225 live days scientific run (2011 - 2012) [152]. Hence, the XENON1T radioassay campaign was performed with an additional screening of materials for their radon emanation rate, for all the detector components that are in contact with the xenon.

^{40}K

Potassium is a light and very common element present in nature, in particular in organic compounds. The ^{40}K half-life is $\sim 1.2 \times 10^9\,\mathrm{y}$ and its natural aboundance is $\sim 1.2 \times 10^{-4}$. As shown in figure 3.4, it decays by β emission with a probability of $\sim 89\%$ directly

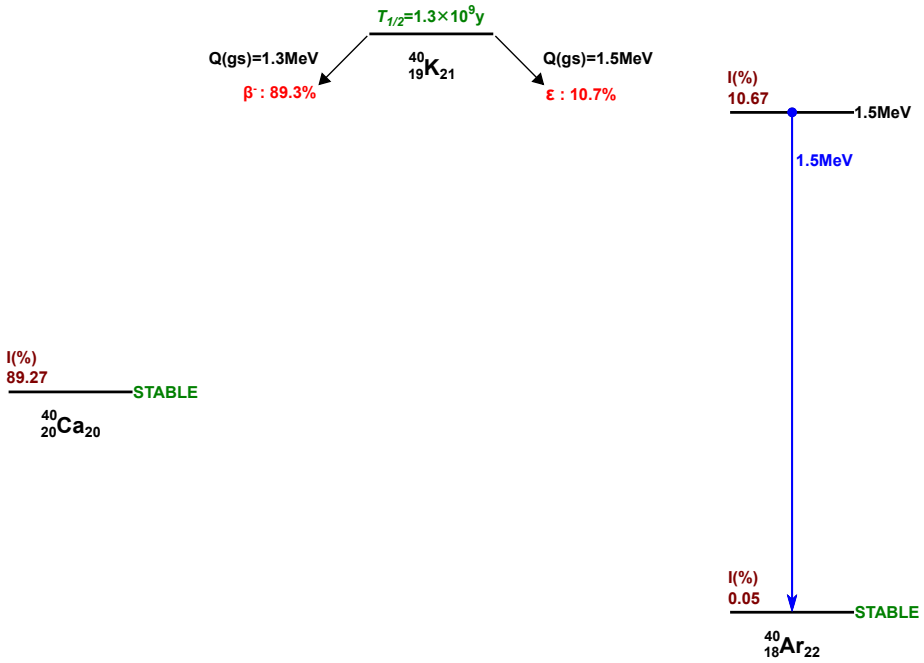

Figure 3.4.: Details of the ^{40}K radioactive decay and of the most important γ-emission. The scheme has been made based on the values available at the NuDat 2.6 online database [174].

to the ground state of ^{40}Ca ($Q_{\mathrm{v}} = 1.31\,\mathrm{MeV}$), and by orbital electron capture (ε decay mode) to ^{40}Ar ($Q_{\mathrm{v}} = 1.50\,\mathrm{MeV}$) with the remaining fraction. With a probability of 98 % the ε decay mode is followed by the prompt emission of a 1.46 MeV γ-ray, which can produce low-energy ER background in the sensitive volume by Compton scattering. Since potassium frequently is found in organic compounds and in human tissues, a simple contact of the detector components with the human skin is sufficient to leave a significant contamination ^{40}K contamination on the surface. Also the oils and greases used for machining of the components usually contain large ^{40}K concentrations, and thus can contaminate their surface. However, as the potassium is soluble in water it is possible to remove it from the surfaces by an accurate rinsing with high-purity deionized water, after a proper degreasing treatment is applied.

^{85}Kr

Krypton is a noble gas that is found in air at concentrations of $\sim 10^{-6}$ mol/mol, about an order of magnitude more abundant than xenon [169]. Its unstable isotopes ^{85}Kr , a product of the human activities linked to nuclear-fuel reprocessing and military nuclear tests, decays with a half-life of 10.8 y by β emission. In the air this radionuclide is found at specific activities of $\sim 1.14\,\mathrm{Bq/m^3}$, increasing with time, corresponding to a fraction of $\sim 2 \times 10^{-11}$ of the natural krypton [175–177]. Since krypton is chemically inert it can be uniformly diffused inside the detector, and thus dissolved in the target volume, and cannot be removed or reduced by the commonly utilised purification systems based on the chemical adsorption of electronegative elements on the surface of hot Zr getters. The natural krypton concentration in the purest xenon available on the market (*scientific grade xenon*) ranges from $\sim 10^{-8}$ g/g to $\sim 10^{-6}$ g/g [g/g], corre-

sponding to a ^{85}Kr concentration in xenon several orders of magnitude higher than the values required by the current generation of xenon-based dark matter detectors. With a probability of $\simeq 99.6\,\%$, ^{85}Kr decays to the ^{85}Rb ground state, that constitutes a low-energy background that cannot be effectively mitigated by event tagging techniques as for the ^{222}Rn background. So far the only efficient technique that allows a strong suppression of the ^{85}Kr is by cryogenic distillation of the xenon using the McCabe-Thiele technique [178, 179], prior to the detector filling or in online recirculation mode. This krypton distillation technique was already successfully applied in XENON100 prior the 2009 commissioning run [165] where the level of Kr was suppressed $\sim$ 50 times, from $\simeq 7\,$ppb to $\simeq 0.14\,$ppb [g/g] [180], thus reducing the ^{85}Kr -induced background to 2.35 mDRU (55% of the total) in the energy region below 100 keV. For the background requirements of XENON1T the concentration of $^{\text{nat}}$Kr in xenon must be kept below $5 \times 10^{-13}\,$g/g in order to limit the background rate to 5.8 μDRU in the 1 ton FV and in the WIMP search energy region [181]. Hence, a custom-made xenon distillation column was designed and tested to fulfill this separation requirements. Recents measurements with the final setup, integrated as XENON1T sub-system, concentrations below 2.6×10^{-14}g/g of ^{85}Kr in xenon have been achieved [182–184], which correspond to an order of magnitude better than the original requirements.

3.3 MATERIALS SCREENING WITH HP-Ge γ-RAY SPECTROMETRY

The γ-ray spectrometry with high-purity germanium (HP-Ge) counters has become a standard and an essential technique for the radio-assay and selection of highly radiopure materials for low-background experiments. Due to the higher radiopurity and superior energy resolution with respect to NaI and organic-based γ-counters, the HP-Ge spectrometers are the most powerful detectors for the detection of the radio impurities at very low concentrations.

The largest advantage in using HP-Ge detectors for the radioassay of materials consists in being the only non-destructive technique able to detect a few ppb [g/g] of almost all the common γ-emitters in the materials, thanks to the relatively high detection efficiency for γ-rays over a spectrum that spans from few tens of keV to several MeV. These features make the HP-Ge based γ-spectrometers sensitive to eventual disequilibrium in the ^{238}U and ^{232}Th decay chains, which is fundamental for a proper prediction of the experimental backgrounds. Since the neutron yield of the ^{238}U and ^{232}Th isotopes can be orders of magnitude different with respect to the neutron yield due to their late sub-chains (^{226}Ra -^{214}Po, ^{210}Pb -^{206}Pb, and ^{228}Th -^{208}Pb), the sensitivity to secular equilibrium breakout provided by HP-Ge detectors is fundamental for an accurate prediction of the XENON1T neutron background and for the choice of the components.

In γ-ray spectrometry the detection sensitivity to radio-impurities depends on the background rate, the counting time, the sample mass, and on the material self-absorption properties, that can significantly reduce the detection efficiency for γ-rays with energies $\lesssim 100\,$keV. Therefore, the drawback in using this technique for the radioassay at the ppb level or below, is in the relatively long counting times ($\gtrsim 15\,$d), thus relatively large sample masses ($\gtrsim$kg) are usually required.

The XENON1T radioassay campaign was performed using the HP-Ge spectrometers located at the LNGS underground laboratory, such as the 3 GeMPIs [185] and the Gator [186] spectrometer, which are among the γ-counters with the lowest background

levels in the world. These spectrometers where used in particular for the radioassay of the most critical components of XENON1T, such as the materials for the cryostat vessels and all the internal components including all the cabling, the PMTs, and the electronic components. In particular, the possibility of using the 4 HP-Ge spectrometers all located in the same underground laboratory, allowed us to measure some critical samples with different counters. It was therefore possible to cross-check for eventual systematics in the radioassay of the same materials, which might be related to a specific detector or analysis method, without exposing the sample to CR and thus avoiding any further cosmogenic activation.

In conjunction with HP-Ge spectrometry, the XENON1T radioassay campaign of for materials selection included mas spectrometry (MS) techniques: the Inductively Coupled Plasma MS (ICP-MS), performed at the LNGS chemistry facility [187], and the Glow Discharge Mass Spectrometry (GD-MS), performed by the Evans Analytical Group (EAG) [188]. These techniques have the advantage of being able to detect specific radio-impurities using samples with a few grams of mass, and the entire measurement process can be performed in a few hours. Hence, MS was employed when the samples to be assayed had the mass too small to yield any reasonable sensitivity with the HP-Ge spectrometers. In addition the MS techniques, ICP-MS in particular, frequently resulted in higher detection sensitivity to the contamination from ^{238}U and ^{232}Th with respect to the γ-counters, and thus several materials were additionally screened with one of the two MS techniques. However, in order to measure the abundances of the elements in the materials, the samples must be destroyed and thus MS was not usable for all the components of XENON1T.

3.3.1 *The Gator HP-Ge spectrometer*

Gator is the UZH low-background HP-Ge detector operated at LNGS underground laboratory since 2007 and is primarly dedicated to the screening campaigns of the XENON experiments [186]. The detector consists of a 2.2 kg coaxial p-type HP-Ge crystal in a vacuum cryostat. The crystal is operated at a temperature T$\sim$ 80 K with a cold finger immersed into a LN_2 bath. The cryostat, the cold finger as well as the crystal holder are made out of Oxygen Free High Conductivity (OFHC) copper, one of the most radio-pure metals commonly employed in the innermost structural parts of low-background detectors [185, 189]. The measurement cavity has internal dimensions of $25 \times 25 \times 33\,\mathrm{cm}^3$, with a total volume of $\sim$ 19 liters, allowing the measurement of large samples in order to improve the detection efficiency. The innermost layer of the cavity shielding is made out of 5 cm of OFHC-Cu, which is surrounded by 20 cm of lead: low activity lead in the innermost 5 cm layer (3 Bq/kg of ^{210}Pb) and higher activity lead for the most external layers (75 Bq/kg of ^{210}Pb). The shield is enclosed by a lateral metal structure and on the top by a glove-box used for the insertion and removal of the samples. Both the metallic enclosure and the glove box are airtight in order to provide a first protection from the Rn in the environment. In order to further suppress the background from Rn, the measurement cavity, the glove box, and the lateral encasing are kept at over pressure with respect to the external environment by a constant purging with clean nitrogen gas from evaporation.

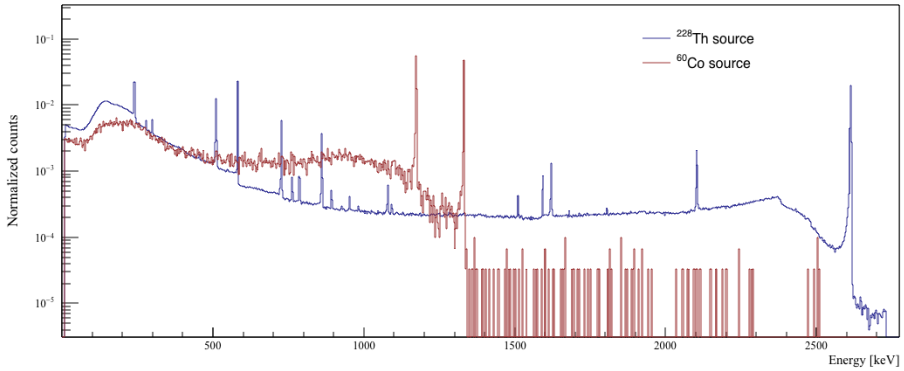

Figure 3.5.: Spectra of the ^{228}Th (blue) and of the ^{60}Co (dark red) sources used for the calibration of the Gator detector. For visualisation purposes in this panel the two spectra are rebinned and normalised by their respective total counts (their area).

Energy calibrations

The energy scale calibration of the Gator HP-Ge was performed by the acquisition of dedicated γ spectra with ^{228}Th and ^{60}Co radioactive sources, shown together in figure 3.5. The first source was chosen as the several emitted spectral lines allow the calibration over an energy region wide enough to detect the γ emissions of the most common radio-impurities in materials. The selection of ^{60}Co as auxiliary calibration source was made since the continuum under its two γ-lines at 1173 keV and 1332 keV is negligible. In the same energy region the ratio between the ^{228}Th spectral lines amplitude and the continuum is not high enough for an accurate extraction of the line position and resolution from the fit.

For an accurate determination of the position and the width of a spectral line on the uncalibrated energy scale, the shape of the peaks must be properly modelled, as well as the continuous background underneath them. Many of the spectral lines used for the calibration are shown in figure 3.6, where it is possible to observe some general features that characterise their spectral shape:

– A dominant Gaussian component with the mean value μ, corresponding to the full absorption peak position, and with the natural broadening σ. This broadening is due to the statistical fluctuations of the electron-hole pair number, $\sigma_N \propto \sqrt{FE_\gamma}$, generated by the absorption of a $\gamma-$ray with energy E_γ in a material with the Fano factor F. As this is an intrinsic property of the detection medium, the resulting broadening is irreducible. In addition, the noise introduced by the acquisition electronics in the pre-amplification, in the shaping and digitisation of the original charge signal contributes to the broadening of the observed line.

– A low-energy tail is present on almost every peak. Events which survived to the spectroscopy amplifier (Ortec 672) capability of pile-up rejection and events where the charge was not completely collected can be responsible for this effect. Furthermore, if in the signal amplification and shaping stages an event is detected before the output baseline of the shaper is restored to its zero level, the signal

would result in a smaller amplitude signal, thus contributing to the tail. This problem is the so called *pole-zero cancellation* [190].

– the background is discontinuous across the low and high energy sides of the peak. This is an effect mainly due to the Compton scattering of the γ-rays with non-sensitive materials before getting absorbed in the Ge crystal, resulting in a continuous spectrum on the low-energy side of the peak centre. Additionally, γ-rays with energies $E_\gamma \geq 2m_e c^2$ can produce $e^- e^+$ pairs in the sensitive volume, which might contribute to the background discontinuity below the peak. This happens when only one of the 511 keV γ-rays produced by pair annihilation is entirely absorbed in the active volume, while the second escapes without depositing its entire energy.

Many analytical functions, tailored to model the features of the full absorption peaks in a semiconductor detector, have been proposed in literature ([191] and references therein). From a comparison of the most popular fitting models, the function employed in the HYPERMET [192] program was the model with the best reduced χ^2 value [191]. Therefore this model was chosen, with a few minor modifications, for the fit of spectral lines used to calibrate the Gator energy scale.

For the modelling of the low-energy tail, the argument of Phillips and Marlow has been followed [192]: in an ideal detector (with $\sigma = 0$) the low-energy tail consists of events subtracted from the main peak that can be modelled as an exponential function with positive slope β at the left of the peak mean, μ, and an identical null function a the right. The fitting model of the low energy tail $T(x)$ is then finalised by applying the energy resolution by convolving the ideal truncated exponential with a normalised Gaussian function:

$$\begin{aligned} T(x) &\propto \int_{-\infty}^{\infty} dz \, \exp\left(\frac{(x-z)^2}{2\sigma^2}\right) \exp\left(\frac{z-\mu}{\beta}\right) \Theta\left(\mu - z\right) \\ &\propto \exp\left(\frac{\sigma^2}{2\beta^2}\right) \exp\left(\frac{x-\mu}{\beta}\right) \operatorname{erfc}\left(\frac{x-\mu}{\sqrt{2}\sigma} + \frac{\sigma}{\sqrt{2}\beta}\right) , \end{aligned} \tag{3.2}$$

where the variable x represent the energy in non-calibrated units (MCA channel), Θ is the step function and erfc the complementary error function. As suggested in [193], in this definition of $T(x)$ the exponential term is not absorbed in the amplitude constant in order to avoid poor fits when the parameter $\beta \lesssim 2\sigma$.

The background discontinuity across the peak centre is simply modelled by an ideal step function, that is convolved with normalised Gaussian results in the function $\operatorname{erfc}(\cdot)$ with the mean point μ and cutoff σ:

$$S(x) \propto \operatorname{erfc}\left(\frac{x-\mu}{\sqrt{2}\sigma}\right) . \tag{3.3}$$

The background under the peaks is usually modelled with a polynomial function. As shown in figure 3.6, in the case of Gator a constant value B provides a satisfactory background description.

$$f(x) = A \cdot \left[\exp\left(-\frac{(x-\mu)^2}{2\sigma^2}\right) + a_{\mathrm{T}} T\left(x\right)\right] + A_{\mathrm{S}} \cdot S\left(x\right) + B\,, \tag{3.4}$$

where A is the Gaussian amplitude, a_{T} and a_{S} are the amplitudes of the low-energy tail and of the step function, respectively, normalised to the Gaussian amplitude. Moreover the amplitudes in this definition absorb all the eventual numerical multiplicative factors of the three functions in the sum.

Some of the spectral lines used for the calibration of the Gator energy scale are shown in top panel of figure 3.6, with their relative best fit curves using the maximum likelihood estimator (MLE) of the 7 free parameters. The log-likelihood function is built assuming in each channel i the counts n_i distributed by a Poisson function with intensity parameter λ_i:

$$\log(\mathcal{L}) = \sum_i \left[n_i \log(\lambda_i) - \lambda_i \right] , \tag{3.5}$$

where the expected counts λ_i are computed by the integration of the fit function between the channel edges, and thus are function of the free parameters. Since this minimisation is highly non-linear, the fit is computed in two steps. The first step consists of a preliminary search for the likelihood maximum by a custom-made algorithm based on the Metropolis procedure for the generation of Monte Carlo Markov Chain (MCMC) steps [194,195]. The maxima parameters values found with the MCMC routine are used as initialisation parameters of the Minuit2 software [196], which provides the parameters MLE and the covariance matrix. The residuals are computed for each MCA channel as the difference between the data and the expected counts at the MLE λ_i^*, and normalised by the standard deviation of the expected counts, $\sqrt{\lambda_i^*}$. The residuals are employed for the determination of the goodness-of-fit (GOF), calculated by the use of the likelihood ratio as described in [197]. The distributions of the residuals for the lines plotted in figure 3.6 are featureless and usually contained within 3σ of the expected counts. The only exception is represented by the ^{208}Tl line at 2615 keV, that is featured by a residuals distribution with an oscillating pattern instead of a featureless random distribution. The observed features of the residual distributions are quantitatively reflected in the degree of freedom (dof) corrected GOF test, that for the first 8 spectral lines results in a $\chi^2/\mathrm{dof} < 100$, while in the case of the 2.6 MeV line the agreement is much worse, resulting in $\chi^2/\mathrm{dof} \simeq 210$. Although the GOF test suggests a bad fit for the 2.6 MeV spectral line of ^{208}Tl in comparison to the other lines, the size of the relative errors for the Gaussian mean and width, the only two parameters of interest of the line fit, are 10^{-6} and 10^{-3}, respectively. The same relative errors are found also for the other lines with a better GOF, which suggest a satisfactory estimation of the only two parameters interesting for the calibration of the energy scale also for this line. In addition this line is located at the far end of the energy range used for the detection of the most common γ emitters, without any other prominent spectral line in the vicinity, and it might provide a reliable calibration of the high-energy region. Hence, for an accurate calibration of the entire energy region, this is the only line always employed even when the GOF test is very unfavourable, as long as the relative errors on the Gaussian mean and width are of the same order as for the other lines.

The interaction of a γ-ray with the target medium produces a number of electron-hole pairs that is ideally proportional to the amount of deposited energy, and thus also the position of the Gaussian mean in the MCA channel scale is ideally proportional to the deposited energy. However, amplification, shaping, and digitisation of the charge signal can introduce an offset of the baseline and some little non-linearity near the end of the energy scale, that must be taken into account. Hence, the energy scale of Gator is

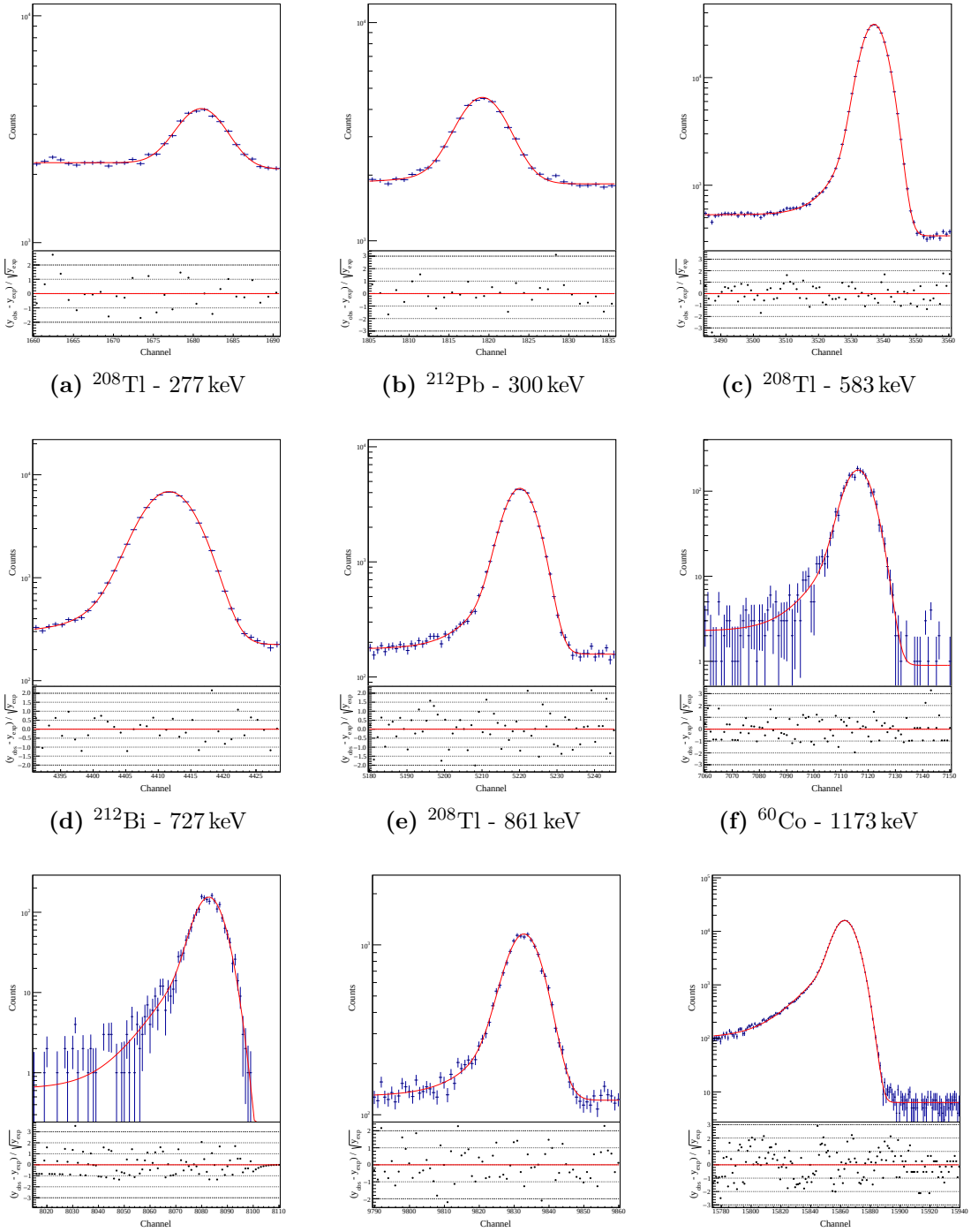

(a) ^{208}Tl - 277 keV **(b)** ^{212}Pb - 300 keV **(c)** ^{208}Tl - 583 keV

(d) ^{212}Bi - 727 keV **(e)** ^{208}Tl - 861 keV **(f)** ^{60}Co - 1173 keV

(g) ^{212}Bi - 1621 keV **(h)** ^{212}Bi - 1621 keV **(i)** ^{208}Tl - 2615 keV

Figure 3.6.: Fits of the spectral lines employed for the calibration of the Gator energy scale. At the bottom of each line the residuals normalized by the square root of the expected counts in each channel are shown.

Table 3.1.: Goodness of fit for the lines usually employed for the calibration of the energy scale of the Gator spectrometer. The p-values are calculated according to [197] and corrected for the degrees of freedom. As reference the χ^2/dof, calculated from the p-values, are reported.

Line energy [keV]	**Source**	**Goodness of fit**	
		p-value	χ^2/dof
239	^{212}Pb	0.52	23
277	^{208}Tl	0.14	31
300	^{212}Pb	0.28	27
583	^{208}Tl	0.88	55
727	^{212}Bi	0.94	20
861	^{208}Tl	0.55	57
1173	^{60}Co	0.71	77
1332	^{60}Co	0.50	88
1621	^{212}Bi	0.29	70
2615	^{208}Tl	0.0066	207

modelled with a second order polynomial, shown in figure 3.7, which provides a sufficient correction for these non-ideal effects. The absolute energy residuals, plotted in the bottom panel of figure 3.7, indicate that the expected error in the energy reconstruction is $< 5 \times 10^{-2}$ keV, with the exception of the two data points relative to the ^{60}Co lines that show a slightly worse agreement with the fit. The correction provided by the second order term of the energy calibration contributes < 0.3 keV at the end of the MCA scale, that corresponds to a part over ~ 104 of the contribution of the linear term over the entire dynamic range. The energy resolution as a function of energy is shown in figure 3.8 with the absolute residuals shown in the bottom panel. The employed fit function is an empirical correction to the ideal behaviour $\sigma_E(E) \propto \sqrt{E}$. A constant a_0 is introduced to correct for eventual offsets that can be introduced by electronic and quantisation (from the ADC) noises, and an empirical correction to the expected line broadening:

$$\sigma(E) = a_0 + \sqrt{a_1 E + a_2 E^2}\,. \tag{3.6}$$

Gator background

The Gator's gamma background, shown in Figure 3.9 together with the best background of a GeMPI spectrometer, has a count rate of $\sim$ 250 counts/day over the 50 keV - 2700 keV energy region. The low background level combined with the high energy resolution (3.5×10^{-3} at 100 keV and 10^{-3} at 1 MeV [186]) make possible to reach the sub-mBq/kg sensitivity for samples with masses of some kg in a reasonable counting time ($\sim$ 10 - 20 days).

The presence of *Rn* in the cavity is inferred from the detection of the 352 keV line from ^{214}Pb and of the 609 keV line from ^{214}Bi in the background spectrum, with respective counting rates of $(3.4 \pm 0.8) \times 10^{-1}$ counts/d and $(3.1 \pm 0.6) \times 10^{-1}$ counts/d. The

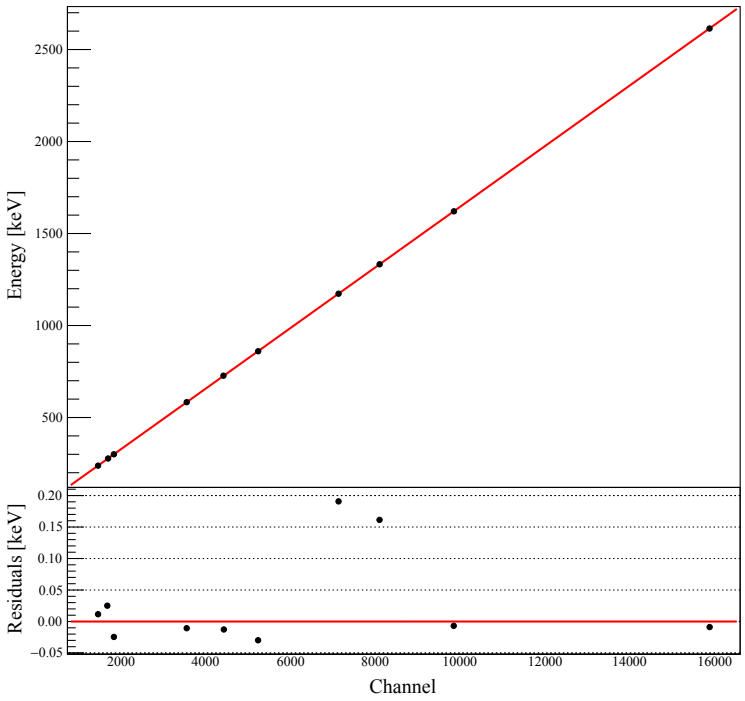

Figure 3.7.: Top panel: energy calibration of the Gator detector. The uncertainties of the lines positions in the MCA scale are taken from the statistical errors of the fits of the center of the Gaussian, while the uncertainties on the true energy of the lines are taken from the literature. The fit of the points is performed with a second order polinomial. Bottom panel: absolute fit residuals for the energy lines used for this calibration.

^{222}Rn in the cavity is most likely transported by the purging nitrogen, which might be contaminated already at the reservoir tank from it is taken. As the liquid nitrogen (LN) tanks at the LNGS underground laboratory are refilled almost weekly, a part of the transported ^{222}Rn might come from original contamination of the LN, while another might be originated by emanation (see section 3.2) from the walls of the resevoir and/or from the internal surface of the long pipeline (> 100 m) that connets the reservoir to the Gator facility. Additionally, ^{222}Rn could also be emanated by the surfaces of the components internal to the encasing and to the glove box, and can come from the outside environment from some imperfection in the sealing of the facility. However, figure 3.10 shows a significative reduction of the integrated background when the purging flow is reduced from 10 slpm to 5 slpm. Hence, it was concluded that most of the ^{222}Rn background should come from the nitrogen line, while the ^{222}Rn produced from internal emanation and from eventual leaks of the sealing system should be negligible in the present setup. This motivated to plan an upgrade of the Gator facicility in order to reduce the ^{222}Rn contamination in nitrogen. At the moment of writing two solutions have been identified two ways to achieve this improvement, both still under study of feasibility. The first consists in replacing the evaporation nitrogen with a proper boil-off nitrogen as for the case of the GeMPI detectors, that however might result in problems due to the much longer distance to the boil-off tank of the Gator facility with respect to the GeMPIs. The second option is based on the same principle used in chromatography and consists in developing a cryogenic trap based on activated charcoals, where the

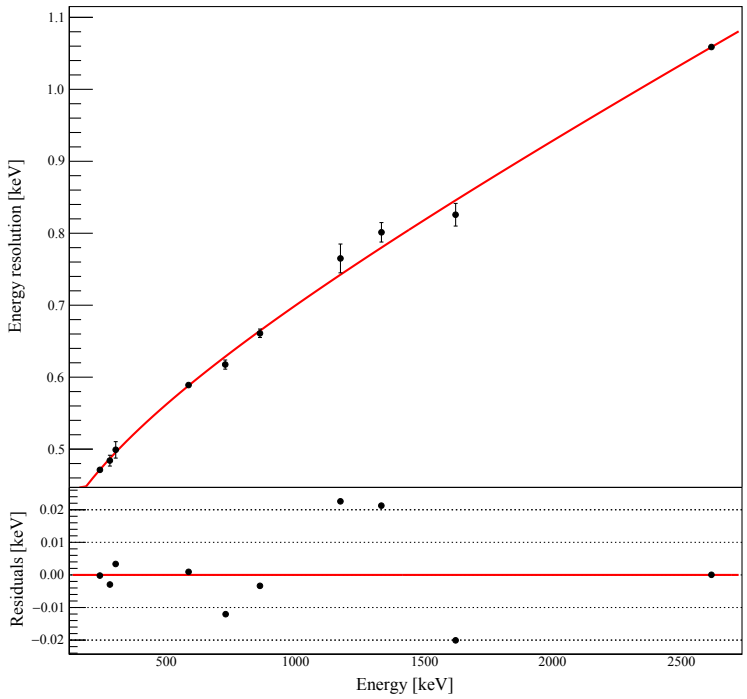

Figure 3.8.: Top panel: calibration of the energy resolution of the Gator detector as function of energy. The values are taken from the σ parameter of the peak fitting function 3.4. The fit is performed with the function 3.6. Bottom panel: absolute residuals for the energy resolution in correspondence to every spectral line employed in the calibration.

radon drift velocity is much lower than the nitrogen because of its higher probability of adsorption on the charcoals internal sufaces. Because of the longer mean time of ^{222}Rn inside the cold trap, the nitrogen exiting the will result cleaned as demonstrated in [198–200].

The presence of ^{40}K is inferred from the spectral line at 1461 keV with a detected rate of (1.6 ± 0.4) counts/d in the background spectrum. As this contamination has not been observed in the original work of Baudis *et al.* [186], the ^{40}K was most likely introduced into the cavity by a non recognised measured sample. As mentioned, the potassium is highly soluble in water and its removal from the internal cavity walls would be easy. However, this requires the opening of the facility in order to operate inside, and will most likely be done during the next upgrade of the Gator detector.

As will be shown from the radioassay results of the materials screening, for the materials radiopurity requirements of the XENON1T experiment both the backgrounds do not compromise at any significant level the detection sensitivity to the radioactive contamination. However, as both the background contribute by Compton scattering to the background of the low-energy part of the Gator energy spectrum, a reduction of this two sources might induce a significant improvement of the detection sensitivity to isotopes that emitting only low energy γ-rays, such as ^{234}Th and ^{235}U .

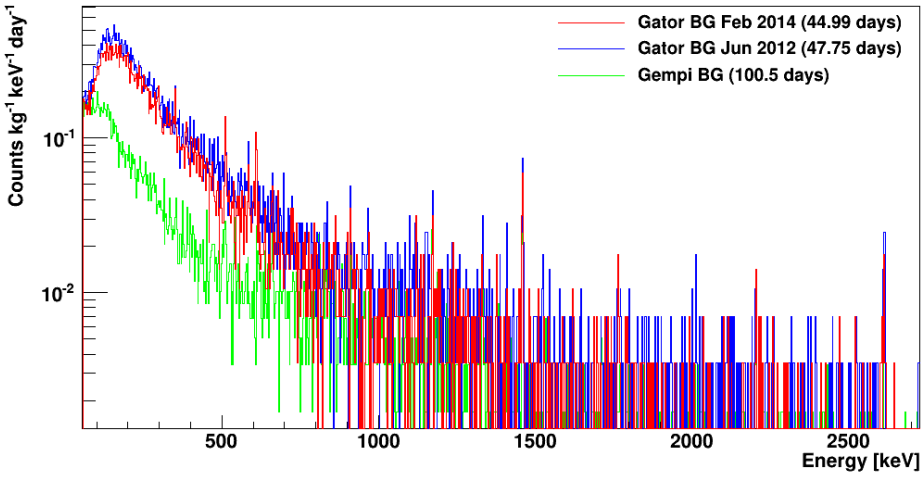

Figure 3.9.: The background spectra of the Gator detector acquired in early 2012 (blue) and between 2013 and 2014 (red). The green histogram is the background spectrum of the GeMPI detector [185], which is currently an HP-Ge detector with the lowest background in the world.

3.3.2 *Analysis of the samples spectra*

The intrinsic radioactivity of the samples is determined by the strength of the full absorption peak, corresponding to the most prominent spectral lines of the radio-isotopes under investigation. For the analysis of the γ-spectrum of the screened samples a C++ based software has been developed, able to operate in manual and automatic modes. In the automatic mode the program computes the specific activities of the radioisotopes based on a database of their spectral lines. Usually this mode is used to determine the contamination of the sample from the most common radioisotopes (e.g. the primordials). After the automatic analysis is performed, the acquired spectrum must be visually scanned in order to search for the presence of additional lines, which may reveal the presence of radioactive isotopes not considered among those searched in the automatic analysis mode. The identification of the new spectral lines is done by using the available catalogs of gamma ray radiation. This process can be performed only manually and depending on the case might be rather long. Once a new radioisotope is identified, the analysis program can be run in manual mode, where the user can implement the necessary information for the new spectral lines. The database is saved in a binary ROOT file as a TTree object [201], where each row represents a line and each column some of its properties such as the energy (from the literature), the relative intensity (from the literature), the detection efficiency (from the simulations), the resolution (from the calibrations), and the definition of the signal and the control regions.

Counting method and model for the analysis

For each spectral line the signal region is defined as the energy interval $\pm 3\sigma$ above and below the centre x_0 of a particular γ line, where σ is the resolution calculated from the calibrations. Under the assumption that the counts relative to a γ line are normally distributed around the central position, with a spread given by the resolution σ, the

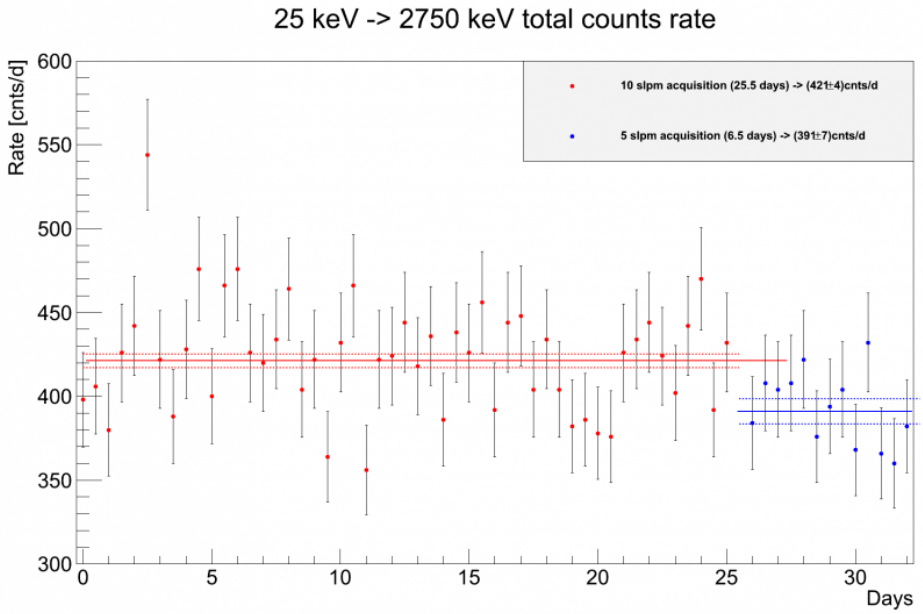

Figure 3.10.: Variation of the integrated rate after the change of the nitrogen purging flow in the Gator measurement chamber. The rate has been calculated integrating the energy spectrum from 25 keV to 2750 keV. The decrease of the background rate with the decrease of the purging flow has been interpreted as the result of less ^{222}Rn injected in the cavity by the nitrogen.

expected fraction of signal counts falling outside the signal region is $\simeq 2.7 \times 10^{-3}$ and thus it is neglected for the analysis of the radioactive contamination of the samples.

The expected number of counts λ_S which determine the strength of a spectral line of a radioisotope with specific activity A in a sample of mass m is given by:

$$\lambda_S = (\varepsilon I) \cdot A \cdot m \cdot t\,, \tag{3.7}$$

where ε and I are, respectively, the detection efficiency and the relative intensity of a specific γ line, and t is the measurement time. The product εI is computed by simulating the decay of the radioisotope using a C++ Monte Carlo code based on the Geant4 [202] toolkit (revision 10.02.p02), where a detailed model of the detector and the sample are implemented, and by counting the number of photo absorption of the specific spectral line. The decays of the radioisotopes of interest are simulated using the G4RadioactiveDecay class [203], where the relative intensities and directional correlations of the γ-rays emitted in the decay are taken into account.

The background expected in the signal region consists of two contributions. The first component, the *continuum background*, is always present and produced by the γ-rays that loose only part of their energy in the sensitive volume and by those that Compton scattered off the components of the detector before being absorbed by the Ge crystal. The second component of background is given from the presence of the same spectral line in the background of Gator (for example the ^{40}K line), that would contribute directly to the total counting rate in the signal region. This component will be called with the jargon expression *peaked background*.

The contribution of the continuum background inside the signal region is modeled with a first order polynomial and is estimated from the lower and upper control regions,

defined as the 3σ energy intervals below and above the signal region, respectively. Hence, the expected background counts in the signal region λ_B are inferred from the expected background counts in the lower and upper control regions $\beta_{\rm L}$ and $\beta_{\rm U}$, respectively:

$$\lambda_{\rm B} = \beta_L + \beta_U \,. \tag{3.8}$$

Depending on the radioisotopes that contaminate a sample it might happen that one or both control regions of a spectral line overlap with the signal region of another spectral line. In this case the overlapping control region cannot be employed as it would lead to an overestimation of the background in the signal region. For such a situation the lower (upper) control region of the line with the overlapping signal region is used in place of the lower (upper) control region of the spectral line of interest. When the original control region of a line is replaced by the respective control region of another line, the estimation of the expected background counts must be corrected for the different distance of the new control regions from the centre of the signal region:

$$\lambda_{\rm B} = \frac{w_{\rm S}}{x_{\rm L} + x_{\rm U}} \left[\beta_{\rm L} \frac{(x_{\rm U} - x_0)}{w_{\rm L}} + \beta_{\rm U} \frac{(x_0 - x_{\rm L})}{w_{\rm U}} \right] , \tag{3.9}$$

where $x_{\rm L,U}$ are the centres of the lower and upper control regions, respectively. The parameters $w_{\rm S,L,U}$ are the widths of the signal region, the lower and the upper control regions, respectively. Given the excellent energy resolution of the Gator spectrometer, it must be noted that in the case when one or both the control regions of a line are replaced with others, not overlapping with the signal region, the difference of their widths is usually negligible ($w_{\rm L} \simeq w_{\rm U} \simeq w_{\rm S}/2$), although calculated starting from the resolution σ relative to different but very close spectral lines.

When the analysis software is run in manual mode, because additional absorption peaks are visually observed by the user, the algorithm controls whether there is any overlap of the control regions of the new spectral lines with the signal regions of the lines in the standard database used in the automatic analysis mode. If an overlapping situation between one of the new visually observed lines and one of the spectral lines of the standard database is determined, it is necessary to replace one control region of a given line in the database with one of the control regions of the new line. In such case analysis for the common isotopes must be run again using the updated control regions for the lines that were overlapping, hence a new database file with updated control regions is generated to perform again the automatic analysis of sample spectrum.

For the determination of the contribution of peaked background in a specific spectral line, the contribution of the continuum to the peak in the background spectrum must be subtracted from the signal region. The contribution of the continuum to the total counts in the signal region of the background peak is inferred from the control regions by using the same method as for the signal, described above (equations 3.8 and 3.9 depending on the case). In order to determine whether a background line has an overlapping another spectral line, only the detected lines during the background analysis are used.

When a peak in the signal region is detected on the background spectrum, its rate $r_{\rm pb}$ is added to the contribution of the background in the signal region of the specific spectral line. In such case the total expected background in the signal region is modified to:

$$\lambda'_{\rm B} = \lambda_{\rm B} + \epsilon_{\rm b}(r_{\rm pb} \cdot t) \,, \tag{3.10}$$

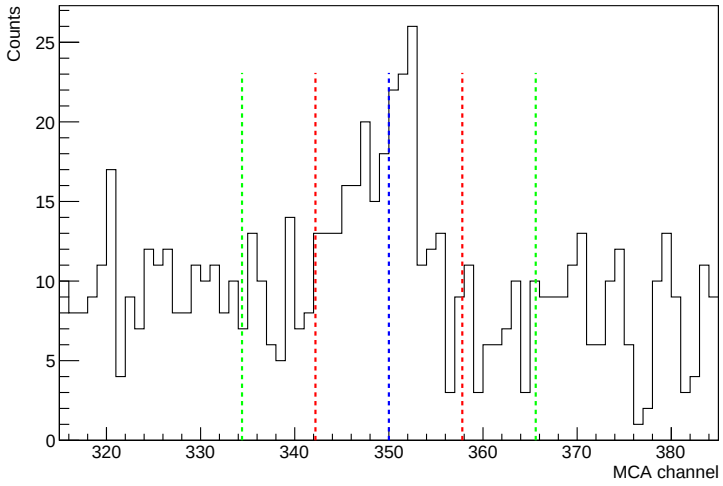

Figure 3.11.: Example showing the method used to divide the spectrum around a spectral line for the analysis of the Gator data. The blu dashed line corresponds to the ideal position of the line. The two red lines around it define the signal region $\pm 3\sigma$ wide, where σ is the gasussian width of the line determined with the calibrations. The two green lines above and below the signal region define the upper and lower signal region, respectively, that are σ wide each. The counts observed in these two control regions are used to infer the count rate, due to the continuos background (Compton scattering), inside the signal region. The widths of the signal and of the control regions can be costomised by the user using external configuration files.

where t is the measurement time of the sample and ϵ_{b} represents the attenuation of the background rate of the specific spectral line, which depends on the shielding power of the sample introduced in the cavity, and on the background source position. When required by precision measurements, the attenuation coefficient can be estimated comparing the detection efficiency computed with Monte Carlo simulations of the radioisotope decays, performed with and without the sample inside the measurement cavity. However this procedure is applicable only when the position of the background source is known with enough accuracy, condition that is rarely met.

Depending on the required precision for a given measurement three different inference methods are used, and are detailed in the following. The first method, already used for the characterisation of Gator [186], is the method with the lowest computational requirements. In this method every spectral line belonging to the same isotope is analyzed independently from the other lines. The total counts in the signal region C_{T} of a line are compared with the detection limit L_{d} at 95 % confidence, defined in [204] as:

$$L_{\mathrm{d}} = 2.86 + 4.78\sqrt{1.86 + C_{\mathrm{B}}}\,, \tag{3.11}$$

where C_{B} are the total estimated counts in the signal region calculated by the 3.9 or 3.10, by replacing $\beta_{\mathrm{L,U}}$ with the actual counts $B_{\mathrm{L,U}}$ in the lower and upper control regions, respectively. A detection is determined when the difference $C_{\mathrm{n}} = C_{\mathrm{T}} - C_{\mathrm{B}} > L_{\mathrm{d}}$,

and the specific activity is calculated as:

$$A = \frac{C_{\mathrm{n}}}{(\varepsilon I) \cdot m \cdot t} \,. \tag{3.12}$$

When the specific line is not the detected, an upper limit is reported by replacing C_{n} with L_{d} in the 3.12.
Finally, the total activity of an isotope is determined as the weighted mean of the specific activity of the detected spectral lines. In the case that no one of the spectral lines of a radioisotope are detected, the reported upper limit is given by the lowest of the upper limits from each analysed line. Furthermore, equation 3.11 can be used to study the detection sensitivity corresponding to a specific spectral line as a function of time by replacing the counts C_{B}, taken from the background spectrum, with the expected counts after a measurement time t:

$$A_{\mathrm{d}}\,(t) = \frac{2.86 + 4.78\sqrt{1.86 + C_{\mathrm{B}} \cdot (t/t_{\mathrm{b}})}}{(\varepsilon I) \cdot m \cdot t} \,, \tag{3.13}$$

where t_{b} is the acquisition time of the background spectrum. This method provides an efficient way for the analysis of the radioactive contamination of the samples, however it does not take advantage of using all the spectral lines in the spectrum and thus does not provide all the possible detection sensitivity that an ultra-low background spectrometer can provide. This is primarily due to the fact that for each radioisotope of interest the analysis is independently performed on each spectral line, combining the results only at the end. In addition this method replaces the expected counts, represented by the unknown parameters λ, with the observed counts, which are Poisson distributed random variables. When the Poisson intensities relative to signal and control regions are very small (i.e. ≤ 10), the observed counts are subject to strong relative fluctuations, and thus a direct substitution might lead to large deviations from the correct inferences. This sometimes happens in the analysis of the spectral lines above 500 keV, e.g. when the cumulated observed counts in the two control regions are 0-1 while 4-5 counts fall in the signal region. In cases similar to this one there is a significant probability that an under-fluctuation occurred in the background, and thus the direct substitution might lead either to a false positive or, if the signal is present, to a significant overestimation of its intensity. On the other hand, in a situation when a strong under-fluctuation of the signal region counts occurs and the counts observed in the control regions are significantly higher, this procedure leads to set upper limits without employing the information contained in the signal region. For a material screening campaign these occurrences would not represent a big issue as in both cases the radioassay provides a conservative result. However, it should be pointed out that a large part of the information present in the spectrum is not efficiently exploited, and thus not the entire detection potentialities of a very low background spectrometer are used. For this reasons a likelihood and a Bayesian approaches, based on proper statistical models and able to take into account correlations between different spectral lines, have been developed. For both methods the data is modelled with the same likelihood, which represents the central object to perform the inference on the specific activity A of a radioisotope of interest. The model likelihood is decomposed in the product of the

likelihoods for each of the considered spectral lines of isotope:

$$\mathcal{L} = \prod_{k}^{N} \mathcal{L}_k \,, \tag{3.14}$$

where the index k runs over all considered spectral lines. The data relative to each line k is modelled by the product of Poisson distributions for the signal and the control regions represented by the functions $P(C|\mu) = (\mu)^C\, e^{-\mu}/C!$:

$$\mathcal{L}_k = P\left(C_{\mathrm{T}_k}|\lambda_{\mathrm{S}_k} + \lambda_{\mathrm{B}_k}\right) \cdot P\left(B_{\mathrm{L}_k}|\beta_{\mathrm{L}_k}\right) \cdot P\left(B_{\mathrm{U}_k}|\beta_{\mathrm{U}_k}\right) \,. \tag{3.15}$$

For the expected background rate in the signal region of the line k either of the equations 3.8 or 3.9 is considered depending on the specific case. In case the isotope of interest is also detected in the background, the λ_{B_k} in the 3.15 is replaced with the definition in equation 3.10, and the Poisson terms for the control regions of the spectral line in the background spectrum are introduced:

$$\mathcal{L}'_k = \mathcal{L}_k \cdot \left[P\left(B'_{\mathrm{L}_k}|\beta'_{\mathrm{L}_k}\right) \cdot P\left(B'_{\mathrm{U}_k}|\beta'_{\mathrm{U}_k}\right)\right] \,, \tag{3.16}$$

where the $\beta'_{\mathrm{U,L}_k}$ and $B'_{\mathrm{U,L}_k}$ are the expected and actual counts in the two control regions of the line k in the background spectrum, respectively.

3.4 MATERIAL SCREENING RESULTS

3.4.1 *Cryostat materials and radioassay of the metal samples*

Among the components of the XENON1T detector the cryostat was one of the most critical. Its geometrical dimensions, in particular the dimensions of the internal vessel, were determined primarily by the amount of LXe target to be used and thus by the dimension of the TPC. Given the total LXe mass of ~ 3 tonnes the internal and external shells composing the cryostat had to be designed in order to be able to bear the total weight. In particular for the internal shell an additional requirement was being able to withstand the absolute pressure of the xenon during the operations (~ 2.3 Pa).

Since the water bath where the cryostat is immersed constitutes, from a thermodynamic point of view, a relatively large heat source to be compensated by the refrigeration and xenon liquefaction system (few 100 W at LXe temperature), the choice of materials was additionally constrained by the thermal insulation requirements. This is particularly critical for the situations when either the cooling system or the insulation vacuum fail, and the thermal insulation of the system should allow for the emergency operations in a condition where the pressure inside the inner vessel does not rise too fast, in order to prevent any damage to the PMTs.

Along with the constraints imposed by the mechanical and thermal requirements, the background impact of the radioactive contamination of the materials based on their total mass had to be evaluated. The materials that have been identified for the construction of the cryostat were the oxygen free (OF) copper, stainless steel and the titanium. Their physical properties, the amount required to fulfill the mechanical constraints, and the estimated neutron flux on the basis of the known contamination values for each material are reported in Table 3.2. For the estimation of the neutron emission rates the neutron

yields used for the three materials were obtained with the SOURCES-4A code [205], already used for the XENON100 experiment [154,167]. The contamination of the copper, the stainless steel and the three titanium grades are reported in table A.1, A.3 and A.5, respectively. For conservative background predictions, the preliminary estimations of the neutron emission rate from the cryostat was perfomed considering the upper limits of the radio-assayed materials as actual measurements.

Oxygen-free electrolytic copper (OFE-Cu) and oxygen-free high conductivity copper (OFHC-Cu) were considered as possible materials for the cryostat, because of the high level of radio-purity that these materials feature. In table A.1 most of the reported radioactive contamination is not detectable neither with γ-ray spectrometry nor with ICP-MS techniques. This is true in particular for the contamination from the U or Th decay chains, which are $\lesssim 10^{-12}$ g/g. Given the relatively low value of the ultimate sustainable strain and the high thermal conductivity, the mechanical constrains could be fulfilled only using rather thick and massive cryostat vessels, while the thermal requirements would have been hardly matched. In spite of the radio-purity of the OF-Cu, the large mass estimated for a copper cryostat would potentially lead to a neutron emission rate about an order of magnitude higher than from a stainless steel or a titanium vessel. Stainless steel and titanium have very similar mechanical and thermal properties leading to similar cryostat masses, and thus both were eligible as construction materials of the XENON1T cryostat. Based on the conservative preliminary estimation of the neutron rate, the stainless steel was selected for the cryostat, although the contamination from γ emitters in stainless steel is much higher than in titanium.

Although, the copper was not suitable for the cryostat construction, most of the screened samples have been employed for the construction of many TPC components, such as the field shaping rings, the support structures of the top and bottom PMT arrays, and some other minor components. The exposure of copper to CRs might yield a relatively high production of medium and long lived radionuclides, such as ^{46}Sc, ^{48}V, ^{51}Cr, ^{52,54}Mn, $^{56-58,60}$Co and ^{59}Fe, which can be efficiently used as indicators of the exposure history of a particular copper sample. The half-lives of most of these isotopes range from a few days to a few months and thus are expected to be decayed out within a year after the detector construction. However, such isotopes as ^{54}Mn, ^{57}Co, and in particular ^{60}Co, can be a challenge for the background requirements because of their long half life and because of their relatively high-energy and penetrating γ emissions. Therefore particular care was taken in the radioassay of the copper samples used for the internal components, in order to establish the level of the cosmogenic activation, reported in table A.2. This allowed to select only copper batches that have not been stored at ground level for too long time after their production.

A sample of OFHC-Cu rods plated with $1\,\mu$m of of gold considered for the construction of the field shaping rings were measured. The gold plating was proposed in order to smooth the surface of the rings, that will be biased at several thousand volts in a very tight environment, when the detector will acquire data with the drift field at the nominal value of 1 kV/cm. Besides the observed cosmogenic radioisotopes, a relatively high ^{40}K contamination was measured and thus no plating has been employed for the rings. As the plating was applied on the copper rods by electrolytic methods and since K is highly soluble in water this is most likely the origin of this contamination.

The 20 stainless steel samples assayed, listed in table A.3, are characterised by a rather variable ^{238}U concentration, spanning from ~ 1 mBq/kg to ~ 100 mBq/kg. The ^{226}Ra

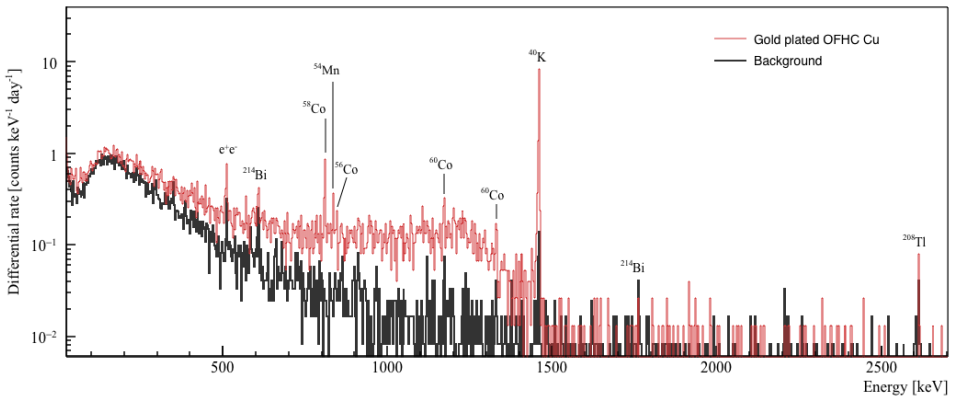

Figure 3.12.: Spectrum of the gold plated OFHC copper, investigated as a candidate material for the field shaping rings. The ^{40}K and other most prominent photo-absorption peaks of some common cosmogenic products of copper, are highlighted.

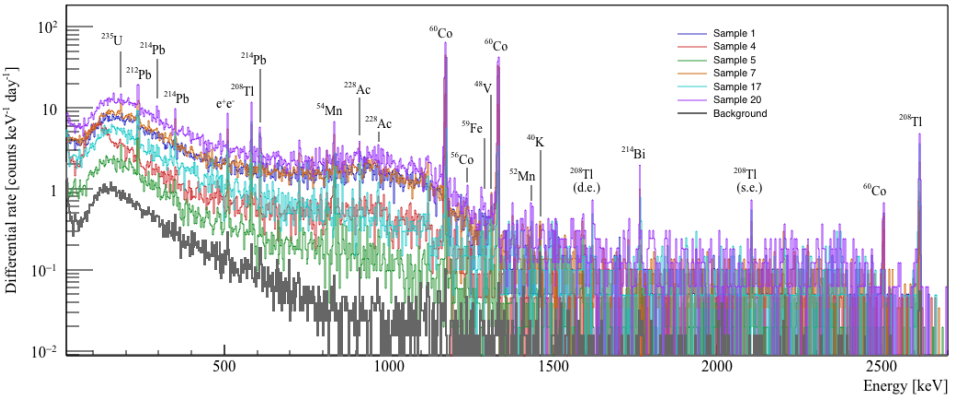

Figure 3.13.: Selected gamma spectra of some of the screened steel samples. The highlighted lines are relative to the most common radioactive impurities found in this material, although they are not present in all the samples.

concentration in stainless steel is observed at levels below few mBq/kg ($\sim 10^{-5}$ ppt in mass), indicating a strong deviation from the secular equilibrium in the ^{238}U chain. The ^{226}Ra depletion in the stainless steel was already observed in a previous survey of steel samples measured with some of the Ge spectrometers used for the XENON1T radioassay campaign [206]. Such a depletion might be produced at any of the production phases: from the chemical separation of the raw ores to the melting in the high-temperature furnaces. However, as pointed out in [207, 208], the relative Ra/U concentration should not change significantly inside the furnaces, but most likely when chemical additives are introduced in the iron-steel conversion. The only exceptions to this behaviour are represented by sample 17 and potentially by sample 1, where no disequilibrium in the ^{238}U chain was observed. Considering the first 6 samples of stainless steel, which are employed as construction materials, the ^{232}Th level is assayed at a few mBq/kg corresponding to the concentration of $\sim 2 \times 10^{-10}$ g/g. The measured ^{228}Th contamination values are frequently found either in secular equilibrium with the early

^{232}Th chain, or in a potential equilibrium state when only upper limits are reported either for the ^{232}Th or the ^{226}Ra (or both) activity. Only in the case of the stainless steel samples 6 and 12 the concentration of the ^{228}Th was found 9 and 7.5 times higher with respect to the ^{232}Th, respectively. However, these samples were assayed only with γ-ray spectrometry, that is sensitive to ^{228}Ra and not directly to ^{232}Th. Hence, the observed disequilibrium in the ^{232}Th decay chain might be again given by the chemistry-induced Ra depletion, that in the case of sample 12 is also observed in the ^{238}U chain. The only cases, where the contamination from ^{232}Th is directly detected by the ICP-MS measurement, and at same time the ^{228}Ra and ^{228}Th sub-chains are detected by γ-ray spectrometry, are samples 3 and 17. In the case of sample 3 there is a very good agreement between the γ-ray measurements of the ^{228}Ra and ^{228}Th sub-chains indicating an equilibrium over the chain, while the measurement performed with the ICP-MS determines a ^{232}Th concentration about 2 times lower. Although the uncertainty intervals of the two measurements slightly overlap with each other, this measurement might indicate an excess of ^{228}Ra with respect to ^{232}Th. However, an opposite behaviour is observed looking at ^{238}U chain where there is a depletion of the ^{226}Ra sub-chain with respect to ^{238}U by a factor of 10. For the sample 17 the situation is more complex as the γ spectrometry measured the ^{228}Ra specific activity about 2 times lower than the specific activity of the late ^{228}Th chain, that indicates a Ra depletion during one or more production phases. However, the same sample is one of the two where the ^{226}Ra is found in secular equilibrium with ^{238}U, which is in tension with a hypothesis of Ra depletion. In addition the ^{232}Th specific activity, resulting from the ICP-MS measurement, lies in the middle of the ^{228}Ra and the ^{228}Th values, within ~ 1 sigma from both, and thus this does not help to clarify the situation.

As suggested in [206], the ratio of the concentrations ^{228}Ra /^{228}Th and the initial ^{226}Ra depletion with respect to ^{238}U can be used for the dating of steel from its production, for an ageing time range not higher than a few decades (depending on the initial Ra depletion). Such an interesting dating method can in principle be applied for any material when one of the two conditions are verified for the ^{226}Ra /^{238}U and ^{228}Ra /^{228}Th ratios. The first consists in a direct measurement of these ratios at the production time, which is unlikely as the manufacturers are hardly interested in such knowledge. A more practical way consists in performing systematic study on samples with a known production date. The measure of the ^{226}Ra /^{238}U, constant over time, and the relative concentration of ^{228}Ra /^{228}Th at time t after the production can constrain the aging of the specific steel sample:

$$R_{1,2}(t) = \frac{R_{0,2}\,(0) + [R_{1,2}\,(0) - R_{0,2}\,(0)]\, e^{-t/\tau_1}}{[1 - R_{1,2}\,(0)]\, e^{-t/\tau_2} + [R_{1,2}\,(0) - R_{0,2}\,(0)]\, e^{-t/\tau_1}}\,, \tag{3.17}$$

where $\tau_1 \simeq 8.3\,\mathrm{yr}$ and $\tau_2 \simeq 2.76\,\mathrm{yr}$ are the mean lifetimes of ^{228}Ra and ^{228}Th, respectively. Therefore the specific activity ratio $R_{1,2}$ depends on the ratio of specific activities $R_{1,2}(t=0) = [A_{^{228}\mathrm{Ra}}/A_{^{228}\mathrm{Th}}]\,(t=0)$ and $R_{0,2}(t=0) = [A_{^{232}\mathrm{Th}}/A_{^{228}\mathrm{Th}}]\,(t=0)$. Since the ^{232}Th activity is constant over time, the ratio $R_{0,2}$ depends only on the ^{228}Th decay time and can be immediately obtained by the activity ratio measured at time t:

$$R_{0,2}(0) = R_{0,2}(t) e^{-t/\tau_2}. \tag{3.18}$$

Hence for a systematic study the ^{232}Th concentration must also be known, and thus mass spectrometry measurements in addition to γ-ray spectrometry are required.

If on one hand most of the analysed steel samples for XENON1T are in general agreement with this hypothesis, on the other hand the only two samples where the mass spectrometry measurement directly observed the ^{232}Th contamination seem to be in tension with the possibility of using the ^{228}Ra /^{228}Th concentration ratio to infer the steel ageing. This tension might be explained by the fact that the chemical concentration of Th itself might be altered during the same processes that cause the Ra depletion. Since at the end time of production the ^{232}Th and ^{228}Ra relative abundances in steel might depend on both the initial contamination of the raw materials and ores as well as on the type of produced steel, a systematic measurement of this ratio as well as of the ^{232}Th concentration at the time of production might clarify whether such an interesting dating technique can be used.

The ^{60}Co isotope is a cosmogenic product, usually produced by spallation or fragmentation of the transition metals nuclei caused by HE nucleons, and thus is expected on steel samples exposed to the CR. However the relatively large and variable ^{60}Co concentration observed in the steel samples listed in table A.4 has mainly anthropogenic origin. As detailed in [208] the ^{60}Co is usually introduced in the steel production cycle by the inadvertent recycling of already contaminated steel scraps (*e.g.* steel capsules containing a sealed ^{60}Co source), and by the addition of ^{60}Co in the furnaces for the control of the melt quality by measurements of the emitted γ-rays . The intense Compton background produced by the ^{60}Co spectral lines at 1.17 MeV and 1.32 MeV is the main cause of the worsening detection sensitivity to the activities of ^{238}U and ^{235}U , which are detected with the γ emissions at 92.6 keV and 185.7 keV, respectively. From the exposure of the steel samples to the CRs, the production of cosmogenic isotopes such as ^{7}Be, ^{56,57}Co, ^{46}Sc, and ^{48}V [206] were also expected, and their missed observation is most likely due to the high background produced by the ^{60}Co spectral lines. The only detected cosmogenic radioisotopes are ^{54}Mn and ^{58}Co, as they have relatively higher production rates with respect to the cosmogenic radionuclei obscured by the ^{60}Co-induced background and emit γ-rays in the energy region where the Compton background is less intense.

Titanium samples of grade 1, grade 2 and grade 4 chemical purity (impurities $<$ 0.505 %, $<$ 0.675 % and $<$ 1.025 %, respectively, according to [209]) were investigated for their radioactive contamination, which is reported in table A.5. With the exception of sample 1, the ^{238}U content in all the Ti grades ranges from 25 to 40 mBq/kg (2.0 – 3.2 ppb in mass), confirmed in one of the cases (sample 5) by ICP-MS measurement. For the titanium samples the ^{235}U spectral line at 186 keV was usually detected in addition to the ^{238}U lines. This allowed for the comparison of the independently detected concentrations of these isotopes, which are in agreement within the uncertainties if their natural abundance ratio is taken into account. The specific activity of the lower part of the ^{238}U chain (^{226}Ra -^{206}Pb) resulted in all the cases more than one order of magnitude lower than the upper part of the chain, with the exception of sample 3 for which neither the ^{238}U nor ^{235}U were detected. This observation might be an indication of a systematic and relatively large depletion of the ^{226}Ra concentration in chemically pure Ti with respect to the secular equilibrium concentration. Therefore, under the assumption that the production processes of chemical pure titanium are the cause of

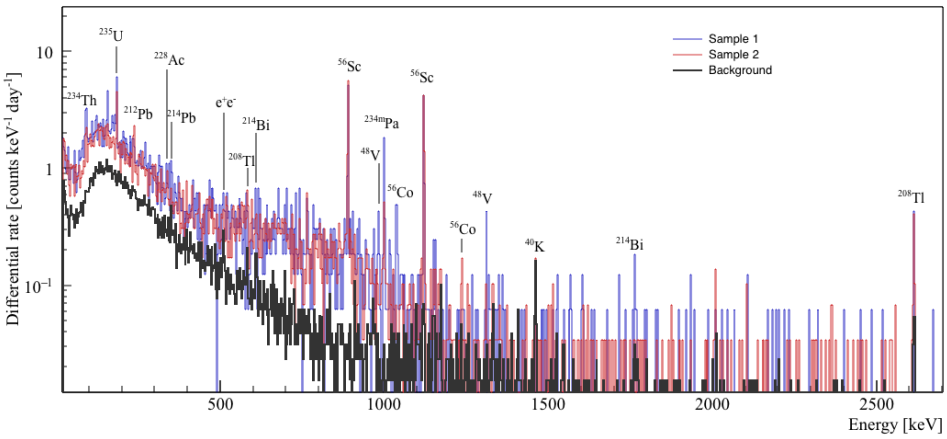

Figure 3.14.: Spectra of some of the titanium samples screened with the Gator detector. The photo-absorption peaks of the most relevant radioisotopes are labeled.

such a depletion, inferring the ^{238}U contamination by the ^{226}Ra activity could lead to a strong underestimation of one of the main neutron emitters.

3.4.2 *Plastic materials for the TPC*

The polymeric materials used for the construction of some parts of the TPC are PTFE, Torlon and ultra high molecular polyethylene (UHMPE). The PTFE is used in relatively large quantity ($\sim 90\,kg$) for the internal reflector panels, the reflector supports, the TPC pillars, the reflector of the PMT arrays and some small electric insulation components. This material is widely used in liquid xenon chambers because of the high reflectivity to the VUV light (95 %), the relative dielectric constant similar to similar to that of LXe, and because it can provide electrical insulation up to $\sim 30\,$kV/mm (depending on the microporosity properties of the material). In addition, PTFE is one of the materials with the highest radiopurity and thus it is largely used for the construction of several components of low-background detectors.

As thoroughly studied in [154], this material can result in a relatively strong neutron emission even with very small concentration of radioisotopes of the decay chains. This behaviour is due to the fluorine, one of the main constituents of PTFE, which has relatively large cross section to (α,n) reactions. Hence, mass- and γ-spectrometry measurements were performed on the first 3 samples listed in table A.6, in order to determine with the highest accuracy the level of contamination in the PTFE samples that were going to be used for the core of the detector. The HP-Ge measurement of the most abundant PTFE batch in the TPC (sample 1), was performed by entirely filling the measurement cavity of the Gator spectrometer with $\sim 40\,$kg of PTFE slabs of different thickness, as represented in figure 3.15, in order to maximise the detection sensitivity to the γ emitters. For this reason a preliminary study of the time dependence of the sensitivity $A_\mathrm{d}\,(t)$, as defined in equation 3.13, was performed for the ^{235}U, ^{238}U, ^{226}Ra, ^{228}Ra and ^{228}Th decay chains. The calculation of the sensitivity curves, shown in figure 3.16, is performed by taking into account the spectral line of the correspondent chain with the smallest A_d at the time $t_* = 1.86 \cdot t_\mathrm{B}/C_\mathrm{B}$, which is the expected

Table 3.2.: Mechanical and thermal properties of the candidate cryostat materials used as input in the preliminary studies, performed to estimate the thickness and thus the mass of the inner and outer vessels. The contamination values, used for the estimation of the neutron emission rate from the cryostat, are those of the sample 3 in table A.1 for the copper, sample 1 in table A.3 for the stainless steel, and samples 3, 4 and 5 in table A.5 for the titanium grades 1, 2 and 4, respectively. The neutron yields employed for this estimation have been calculated with the software SOURCES-4A [205]. The values reported in this table are only preliminary estimations, performed for the selection of the cryostat material based on a simplified detector model, and not the actual values relative to the final design used for the background predictions for the XENON1T experiment [181].

		Copper cryostat	Stainless steel cryostat	Titanium cryostat		
				Grade 1	Grade 2	Grade 4
Density	[gcm^{-1}]:	8.94	8		4.51	
Thermal conductivity	[$Wm^{-1}K^{-1}$]:	401	16.2		16.0	
Cryostat thickness	[mm]:	55	3		6	
Internal vessel mass	[kg]:	3800	780		440	
External vessel mass	[kg]:	7000	870		490	
Total cryostat mass	[kg]:	10800	1650		930	
Estimated neutron rate	[s^{-1}]:	3.4×10^{-4}	2.1×10^{-6}	4.1×10^{-5}	6.4×10^{-5}	7.1×10^{-5}

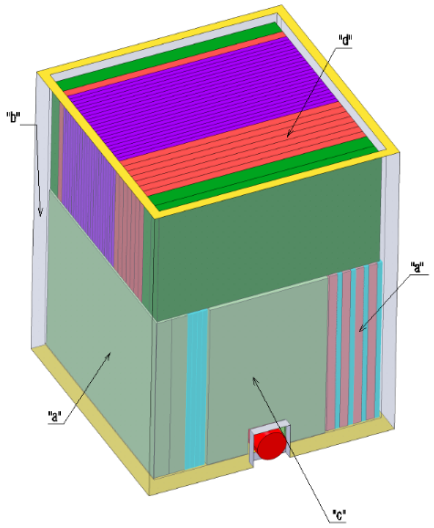

Figure 3.15.: Technical drawing of the disposition of the screened PTFE slabs inside the Gator detector. The purple slabs are 5 mm thick and used for the internal reflectors of the field cage; the red slabs are 8 mm thick and used for the holders of the reflector panels; the green slabs are 15 mm thick and used for the field cage pillars, as support for the copper field shaping rings. The mass distribution of the three PTFE slabs inside the Gator cavity matches their mass distribution of the XENON1T TPC.

counting time when the two terms inside the square root in the equation 3.13 give the

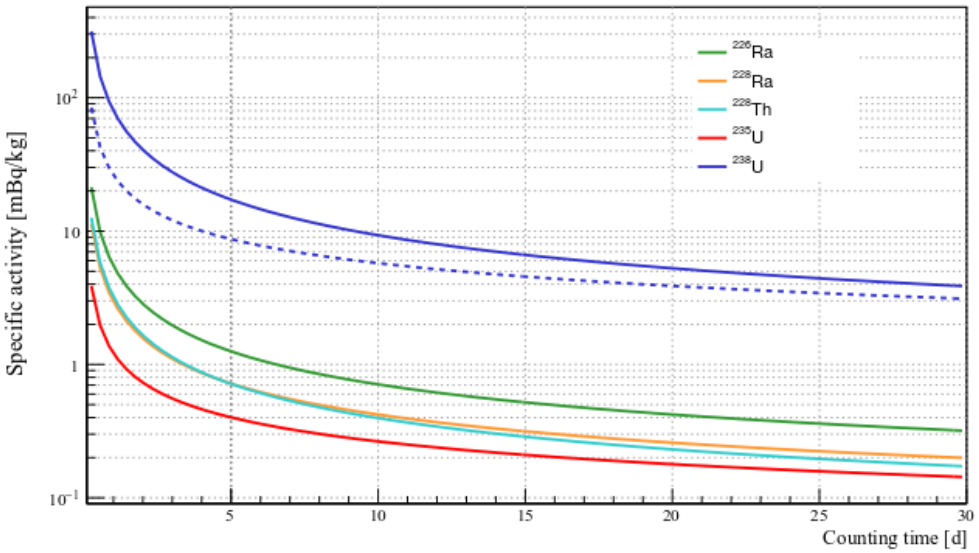

Figure 3.16.: Sensitivity curves for the radioisotopes of the primordial decay chains as a function of the counting time for the PTFE measured with the Gator spectrometer. For each chain the most sensitive spectral line was used as defined in equation 3.19: the ^{214}Bi line at 1764.5 keV for the ^{226}Ra sub-chain; the ^{228}Ac line at 911.2 keV for the ^{228}Ra sub-chain; the ^{208}Tl line at 2614.5 keV for the ^{228}Th sub-chain; the ^{235}U line at 185.7 keV for the entire ^{235}U chain; the ^{234m}Pa line at 1001.0 keV for the ^{238}U sub-chain. The dashed blue line represents the sensitivity to the ^{238}U sub-chain as derived from the ^{235}U activity assuming a natural mass ratio ^{238}U /^{235}U of 137.818 ± 0.050 [171].

same contribution:

$$A_{\mathrm{d}}\left(t_{*}\right)=\frac{6.49 C_{\mathrm{B}}}{(\varepsilon I)\, m t_{\mathrm{b}}}, \tag{3.19}$$

where C_{B} are the counts in the signal region of the specific line taken from the background spectrum, and t_{b} is the background counting time. The study of the sensitivity as a function of time shows that for almost all radioactive chains, with the exception of the ^{238}U early chain, it is possible to get a sensitivity of a few 10^{-1} mBq/kg in about 20 days of counting time. Such sensitivity would correspond to $\lesssim 7 \cdot 0^{11}$ g/g of ^{232}Th, if it is in equilibrium with its daughters ^{228}Ra, $\lesssim 10^{-12}$ g/g of ^{235}U, $\lesssim 10^{-17}$ g/g of ^{226}Ra, and $\lesssim 10^{-20}$ g/g of ^{228}Th, which are satisfactory values for the XENON1T requirements. As the sensitivity to the ^{238}U early chain was not sufficient, ICP-MS measurements were necessary to assay directly this isotope as well as ^{232}Th.

Although the original plan was to measure the PTFE sample for $\sim$ 30 days, the sample was measured for a total of 58 days because of the high degassing rate of Rn, absorbed prior to its insertion in the purged chamber environment. This behaviour is shown in figure 3.17, where the total counting rate in the $(50-2700)$ keV energy range in a function of time is well described by an exponential decay toward a constant level. The decay mean time is constrained by the fit to $\tau = (4.6 \pm 0.7)$ d, about 17 % lower than the ^{222}Rn lifetime. This might be explained by taking into account the N_2 purging of the measurement cavity that flushes the degassed Rn out from the Gator

shielding part. The spectra of the PTFE measurements are shown in figure 3.18, with and without the first 15 days, the sufficient time to let the total rate to decrease below 3σ from the constant rate level $C_0 = (143 \pm 2)$ cnts/d. Although the counting rate has a clear cool-down behaviour, the spectrum with shorter acquisition time shows an intensity reduction of the ^{214}Pb and ^{214}Bi spectral lines, which are the lines that reveal the presence of ^{222}Rn. Hence, the entire run was used to analyse the contaminations reported in table A.6, with the exception of ^{226}Ra that was assayed using the reduced spectrum. This improved the final sensitivity to the primordial radioisotopes by about 7 % for ^{235,238}U, and up to 20 % for ^{228}Th.

The background of the Gator detector results in a general higher counting rate than the spectra of the PTFE measurement, especially in the lower energy region where there are the spectral lines used to infer the specific activity of the ^{235,238}U. This effect is due to the reduced amount of ^{222}Rn in the measurement cavity, almost entirely occupied by the PTFE slabs, that resulted in a general background reduction. Such a reduction allowed for the improvement of the detection sensitivity: by $\sim$ 20 % for ^{238,235}U and by $\sim$ 50 % for ^{228}Th. However, the ICP-MS measurement constrained the ^{238}U and ^{232}Th concentrations to values about 10 times lower than the sensitivity reached with the γ-ray spectrometry.

Sample 1 was additionally contaminated by (0.17 ± 0.03) mBq/kg of ^{137}Cs and by (0.17 ± 0.05) mBq/kg of ^{8}Be at the start of the measurement. The presence of the first radioisotope is most likely due to an the initial contamination of the pellets used to produce the PTFE slabs by extrusion. The second is the result of fast nucleon reactions of the CR with the fluorine nuclei, happened during the production and storage of the material before the transport to the underground laboratory. However, this cosmogenic product has an half-life of 53.2 d, and thus the contribution to the background by its only spectral line at 477.6 keV is expected to become negligible after a cool-down time of a few months in the underground laboratory.

The PTFE sample 2, used to make the reflectors for the two PMT arrays, was measured with both γ-spectroscopy and mass-spectrometry techniques. In this sample the directly detected ^{238}U and ^{232}Th concentrations with ICP-MS are in agreement within the uncertainty with ^{226}Ra and ^{228}Th concentrations measured by the HP-Ge measurement, respectively. This provides an indication that the production of the PTFE does not involve chemical processes that can cause a significant disequilibrium in the decay chains, and therefore for this material it would be possible to infer the ^{238}U and ^{232}Th concentrations from the concentrations of the their respective late sub-chains and vice versa. However, measurements oriented to a systematic study of the secular equilibrium in the primordial chains in PTFE is still missing, and this hypothesis is not so far supported by similar measurements for other samples.

Another assayed PTFE sample, used for minor TPC parts, showed the same purity level in ^{238}U and ^{232}Th as samples 1 and 2. Finally it is worth to point out that all the measured PTFE samples, listed in table A.6, have a level of contamination from primordial radionuclei, including ^{40}K , at least as low as that of the PTFE employed in the XENON100 experiment [180, 210].

Two grade 4203L Torlon samples (6 and 7 in table A.6) were investigated as candidate materials for the field cage pillars and the reflector panel holders. As the dielectric strength of this polymer is similar to PTFE ($\sim$ 20 kV/mm), from the electrical point of view this material would provide the same insulation between the field shaping rings

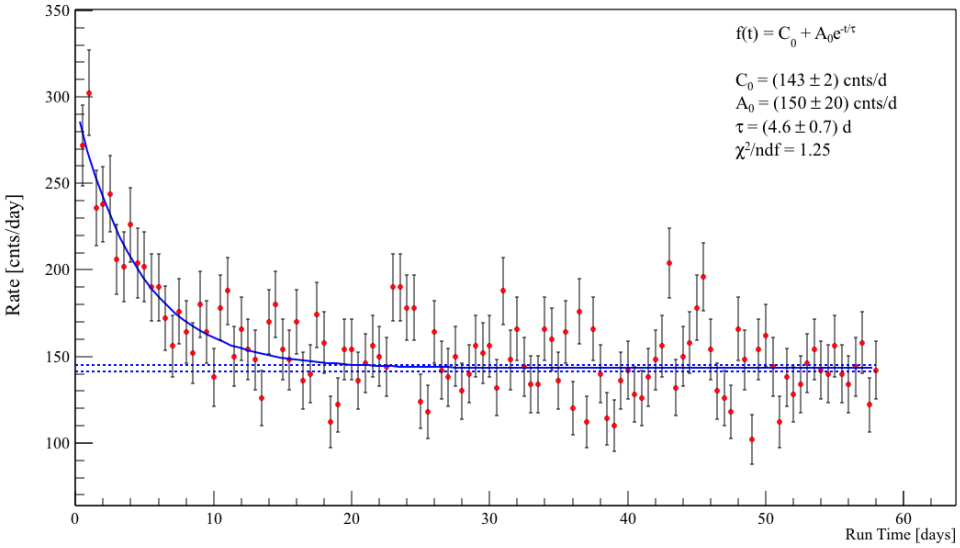

Figure 3.17.: Integrated counting rate in the $(50-2700)$ keV energy interval as function of the measurement time of the 61 PTFE slabs (sample 1 of table A.6). The evolution of the rate is attributed to the degassing of the ^{222}Rn from the surfaces of the material. Each data point represent an acquisition 12 h long.

and the other voltage biased components. This material has, additionally, a much larger tensile modulus (~ 50 kPa), and a much smaller coefficient of linear thermal expansion ($\sim 10^{-5}\,\mathrm{K}^{-1}$) with respect to PTFE. Hence, the mechanical and thermal properties of Torlon would allow the construction of a field cage external structure with a larger mechanical strength than PTFE, and with a linear contraction at $-100\,^{\circ}$C, about an order of magnitude lower than PTFE. However the radioactive contamination of the assayed Torlon was too large, especially for the radionuclei that would yield direct or indirect neutron emitters, and thus this material was used only for small insulating components near the supporting rings of the electrode meshes.

3.4.3 *Cabling of the TPC*

The HV is distributed to the PMTs by Kapton-insulated copper wires ~ 0.1 mm thick from Accuglass [211], rated to operate in ultra-high vacuum environment, with pressures down to 10^{-10} mbar, ensuring, thus, a negligible degassing of electronegative chemical impurities as required by XENON1T. A total number of 259 wires deliver the power to the 248 PMTs. Additional 11 cables are used as common return channel shared by the PMTs powered by the same power supply module. Their estimated total mass inside the vessel is ~ 0.5 kg for a combined total length of 683 m. A sample of 78 g for a total length of ~ 100 m was measured in the Gator spectrometer for 14.2 d. The only radioactive contamination that was detected is from ^{40}K with a specific activity of (464 ± 77) mBq/kg. Given the relatively small mass of the sample only upper limits were inferred for the radionuclides belonging to the two primordial decay series. The auxiliary measurement performed with ICP-MS measured ^{238}U and ^{232}Th concentrations of (4.2 ± 1.3) mBq/kg and (0.71 ± 0.21) mBq/kg, respectively.

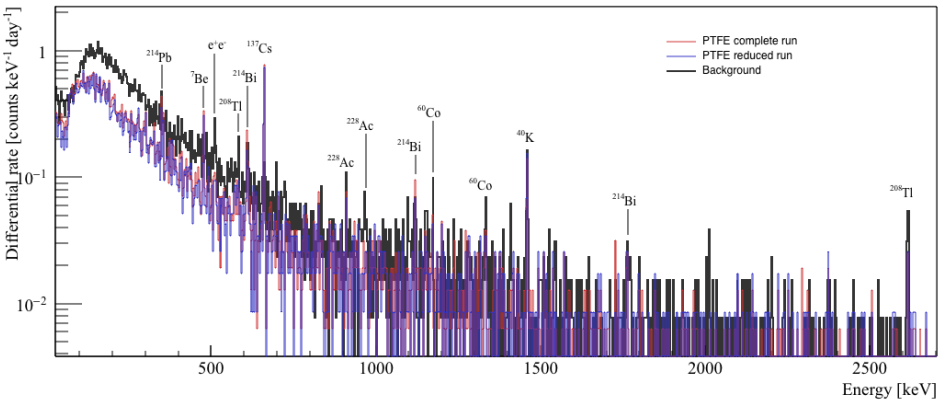

Figure 3.18.: Spectra of the entire (58 d) and of the reduced (43 d) acquisition run of the 61 PTFE slabs (sample 1 of table A.6) measured with the Gator spectrometer. As explained in the text, the reduced run is a subset of the entire run, where the first 15 days of data have been removed. It is possible to observe that, with the exception of the ^{222}Rn progenies, the two spectra do not show noticeable differences. An interesting feature that can be observed is the lower counting rate of the PTFE sample with respect to the Gator background. This is an effect due to the small amount of the Gator cavity left to ^{222}Rn contaminated nitrogen as the PTFE sample fills almost entirely the measurement chamber.

The PMTs signals are transmitted by 248 coaxial cables, with silver coated copper central wires and shielding mesh. Both the signal wires and the shielding mesh are electrically insulated by ~ 0.5 mm thick PTFE layers. In addition to the signal cables for the TPC PMTs, other 64 coaxial cables are employed for six diagnostic Hamamatsu R8520 PMTs, for the temperature monitors (Pt100) and for the level meter readout. The estimated total mass of the installed coaxial cables is ~ 6 kg, distributed all around the field cage, for a total length of ~ 670 m. The HP-Ge measurement of a ~ 1.8 kg (00 m) sample of this cable revealed (0.6 ± 0.2) mBq/kg of ^{228}Th and (33 ± 4) mBq/kg of ^{40}K . Other cosmogenic radionuclides were observed at the sub-mBq/kg level, but given their relatively short half-life and weak activity they could be neglected.

Predictions of the ER and NR backgrounds have been performed for both cable types, by Monte Carlo simulations of the radioactive decays inside the cable materials, employing a GEANT4 code where accurate geometry model of the detector had been implemented. The calculations were performed assuming secular equilibrium in the primordial chains, and a rejection efficiency for ERs of 99.5 %. With these assumptions the predicted total background (ERs and NRs) from the HV wires in the $8 - 50\,\mathrm{keV_{NR}}$ energy region and in the 1 ton fiducial volume is $< 5.8 \times 10^{-2}$ ev/yr, a negligible rate for the life-time scale of the XENON1T experiment. An upper limit of 5×10^{-2} ev/yr results also for the combined ER and NR background from the coaxial cables, where upper limits on the measured contaminations have been used for the calculation of the event rates.

3.5 DEVELOPMENT OF IMPROVED RADIO PURE PMTS

Among the many radio-assayed components in the vicinity of the xenon target, the PMTs are the most complex multi-material components, and special efforts were undertaken for their screening campaign. Photomultiplier tubes were already shown to

give one of the major contributions to the ER and NR radiogenic background in the XENON100 [167, 180] and LUX experiments [212]. In particular, most of the PMT-related ER background was due to ^{226}Ra , ^{228}Th , ^{60}Co , and ^{40}K contamination. Hence, within the material screening program, the XENONcollaboration developed together with the Hamamatsu Photonic company the R11410-21 3-inch, high quantum efficiency ($\simeq 35\,\%$ at a wavelength of $\sim 175\,$nm) PMTs, with special efforts put on their radiopurity improvement [213].

The R11410-21, employed in XENON1T, is a PMT based on 12 dynodes for electron multiplication, insulated by L-shaped quartz plates, able to provide an average amplification factor of 3.5×10^6 at a bias voltage of 1500 V [214]. The optical window consists of VUV-transparent quartz with a bialkali, low-temperature deposited, photocathode. The PMT body is about 115 mm long, made out of Co-free Kovar metal, which is a FeNi alloy with the same thermal expansion coefficient of the window material, for a large reduction of the ^{60}Co contamination. A radiopure alluminum ring is employed for the sealing of the optical window to the Kovar front flange. A back stem made out of ceramic provides electrical insulation between the leads, which provide the connection to the base where the voltage divider network and the signal readout are.

The R11410 radiopurity was improved by a careful radioassay of the raw materials, accomplished with both γ and glow-discharge mass spectrometry techniques, identifying, from one version to the next, the most critical components to replace. These components are the back stem (Al_2O_3), the lateral body, the internal insulator, and the Al seal of the optical window, which are listed in table 3.3 for an overview of the steps undertaken for the improvement of the PMTs radio-purity, from the first version of the R11410 to the last version, the R11410-30. This last version was not employed as the XENON1T photosensor as the impact on the background was negligible while the production efforts and costs where much higher..

Table 3.3.: Evolution steps of the Hamamatsu R11410 PMTs components based on their radio purity. The PMT revisions at the right are the most recent and those with lower radioactive contamination. The R11410-10 revision was also available on the market with the commecial name R11410-MOD. The R11410-30 employes a sapphire stem instead of a ceramic stem. This revision was developed by Hamamatsu in order to reduce the contamination from uranium. However, the radioimpurity improvement was too small compared to the difficulties found in manufacturing this model and to the large increase of their costs.

Component	**PMT revision**				
	R11410	**R11410-10**	**R11410-20**	**R11410-21**	**R11410-30**
Stem	Glass	Ceramic	Ceramic	Ceramic	Sapphire
Body	Kovar (std. purity)	Kovar (std. purity)	Co-free Kovar	Co-free Kovar	Co-free Kovar
Insulator	Ceramic	Quartz	Quartz	Quartz	Quartz
Al seal	Std. purity	Std. purity	High purity	High purity	High purity

The mass model of the R11410 PMT, detailed in table 3.4, was necessary to obtain an accurate radioactivity model with the contamination of the raw materials listed in tables A.7 and A.8. For each radioisotope a conservative and an optimistic radioactivity models are represented as bar charts in figure 3.20. The first of the two models is built

Table 3.4.: Mass model of the R11410 PMT and quantity of each component material for the radioassay HP-Ge measurements.

Sample	Material	Use	Mass per PMT [g]	Sample mass for HP-Ge measurement [g]
1	Quartz	Optical window	30	1179
2	Aluminium	Sealing ring	0.6	515
3	Co-free Kovar	PMT body	78	500
4	Stainless steel	Electrode disk	8.2	555
5	Stainless steel	Dynodes	7.2	510
6	Stainless steel	Shield	4	519
7	Quartz	L-shaped insulator	14.4	838
8	Std. Kovar	Optical window flange	18	525
9a	Ceramic	Stem	16	597
9b	Ceramic	Stem	16	498
10	Std. Kovar	Stem back flange	14	511
11	Zr alloy	Internal getter	5.8×10^{-2}	0.58

considering the upper limits of the radionuclei activity, when neither HP-Ge nor GD-MS (only in the case of ^{238}U and ^{232}Th) detect the specific radio impurity. For the optimistic model only with the actual detected radionuclides in each component are considered for the total radioactivity.

3.5.1 *Radioassay of the R11410-21 materials*

The materials screened and listed in tables A.7 and A.8 have been specifically employed in the production of the XENON1T photosensors. The ceramic stem, as shown in the bar chart in figure 3.20, provides the largest fraction to the total PMT contamination for the radioclei belonging to the U and Th primordial chains as well as for ^{40}K . As the GD-MS measurement of ^{238}U and ^{232}Th was not reproducible over different attemps, the specific activity of these two isotopes in the ceramic was determined by HP-Ge measurements, assuming for ^{232}Th the secular equilibrium with its direct daughter ^{228}Ra. In order to have a better control on the systematics for this material the HP-Ge measurement was accomplished with two different spectrometers, which are in good agreement for the ^{238}U , ^{232}Th as well as for the other radioimpurities.

Although the getter is the PMT component with the smallest mass its expected contribution to the total ^{235,238}U and ^{226}Ra contamination is about $10 - 15\,\%$, and about $\sim 5\,\%$ to the total ^{40}K contribution. The $\sim 30\,\%$ of the ^{226}Ra contamination is

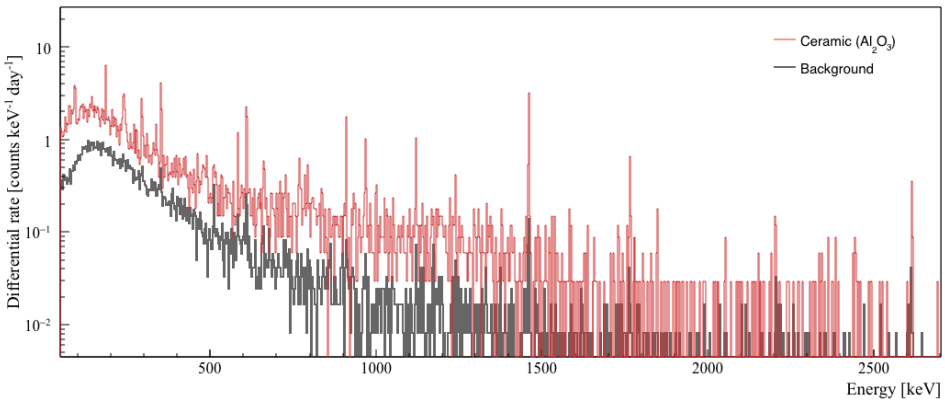

Figure 3.19.: Spectrum of the ceramic stems measured in the Gator detector. The ^{110m}Ag lines at 658 keV, at 885 keV and at at 937 keV are clearly visibile. A strong contamination from ^{40}K and ^{208}Tl can also be observed.

almost evenly shared between the optical window, the internal steel components, the internal L-shaped insulator, and the Kovar for the optical window flange. About 75 % of the total ^{60}Co radioactivity is expected, with almost an equal contribution, from the front and back flanges, which are made out of standard purity Kovar. The remaining ~ 25 % of ^{60}Co is expected from the internal stainless steel components, and from the PMT body made out of Co-free Kovar. In particular remarkable is the fact that this last component, the largest component in mass, containing about 3 times lower ^{60}Co contamination with respect to the standard purity Kovar, provides one of the most significant reduction of the γ background from the PMTs. The content of ^{137}Cs is found to be very modest and is expected only from the two Kovar flanges.

Table 3.5.: Radioactivity models of the R11410-21 PMT built based on the radioassay of the components of table 3.4 and condidering their masses in the final product. The optimistic model has been built assuming zero all the concentrations of non detected radioimpurities, while the in the conservative model the upper limits are summed to the values of positive detections.

Isotope	**Specific activity [mBq/PMT]**	
	Optimistic	**Conservative**
^{235}U	$1.3(2) \times 10^{-1}$	$< 4.3 \times 10^{-1}$
^{238}U	2.5(4)	< 4.0
^{226}Ra	$4.4(2) \times 10^{-1}$	$< 7.3 \times 10^{-1}$
^{232}Th	$2.6(3) \times 10^{-1}$	$< 3.2 \times 10^{-1}$
^{228}Th	$1.2(2) \times 10^{-1}$	$< 5.7 \times 10^{-1}$
^{40}K	1.5(2)	< 2.6
^{60}Co	$6.3(4) \times 10^{-1}$	$< 6.6 \times 10^{-1}$
^{137}Cs	2.2×10^{-2}	$< 1.7 \times 10^{-1}$

Considering the conservative model a potential large contribution to the contamination from the ^{232}Th decay chain, ^{40}K , and ^{137}Cs could come from the PMT body. For ^{235}U the potential large contribution of this component (0.17 mBq/PMT) would be

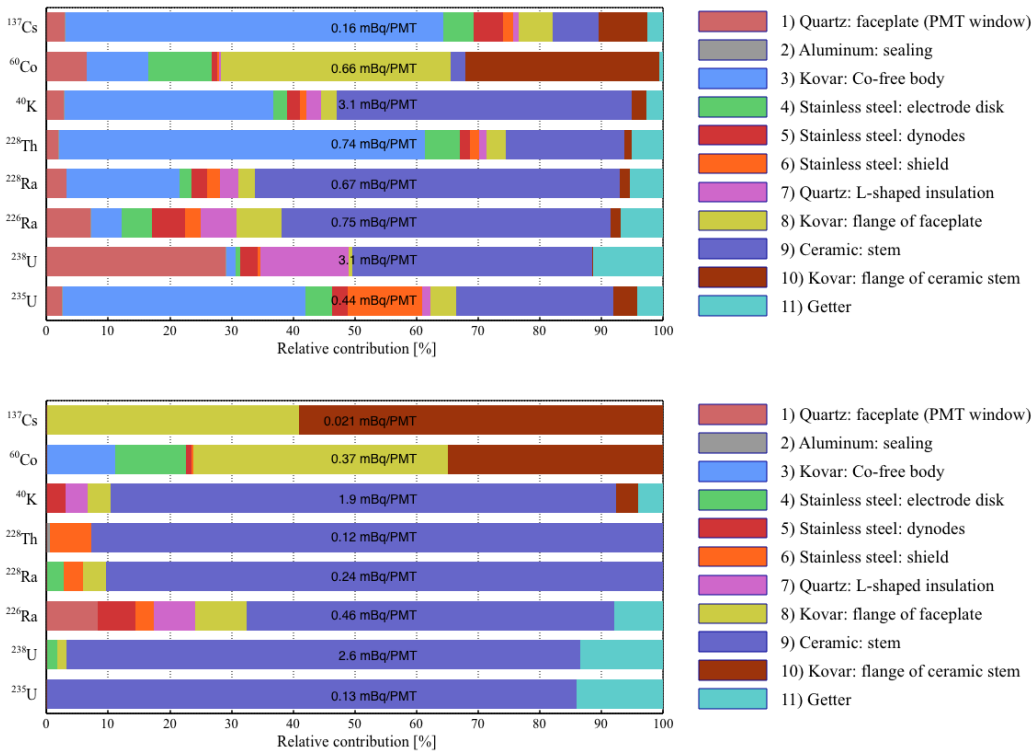

Figure 3.20.: Conservative (*top*) and optimistic (*bottom*) radioactivity models of the 3-inch Hamamatsu R11410-21 PMT represented as a bar-chart. Each color represents the relative contribution of a particular PMT component to the specific radioisotope contamination. For each radiosotope the sum of expected contaminations from the materials is superimposed to each bar. In the optimistic model only detected values for each component are considered for the total contribution of a specific radioisotope. In the conservative model the upper limits are considered as detected values for the total contribution of a specific isotope.

more than 2 orders of magnitude lower, and negligible, if this upper limit was derived from the ^{238}U upper limit assuming the isotopic natural abundances [171]. From the conservative radioactivity picture also the optical window and the L-shaped insulator can potentially increase the total ^{238}U concentration by 0.53 mBq/PMT. For those samples the reduced sensitivity to ^{238}U of the GD-MS is due to the non-conductive nature of quartz which implies a reduced efficiency of the argon plasma used for the atomization and ionization of the sample. The upper limits on the ^{235}U specific activity, determined by the HP-Ge direct measurement of these two quartz components, constrain the ^{238}U contamination to $\simeq$ 0.37 mBq/PMT, that is only $\simeq$ 30 % lower than the ^{238}U direct measurement.

3.5.2 *Radioassay of various PMT production batches*

After the selection of the materials for the PMTs production, all the photosensors to be installed in XENON1T have been screened in order to verify the actual contamination and build an accurate background model. The post-production screening was accomplished mainly with the Gator spectrometer, that could host up to 16 PMTs inside the measurement cavity.

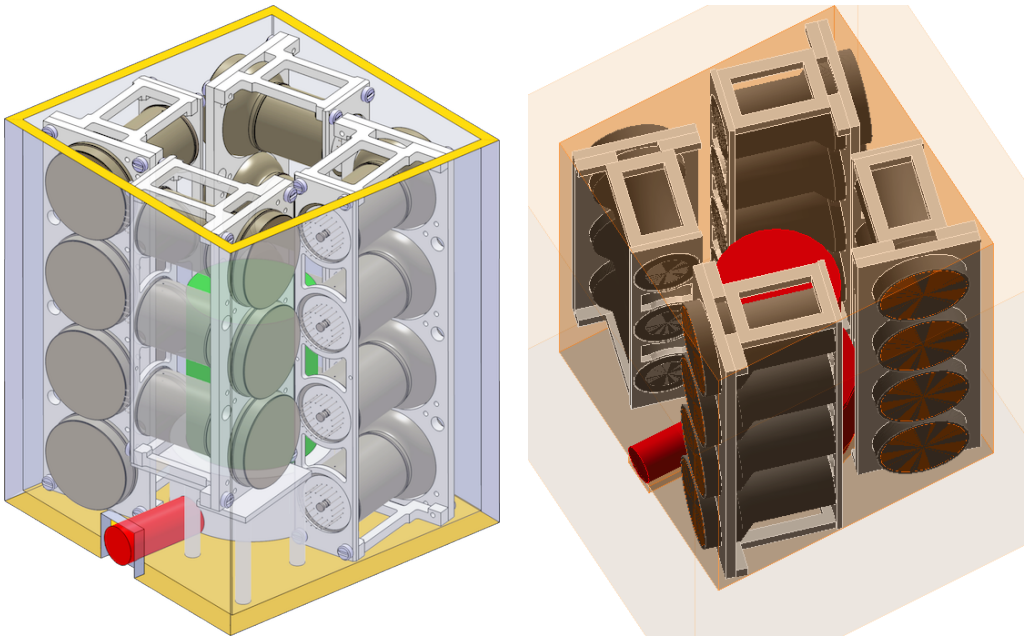

Figure 3.21.: (Left) A rendered CAD model of 15 PMTs in the PTFE holders inside the Gator measurement cavity. (Right) Geant4 model of 15 PMTs in the cavity employed for the MC simulations of the radioactive decays inside the PMTs. For the measurements with less PMTs this model was accordingly modified taking into account the missing PMTs. This configuration have been used for the simulations to compute the sensitivity curves shown in figure 3.22. The orientation of the PMTs encoded for the simulation, opposite to the CAD drawing, represents the actual placecement of the PMTs in the cavity, while the CAD drawing was employed only for the deterination of the holders dimensions prior to their construction.

In order to maximise the detection sensitivity with a reasonable counting time ($\sim 15 - 20\,\mathrm{d}$), especially to the ^{238}U early chain, it was a critical point to introduce in a safe way as many photosensors as possible at the same time. For this purpose, 4 custom-made high-purity PTFE holders, able to host up to 15 PMTs, were designed and realized at the University of Zurich. In figure 3.21 a picture of 8 PMTs inside two of the three holders able to carry 4 PMTs is shown. As the detector's cold finger did not allow for a fourth column of 4 PMTs one of these holders was designed to carry only 3 PMTs. An additional PMT, not shown in figure 3.21, can be placed in the middle of the cavity, sitting on top of the cryostat.

The detection efficiency for 15 PMTs as a function of the counting time is shown in figure 3.22. Although each PMT component is expected to give a different contamination for a specific isotope, the arrangement of the PMTs in the cavity does not allow the disentanglement of these contributions as all the PMT parts have almost the same exposure to the Ge crystal. Hence, the detection efficiency for the spectral lines of the radioisotopes of interest were performed by simulating the decays of the radionuclides with a uniform distribution over the PMTs parts.

Despite OFHC copper could fulfil the radiopurity requirements of the PMTs holders, PTFE was preferred because of the lower self-shielding to low-energy γ-rays, increasing thus the detection efficiency. In additional PTFE is much to easier machining with respect to OFHC-Cu, and also the risk to damage the fragile PMTs during the installation and removal operations of the units in the measurement cavity in much reduced using PTFE holders. In addition the only known and observed cosmogenic radioiso-

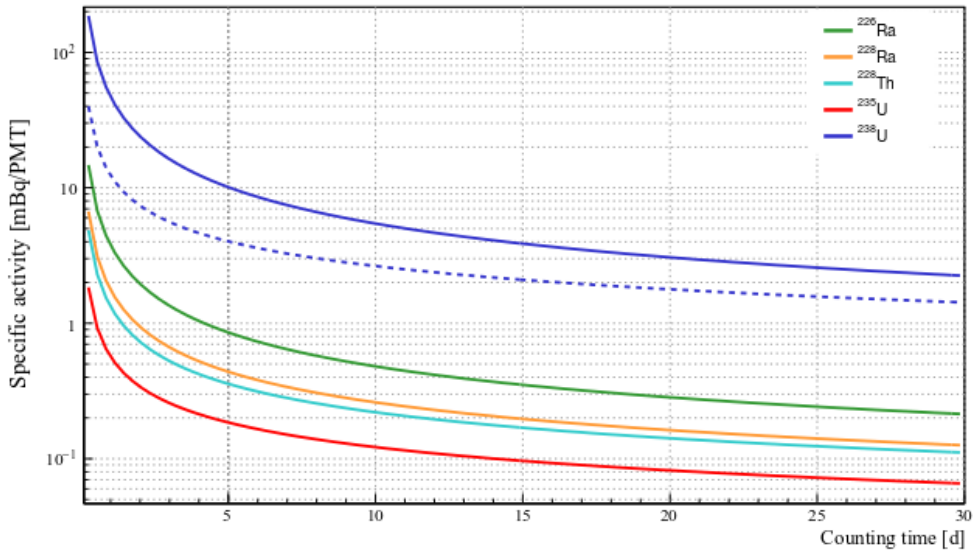

Figure 3.22.: Detection sensitivity to the contaminations of radioisotopes of the uranium and thorium chains as function of the measurement time.

tope in PTFE is ^{8}Be, which has a relatively short life time with respect to many of the cosmogenic radionuclides that are activated in copper, such as ^{56}Co , ^{60}Co , and ^{54}Mn .

Before their use the holders were measured in Gator for 21.5 d in order to verify their radio-purity and recalculate the sensitivity. After about an year of their first use, and following the screening of several other samples for the XENON1T components, the holders were measured a second time for 33.5 d soon after the acquisition of the background run at the beginning of 2014. The two spectra of the holders and the 2014 background spectrum are shown in figure 3.24a. The holders contamination relative to the two runs is reported in table 3.6, where only contamination from the primordial and ^{137}Cs radionuclei have been investigated. In both the runs no radioisotope was detected, and the detection limits are in agreement with the sensitivity studies shown in figure 3.22 for a 15 days acquisition. Hence, any eventual contamination in the holders is expected to have a negligible effect on the detection sensitivity of the PMTs radio-impurities.

The measured contaminations of the PMTs batches from the primordial chains and from the γ-emitters are detailed in tables A.9 and A.10, respectively. One batch of R11410-20 (the number 0) and 22 batches of R11410-21 PMTs were measured in Gator. Additional and independent measurements of the 3 out of 22 batches of R11410-21 (batches number 2, 6 and 8), were accomplished with GeMPI spectrometer, that however allowed a maximum of 4 PMTs inside the measurement cavity. Some example of the PMT batches γ-spectra are shown in figure 3.24b, where they are also compared to the PTFE spectrum and background spectrum from 2014.

For each investigated isotope the contamination of the PMTs is given in table 3.7, that represents an estimation of the specific activity average $\overline{A}$ and dispersion $\sigma(A)$ of the PMTs installed in XENON1T. Both the quantities are computed taking into account only the PMTs that gave a positive measurement for the specific isotope in

Figure 3.23.: PMTs mounted in their PTFE holders inside the glove box of the Gator γ-spectrometer before the measurement.

the Gator measurement. Average sample mean is computed taking into account the number of units n_i relative to the batch i as the statistical weight associated to the specific activity A_i. As dispersion the square root of the unbiased sample variance was considered:

$$\overline{A} = \frac{\sum_i n_i \cdot A_i}{N_{\text{tot}}}, \tag{3.20a}$$

$$\sigma(A) = \sqrt{\frac{\sum_i n_i \cdot \left(A_i - \overline{A}\right)^2}{N_{\text{tot}} - 1}}, \tag{3.20b}$$

where $N_{\text{tot}} = \sum_i n_i$ is the total number of PMTs found contaminated by a specific isotope.

The ^{238}U radioisotope was not detected in any of the batches, and the reported upper limits are slightly higher than the sensitivity expected from the preliminary studies for the same counting time. This is the effect of a higher Compton background in the low-energy region with respect to that used for the sensitivity estimation (figure 3.24a), which is mainly induced by the ^{40}K and ^{60}Co contamination of the PMTs. Hence the ^{238}U value reported in table 3.7 is inferred from that of ^{235}U , detected in 5 out of 22 batches. Batch 2 is the only batch where it is possible to observe an agreement of the ^{235}U concentration detected with Gator, with the upper limit reported by the GeMPI measurement. The observed ^{238}U contamination is ~ 3 times higher than the optimistic radioactivity model and ~ 2.6 times higher than the conservative model, while the ^{235}U contamination is between that predicted from the two models.

The measurements of the ^{226}Ra concentration over different batches are rather uniform, and the three measurements performed with the GeMPI spectrometer agree

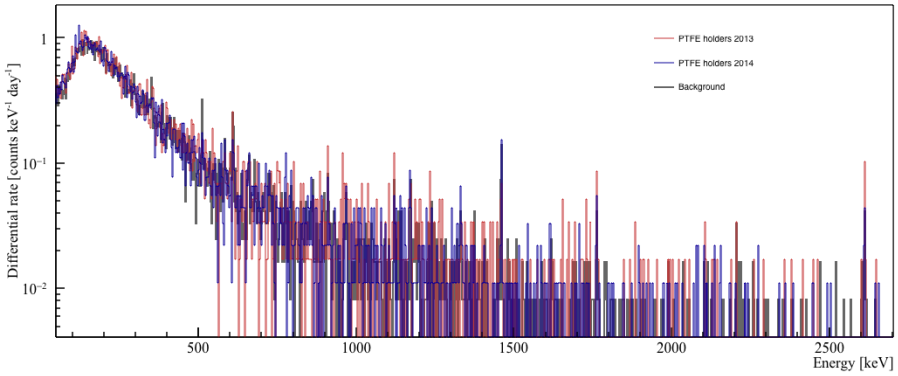

(a)

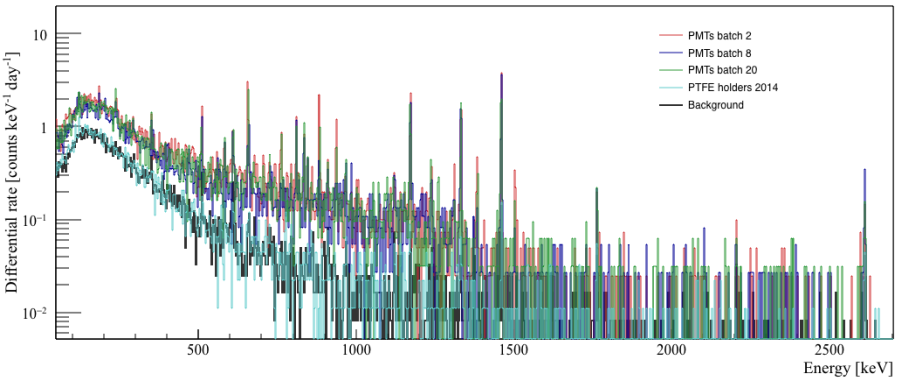

(b)

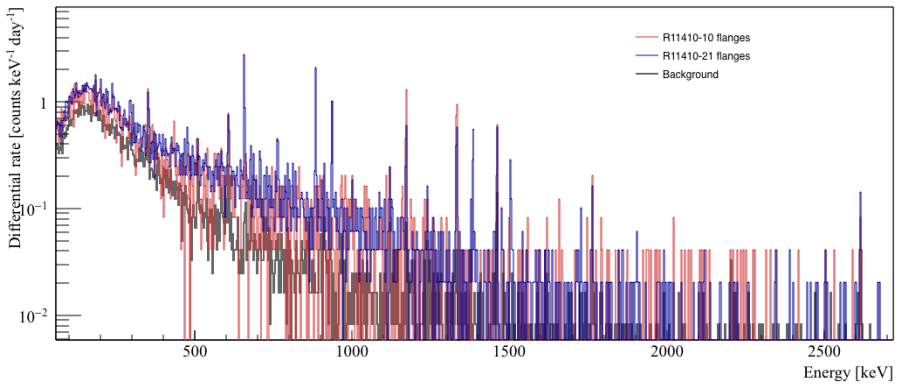

(c)

Figure 3.24.: (a) Spectra of the PTFE holders acquired in 2013 and in 2014, compared to the background. With the exception of few lines of the ^{208}Tl , that however are statistically compatible with the background, the two measurements are perfectly compatible with the background.
(b) Typical spactra of some PMT batches, compared both to the background spectrum and to the spectrum of the PTFE measurements of 2014 (the longest).
(c) Comparison of the spctra relative to two sets of back flanges used for two different revisions of the R11410 photomultipliers. The flanges of the revision -21 use an ^{110m}Ag contaminated silver for the sealing of the steel leads into the ceramic stem holes.

Table 3.6.: Results of the two γ-ray measurements of the PTFE holders for the PMTs radioassay. Since the spectra used to determine these results are used as background spectrum of the PMTs screening measurements, in this table the holders contaminations are expressed in equivalent activity per PMT units.

Isotope	**Holders contamination [mBq/PMT]**	
	2013 (21.5 days)	2014 (33.5 days)
^{235}U	< 0.34	< 0.28
^{238}U	< 6.33	< 5.5
^{226}Ra	< 0.35	< 0.27
^{228}Ra	< 0.52	< 0.32
^{228}Th	< 0.36	< 0.26
^{40}K	< 1.59	< 1.2
^{137}Cs	< 0.13	< 0.11

within the error. Considering the batches where ^{235}U is detected, the ^{238}U /^{226}Ra ratio ranges between ~ 9 and ~ 27 with the mean value of 13 ± 3, indicating a strong deviation from the secular equilibrium of the ^{238}U chain, a feature already observed in the steel samples and most likely present in many Fe-based alloys.

Both the ^{235}U and ^{226}Ra specific activities are between the values predicted the two radioactivity models, while the ^{238}U concentration is about twice than the prediction of the conservative model. This under-estimation of the ^{238}U from the radioactivity models is mainly because its concentration is inferred from the direct measurements from the lines of ^{234}Th and ^{234m}Pa. Inferring the ^{238}U from the ^{235}U for the components 3, 6 and 10 of the PMTs, the resulting upper limit would increase by about 5 mBq/PMT and thus would be consistent with the ^{238}U contamination of the batches. However, for the electrode disk (component 6) the ^{238}U upper limit, inferred from ^{235}U upper limit, would be about ~ 3 times higher than the sensitivity reported for this measurement by the GeMPI spectrometer. Hence, the actual contribution of this component to ^{238}U is most likely smaller than that inferred by ^{235}U, and considering the limit placed by the GeMPI measurement for component 6, the total conservative estimation of the ^{238}U would still be in agreement with that reported by the screening of the PMT batches. For all the other PMT components the variation of ^{238}U if inferred from ^{235}U would be negligible, and for the components 4 and 8 the ^{238}U activity was directly detected by the GD-MS measurement. These considerations might provide an explanation for the unexpected ^{238}U contamination of the batches, in disagreement with the upper limits placed by the GD-MS measurements. On the other hand, the only other reasonable explanation is that $\gtrsim 4$ mBq/PMTof^{238}U are introduced in the PMTs fabrication process.

In almost all the PMT batches where both ^{228}Ra and ^{228}Th contaminations are detected, the specific activity of the two subchains agree within the 1 sigma uncertainty, and thus the ^{232}Th chain is not found in substantial equilibrium. Also the GeMPI measurements of batches 6 and 8 support this conclusion, although their absolute contamination result is ~ 50 % lower than those performed with the Gator spectrometer. This tension between the two measurements might be due to a systematic over-estimation of

Table 3.7.: Summary table of the PMTs radioactive contamination, averaged over the batches. The mean activity $\overline{A}$ and the dispersion $\sigma(A)$ are evaluated using the equations 3.20, taking into account only the batches where the specific radionuclide has been detected.

Isotope	Specific activity [mBq/PMT]	
	$\overline{A}$	$\sigma(A)$
^{235}U	0.37	0.07
^{238}U	8	1
^{226}Ra	0.6	0.1
^{228}Ra	0.6	0.1
^{228}Th	0.6	0.1
^{40}K	12	1
^{60}Co	0.8	0.1
^{54}Mn	0.23	0.05
^{110m}Ag	0.5	0.2

the spectral lines detection efficiency for the ^{232}Th chain with the configuration used for the measurement in the GeMPI spectrometer. The ^{228}Ra and ^{228}Th values, reported in table 3.7, are at the edge of the upper limit predicted by the conservative model for the ^{228}Th sub-chain, hence it might be possible that some ^{228}Ra was introduced in the PMTs production. However, the ^{232}Th upper limit prediction from the conservative model, including also the information from the GD-MS measurements, is about half of the measured ^{228}Ra value in the PMT batches and might be an hint of some disequilibrium in the chain between the ^{232}Th and ^{228}Ra radionuclides.

The measured ^{40}K contamination resulted ~ 8 and ~ 4.5 higher than the predictions of the optimistic and conservative radioactivity models, respectively. Hence a large amount of potassium is introduced in the fabrication process, most likely during the deposition of the bi-alkali compound for the photocathode. The GeMPI measurement confirms this measurement in the case of batch 2, while in the case of the batches 6 and 8 the GeMPI measurements detected the ^{40}K at levels $2\,\sigma$ below than the Gator results.

The ^{60}Co contamination of all the batches is almost uniform and there is substantial agreement across different batches. Only batches 8 and 22 have a slightly higher contamination than those reported in table 3.7. The additional measurements performed with the GeMPI spectrometer agree within $1\,\sigma$ uncertainty with the measurements of Gator.

The ^{137}Cs was not detected in any of the measured batches and thus is not reported in the summary of table 3.7. The best upper limit of 0.11 mBq/PMT reported by the GeMPI measurement is below the upper limit predicted by the conservative radioactivity model and just ~ 5 times higher than the prediction of the optimistic model. Hence, it is safe to conclude that no significant ^{137}Cs content is introduced in the fabrication of the PMTs.

An additional radio-impurity observed in several PMT batches is the ^{110m}Ag isomer, confirmed by the GeMPI measurements. This radio isotope has a relatively long half-life of ~ 250 d and decays with a probability of ~ 1 % to ^{110}Ag and of ~ 99 % to one of the energy levels of ^{110}Cd. The ^{110}Ag half-life is ~ 25 d, and it decays by β-emission to one of the ^{110}Cd levels with a probability of 99.7 %, and by electron capture to ^{110}Pd with a probability of 0.3 %. The ^{110m}Ag can be produced either by the HE CR induced fragmentation of heavier nuclei, or by capture of thermal neutrons, mainly by the stable ^{109}Ag , or as a nuclear power plant waste. The presence of this radioactive impurity is confirmed by the GeMPI measurements, that are in very good agreement with those performed with Gator on the same batches.

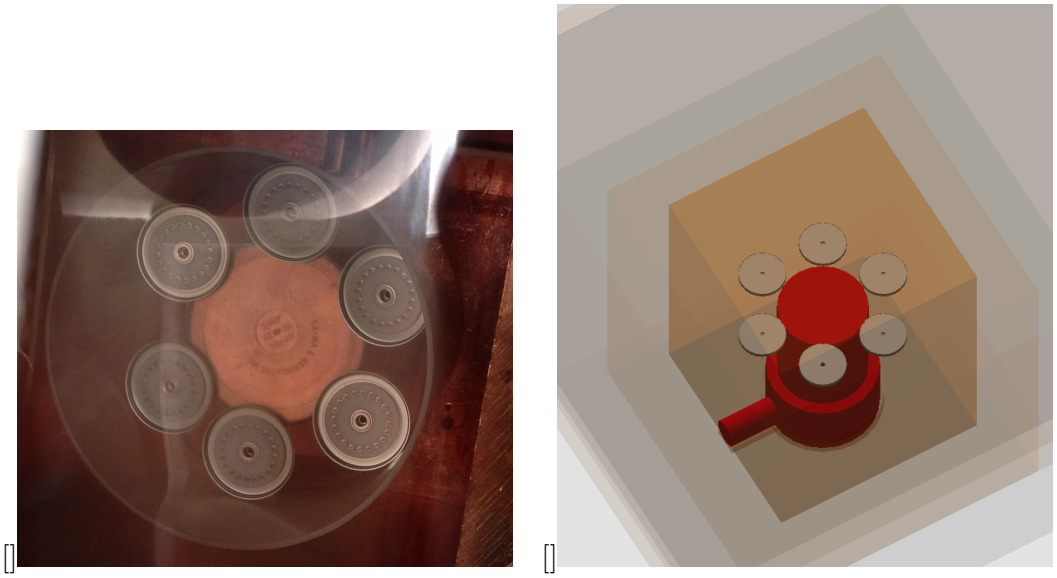

Figure 3.25.: (a) Picture of the back flanges of the R11410 inside the Gator cavity for the measurement of their ^{110m}Ag content. (b) Geant4 geometry model of the 6 flanges inside the Gator cavity used to determine by MC simulations the detection efficiency of specific radioisotopes.

In order to verify that the ^{110m}Ag contamination is due to the silver used for the leads sealing, 6 back flanges used in the production of the R11410-10 (measured in [210]) and other 6 flanges used for the production of the R11410-2x were measured in Gator for 9 d and 18 d, respectively. The flanges arrangement into the Gator cavity is shown in figure 3.25, together with the Geant4 geometry model and their γ-spectra. No ^{110m}Ag contamination was observed in the flanges used for the R11410-10 version, resulting in an upper limit of < 0.25 mBq/flange, while the flanges used for the R11410-2x tubes an activity of (1.1 ± 0.1) mBq/flange was detected. This measurement is in remarkable agreement with the ^{110m}Ag concentration observed in the batches 0, 1 and 2, listed in table A.10. At the same time two silver samples, with masses of 160 g and 50 g, respectively, were provided from the manufacturer for HP-Ge measurements, that were accomplished with a GeMPI spectrometer. Taking into account the total mass of silver used in the construction of the flange, the detected ^{110m}Ag contamination was (2.38 ± 0.09) mBq/flange, about twice of that detected in the screening of the flanges. However, it is possible that the quantity used for the PMT production is actually lower than that was communicated by the Hamamatsu company. In addition this measurement revealed also the presence of ^{108m}Ag at a level of (41 ± 3) μBq/flange, well below the detectable level of the Gator spectrometer for the total quantity employed in the six flanges. The

^{208m}Ag isotope decays with a half-life $T_{1/2} \simeq 440$ y and as in the case of ^{110m}Ag can be produced by HE CR nuclear reaction, by thermal neutron capture by stable ^{107}Ag, or by the human activity in power plants. Starting from batches 3 and 4, a significant reduction if the ^{110m}Ag contamination is observed, as the result of replacing the silver employed in the production of the PMTs. Although the ^{110m}Ag contamination, reported in table 3.7, represents the contamination of the PMTs at the start of the measurements, a more detailed inspection of table A.10 reveals about 3 sub-groups that can be distinguished: those with ~ 9 mBq/PMT, those with ~ 5 mBq/PMT, and those with ~ 2 mBq/PMT. However, considering the ^{110m}Ag half-life and the time between the HP-Ge measurements and the first scientific run of XENON1T, planned for the end of 2016, the average ^{110m}Ag activity should already be reduced by more than an order of magnitude with respect to the screening values.

The presence of silver radionuclei in the samples excludes their cosmogenic origin as the primary explanation. The thermal neutron activation of silver is pretty unlikely, as it would require the exposure of the silver to a relatively intense flux of thermal neutrons, possible only in the proximity of a nuclear power plant core. Hence, the anthropogenic origin is the hypothesis that most likely explains the presence of these isotopes. For this reason the event that most likely caused the silver pollution was identified in the nuclear accident of 2011 in Fukushima, a few hundred km away from the Hamamatsu production place. In this accident were released into environment, additionally to the two Ag radioisotopes detected in the silver samples, also relatively large quantities of ^{137}Cs , ^{134}Cs , and ^{207}Bi among many others with much shorter half-life [215–218]. However, neither in the Gator radioassay of the flanges nor in the GeMPI measurements of the silver samples these long-lived radioisotopes were observed.

The measurement of the 6 back flanges for the R11410-21 tubes revealed an ^{235}U contamination of (0.5 ± 0.1) mBq/PMT, in agreement within the uncertainty with the results reported in table 3.7. This suggests that almost all the uranium contamination of the photosensors is located at the back flange of the PMT. This also applies to the ^{226}Ra contamination that is detected in the flanges at a level of (1.0 ± 0.3) mBq/PMT, slightly higher but consistent within the uncertainties with the values resulting from the batches screening. Hence, for the PMT contamination by the primordial chains, the optimistic model, where the ceramic stem contribution is dominant, provides a better description of the radioactivity distribution among the PMT parts. The ^{40}K contamination in the flange implies a contribution of (2.0 ± 0.6) mBq/PMT from this part to the total PMT radioactivity, which corresponds to ~ 1.2 times the contamination predicted from the sum of samples 9b and 10 of table A.8. The ^{60}Co contamination in the flanges is (0.34 ± 0.05) mBq/PMT, about $\sim 42\,\%$ of the value measured in the batches screening, and $\sim 54\,\%$ of the value predicted by the optimistic radioactivity model.

In table 3.8 the radioactivity of several PMTs types used in other low-background experiments is compared. The concentration of the radioimpurities is normalized to the optical window active area in order to compare different PMT types. The R11410-10 PMT is the photosensor operated in the PandaX experiment, and was independently assayed for the radioactivity content by the XENON [210], LUX [219] and PandaX [113] collaborations. The results of PandaX and XENON100 for this PMT type agree each other for all the investigated radioisotopes, while the concentration values reported by LUX for the ^{40}K and ^{60}Co are lower by a factor ~ 2. It must be noted that the R11410-10 PMTs were previously available on the market with the product name R11410-MOD,

that was later changed by Hamamatsu. The R8778 model is the 2-inch diameter photosensor employed in the LUX experiment and R8520 is the 1-inch square photosensor operated in the XENON100 experiment. The accurate choice of radiopure materials allowed for a significant reduction of the radioactivity normalised per photocathode area of the R11410-21 phototube compared to all the previous versions. In particular, the radiopurity of the XENON1T PMTs was improved with respect to the XENON100 photosensors, by factor ~ 5 for all the neutron emitters, and by a factor ~ 20 for strong gamma emitters as ^{40}K and ^{60}Co .

Table 3.8.: Comparison of the activity normalised to the sensitive area of several photomultipliers developed and/or used in dark matter search experiments. The list is sorted starting with the most recent PMT type on the first raw. In parenthesis are indicated the experiment that uses the specific PMT type. For each radioisotope a general reduction of the concentration in the more recent versions can be observed. The comparison is done only for the most common radioactive contaminations in materials.

PMT type	**Normalised activity [mBq/cm^2]**							**Ref.**
	^{235}**U**	^{238}**U**	^{226}**Ra**	^{228}**Ra**	^{228}**Th**	^{40}**K**	^{60}**Co**	
R11410-21 (XENON1T)	$2.9(5)\times\dot{1}0^{-3}$	$6.2(8) \times 10^{-2}$	$4.7(8) \times 10^{-3}$	$4.7(8) \times 10^{-3}$	$4.7(8) \times 10^{-3}$	$9.3(8) \times 10^{-2}$	$6.2(8) \times 10^{-3}$	This work
R11410-20	$< 6.1 \times 10^{-3}$	$< 1.4 \times 10^{-1}$	6.4×10^{-3}	8.5×10^{-3}	$7(2) \times 10^{-3}$	$9(2) \times 10^{-2}$	$1.0(2) \times 10^{-2}$	This work
R11410-10	$< 1.3 \times 10^{-1}$	< 3.0	$< 7.5 \times 10^{-2}$	$< 3.0 \times 10^{-2}$	$< 8.0 \times 10^{-2}$	$4(1) \times 10^{-1}$	$1.1(2) \times 10^{-1}$	[210]
R11410-10 (PandaX)	$4(4) \times 10^{-2}$	NA	$< 2.0 \times 10^{-2}$	NA	$< 2.0 \times 10^{-2}$	$5(3) \times 10^{-1}$	$1.1(1) \times 10^{-1}$	[113]
R11410-10	NA	$< 1.9 \times 10^{-1}$	$< 1.3 \times 10^{-2}$	$< 9.0 \times 10^{-3}$	NA$^{(1)}$	< 0.26	$6.3(6) \times 10^{-2}$	[219]
R11410	$1.0(2) \times 10^{-1}$	1.6(6)	$1.9(2) \times 10^{-1}$	$< 2.1 \times 10^{-2}$	$9(2) \times 10^{-2}$	1.6(3)	$2.6(2) \times 10^{-1}$	[210]
R8778 (LUX)	NA	< 1.4	$5.9(4) \times 10^{-1}$	$1.7(2) \times 10^{-1}$	NA$^{(1)}$	4.1(1)	$1.60(6) \times 10^{-1}$	[219]
R8520 (XENON100)	$9(2) \times 10^{-3}$	$< 3.3 \times 10^{-1}$	$2.9(2) \times 10^{-2}$	$1.97(7) \times 10^{-2}$	2.6×10^{-2}	1.8(2)	$1.3(1) \times 10^{-1}$	[210]

3.6 BACKGROUND BUDGET OF THE XENON1T DETECTOR

The background from low-energy ERs was obtained assuming for XENON1T the same performance measured in the XENON100 experiment [153]. Namely an ER discrimination efficiency of 99.5 % at 50 % acceptance, and a multiple scattering was determined when the second largest charge signal was larger than 5 electrons, with the corresponding interaction vertex separated by more than 3in the vertical direction with respect to the first. The details about the LXe physics assumed for the generation of the light and charge signals are beyond the scope of this thesis and are thoroughly discussed in [181]. The total background predicted for XENON1T in the $(1-12)\,\mathrm{keV_{ee}}$ energy range from single scatter ERs is $(1.80 \pm 0.15) \times 10^{-1}\,\mathrm{mDRU}$, which corresponds to $(720 \pm 60)\,\mathrm{events/y}$, before discrimination is applied.

The 85 % of the predicted low-energy background is induced by the unstable daughters of ^{222}Rn , that, according to the radon emanation measurements of the materials, is expected in the LXe with a concentration of $\sim 10\,\mu\mathrm{Bq/kg}$. On the other hand the ^{220}Rn contribution to ER background is estimated to be $< 1\,\mu\mathrm{Bq/kg}$, mainly due to lower probability to diffuse into the active LXe volume, and therefore is neglected.

The materials contribution to the total ER background is $(7.3 \pm 0.7) \times 10^{-3}\,\mathrm{mDRU}$ corresponding to $\sim 4.1\,\%$ of the total, and becomes dominant for electron recoils with energies $> 500\,\mathrm{keV}$. It was obtained with Monte Carlo simulations of the radionuclides decays in each of the detector components, taking into account the material contamination obtained in the XENON1T screening campaign. The stainless steel of the cryostat shells and flanges produces $\sim 61\%$ of the background from materials, in particular because of the relatively high ^{60}Co concentration. A contribution of $\sim 23\,\%$ comes from the PMTs and their bases, and $\sim 15\,\%$ from the internal stainless steel parts such as the reservoir, the diving bell, and the electrode rings. The contributions of the PTFE for the field cage and the OFHC copper for the field shaping rings is only $\sim 1\,\%$. A minimal radioactivity model of the background from materials, computed by setting to zero all the contributions of the radioisotopes that gave only upper limits in the radioassay measurements, predicts a ER rate 10 % smaller than the conservative estimate.

The ER background from other sources such as ^{85}Kr , the double-β decays of the ^{136}Xe ($\sim 8.9\,\%$ of the natural xenon), and solar neutrinos was estimated to be $\sim 10.6\%$ of the total, where the ^{136}Xe contribution is only $\sim 1.4\,\%$.

The NR background induced by the radiogenic neutrons, due to the ^{235}U , ^{238}U and ^{232}Th contamination of the detector components, is estimated to be $(0.6 \pm 0.1)\,\mathrm{ev/y}$ in the 1 ton FV and in the $(4-50)\,\mathrm{keV}$ energy region, and is the dominant component of this type of background. The 28 % come from the cryostat stainless steel, the 26 % from the PMTs, the ceramic stems in particular, the PTFE contributes 20 %, the internal stainless steel for the TPC components and the reservoir 17 %, and finally the PMT bases contribute for a 5 % of the total.

The estimated NR background rate from muon-induced neutrons is $< 10^{-2}\,\mathrm{ev/y}$, and thus is considered negligible. Such a low contribution to the NR background from the cosmogenic neutrons is possible thanks to the active muon veto provided by the instrumentation of the water tank with the 84 8-inch Hamamatsu R5912ASSY PMTs. According to the studies published in [164], this veto system is able to discriminate 99.5 % of the NR events where a muon crosses the water tank, and 70 % of those where the muon drifts outside the muon veto but the neutron event is associated with a shower.

The last contribution to the NR background comes from the coherent scattering of low-energy neutrinos off Xe nuclei (CNNS). The background rate from this process is $(1.8 \pm 0.3) \times 10^{-2}$ ev/y, which is entirely due to the *hep* solar neutrinos generated from the ^{8}B decay. Although the integrated rate of the CNNS background in the $(8 - 50)$ keV energy region is negligible compared to the NRs from radiogenic neutrons, the peaked NR spectrum at low-energy (5 keV), induced by energy threshold effects on the real recoil spectrum, must be taken into account when the WIMP-nucleus detection sensitivity is performed [181].

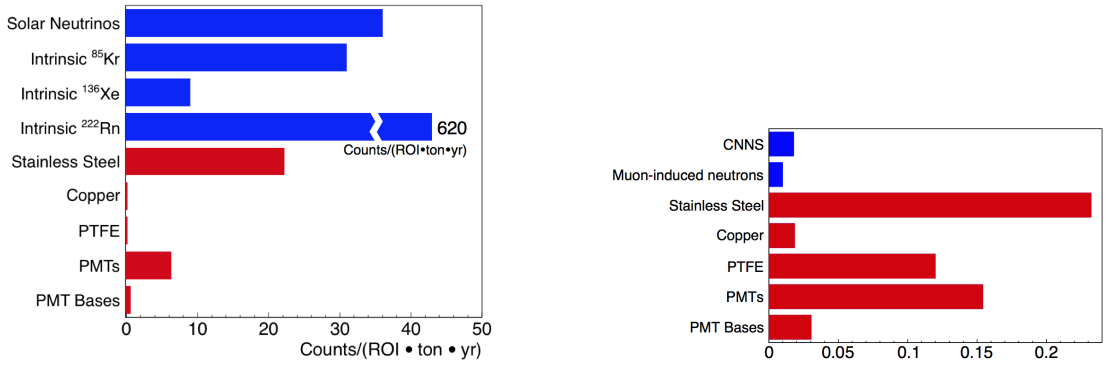

(a) **(b)**

Figure 3.26.: XENON1T background budget. (a) Expected contributions to the ER background in the 1 tonne and in the $(1, 12)$ keV$_{\mathrm{ee}}$ energy range. (b) Expected contributions to the NR background in the 1 tonne and the $(4, 50)$ keV$_{\mathrm{nr}}$ energy range.
The blue bars refer to the intrinsic and external background sources, while the dark red bars represent the contribution from material contaminations. Figure taken from [163].

4

COSMOGENIC ACTIVATION STUDY OF NATURAL XENON

In this chapter the first dedicated experimental study of the xenon cosmogenic activation, published in [220,221], is presented. As will be detailed, this study is relevant for the next generation, multi-tonne LXe DM detectors, which will gradually approach the ultimate WIMP-nucleon detection sensitivity.

4.1 MOTIVATIONS FOR THE STUDY OF XENON COSMOGENIC ACTIVATION

The LXe is playing an increasingly important role as particle detection medium in current and future rare event search experiments, such as dark matter and neutrinoless double-beta decay decay searches. With the exception of few very long-lived double-beta emitters such as ^{124}Xe , ^{126}Xe , ^{134}Xe and ^{136}Xe , where only the decay of the latter has been observed so far, xenon has no other unstable isotopes.

The scientific goal of the next multi-ton scale LXe based dark-matter detectors, such as XENONnT [181], LZ [222], is to probe the WIMP-nucleon spin-independent cross-section down to few $\times 10^{-48}\,\mathrm{cm}^2$ with typical exposures of $\sim 20\,\mathrm{yr} \times$ tonne. Ultimate dark-matter detectors such as DARWIN [119], currently in study phase, aim to be sensitive to cross sections as low as $\sim 10^{-49}\,\mathrm{cm}^2$ with exposures of the order of $\sim 10^2$ tonne $\times$ yr, where the coherent neutrino-nucleus scattering events will constitute an irreducible background for the direct WIMP detection [120–123]. For LXe detectors of these mass scales the γ background from materials will be negligible, while intrinsic background from the radionuclides dissolved in the detection medium, such as ^{222}Rn and ^{85}Kr , might constitute the primary limitation to the aimed detector sensitivity. An additional contribution to the intrinsic background can come from the unstable radionuclides that can be produced during the xenon production and the storage above ground and by CR-induced nuclear activation processes. Hence, in order to fulfil the experimental challenges, it will be critical to be able to estimate the maximum tolerable exposure to the cosmic radiation by reliable predictions of the xenon cosmogenic activation.

Software packages like ACTIVIA [223] and COSMO [224] are able to predict the activation yield of various materials given their isotopic composition, the nuclear CR spectrum and the exposure time. These calculations were performed with both codes for the XENON100 experiment, resulting in activation rates too high to be compatible with the measured ER background [154, 180]. The main cause of the discrepancy was attributed to the lack of knowledge of the production cross sections for Xe, which are implemented in the codes using semi-empirical models developed by Silberberg and Tsao [225–227].

As no data was available for the xenon activation functions, a dedicated experimental study was performed by exposing a natural xenon sample to the cosmic radiation for 245 days at the High Altitude Research Station Jungfraujoch (hereafter HARSJ) [228] at an altitude of 3450 m above sea level (asl). In order to provide a benchmark for our activation measurements and predictions, a sample of OFHC copper has been simultaneously exposed at the same location. As discussed in the previous chapter, because of the high purity and low concentration of radionuclides, this material is one of the most-frequently used materials for the construction of low-background detectors, and thus it is a well validated material in the software packages.

4.2 COSMIC RAYS NUCLEAR ACTIVATION

The nuclear interactions of high-energy projectiles with target nuclei at energies $E \gtrsim 10 \times A\,[\mathrm{MeV}]$, where A is the projectile mass number, are responsible for large variety of phenomenology related to the production of secondary, lighter nuclei. The most relevant reactions are the spallation, fragmentation and fission processes, which all consist in the de-excitation of a highly excited system of nucleons, with typical mean energies of some MeV per nucleon, by the emissions of secondary particles such as lighter nuclei and nucleons, frequently accompanied by prompt γ and β radiation. All these processes are very similar to each other and are distinguished based on the observed phenomenology of the reaction residuals. Spallation processes are those where the projectile can knock out a few nucleons leaving the target in an excited state, which will cool-down by the emission of other nucleons and lighter fragments. This process includes also the stripping of one or few nucleons from the target nucleus. A fragmentation reaction consists in a fast and simultaneous emission of many nucleons as well as light nuclei, and it is believed that in this process phase transition of the nuclear matter plays a crucial role. On the other extreme the fission process consists in a de-excitation of the target nucleus into two lighter nuclei with a relatively longer life-time compared to the other two processes. Obviously all the processes are part of a single excitation-deexcitation process of the target nuclei into different final states. Hence, the differentiation in various subprocesses is only because of the extreme difficulty to provide a general description of the energy transfer and the following cool-down of the target nucleus, in order to predict the branching ratio of each of the final channels. As the production of secondary nuclides is a stochastic process, most of these are unstable γ emitters and some have life-times long enough to be observed by γ spectroscopy over time intervals from few days to some months if not years (e.g the ^{60}Co cosmogenic radioisotope). The charge-exchange reactions of leading particles, is an additional process that become relevant for projectile energies $\gtrsim 500 \times A\,[\mathrm{MeV}]$.

The most relevant cosmic ray components in the atmosphere at sea level or mountain altitudes (up to few thousand meters) are charged hadrons, such as protons and pions, neutrons, and muons. All the listed hadronic components are secondary components of a typically much richer hadronic cascade triggered by the nuclear interaction of high-energy primary particles, usually protons or light nuclei, with the air components at the top of the atmosphere. However, because of the very short life-time of the pions, the hadronic components of the cosmic rays relevant for nuclear activation studies are essentially protons and neutrons. Their observed spectra range from few MeV up to some 10 TeV with an energy dependence well described above 1 GeV by the power law

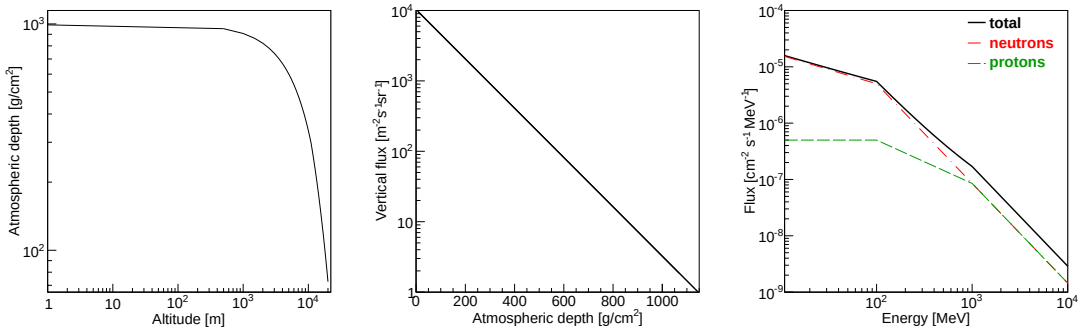

(a) (b) (c)

Figure 4.1.: (a) Relation between atmospheric depth and altitude from the U.S. Standard Atmosphere Model [234]. A sea level value of 1030 g/cm^2 [235, 236] is adopted throughout this specific study.
(b) Vertical nucleon flux as a function of the atmospheric depth [237, 238].
(c) The cosmic ray spectrum from Activia and Cosmo, based on parametrization from Refs. [239, 240]. Only the total flux is used in the calculations as protons and neutrons interact similarly at these energies.

$I(E) \propto E^{-\alpha}$, were I is the differential intensity and $\alpha \sim 2.9$ [229, 230]. The atmospheric muons are mainly produced in the decay of pions and for a smaller amount by the decay of kaons, both produced in the hadronic cascades in the higher parts of the atmosphere. However, because of the lower muon flux [231] and the much lower cross-sections for nuclear reactions [232, 233] with respect to the nucleonic CR component, they play only a marginal role in the activation processes in atmosphere, and thus will be neglected within the scope of the present study.

The nucleon flux is exponentially attenuated with the depth of the atmosphere they traversed, that is shown in figure 4.1b based on the available literature [237, 238]. Since protons interact with atmospheric molecules with both nuclear and electromagnetic interactions, while neutrons only through nuclear interactions, the proton flux at lower energies is attenuated more than an order of magnitude. Measurements of the vertical differential fluxes of the protons and neutrons at several altitudes showed a negligible change of the spectral shape with the atmospheric depth [239, 241–244]. Hence, the knowledge of integrated flux of the nucleons at sea level and the attenuation factor for a specific atmospheric depth is sufficient to infer the nucleon flux and its spectrum at different altitudes, with an accuracy sufficient for this study. This allows the comparison of the activation results with other measurements and with theoretical predictions as saturation activities at sea level. The conversion from altitude to atmospheric depth has been performed for the locations relevant for this study, as reported in table 4.1, taking into account the U.S. Standard Atmosphere Model [234], shown in figure 4.1a, with a sea level value of 1030 g/cm^2.

The predictions of the cosmogenic activation were performed with both the Activia software [223] and a revised and updated version of the Cosmo software [224]. The CR spectrum encoded in both the codes is based on a parametrisation of the model developed by Armstrong *et al.* [239] for neutrons and of the measured spectrum by Gehrels [240] for protons. They are shown together in figure 4.1c. The calculations of the saturation activities were performed sampling the spectra in intervals of 10 MeV, from a minimum energy of 10 MeV to 10 GeV. The lower integration boundary was

Table 4.1.: Altitude, atmospheric depth, and vertical flux of protons and neutrons, as well as scaling factors to relate the flux to sea level values for the various locations in our study. Values taken from [220] .

Location	**Altitude [m]**	**Atm. depth [g/cm^2]**	**Vert. Flux [m^{-2}s^{-1}sr^{-1}]**	**Scaling factor**
Sea level	0	1030	2.6	1.0
Lauterbrunnen	795	954	4.7	1.8
LNGS	985	936	5.4	2.1
Jungfraujoch	3470	728	29.0	11.2

chosen because it corresponds to the threshold of almost all the known nuclear excitation functions. The upper boundary was chosen because of the negligible contribution of nucleons with energies above 10 GeV to the integral, due to the negative power law spectrum. Both the codes perform the calculation of the cross-sections for nuclear processes such as spallation, fission, fragmentation, evaporation, and charge-exchange reactions, based on semi-empirical model developed by Silberberg and Tsao [225–227]. Because of the relatively high energies of the nucleons, the nuclear isospin symmetry is assumed in the nuclear interactions, and thus both the codes use identical parameters for the cross-section calculations for both protons and neutrons. The models define the formulae to be used for the cross-sections of the different nuclear processes in different regions of the parameter space, depending on the energy and the masses of the target and product nuclides. In addition, above the nucleon energy of ~ 3 GeV almost all the relevant cross-sections for the most common materials, so far investigated, are assumed constant [223, 225–227]. For this work the calculation of the activation was performed for sea level exposure and, in order to get the saturation values of the radioisotopes relevant for this study, an exposure time of 100 yr was assumed.

4.3 SAMPLES PREPARATION AND MEASUREMENT

The xenon sample consisted of 2.04 kg research-grade xenon (impurities <10 ppm) from Praxair with natural isotopic composition (see Table 4.2), the same as used by the XENON100 experiment. It was contained in a 1 liter stainless steel bottle at a pressure of ∼100 bar (at $\overline{T} \sim 20$°C). To avoid the measurement results to be dominated by activation products of the bottle ($m = 2.9$ kg), two identical bottles were used for the γ-screening and for the activation procedure. The first one never left the underground laboratory, where the gas transfers took place. Both bottles were evacuated down to pressures of 10^{-5} mbar and baked at > 100°C for several days before being filled with the xenon.

The 10.35 kg copper sample consisted of 5 blocks of OFHC copper (purity 99.99%, isotopic composition in Table 4.2) from Norddeutsche Affinerie (now Aurubis). It came from the batch used to construct the inner parts of the XENON100 detector (sample 6 in [210]). Before each measurement, surface contaminations were removed in an ultrasonic bath filled with the acid detergent Elma Clean 60 diluted with deionized water.

Table 4.2.: Isotopic composition of natural xenon and copper [170]. The half-lives of the double-beta decay isotopes ^{124}Xe, ^{134}Xe and ^{136}Xe are from the NuDat 2.6 database [174], the range for the double electron capture of the isotope ^{126}Xe is a theoretical prediction from [245].

Isotope	Abundance [%]	Half-life [yr]
^{124}Xe	0.09 ± 0.01	$> 1.6 \times 10^{14}$
^{126}Xe	0.09 ± 0.01	$(5 - 12) \times 10^{25}$
^{128}Xe	1.92 ± 0.03	Stable
^{129}Xe	26.44 ± 0.24	Stable
^{130}Xe	4.08 ± 0.02	Stable
^{131}Xe	21.18 ± 0.03	Stable
^{132}Xe	26.89 ± 0.06	Stable
^{134}Xe	10.44 ± 0.10	$> 5.8 \times 10^{22}$
^{136}Xe	8.87 ± 0.16	2.126×10^{21}
^{63}Cu	69.17 ± 0.03	Stable
^{65}Cu	30.83 ± 0.03	Stable

The sample was then rinsed and wiped with pure ethanol ($> 98\%$), and stored under boil-off N_2 atmosphere for several days in order to let the ^{222}Rn diffuse out and decay.

Prior to the exposure, both the xenon and copper samples have been stored for more than 1.5 y at the LNGS underground laboratory, where the hadronic component of the cosmic radiation is absent, and the muonic component is reduced by 6 orders of magnitude compared to the above ground flux. Therefore, it is assumed that no cosmogenic activation takes place in the underground laboratory.

The samples exposure at the HARSJ took place from October 31st, 2012 to October 15th, 2013. Considering the transportation of the samples, the total cumulated activation time is 345.0 days. The initial transport from the underground laboratory to Jungfraujoch took less than 5 days and is neglected in the analysis. Following the activation, the samples were brought to Lauterbrunnen (795 m), where they were stored for about 4 days before being transported by car to LNGS for the γ-measurement. Transport to and storage at the LNGS aboveground laboratory (985 m) lasted about 1 day. The cool-down times, from the time when the samples were brought underground until the start of the measurement, were 2.5 days and 14.8 days for the xenon and copper samples, respectively.

The intrinsic radioactivity of the two samples was measured, prior and after the activation, with the HPGe spectrometer Gator [186] (see 3.3.1 for more details on the detector). Before the activation the xenon sample was measured in the cavity for 26.5 days and the copper sample for 34.3 days. The pre-activation spectra were used to establish the detection sensitivity to the γ-lines of the expected activation products as a function of measuring time. The post-activation spectra, used to determine the

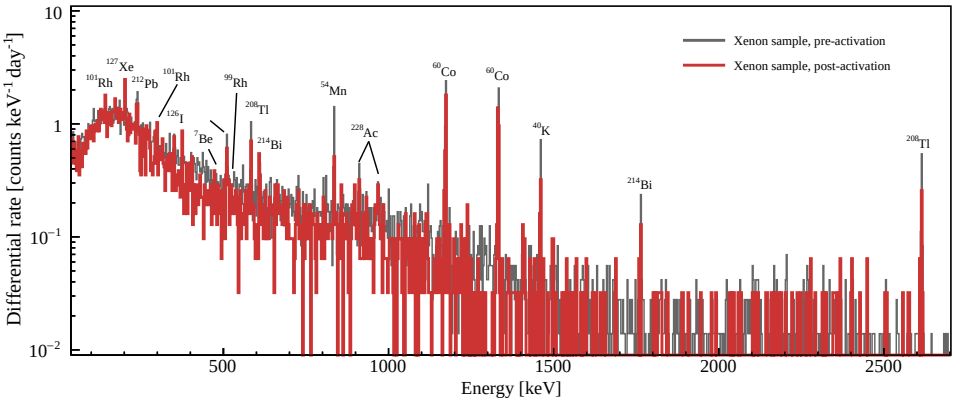

Figure 4.2.: Pre- and post-activation spectra of the 2.04 kg xenon sample. One can identify the ^{127}Xe lines at 202.9 keV and 375.0 keV, and the ^{126}I line at 388.6 keV. Other prominent lines are from radioactive contaminations in the stainless steel bottle containing the xenon (primordial ^{238}U and ^{232}Th chains, ^{40}K , cosmogenic ^{54}Mn , ^{60}Co. Figure from [220].

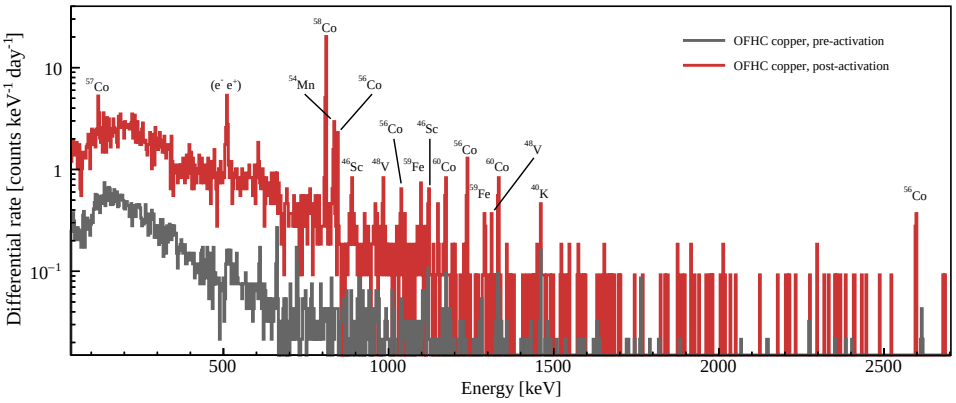

Figure 4.3.: Pre- and post-activation spectra of the 10.35 kg OFHC copper sample. The entire post-activation spectrum is dominated by the cosmogenic activation products. Figure from [220].

production rates of the cosmogenic products, were acquired over 11.5 days for the xenon sample and 4.0 days for the copper sample. The pre and post-activation spectra of the two samples are shown in figures 4.2 and 4.3.

4.4 DATA ANALYSIS

A Bayesian method based on [246–248], modified and adapted for these specific measurements, was employed to infer the activity of an isotope using all its spectral lines with a minimal relative intensity of 10 %. The spectrum around each line is divided into three regions, a central one for the signal and two side regions for the background estimation, with the same criteria detailed in section 3.3.1. The total expected counts in the signal region are $\gamma_S = \lambda_S + \lambda_B$, where λ_S is the number of counts in the signal region defined by the equation 3.7, and λ_B is the background rate as defined by either equation 3.8 or 3.9, depending on the specific case. Since, the spectral lines of the xenon

and copper activation products cannot be present in the pre-exposure measurements, for the analysis of the post-activation spectra the case of the peaked background never occurs. Hence, the model likelihood 3.14 is always defined by equation 3.15 for each spectral line k, and for each isotope the resulting total number of parameters p is always given by $p = 2n + 1$, where n is the total number of lines employed in the analysis. The posterior density functions (PDF) are generated by Markov Chain Monte Carlo (MCMC) methods implemented in the Bayesian Analysis Toolkit (BAT) [249] and by assuming flat prior distributions on all the γ_{S_k}, β_{L_k} and β_{U_k} parameters of the model. The marginalised PDF of the activity A, shown in figure 4.4 for some of the investigated activation products, is used to decide whether a specific isotope is detected or not: if the PDF mode and the lower edge of the shortest 68.3 % credibility interval (C.I., the green interval in figures 4.4) are positive, a detection of the radioisotope is claimed and the mode is taken as the best estimator of the activity, and the shortest 68.3 % C.I. as the $\pm 1\sigma$ uncertainty. If only the mode is positive but the lower edge of the shortest 68.3 % C.I. is zero, an upper limit is reported, since the presence of the radioisotope is likely but its activity is too weak to be well determined. Finally the last case is when the PDF mode is zero, and also in this case an upper limit is reported. All the upper limits are given as the 95.5 % quantiles of the marginalised posterior PDF (the upper edge of the yellow region in figures 4.4).

Since the half-lives of several potential activation products are comparable with the integral time of the measurement, the activity value or upper limit obtained from the posteriors represent a mean value $\overline{A}$ over the counting time t. Hence a correction is necessary to determine the activity at the start of the measurement A_0:

$$A_0 = \overline{A} \cdot \frac{t}{\tau \left(1 - e^{-t/\tau}\right)} , \tag{4.1}$$

where τ is the isotope's mean life time.

The specific activity of a sample of mass m after an activation time t_a is:

$$A(t_a) = \frac{N(t_a)}{m\tau} = R_a \left(1 - e^{-t_a/\tau}\right) , \tag{4.2}$$

where R_a is the specific activation rate. It is easy to observe that the production rate corresponds to the saturation activity:

$$R_a = A(t_a \to \infty) = A_{sat} , \tag{4.3}$$

where A_{sat} is the saturation activity. Because of this correspondence, hereafter the saturation activity will be used in place of the production rate.

The production rates at the Jungfraujoch site A_J are calculated from the activities at the start of the measurement A_0, taking into account the activation time t_a and the cool-down time t_c. An additional time interval t_t, that accounts for the transportation and storage at lower altitudes, is considered. During this rather short time interval the samples were exposed to a reduced CR flux, which induces a lower activation rate A_t. Hence the corrected specific activity A_J is:

$$A_J = \frac{A_0 e^{\left(\frac{t_c + t_t}{\tau}\right)}}{\left[\left(1 - e^{-t_a/\tau}\right) + r\left(e^{t_t/\tau} - 1\right)\right]} , \tag{4.4}$$

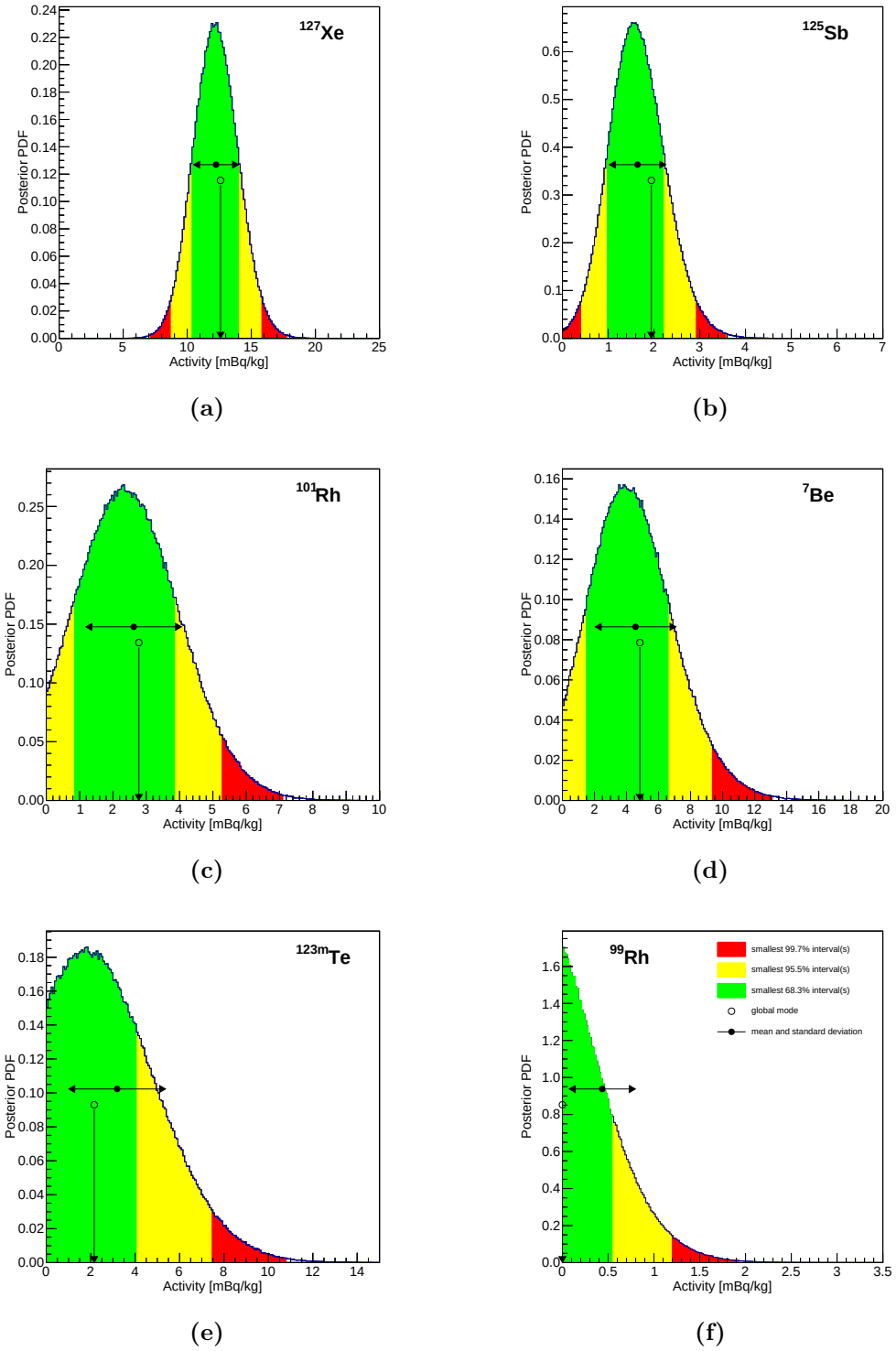

Figure 4.4.: (a) Posterior PDF for the detected ^{127}Xe activity, clearly visible in figure 4.2. The green region represents the shortest 68.3% C.I., which is taken as $\pm 1\sigma$ uncertainty. (b) ^{125}Sb, (c) ^{101}Rh and (d) ^{7}Be are detected as well, but with larger uncertainties. (e) For $^{123\mathrm{m}}$Te a signal is present, but an upper limit is reported since the intensity is too low to be determined. (f) An upper limit is reported for the activity of ^{99}Rh. The right edge of the yellow region represents the 95.5% upper limit (or the lower 95.5% credibility interval). Figures taken from [220].

where $r = A_t / A_J$ is the ratio of the production rates at Lauterbrunnen and Jungfraujoch, respectively. The storage and and transport time are combined to $t_t = 5$ days, assuming an altitude of 795 m for the whole period. Finally, the production rate at the Jungfraujoch site A_J is rescaled by the correspondent conversion factor in table 4.1, in order to obtain the production rate at sea level.

4.5 RESULTS

The radioisotopes of interest were selected based on their half-life ($T_{1/2} \gtrsim 5$ days), on their production rates as predicted from the Activia and Cosmo codes, and on the some minimal requirements on their γ-spectra. These requirements consist in asking that there is at least one spectral line with energy $E_\gamma > 60$ keV, with relative intensity $I \geq 10\,\%$ and with a minimal separation of $\pm 6\sigma$ from a prominent background line, where σ is the energy resolution at the specific energy as detailed in section 3.3.1.

4.5.1 *Copper*

The production rates at sea level for the copper sample are presented in table 4.3. The measured values are compared with the predictions performed within the scope of this work [220] using the Activia and Cosmo codes, with another measurement performed at LNGS in 2009 [206], and with some additional predictions present in literature. These are calculations performed with the Activia code from its reference publication [223], with semi-analytical approach [250], and with the TALYS 1.0 code [251, 252].

All the observed radinuclides are well known products of spallation processes on the ^{63,65}Cu stable isotopes [206, 223, 250]. The agreement between the measured production rates and the predictions from Activia of this work is remarkable, with most of the predicted values falling within the $1\,\sigma$ uncertainty of the measurement. The highest production rate, of about 0.8 mBq/kg, is measured for ^{58}Co which has a half-life of 71 days. This isotope and ^{57}Co are the only radionuclides where Activia predicts significantly lower yields than this measurement, by $\sim 20\,\%$ and $\sim 30\,\%$, respectively. The predictions performed with Cosmo agree very well with this measurements only for ^{48}V , ^{54}Mn and ^{59}Fe , while the production of all the other radionuclides is systematically lower than the observations. In addition this code predicts systematically lower production rates by $\sim 10\,\%$ compared to Activia, with the exception of ^{48}V and ^{59}Fe where they show a fair agreement. For five out of eight isotopes, the results of this work agree with the only other measurement present in literature, which was performed at LNGS [206]. For ^{54}Mn , ^{57}Co and ^{60}Co the observed production rates are (2.5 ± 0.6), (1.7 ± 0.5) and (2.9 ± 0.8) times lower, respectively. The predictions performed with Activia are almost identical to those of the original work [223], when the Silberberg and Tsao semi-empirical models are used for the excitation functions (case *a*). The predictions using the MENDL-2P database [253] for the cross-sections (case *b*) frequently yield an underproduction with respect to the semi-empirical models. However in the case of ^{54}Mn and ^{57}Co the MENDL-2P based prediction provides a better agreement with the measured values of this work. The semi-analytical study [250] predicts much higher production rates than observed for both the CR spectra employed for the calculations (cases *c* and *d*). The TALYS-based work [251] yields reasonable values, which

are 20-60 % higher than measured, and show a better agreement with the measurements of this work than with those of Ref. [206].

4.5.2 *Xenon*

The derived production rates at sea level from the xenon sample measurement are presented in table 4.4. The measurement is compared to the Activia and Cosmo predictions performed for this work, to the measurement performed by the LUX Collaboration [212], and to predictions performed with the TALYS code [251]. The values measured by LUX have been rescaled to sea level production rate with the procedure detailed in section 4.4 with the information present in the original publication [212]. Namely, it is assumed that all the xenon was activated at sea level for 150 days. After this period 50 % of the total xenon amount was activated at the SURF above ground laboratory over a period of 49 days, while for the remaining 50 % of the inventory the activation at the same location lasted only for 7 days. The following cool-down time underground was 90 days for the first half of the inventory and 152 days for the remaining part. The atmospheric depth at the SURF altitude of 1600 m is estimated to be 881 g/cm, corresponding to a nucleon flux of $8.5\,\mathrm{m^{-2}s^{-1}sr^{-1}}$. This yields a conversion factor of 3.3, in agreement with the value given by LUX [212].

After the activation five radio-isotopes were detected as cosmogenic products of the xenon: ^{7}Be , ^{101}Rh , ^{125}Sb , ^{126}I , and ^{127}Xe . The first four radionuclides were not observed prior to this measurement, while the latter has been observed also in the LUX experiment. The ^{127}Xe production rate derived from the LUX measurement agrees within 1σ with the production rate measured in this work [212]. The ^{126}I is the only activation product for which the predictions agree within the uncertainty with the value derived from the measurement. For the light isotope ^{7}Be the derived production rate is $\sim$ 50 times higher than that predicted by the two codes. For ^{101}Rh the measured production rate resulted a factor $\sim$ 90 higher than the calculations using Activia and Cosmo codes, and a factor (2840 ± 910) higher than the studies using TALYS [251]. The observed production rate of ^{125}Sb is a factor (2900 ± 1200), (44 ± 17) and (1180 ± 490) higher than the calculations from Activia, Cosmo and those relative to the TALYS studies [251], respectively. The measured production rate of the ^{127}Xe was found in agreement, within 1σ uncertainty, with the value derived from the LUX measurement [212]. For this isotope the two codes predict lower production rate than observed by a factor $\sim$ 4. The sensitivity of this measurement did not allow the detection of the short-lived xenon isotopes, ^{129m}Xe , ^{131m}Xe and ^{133}Xe . This is also the case for several other isotopes predicted by Activia, Cosmo and TALYS codes [251]. The ^{132}Cs is the only case where both the Activia and Cosmo codes predict a significant overproduction with respect to the reported upper limit from this measurement.

Finally, it is interesting to note that for the xenon radioisotopes the production rates predicted by Cosmo resulted systematically higher than those provided by Activia. This is most likely due to different implementations of the semi-empirical models inside the two codes, for the calculation of the xenon excitation functions.

4.6 DISCUSSION

The study of the cosmogenic activation of the OFHC copper, often used as ultra-pure construction material for low background experiments, shows agreement with the predictions performed for this work with the Activia [223] and Cosmo [224] codes and with the only existing experimental measurement, performed at LNGS [206], prior to the one presented here. The three out of eight detected radioisotopes in natural copper after its exposure to CRs resulted in production rates up to a factor ~ 3 lower than the prior measurements (see table 4.3). The origin of the tension between the two measurements is not clear and further independent measurements of copper activation would be of great help in understanding better the observed discrepancy. The good agreement of the measurements of production rates with the predictions performed in this work using Activia and Cosmo codes provides a strong indication of the validity of the cosmic ray models employed here for the xenon cosmogenic activation studies.

After the activation of the xenon sample five radioisotopes were detected, four of which were not observed prior to this measurement. With the exception of the ^{126}I radioisotopes, the predictions of the production rates provided by Activia and Cosmo codes for xenon results in significant deviation from the measured values. Namely, the two codes underestimate the production rates for all these isotopes by a factor of a few to $\sim 10^3$. This is potentially worrisome, as some of these isotopes have relatively long half-lives (3 yr), and might constitute a non-negligible additional source of intrinsic background for multi-scale LXe based detectors. For the short-lived ^{129m}Xe , ^{131m}Xe and ^{133}Xe the sensitivity of the γ-measurement was not enough to probe these isotopes at the required level.

For multi-ton scale LXe-based dark matter detectors the main sources of background are the ones which are uniformly distributed in the target volume, such as ^{222}Rn and ^{85}Kr, and interactions of solar neutrinos [254]. Among the observed cosmogenic products of xenon only ^{101}Rh and ^{125}Sb might have half-lives long enough to affect an experiment with a foreseen operation time-scale of a few years. The relatively high electronegativity of both elements might allow for an easy removal with the zirconium-based hot getters, commonly used for the xenon gas purification. However this has not yet been demonstrated.

The ^{101}Rh decays by electron capture to one of the excited states of the stable ^{101}Ru. With a probability of 89 % the final state is the 325 keV excited state of ^{101}Ru, followed either by prompt internal transition to the ground state or by a fast sequence ($T_{1/2} < 1$ ns) of internal transitions. Only in 8 % of the cases the ^{101}Rh decays directly to the ^{101}Ru ground state. Each of the internal transitions yields a γ-emission that produces ERs in LXe with a minimum energy of 127 keV, that would contribute to the background at energies at least one order of magnitude higher that the WIMP search region. However, it must be noted that the decay of this isotope is featured also by Auger and X-Ray emissions. There are two significant Auger emissions, at 2.53 keV from the shell L and at 16.2 keV from shell K, that will produce monoenergetic ERs with relative intensities of 107 % and 20.1 %, respectively. Considering the quenching of the NRs the second Auger emission might provide a contribution to background near the top edge of the WIMP search region, while the Auger emission from the shell L would produce a background inside the relevant region. In addition there are two X-Ray emissions at 19.15 keV and 19.28 keV, with relative intensities of 22.8 % and 43 %,

respectively, thus producing a ER background slightly above the top of the WIMP search region. It should be noted that all the emissions from the atomic system might be in time coincidence with one of the γ-emissions. Hence, such a pile-up of nuclear and atomic emissions would up-shift the observed signal to effective energies well above the WIMP search region. Therefore, it can be concluded that ^{101}Rh should not be a dangerous background source for LXe-based WIMP search experiments.

The ^{125}Sb decays by β-emission to the one of the excited levels of ^{125}Te, followed by fast sequences ($T_{1/2} < 1$ ns) of γ-emissions that shift the effective energy signal well above the WIMP-search region. However, with a probability of 13.6 %, the final state of the β-decay is the metastable state at 144.8 keV of the ^{125}Te, with a half-life of 57.4 days. The β-emission of this decay channel can be particularly dangerous for WIMP search experiments, since it is not accompanied by any other nuclear or atomic emission, and thus the low-energy tail of the β-spectrum will overlap with the entire WIMP signal region. Comparing the production rate derived from the xenon γ-measurement with the published electronic background of the LUX experiment [212], this ^{125}Sb decay channel should produce in the low-energy region a background of $\sim 3 \cdot 10^{-3}$ events keV^{-1}kg^{-1}day^{-1}, assuming that Sb is not significantly removed by the xenon purification system employed in the experiment. However, this background rate estimation seems to be too high for the low-energy ER background rate of $(3.6 \pm 0.4) \times$ events keV^{-1}kg^{-1}day^{-1}, measured by the LUX experiment [212]. Hence, it should be concluded that the true activation rate is either close to the lower end of the quoted credibility interval in table 4.4, or antimony is efficiently removed by the zirconium-based getters, or it plates out at the internal surfaces of the detector components.

The ^{125m}Te isomer ($T_{1/2} = 57.4$ days) is continuously produced by the ^{125}Sb decays and, because of the 2.19 keV Auger emission and the 3.69 keV conversion electron from the K shell, with relative intensity of 159.5 % and 85.3 %, respectively, might be an additional LXe intrinsic background source inside the WIMP search region. However, both the emissions might be in coincidence either with the nuclear γ-emission at 35.5 keV, with relative intensity of 7.3 %, or with one of the several conversion electrons or X-rays simultaneously emitted with the nuclear deexcitations. Because of this, the signals of the two dangerous keV-scale secondary electrons might be up-shifted in energy with significant probabilities by pile-up well above the WIMP search region. Hence, it can be concluded that also the ^{125m}Te second generation isomer should not constitute a serious threat for future large-scale LXe-based dark matter detectors.

In addition the chemically inert noble gas radioisotopes could also significantly affect the next-generation WIMP dark matter searches. In this dedicated experimental study of xenon cosmogenic activation only the ^{127}Xe was observed, which has a relatively short half-life ($T_{1/2} = 36.3$ days), similarly to other cosmogenically produced xenon radionuclides observed in [212]. All these isotopes will not pose a problem for WIMP search experiments as their contamination will be reduced by an order of magnitude or more after a few months of storage in underground laboratories.

As a final remark it is worth to note that for the foreseen multi-ton scale LXe detectors, such as XENONnT [164], LZ [222] and DARWIN [254, 255], also the cosmogenic activation from the high-energy muon fluxes in underground laboratories should be studied, as in this case the in-situ production of short-lived isotopes might significantly contribute to the intrinsic background.

Table 4.3.: Results for the production rates of natural copper at sea level, derived from the measurements of the cosmogenic activation. These are compared the predictions from Activia and Cosmo performed for this work, using semi-empirical formulae for the cross sections as described in the text. Both the measurements and the predictions performed for this work are compared to a measurement performed at LNGS [206] (scaled to sea level by a factor 2.1 and corrected for an evaluation error in case of ^{54}Mn and ^{59}Fe [256]), to predictions with Activia [223] using (*a*) the same semi-empirical formulae and (*b*) the MENDL-2P database for the cross sections, to semi-analytical calculations [250] using cosmic ray spectra from (*c*) Ziegler [235] and (*d*) Gordon *et al.* [257], and to predictions using TALYS [251]. Deviations from the measured values beyond $+1\sigma$ and -1σ are indicated by **bold** or *italic* font styles, respectively.

Isotope	$T_{1/2}$	Copper: production rates at sea level [μBq/kg]								
	[days]	This work			Literature values					
		Measurement	Calculations		Measurement	Activia [223]		Calc. [250]		Calculation
			Activia	Cosmo	LNGS [206]	*a*	*b*	*c*	*d*	TALYS [251]
^{46}Sc	83.79	27^{+11}_{-9}	36	17	25.2 ± 8.6	36	36	**44**	31	–
^{48}V	15.97	39^{+19}_{-15}	34	36	52 ± 19	–	–	–	–	–
^{54}Mn	312.12	154^{+35}_{-34}	166	156	$\mathbf{394 \pm 39}$	166	145	**376**	**321**	188
^{59}Fe	44.50	47^{+16}_{-14}	49	50	57 ± 14	49	*21*	**75**	57	–
^{56}Co	77.24	108^{+14}_{-16}	101	*81*	110 ± 14	101	**163**	**153**	**231**	–
^{57}Co	271.74	519^{+100}_{-95}	*376*	*350*	$\mathbf{860 \pm 190}$	*376*	421	**1022**	**858**	**650**
^{58}Co	70.86	798^{+62}_{-58}	*656*	*632*	786 ± 43	*655*	*441*	**1840**	**1430**	–
^{60}Co	1925.28	340^{+82}_{-68}	304	297	$\mathbf{1000 \pm 90}$	304	*112*	**1130**	**641**	**537**

Table 4.4.: Results for the cosmogenic activation of natural xenon at sea level. The specific saturation activities at sea level are compared to the predictions based on Activia and Cosmo, to a measurement by LUX [212] and to a calculation using the TALYS code [251]. The half-lifes refer to the numbers used in the software packages. Deviations from the measured values beyond $+1\sigma$ and -1σ are indicated by **bold** or *italic* font styles, respectively.

Isotope	$T_{1/2}$	Xenon: production rates at sea level [μBq/kg]				
	[days]	This work			Literature values	
		Measurement	Calculations		Measurement	Calculation
			Activia	Cosmo	LUX [212]	TALYS [251]
^{7}Be	53.3	370^{+240}_{-230}	*6.4*	*6.4*	–	–
^{85}Sr	64.8	< 34	5.3	4.6	–	–
^{88}Zr	83.4	< 52	6.7	4.6	–	–
^{91m}Nb	62.0	< 1200	5.6	5.0	–	–
^{99}Rh	15.0	< 120	8.3	8.2	–	–
^{101}Rh	1205.3	1420^{+970}_{-850}	*16.6*	*15.3*	–	*0.5*
^{110m}Ag	252.0	< 49	0.9	0.8	–	–
^{113}Sn	115.0	< 55	51	47	–	–
^{125}Sb	986.0	590^{+260}_{-230}	*0.2*	*13.5*	–	*0.5*
^{121m}Te	154.0	< 1200	299	276	–	135
^{123m}Te	119.7	< 610	14.7	14.4	–	140
^{126}I	13.0	175^{+94}_{-87}	247	247	–	–
^{131}I	8.04	< 190	147	170	–	–
^{127}Xe	36.4	1870^{+290}_{-270}	*415*	*555*	1530 ± 300	–
^{129m}Xe	8.89	$< 8.7 \times 10^3$	238	421	1360 ± 250	–
^{131m}Xe	11.77	$< 3.6 \times 10^4$	251	313	1620 ± 370	–
^{133}Xe	5.25	$< 1.2 \times 10^5$	159	196	1140 ± 230	–
^{132}Cs	6.47	< 120	**166**	**164**	–	–

5

A DETECTOR FOR LOW-ENERGY NUCLEAR RECOIL STUDIES IN LIQUID XENON

In this chapter I will describe the small LXe time projection chamber constructed at the University of Zürich for the precision measurements of the LXe response to low-energy NRs, called Xurich II .

5.1 NEED OF FURTHER STUDIES OF NUCLEAR RECOILS IN LIQUID XENON

The energy scale of several LXe based dark matter detectors has been hystorically based on the direct scintillation signal (S1), while the charge signal (S2) was commonly used only for the discrimination of the electronic recoil background. Only recently, the two signals have been used in combination in order to determine the sum of the absolute number of emitted photons and drifted electrons, and thus the energy deposited in LXe by an interaction. However, in both the cases it is necessary to know the light yield, defined as the number of photons per unit recoil energy, which depends on the type of recoiling particle and on the deposited energy.

As discussed in chapter 2 the liquid xenon medium for particle detection has many desirable properties required for a low-background WIMP searching detector. However, an important key for the success of a LXe detector, that exploits both the scintillation and the charge signals, is the ability to detect low-energy nuclear recoils, possibly down to 1 keV. Hence, because of the quasi-exponential spectrum shape of the nuclear recoils expected from a WIMP-nucleus elastic interaction, the understanding of the LXe light and charge yields at low energies will have a large impact on the WIMPs-search result.

Several measurements of the absolute light yield, defined as the number of photons produced by an energy deposit E_0, for relativistic and non-relativistic ionising particles, have been performed in the past 30 years with increasing precision [125, 135, 258–260]. However, in all these measurements the interaction of the radiation with matter produced mainly ERs, while for NRs direct absolute measurements of the absolute light yield are in general very difficult as the energy-dependent Lindhard quenching factor also enters in the equations. Therefore the relative scintillation efficiency L_{eff} , defined as the ratio of the light yield (Ly) of a NR relative to the Ly of a "standard candle" interaction, was used to convert the S1 signals to recoil energy. Historically and thus in much of the literature the ERs produced by the ^{57}Co 122 keV spectral line at zero field have been used as the standard candle light yield, although the choice of any other well recognisable interaction would not have any effect on the energy reconstruction.

There are several measurements of L_{eff} quantity (see chapter 2 for its definition) at low energies using direct methods [265–268], as well as indirect measurements [269–271]. These measurements show good agreement above $\sim$ 10 keV, whereas for lower energies

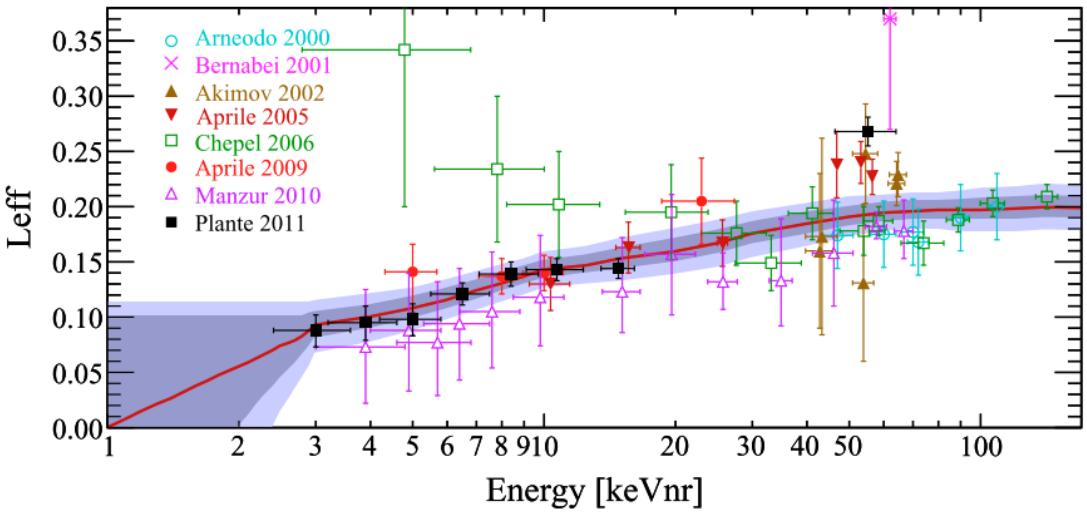

Figure 5.1.: Direct measurements of L_{eff} LXe NRs as of 2011, from Arneodo et al [261]; Bernabei et al [262], Akimov et al [263]; Aprile et al in 2005 [264] and again in 2009 [265]; Chepel et al [266]; Manzur et al [267]; Plante et al [268]. Figure taken from [166] and adapted for this thesis. Althogh, other measurements have been performed along the time this plot represents the state-of-the-art that motivated the Xurich II project.

the trends from different experiments show some disagreement, indicating the presence of systematic effects, different in each detector, when NRs with energies $\lesssim 5\,\text{keV}$ are investigated. In figure 5.1 is shown the state-of-the-art of the L_{eff} measurements from many experiments when the Xurich II RD project for the measurements of low-energy NR was proposed. The uncertain behaviour of L_{eff} at low-energy is the dominant systematic of many DM searching experiment [152,165,272,273], hence one of the main goals of the Xurich II R&D project is to perform precise measurements of L_{eff} , of the absolute charge yield Q_{y} , and of the Lindhard factor $\mathcal{L}$, with improved control and reduction of systematic effects in the low-energy range with respect to the former experiments.

As in many liquid xenon DM experiments, sensitive both to light and charge channels, the S2 signal has been mainly used only for ER discrimination, compared to the case of the L_{eff} many less investigations have been performed for the measurement of the LXe absolute charge yield Q_{y} for low-energy NRs. In figure 5.2 the Q_{y} versus the NR energy is shown, where the only direct measurement below 10 keV is from Manzur *et al.* [267], that shows an increase of the charge yield in this energy region. Hence, using the charge signal in the energy reconstruction might have many advantages, among these:

- The typical efficiency in detecting one scintillation photon in LXe is of the order of 10% or below, while for one electron extracted into the gas phase is almost 100 % [157]. This leads to an improved energy resolution with respect to the scale based on the primary scintillation signal.

- The energy threshold of dark matter LXe detectors can be lowered down to a few keV level. This could improve the sensitivity to low-mass WIMP-nucleon interactions up to one order of magnitude [267,275].

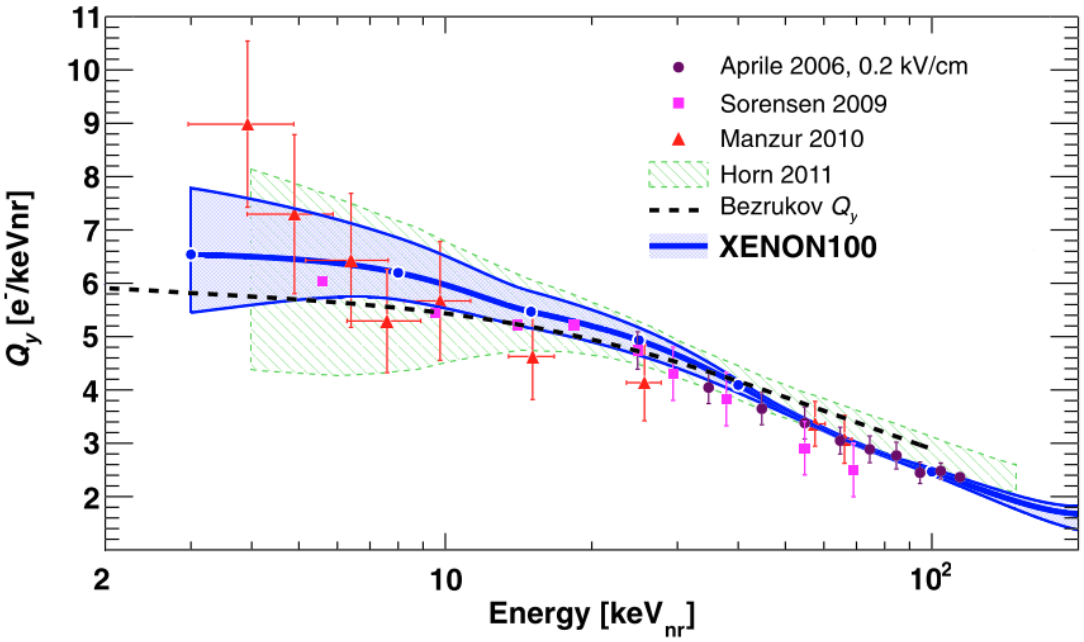

Figure 5.2.: Direct measurements of the LXe NR absolute Q_y from Aprile et al in 2006 with drift field of 0.2 kV/cm [151] (purple circles), and Manzur in 2010 with drift field of 1 kV/cm [267] (red triangles). Indirect measurements of Q_y are from XENON10 experiment [269] (magenta squares), and from the ZEPLIN-III experiment [274] (green hatched area). The blue points connected by an spline are indirect measurements from the XENON100 experiment and the shaded blue region refers to the $1\,\sigma$ uncertainty [271]. Figure taken from the latter publication and adapted for this thesis. Althogh, other measurements have been performed along the time this plot represents the state-of-the-art that motivated the Xurich II project.

– The best energy resolution in a dual-phase LXe detector can be achieved with the "combined energy scale" (hereafter *CES*) [276], which exploits the anti-correlation between the S1 and S2 and leads to a combined signal with lower level of fluctuations [277, 278]. For the electronic recoils, where the energy is released only via excitation and ionization of Xe atoms, the CES is linear with energy. However, for nuclear recoils a non negligible part of the energy is released as heat and thus not detected [279, 280]. This non-linear dependence on the energy should be taken into account for both the L_{eff} and Q_y parameters.

Predictions of absolute photon and electron yields for both ER and elastic NR interactions in LXe can be performed with the NEST software [281] for different electric fields. However, the charge yield predictions from this software for NRs at keV come with a relatively high estimated uncertainty ($\sim 30\,\%$), which can be narrowed by further measurements. In addition, simultaneous measurement of the L_{eff} and Q_y can contribute to the understanding of the energy dependency of the Lindhard factor at low-energy, which is still an open and debated question for the LXe based DM detectors [280].

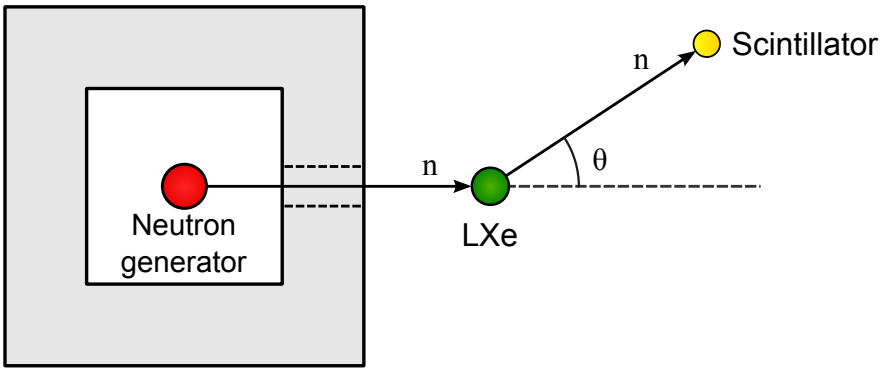

Figure 5.3.: Schematic drawing representing the direct measurement principle of neutron-induced NRs in liquid xenon planned for the Xurich II R&D project.

5.2 NUCLEAR RECOILS DIRECT MEASUREMENTS

The plan for direct measurements of the light and charge yields of low-energy NRs in LXe consists in exposing a small xenon dual-phase chamber to a mono-energetic beam of neutrons. After the first scatter off a xenon nucleus, the neutrons will eventually interact a second time with a neutron detector, placed downstream the LXe detector at an angle θ. Hence, for those neutrons interacting in both detectors the energy deposited as recoiling Xe nucleus (E_{NR}) is constrained by the kinematics. For non-relativistic neutrons and scattering off target nuclei with mass $M_{\mathrm{Xe}} \gg m_{\mathrm{n}}$, where m_{n} in the neutron mass, the recoil energy dependence on the scattering angle is well approximated as:

$$E_{\mathrm{NR}} \simeq 2K_0 \frac{\mu_{\mathrm{n,Xe}}}{M_{\mathrm{T}}} \left[1 - \cos(\theta)\right] , \tag{5.1}$$

where K_0 is the initial kinetic energy of the neutron. $M_{\mathrm{T}} = M_{\mathrm{n}} + M_{\mathrm{Xe}}$ and $\mu_{\mathrm{n,Xe}} = m_{\mathrm{n}} M_{\mathrm{Xe}} / M_{\mathrm{T}}$ are, respectively, the total and the reduced masses of the neutron-Xe system.

The neutron generator is an NSD-1e7-DD-C purchased from the NSD-Fusion company, installed in a shallow underground laboratory at the Irchel campus of the University of Zürich. The generator provides mono-energetic neutrons of 2.45 MeV emitted isotropically from the deuterium nuclear fusion reaction. The reactor is based on a *fusor* design, that consists of a reaction chamber, where low pressure ($P \sim 10^{-2}$ mbar) D-enriched hydrogen is kept at a temperature $T \sim 500\,^{\circ}\mathrm{C}$. The reaction chamber is contained in a metal cylindrical vessel, with a central perforated cylindrical cathode, biased at voltages > 20 kV with respect to the metallic vessel (grounded), that generates the electric field necessary to ionise the gas and to sustain the glow discharge current in the formed plasma. The ionised atoms, under the action of the electric field, are accelerated from the outer regions, near the vessel wall, toward the centre of the cathode structure, where they can collide with each other producing the following reaction chain:

$$\begin{aligned} {}^2\mathrm{H} + {}^2\mathrm{H} &\rightarrow {}^4\mathrm{He}^* \\ {}^4\mathrm{He}^* &\rightarrow {}^3\mathrm{He}(0.82\,\mathrm{MeV}) + \mathrm{n}(2.45\,\mathrm{MeV}) \\ {}^4\mathrm{He}^* &\rightarrow {}^3\mathrm{H}(1.01\,\mathrm{MeV}) + \mathrm{p}(3.02\,\mathrm{MeV}) \end{aligned}$$

According to the manufacturer this generator is able to generate neutrons with a rate up to $\gtrsim 10^7\,\mathrm{s}^{-1}$, although with the recommended operative conditions the rate is an order of magnitude lower. The generator is specifically located in a 4π shielded chamber, with an internal layer of borated polyethylene 20.0 cm thick, surrounded by a concrete wall 1.0 m thick. This shielding provides the proper suppression for the neutron and neutron-induced γ-radiation (from activated materials) to fulfil the radio-protection requirements [282]. The neutrons are propagated from the generator chamber to the experimental hall through a 10 cm diameter bore inside the common wall. The bore is aligned with the neutron generator internal chamber, and provides a mild collimation of the neutron beam. Since the neutrons are isotropically emitted by the deuterium fusion reaction, only a small fraction emerges from the bore window. In order to predict the features of neutron beam at the exit window of the neutron chamber, Monte Carlo simulations based on a detailed GEANT4 model of the experimental setup, have been performed within the scope of a bachelor project [283]. From the results the fraction of neutrons that exit from the bore window is $\sim 10^{-3}$, with a mean beam divergence of $\sim 10\,°$. The neutron beam comes with a contamination of γ-rays of $\sim 37\,\%$, mostly due to the activation of ^{56}Fe and ^{207}Pb in the components of the generator [284]. However, it was found that the contamination of the neutron beam by the γ radiation can be reduced by a factor of ~ 10 with just 5 cm of lead installed inside the bore where the neutron beam propagate to the detector, with a negligible impact on the quality of the neutrons beam.

The neutrons are tagged downstream by an M510 detector assembly provided from Eljen Technology, consisting of a 3-inch diameter aluminium vessel, filled with the EJ-301 organic liquid scintillator[1], and optically coupled to a ET Enterprises 9821B photomultiplier by a glass window that also seals the liquid in its container. This scintillator is capable to discriminate the interactions produced by fast neutrons from produced by the γ-radiation with an efficiency $> 99\,\%$, due to the different pulse shape of two kind of signals (NR and ER, respectively) [285].

The signal from the M510 detector is fed to an MPD-4 module that performs the pulse shape discrimination (hereafter PSD), based on the decay time of the signal tail [286]. For each of the 4 input channels the device provides the analog AMP and the PSD signal outputs[2]. The first signal amplitude is proportional to the pulse integral in a time window defined by the manufacturer and hardcoded internally to the device. The PSD signal comes from an internal time-to-amplitude converter (hereafter TAC) of the module, and is proportional to the time difference between two characteristic times of the pulse. Namely the "start" time of the TAC, is provided by an internal constant fraction discriminator (hereafter CFD), and corresponds to the rising edge of the pulse taken at the 20 % of its maximum height in the first 20 ns. The "stop" time is given by the crossing time of the internally shaped signal (by 6-th order trapezoidal filter) with the level that determined the CFD threshold. This is shown in figure 5.4. The M510 detector coupled to the MPD-4 module has been thoroughly characterised in 2012

1 EJ301 is the commercial name used for $C_6H_4(CH_3)_2$. It is identical to the more commonly known proprietary names of NE213 and BC501A.

2 Strictly speaking the PSD output provided by the MPD-4 is named TAC on the front panel, as it comes from the internal time-to-amplitude converter. However in this chapter it will be always referred as the PSD signal, since the TAC naming is reserved for the signal provided by the TAC NIM module employed for the time-of-flight elapsed between the first interaction in the LXe chamber and the second in the EJ-301 scintillator.

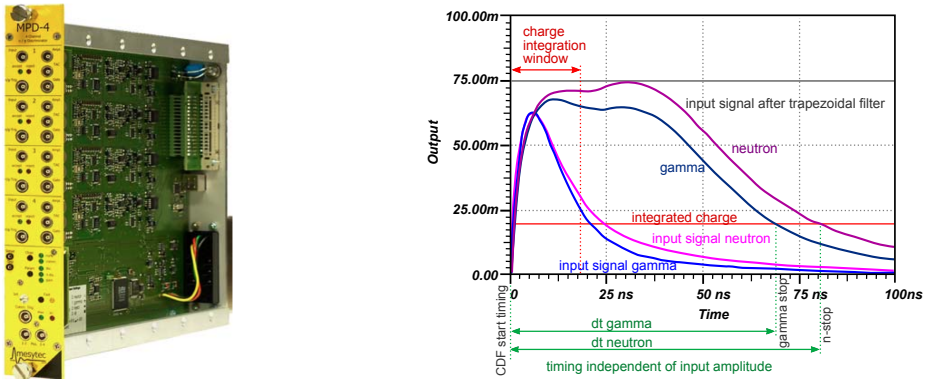

Figure 5.4.: (*Left*) Picture of the MPD-4 NIM module. (*Right*) Pulse shaping diagram which illustrates the method employed by the MPD4 to analogically discriminate two pulse signals: one with "short" decay time component that comes from a γ-interaction, and a second pulse with "long" decay time component from a neutron interaction. Both the picture and diagram are taken from their source reference [286].

within the scope of a master thesis project, where the scintillator was exposed separately to neutron beam from the deuterium fusion and to several radioactive γ-emitters [287]. It was shown that, after an optimal tuning of some parameters of the MPD-4 module and the voltage supply of the EJ-301 PMT, the electron recoils can be discriminated with an efficiency $> 99\,\%$ almost independent of the energy.

In order to reduce the uncertainties on the solid angle between the LXe chamber and scintillator chamber, the neutron detector has to be placed at a distance ranging from $\sim 0.7\,\mathrm{m}$ to $\sim 2\,\mathrm{m}$. The choice of the distance must be done with some compromise: if on one side the longer distance improves the uncertainty on the scattering angle between the two detectors, and thus also on the inferred E_{NR}, on the other side the rate of the coincident events will decrease, roughly as d^{-2} where d is the distance between the detectors, as a consequence of the solid angle reduction. The neutron detector is shielded on the top, the back and the sides by an inner layer of lead bricks 5 cm thick, surrounded by borated polyethylene bricks with the same thickness. Only a 10 cm square window in front on the neutron detector is left open in order to not shield the neutrons that have previously scattered in the LXe, as shown in the picture of figure 5.5. Additionally, an optional borated polyethylene collimator 70 long, with the same square cavity dimensions of the neutron entrance window of the scintillator shielding, can be employed to better collimate the neutrons when the neutron detector is placed at a distance from the LXe detector $\gtrsim 1\,\mathrm{m}$. The outer layer is employed in order to moderate and eventually absorb scattered neutrons that accidentally would produce a coincidence event with an interaction in the LXe. The internal layer of lead bricks, provides the shielding to the γ-radiation, produced after a neutron absorption, that could also produce an unwanted coincidence, although in this case the γ-discrimination capability of the organic scintillator combined with the MPD-4 can also provide a further suppression of such events. In order to reduce the background from accidental coincidences, also the time-of-flight (TOF) from the LXe detector to the neutron detector is measured

Figure 5.5.: Two pictures of the setup for the measurements of the neutron-induced NRs in LXe. The left picture shows the Xurich II detector, as viewed from the neutron detector, in front of the wall between the neutron generator chamber and the experimental room. The window where the neutrons come from is hidden behind the LXe detector. At the left of the detector the xenon gas purification system can be seen. The right picture shows the shielding of the neutron detector, as viewed from the Xurich II position. In front of the neutron detector the collimator, aligned with the xenon detector can be seen.

by means of a TAC NIM module. For a distance d and an angle θ, the neutron TOF between the two detectors is determined by the kinematic of the scattering process:

$$TOF(d,\theta) = d\left[\frac{M_{\mathrm{n}}}{2\left(K_0 - E_{\mathrm{NR}}\right)}\right]^{1/2} = d\left[\frac{2K_0}{M_{\mathrm{n}}}\left(1 - \frac{2\mu_{\mathrm{n,Xe}}}{M_{\mathrm{T}}}\left(1-\cos\theta\right)\right)\right]^{-1/2}. \quad (5.2)$$

where K_0 is the neutron initial kinetic energy. The triggering and the acquisition system will be detailed in section 5.3.4.

5.3 THE XURICH II DETECTOR

The Xurich II detector consists of a small dual-phase (liquid-gas) xenon TPC, which is the core of the detector, and of auxiliary systems to allow the cooling and liquefaction of the xenon and its chemical purification through recirculation in the gas phase through a hot zirconium getter.

5.3.1 *TPC design*

The TPC, schematically shown in figure 5.6, consists in a cylindrical chamber with a diameter of 31 mm. The gate and the cathode electrodes are vertically separated by 30 mm and define, respectively, the top and bottom limits of the drift chamber. The anode electrode is above the gate in gas phase, separated by a 4.0 mm thick Torlon insulator. All three electrodes consist of 0.1 mm thick stainless steel meshes with an hexagonal pattern, produced by chemical etching. The meshes hexagonal openings are 2.7 mm wide, resulting in a geometrical transparency of 93 %. They are welded by laser spotting to a 1.0 mm thick stainless steel ring, that provides the support. The gate and the anode meshes are horizontally displaced with respect to each other in a way

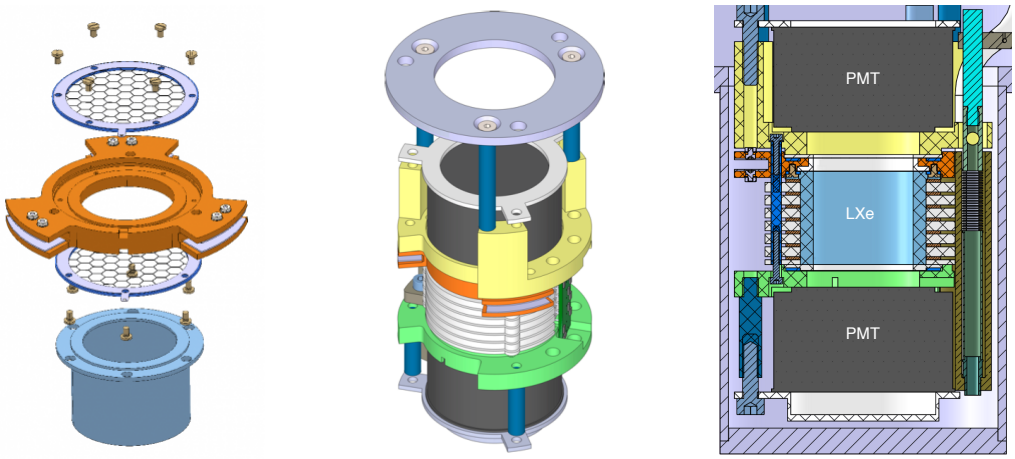

Figure 5.6.: Technical drawings of the Xurich II TPC. (*Left*) Assembling details of the anode and gate meshes on the Torlon insulator (orange), that also houses the three plate levelmeters, and of the internal PTFE reflector (azure) that defines the drifting chamber of the TPC. (*Centre*) Layout of the entire TPC, supported by the three PEEK pillars (blue) connecting the top PMT holder (yellow) to the support ring. (*Right*) Section of the TPC housed inside the internal cryostat vessel. At the left of the TPC reflector one of the three PEEK pillars (in blue) that provide the clamping of all the components between the top and the bottom PMT holders is shown. On the right side the section of the brass cup (brown) for the xenon recirculation housing the weir for the liquid level adjustment. It is composed by a top and bottom hollow tubes connected by a bellow as described in the text.

that the vertexes of the hexagons of one mesh corresponds to the hexagon centres of the other mesh and vice versa. According to the electric field simulations performed with detailed and full 3D geometry model of the detector, implemented with the KEMfield toolkit [288], this configuration of the two meshes is the one providing the best electric field uniformity of $\simeq 1.4\,\%$. This quantity is defined as the ratio $\Delta E/\overline{E}$, where ΔE and $\overline{E}$ are, respectively, the root-mean-square and the mean of electric field, both determined in the gas gap between the liquid surface and the anode mesh, where the electro-luminescence signal is produced. The same simulations showed that across the gas-liquid interface the electric field has a discontinuity from $\sim 5\,\mathrm{kV/cm}$ below the interface to $\gtrsim 10.2\,\mathrm{kV/cm}$ above the surface, not significantly dependent of the voltage bias of the cathode mesh. At these fields the expected extraction efficiency is $\sim 100\,\%$ and almost independent from small fluctuations of the field value (saturation regime) [155–157], as shown in figure 2.11. The anode and gate supports are fastened on the spacer with PEEK screws, as shown in figure 5.6 (left), in order to avoid that their displacement changes during the construction, the installation and the cool-down of the detector. In particular, among several choices of insulating materials able to provide the required electrical insulation (PTFE for instance), the Torlon was chosen thanks to its linear thermal expansion coefficient which is very close to that of stainless steel. This prevents compression stress on the electrode rings at the LXe temperature and thus the warping or even the breaking of the fragile meshes. In order to maximise the light collection efficiency (LCE) the electrode supports and the Torlon spacer are covered with PTFE reflectors, which prevent the direct exposure of these components to the internal region where the S1 and S2 signals are generated.

The chamber is viewed by two cylindrical Hamamatsu R9869 PMTs, developed for applications in LXe. Their optical window is made of synthetic silica (SiO_2) with

an effective sensitive surface of $16\,\mathrm{cm}^2$. The photocathode is made out of a bialkali compound which features a relatively high QE of $\sim 30\,\%$ for the detection of the 7 eV xenon scintillation photons. The top and the bottom PMTs are separated from the anode and cathode electrodes by 8 mm and 5 mm thick PTFE holders, respectively, which provide the required electrical insulation. The top and bottom PTFE holders that house the respective PMTs are identified in figure 5.6 with the yellow and green colours, respectively. The top PMT is secured to its PTFE holder by a PTFE cap, which is is directly fastened to the holder itself. The PTFE cap that secures the bottom PMT is held by three PEEK pillars, that are fastened to the holder.

The chamber is designed to operate with a voltage bias ΔV between the cathode and the gate from $\sim 500\,\mathrm{V}$ to $\sim 9\,\mathrm{kV}$, corresponding to the electric field strengths of $\sim 0.170\,\mathrm{kV/cm}$ and $\sim 3\,\mathrm{kV/cm}$, respectively.

The PTFE chamber wall is surrounded by a stack of 7 copper rings 1.0 mm thick alternated with 3.0 mm thick insulating PTFE rings, which are necessary to produce a uniform electric field inside the electron drifting chamber. Three PEEK pillars fixed with steel screws to the top and the bottom PMT holders, passing through the 7 PTFE ring spacers and displaced around the TPC at 120° each other, keep the entire structure together and prevent horizontal displacement or rotation of the TPC components. The pillars also provide the required rigidity against the thermal contraction of the PTFE components, that at the operational temperature of 184 K would reduce the drift length by 0.46 mm, assuming the thermal contraction of the PTFE of $16.5 \times 10^{-5}\,\mathrm{K}^{-1}$.

The number, the position and the voltage bias of the field shaping rings were optimised based on the electric field simulations performed in 2014 with the COMSOL software [284], assuming the anode and the cathode biased at $+4.0\,\mathrm{kV}$ and $-5\,\mathrm{kV}$, respectively, and the gate mesh grounded (0 V). The schematic of the resistive circuit employed to deliver the proper voltage to the shaping rings is shown in figure 5.7. The resistance ratios R_A, R_G, R_C are fixed by the simulations, while the resistance R was chosen in order to fulfil the maximum power and current specification of the HV power supplies, with the cathode voltage at the extreme value of $-9\,\mathrm{kV}$. A resistive circuit mounted on a printed circuit board (PCB) consisting of a polyamide substrate, delivers the voltage to each ring. Later full 3D simulations performed with a more detailed detector model, implemented with the KEMfield toolkit, confirmed the preliminary studies used for the development of the resistive chain with higher accuracy.

From the simulations performed with different voltage biases, it was found that in the drift chamber (or S1 region) the field uniformity ranges from $\Delta E/\overline{E} \simeq 15\,\%$ for a cathode voltage of $-450\,\mathrm{V}$ ($\overline{E_\mathrm{d}} \simeq 0.2\,\mathrm{kV/m}$), to $\Delta E/\overline{E} \simeq 3\,\%$ for a cathode voltage of $-4000\,\mathrm{V}$ ($\overline{E} \simeq 1.3\,\mathrm{kV/m}$).

The outer part of the Torlon spacer is shaped in order to hold three capacitors based on horizontal parallel plates, displaced at 120° all around the outer circumference. The bottom edges of the top capacitor electrodes are vertically aligned with the anode mesh, and conversely the top edges of the bottom capacitor electrodes are vertically aligned with the gate mesh. Hence these three level-meters provide at the same time a monitor for the liquid level above the gate and a monitor for the tilting of the TPC with respect to the vertical. In an ideal capacitor, consisting of two parallel conducting plates at a distance d, electrically separated by two dielectrics with different electric relative permittivities ϵ_g and ϵ_l (for gaseous and liquid xenon, respectively), such that

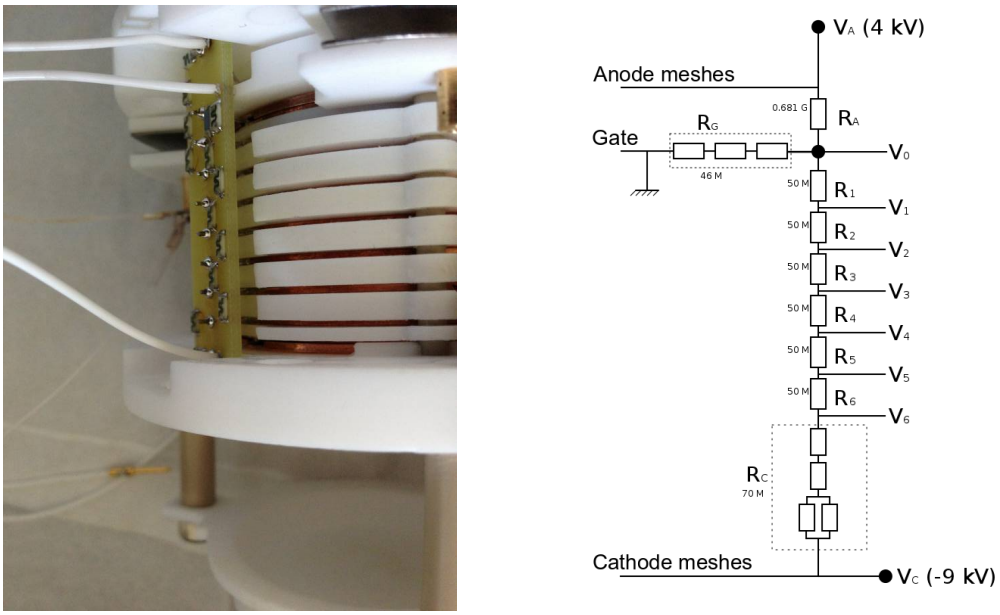

Figure 5.7.: (*Left*) Picture of the PCB employed to deliver the HV to the electrodes and to the field shaping rings of the TPC. The three white PTFE insulated wires are connected directly to the anode (top wire), to the gate (middle wire), and to the cathode (bottom wire) electrodes. (*Right*) Electrical scheme implemented on the HV board.

$h_\mathrm{g} + h_\mathrm{l} = d$, where $h_\mathrm{g,l}$ are the thicknesses of the two dielectrics, the capacitance is given by:

$$C(h_\mathrm{l}) = (A\epsilon_0/d)\,\frac{\epsilon_\mathrm{g}}{1-(h_\mathrm{l}/d)\,(1-\epsilon_\mathrm{g}/\epsilon_\mathrm{l})} = \frac{C_0}{1-(h_\mathrm{l}/d)\,(1-\epsilon_\mathrm{g}/\epsilon_\mathrm{l})}\,, \tag{5.3}$$

where A is the surface of the plates, ϵ_0 the dielectric constant of the vacuum, and the second equality follows by replacing $C_0 = A\epsilon_0\epsilon_\mathrm{g}/d$. Since $\epsilon_\mathrm{g} < \epsilon_\mathrm{l}$ the capacitance value increases with the LXe level h_l. However, since the geometry of the plates is very different from that of an ideal plane capacitor, a proper calibration for an accurate level readout was performed. This operation is usually done at the start of every acquisition run when the liquid level is set, and the TPC tilting with respect to the vertical line is optimised.

Between two of the three levelmeters a brass round-shaped cup, used for the recirculation of the liquid xenon, is fastened to the top PTFE holder. A copper syphon tube, connected to the pump of the recirculation system, enters into the the cup from the top and sucks out the LXe present inside the cup. The liquid xenon enters into the recirculation cup from a hollow steel cylinder with an overflow hole. This hollow cylinder is connected with a bellow to a bottom cylinder, also hollow inside, that sticks outside the cup through the bottom. The LXe can flow inside the recirculation cup only by falling from the overflow hole, that is mechanically connected to a manually driven graduated motion feedthrough outside the cryostat. Hence with this weir system it is possible to change LXe level inside the chamber, which corresponds to the vertical position of the overflow hole. Since the LXe is recirculated from the cup which provides the physical decoupling with the LXe of the TPC, the pumping does not produce streams or convections inside the detector sensitive volume.

The entire structure is supported by a steel ring connected to the top flange (hereafter the *internal flange*). The top PMT holder is connected to the steel ring by three PEEK pillars fastened on both sides.

The Xurich II TPC is housed inside a stainless steel vessel with 2.6 mm thick wall (the *inner cryostat*), sealed to the internal flange, where the liquefaction of the xenon takes place. The bottom part of the vessel has an internal diameter of 83.7 mm, just larger than the TPC structure, in order to minimise the amount of LXe outside the drift chamber and thus to reduce as much as possible eventual neutron scattering before the interaction inside the target volume. On the internal flange there are 5 electrical feed-throughs. For the cathode HV, a dedicated electrical feed-through that can withstand voltages > 10 kV is used. Internally, the cathode voltage is transported to the main chamber with a 1.5 mm wide copper rod, which extends few mm below the internal flange. The copper rod is insulated for its entire length from the feed-through grounded walls by a ~ 1 cm thick PTFE tube with a central bore large enough to fit the copper rod. The end of the copper rod is connected by a brass female pin to a PTFE insulated wire, which at the other end is directly soldered to the HV breakout board, as shown in the picture of figure 5.7 left. A second electrical feed-through is used for the connection of the anode and gate HVs and for the power supply of the PMTs (1000 V maximum). A feed-through is dedicated only for the PMT signals transportation. Another feed-through is used for the optical fibres, used for the gain calibration of the PMTs, and for the readout of the Pt100 sensor, which monitors the LXe temperature. Finally, the fifth electrical feed-through is used for the cabling of the 3 plate levelmeters readout.

All the active components of the detector, with the exception of the anode, cathode and gate electrodes, are connected to three patch panels, by PFA or PTFE insulated coaxial cables, each of which terminates with a male SMA connector. The patch panels, visible in figure 5.8, consist of L-shaped metallic plates, fastened to the flange and able to host up to 4 SMA female connectors, connected to their respective feedthrough by the same kind of coaxial cables used for the "male side". This system was designed in order to simplify the assembly, the installation, and the bake-out of the TPC, that must be performed without the PMTs in the hot xenon atmosphere (~ 100°C), inside the sealed internal cryostat.

Other three feedthroughs are used for the liquid level adjustments, for the outlet of the LXe and the inlet of the xenon gas, and the last is used for the monitoring of the pressure of the chamber and for the evacuation of the vessel before a new xenon filling operation.

5.3.2 *The cryostat and temperature control system*

The inner cryostat consists of a stainless steel can that houses the TPC and is sealed to the internal flange with a copper gasket. The liquefaction of the xenon occurs on the internal flange which is mechanically and thermally connected to the cooling system, based on a copper cold-finger which will described later.

The eight feedthroughs of the internal flange are welded to the corresponding feedthroughs on the external flange (ISO250 standard), and provide thus the mechanical connection between the two flanges. The external cryostat consists of a 254 mm diameter steel cylinder with a 2 mm thick wall, sealed to the external flange by a viton gasket. The bottom part of the external cryostat consists of a narrow long tube, which houses the

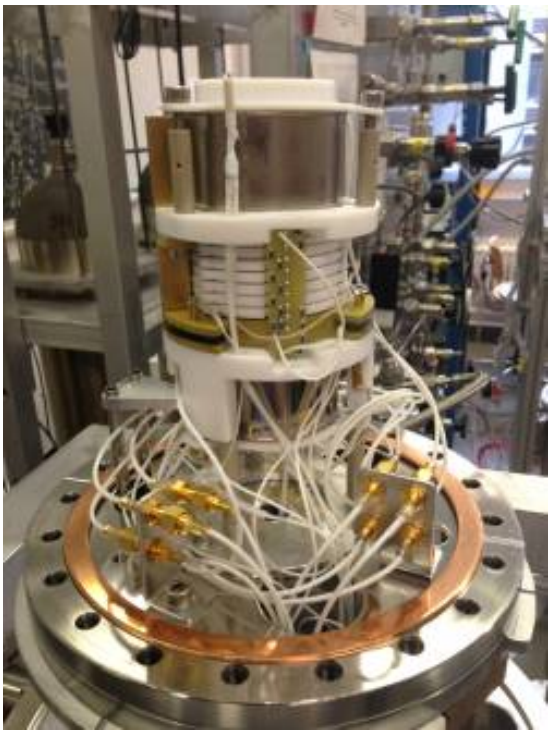

Figure 5.8.: TPC during its final assembly after the bake-out stage. Since the PMTs cannot withstand the bake-out temperatures, the internal vessel is opened again and they are assembled on the structure only at this stage. The assembly procedure is performed with the TPC reversed up side down and only after the internal vessel is sealed to the flange, the entire top structure is flipped into its operational position. At the front of the "bottom PMT" (here is the top one) it is possible to see the Pt100 for the LXe temperature monitoring. At the bottom, fixed on the "internal flange" (as defined in the text), two out of the three patch panels for the connection of the cabling are visible.

copper cold-finger used by the cooling system and its bottom end is immersed in a liquid nitrogen bath. Inside the external cryostat a vacuum of few 10^{-7} mbar provides the thermal insulation for the internal vessel and for the cooling system. In addition to the feed-throughs in common with the internal flange, the external flange has some other feedthroughs, two of which are used for the vacuum pumping and for the monitoring and control of the cooling system.

The cooling is provided by a copper made cold-finger that sticks along the cold-finger vacuum jacket of the external cryostat until the end of this, where a mechanical contact is established for the thermal transfer. The copper rod is fastened at the bottom of an aluminium cylinder, that is tightened by several screws to the internal flange where the heat exchange takes place. Further, the aluminium cylinder is insulated by a mylar jacket that reflects the IR radiation coming from the walls of the external cryostat at room temperature, and thus prevents loss of cooling power by radiative exchange.

On top of the internal flange, a Pt100 temperature sensor and an electric heater are used to monitor and control the flange temperature. Both the components are connected to one of the two channels of a CryoCon 34, able to provide up to 5 W of heating power. The temperature of the flange is then stabilised by the device's PID automatic feedback system. Another channel of the same device is connected to the

Pt100 that sticks inside the internal vessel (visible in the picture of figure 5.8), close to the bottom PMT for the monitoring of the LXe temperature.

The stability of the temperature and pressure required to operate a liquid xenon detector is provided by a system based on a vacuum-insulated cryostat, mainly consisting in an internal and external stainless steel vessels and some other components for the cooling. The plots of these quantities as function of the time are shown in figure 5.9, together with the plot of the internal flange external temperature which is directly controlled by the PID-based feedback system of the Cryocon 34. The flange temperature is featured by downward spike fluctuations, corresponding to the automatic refillings of the LN_2 bath, where the cold finger is immersed. However, the same kind of fluctuations are not observed in the plots of the LXe temperature and xenon gas pressure, which feature fluctuations relative to their mean values lower than 10^{-3} and 5×10^{-3}, respectively. This is mainly because the temperature is controlled outside the internal flange, that because of its relatively high thermal capacitance and low thermal conductivity dumps, the short time temperature fluctuations. The cost of this feature is the reduced cooling power for the xenon inside the internal vessel, that limits the operations to a LXe temperature not lower than 184 K. However, this temperature was low enough to have stable conditions of the at a pressure of ~ 2 bar for the measurements we reported in section 5.5. Many of the components that are going to be described in what follows have already been used for the Xurich I experiment [289, 290].

5.3.3 *The Xurich II gas system for the xenon purification*

The detector uses a dedicated gas system for the operations of xenon filling and recuperation and for the xenon chemical purification by recirculation. Its schematics is shown in figure 5.10. This system was initially developed and used for the Xurich detector [289, 290], and for the Xurich II detector some minimal modifications have been applied. Among these modifications the most relevant consists in an upgraded line for the ^{83}Rb emanation chamber connection to the rest of the gas system. This modification allows for the injection of the ^{83m}Kr , emanated in the chamber by the decay of the ^{83}Rb, into the detector. As will detailed in section 5.5, the ^{83m}Kr isomer is used for low-energy ER calibrations of the detector and for the calibration of the detector response parameters. The gas system upgrade allows to inject the ^{83m}Kr both in "diffusion" mode when only the valve V20 and V21 are open, or in "flushing" mode when the valve V20 is closed and both the valves V21 and V25 are open (referred to the scheme of figure 5.10). In the previous setup system only the "diffusion" mode was possible resulting in a lower injection efficiency that made the calibrations difficult when the ^{83}Rb activity decreased below a certain value. As will be detailed in section 5.5.2, electronegative chemical impurities in xenon, such as H_2O, O_2 or N_2O, might compromise the charge response of the LXe because of electron capture. Since these molecules are continuously emanated by the surfaces of the internal detector components, a continuos chemical purification of the xenon is necessary. In the Xurich II detector this is done by a continuos recirculation of the xenon through a standard SAES Monotorr getter, where the xenon chemical impurities are adsorbed on hot zirconium metal plates. The xenon is drawn in liquid state by a KNF diaphragm recirculation pump. The liquid quickly vaporises when in contact with the pipes, at room temperature, and thus the xenon reaches the recirculation pump inlet in gas state. In this state the xenon is pushed

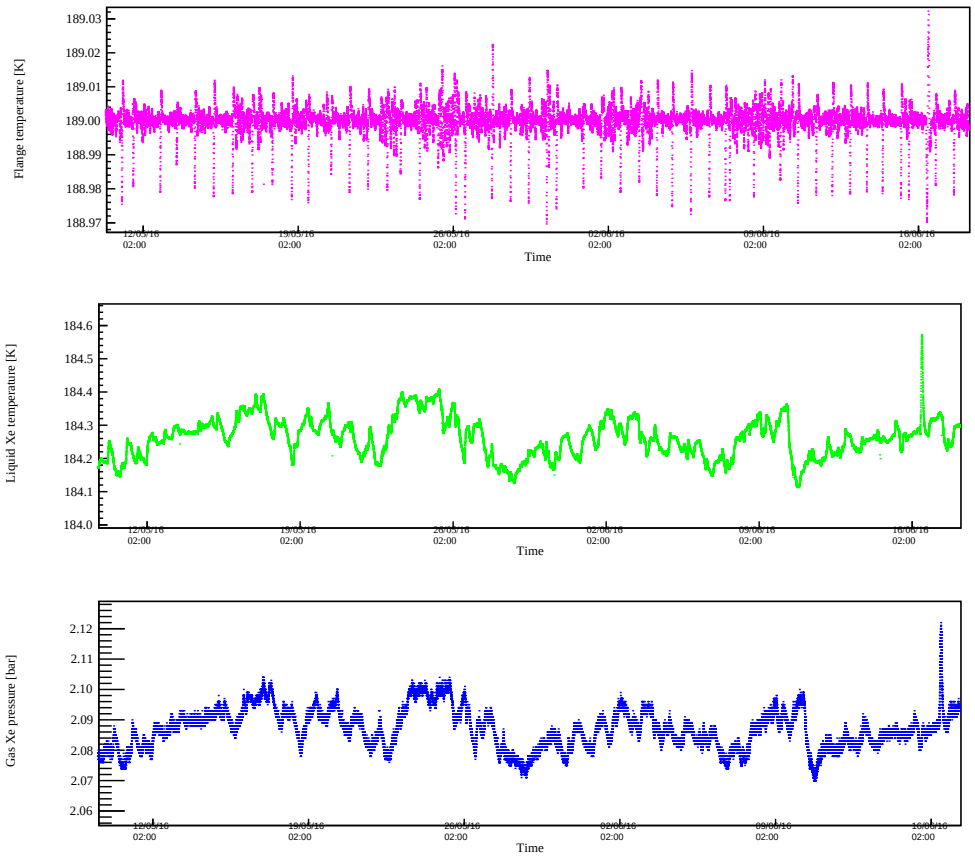

Figure 5.9.: Operative parameters of the Xurich II detector over the time period relative to the low-energy ER calibrations performed the ^{83m}Kr source and reported in section 5.5. (Top) Time series of the internal flange temperature stabilised thanks to the PID-based feedback system provided by the Cryocon 34 device as described in the text. The quasi periodic downward temperature spikes correspond to the refillings of the LN_2 bath. The few positive temperature spikes correspond to lower levels of the LN_2 bath. These occasionally occurred when the dewar used for the refilling of the LN_2 bath was running out of nitrogen and an exchange with a freshly refilled dewar was necessary. (Middle) Time evolution of the LXe temperature measured by the the Pt100 sensor placed near the bottom PMT as detailed in the text and shown in the picture of figure 5.8. The relative deviation of the LXe temperature with respect to the absolute value is limited to a level of 10^{-3}. (Bottom) Time evolution of the xenon gas pressure inside the chamber. It is possible to observe the strong time correlation of this parameter with the LXe temperature. The maximum relative fluctuations of the pressure values with respect to the mean pressure are lower than 5×10^{-3}.

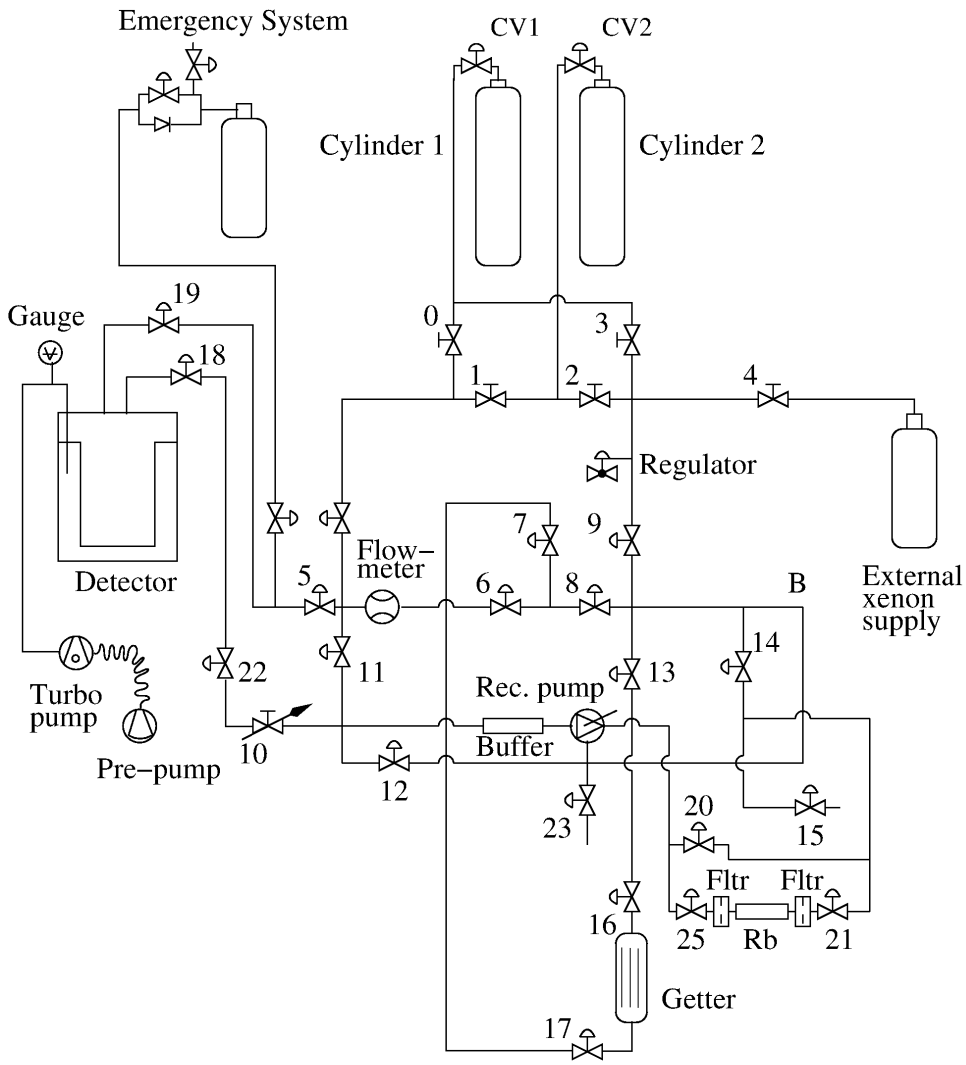

Figure 5.10.: SChematics of the layout of the detector gas system for the xenon recirculation and chemical purification and of the pressure emergency system.

through the rest of the gas system until the getter, where it is chemically purified and ready to be reinjected into the cryostat. The mass flow can be manually regulated by a needle valve (V10 in figure 5.10) placed between the pump inlet and the cryostat.

5.3.4 *Data acquisition system*

The DAQ system is designed to acquire full waveforms from both PMTs at each triggered event. In figure 5.11 the diagram of the acquisition chain is shown for the two main operative configurations: one for the ER calibration with internal and external γ-emitters (only green connection lines); and the other for the neutron-induced NRs measurement (green plus purple connection lines). The core of the acquisition system consists of a CAEN V1724 fast ADC module with 8 unipolar channels, powered by a CAEN VME008 crate. The dynamic range of this module is 2.25 V (nominal) with 14 bit resolution (16384 channels), and the analog signals are digitised at 100 MHz. The total length of the recorded waveform is fully customisable within a range of 100 μs by

the user, through the acquisition software. Depending on the electric field, the maximum drift time of the electrons ranges from $\sim 15\,\mu$s to $\sim 25\,\mu$s (see section 5.5.3). A CAEN A2818 PCI board, mounted on the acquisition PC, is optically connected to the digitiser, providing thus the link to record the acquired waveforms.

The signals coming from each PMT are fed into a CAEN 625 quad linear fan-in/out NIM module, which has a maximum dynamic range of 2 V. Hence, it is not necessary to calibrate the end of the dynamic range of the digitiser channels, where some non-linearity response is usually present, as the signal amplitudes after the fan-in/out module cover only $\sim 90\,\%$ of the ADC dynamic range. It was observed that ER events of energy as low as ~ 40 keV produce proportional scintillation signals that saturate the output of fan-in/out channels. Hence, in order to have usable data for the ER energy scale scale calibration, each PMT signal is fed to a $\times 10$ attenuator with a bandwidth of 2 GHz, prior to the fan-in/out module. This prevented to reduce the PMTs gain for ER calibrations, using therefore always the same working point for each type of measurement. In both the ER and NR DAQ configurations, one of the two copies of the signals from each PMT is directly fed into a digitiser channel. The second copy of the top PMT signal is fed into a CAEN N840 leading edge discriminator, which provides the trigger signal to the digitiser for the waveform acquisition. Since for the measurements of both ERs and NRs only events with both light and charge signals are considered, the discriminator threshold is set to a level that most of the triggers are due to S2 signals, and only a minor fraction due to relatively strong S1 signals.

The second copy of the bottom PMT signal, used only for the neutron data, is fed to a $\times 10$ low-noise linear amplifier with a bandwidth > 100 MHz, a prototype for the XENONnT and DARWIN research projects. After the amplification the signal is fed into one channel of the CAEN N840 discriminator, which produces the trigger signal for the start of a TAC module, used for the measurement of the TOF of the neutron from the xenon chamber, where the first interaction happened, to the scintillator.

Since for each interaction the S1 signal comes before the S2, and because of the internal reflections at the liquid surface of the VUV light, the primary scintillation is mainly detected by the bottom PMT, and thus the most likely signal generating the trigger for the start of the TAC is the S1 signal.

The signal generated in the scintillator is directly fed into one of the input channel of the MPD4 NIM module. The AMP signal is fed into the fan-in/out input channel, while the PSD signal is fed directly to one digitiser channel. One of the two copies of the AMP signal provides the trigger for the stop of the TAC and the other is fed directly to a channel of the digitiser. The signal from the TAC module is also digitised, with the amplitude proportional to the time elapsed from the start and stop signals.

All the channels used for the digital acquisition of the waveforms can be activated on demand by the DAQ software, through a configuration xml file. Other hardware configurations specific for each channel, such as the baseline level, can be set in the same configuration file, which contains also some other settings relative to the hardware configuration necessary for the processor of the waveforms. Namely these settings are the channels corresponding to the top and bottom PMTs with their respective SPE gains and the settings corresponding to the AMP, PSD and TAC signals when they are used.

Finally, the data are copied and stored on two different disks of the cluster of the UZH Physik-Institut. In one of those disks, the *working disk*, the data are available

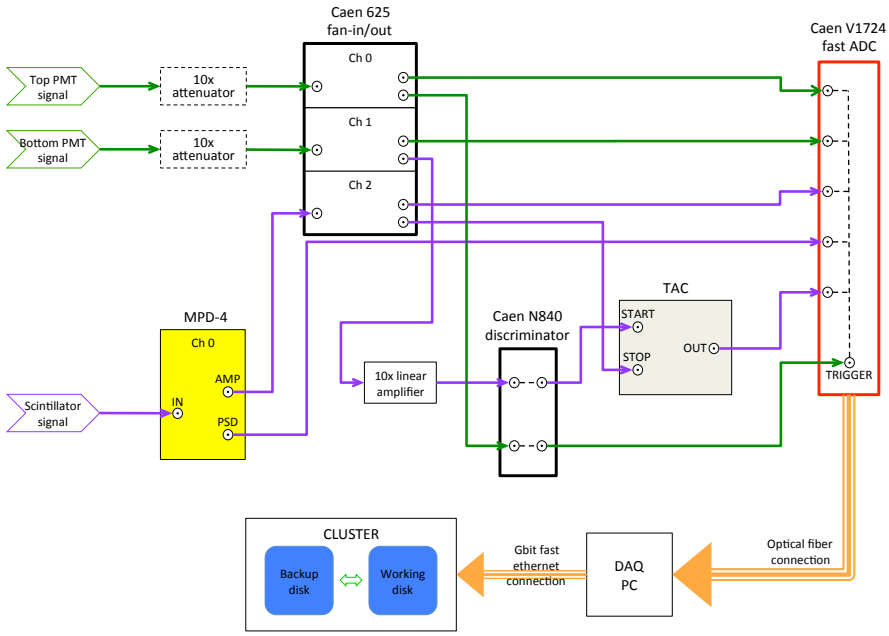

Figure 5.11.: Layout of the data acquisition system of the Xurich II detector. The green connections are always used both for ER measurements (detector calibrations) and for the NR measurements. As detailed in the text the attenuators are used only for ER calibrations, while for NR measurements the signals from the PMTs are directly fed into the fan-in/out. The purple connection is activated by software, only when the coincidences between neutron interactions in LXe and in the EJ-301 scintillator are measured.

for processing and for analysis, while the other disk is used as a backup in case of data loss or when some old data not available anymore on the working disk has to be reprocessed/reanalysed.

5.4 DATA PROCESSOR OF THE RAW WAVEFORMS

A data processing software was specifically developed for this experiment, and consists of three programs. A Python program allows to take advantage of all 144 cores of the batch cluster for the processing of a data set, typically consisting of several hundred raw files, reducing in this way the processing time by $\gtrsim 100$ times compared to a serial processing. A C++based program, *xurawproc*, runs on this batch computing cluster, parses the raw waveforms, and extracts and saves the physical quantities of interest into a new made ROOT file. A third program, also written in C++, allows the user to interactively visualise and inspect the waveforms, which provides a powerful debugging tool for the development of the S1 and S2 searching algorithms. These are based on modular libraries, with the aim to easily implement improvements and upgrades to the code, and to easily implement them in different programs, such as the waveform visualiser, by using a self consistent interface.

In each of the raw files saved by the DAQ program the data are organised in events, corresponding to the triggers of the fast-ADC module. Each event is a collection of 2 waveforms (the 2 PMTs signals), in the case of ER calibrations data, or 5 waveforms in the case of the neutron data, where beside the channels corresponding to the 2 PMTs, also the 3 channels corresponding to the AMP and PSD signals from the MPD-4 module and to the TAC signal for the TOF are recorded. Each waveform consists of an array of integers, whose length is at least twice of the total drift time length, where the trigger time corresponds to the middle.

For the parsing of the waveforms the processor needs a file of the hardware settings and a file of the processing settings, both written in *xml* format. The file of the hardware settings, saved at the start of the data acquisition of each dataset, contains some parameters that are fundamental for the processing of the waveforms. These are the active f-ADC channels, the polarity of the signals fed into them, and a device connected to each channel. In particular for the processing of the PMT waveforms, additional information such as the PMT gains, obtained with dedicated light calibrations, is also required in order to convert the amplitudes in V units to PE/channel units. The second file required by the processor is not strictly linked to a specific dataset, and the settings can be changed before the data processing. This allows to reprocess the same dataset in order to find the optimal settings of some critical parameters employed for the identification of the S1 and S2 pulses.

The raw data processing consists of three main stages:

- **Pre-processing.** In this stage the information from the xml files is loaded and its consistency is verified. For each waveform the baseline and its RMS, as a noise quantification, are calculated on the first and last 50 time samples (1 sample= 10 ns) by default, and can be manually changed through the file of the processing settings. These quantities are used to shift the waveform in order to have a zero baseline, and, after changing its sign, when the signal polarity is negative (e.g. for the PMTs), the flattened waveform is computed. This is obtained by setting to zero all the samples which are below $t\times$RMS, where t is a parameter chosen by the user at processing time (by default $t = 3.0$), and keeping unaltered all the other samples. These steps, applied to a specific waveform are, are shown in figure 5.12.

- **S1 and S2 signal identification.** This stage is the core of the entire processing flow, where the waveforms of the PMTs are singularly analysed in order to detect every pulse. By means of several filters built from the flattened waveforms the algorithm aims to identify each pulse as an S1 or an S2 candidate signal. This will be detailed in 5.4.1. At this stage several physical quantities and pulse shaping parameters are calculated and saved for each detected pulse, in the principal data tree of the ROOT file (*T1*). Many of these quantities will then be used in the analysis to develop several selection cuts.

- **MPD4 and TAC signal processing.** This last stage of waveforms processing, that is detailed in section 5.4.2, is executed when the scintillator for the neutron detection and the TAC module for TOF measurement are in-line. The processing of these waveforms is rather basic and computes very basic quantities for each detected pulse such as the position, the length, the height, the area. For the AMP and PSD related waveforms the algorithm also determines whether a temporal

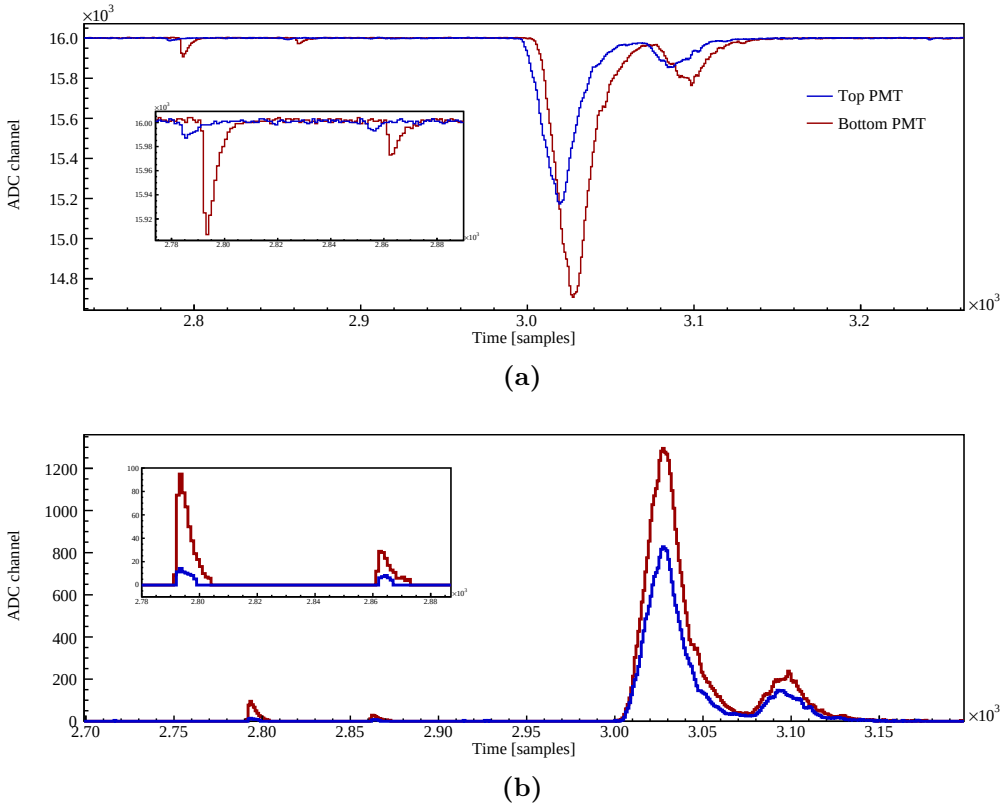

Figure 5.12.: Pre-processing of the two PMT waveforms, corresponding to a selected ^{83m}Kr decay event, where both the 32 keV and 9 keV de-excitations, separated by $\sim 0.8\,\mu$s, can be observed both in the S1 and S2 channels.
(a) Raw waveforms of the top (dark blue) and bottom (dark red) PMTs as they come from the DAQ are shown. In the inset it is shown the detail of the S1 signals from the two PMTs, where a delay of 80 ns (8 time samples) of the bottom PMT signal is visible with respect to the top PMT.
(b) Waveforms shifted to zero baseline, corrected for the polarity (negative only for the signals from the PMTs), and realigned for the time delay. In the text these waveforms are called *original waveforms* and denoted with the symbol W_f.

coincidence is present. All this information is saved in the same ROOT file as the S1 and S2 signals, but using a dedicated data tree (*mpd4T1*), that in analysis stage can be used in combination with the *T1* tree.

5.4.1 *The S1 and S2 identification algorithm*

The identification of S1 and S2 candidates is primarily performed by two width-based filters. An additional χ^2 filter is also employed to improve the discrimination of the S1s from the S2s signals based on pattern recognition. All the filters that are going to be introduced are based on some parameters that have been optimised and are reported in table 5.1.

The first filter that is computed is the *flattened waveform* $W_{\rm ff}$, that is obtained by the waveform after the baseline has been subtracted and the signal polarity has been applied

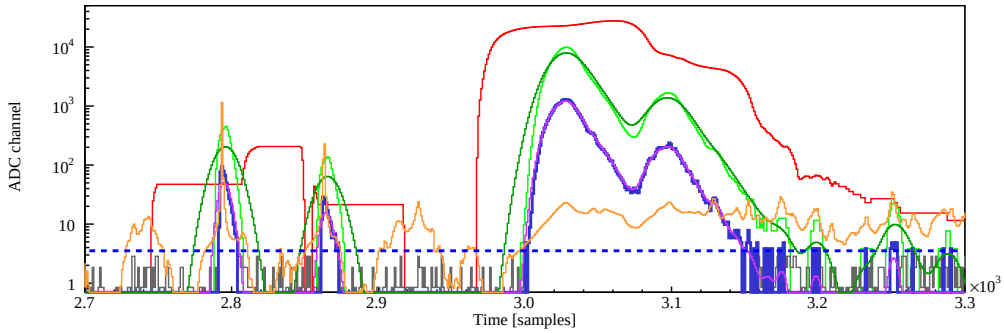

Figure 5.13.: Waveform filters computed in the last pre-processing step, shown here only for the bottom PMT waveform. In order to be able to visualise both the S1 and S2 signals the amplitudes are shown in logarithmic scale. The solid and dashed blue lines are the flattened waveform (W_{ff} in the text) and the flattening threshold level, respectively. The grey line is the original waveform (W_{f} in the text) that is below the threshold, corresponding thus to the regions where the W_{ff} is padded with zeroes. The Gaussian convolution of the flattened waveform (W_{ff} in the text) is represented by the solid light purple line. The light and dark green solid lines are the F_1 and its Gaussian convolution ($F_{1\mathrm{s}}$ in the text), respectively. The red solid line is the F_2 filter which defines the *S2 search regions*. The orange solid line is the reciprocal of the χ^2 filter, which for visualisation purposes it is plotted in place of the χ^2. Hence, the waveform parts featured by an higher similarity to an S1 signal correspond in this plot to higher values of the orange line.

(W_{ff}), as show in figure 5.12b. For each sample k, the $W_{\mathrm{ff}}[k] = W_{\mathrm{f}}[k]$ if the amplitude of the W_{f} is above a specific threshold T and is zero over all the other intervals:

$$W_{\mathrm{ff}}[k] = \begin{cases} W_{\mathrm{f}}[k] & \text{if } W_{\mathrm{f}}[k] > T \\ 0 & \text{if } W_{\mathrm{f}}[k] \leq T\,. \end{cases} \tag{5.4}$$

The threshold T is obtained from the product of the baseline RMS value by a numerical (positive) factor, usually set equal to 3.0 (as reported in table 5.1), that can be changed by the user through in the configuration file for the processing. Assuming a gaussian distribution of the noise amplitude the probability to have a fluctuation above the threshold is $\simeq 1.3 \times 10^{-3}$. Hence, the intervals where $W_{\mathrm{ff}}[k] > 0$ are most likely due the PMT's collected charge at the anode, and thus to a real signal from photoelectrons.

After this step the F_1 filter is computed by convolving the flattened waveform W_{fl} with a squared kernel of amplitude 1 and of width w_1 time samples (hereafter *box car*):

$$F_1[i] = \sum_{k=i-(w_1/2)}^{k=i+(w_1/2)} W_{\mathrm{ff}}[k]\,, \tag{5.5}$$

where $F_1[i]$ is the amplitude of the filter in correspondence to the time sample i, and $W_{\mathrm{ff}}[k]$ is the amplitude of the flattened waveform at the time sample k. This filter(light green line in figure 5.13) is designed to react to the waveform unipolar (positive) signal content inside a w_1 wide region, which should enclose almost entirely an S1 signal and at the same time should be narrower than the typical S2 pulse ($\sim 1 - 1.5\,\mu$s). The regions where $F_1 > 0$ are called *pulse search regions* (PSR), where one or more pulses can be found.

Table 5.1.: Tunable parameters used for the processing of raw waveforms in Xurich II . Their definitions and descriptions are found in the text. The optimised values reported for each parameters are those used for the data processing of the calibrations reported in section 5.5.

Parameter	**Values**
Left baseline calculation	50 samples
Right baseline calculation	50 samples
RMS threshold multiplicator	$\times 3$
w_1	8 samples
w_2	100 samples
σ_1	3 samples
σ_2	7 samples
S1 template length	21 samples
S1 χ^2threshold (top PMT)	0.02
S1 χ^2threshold (bottom PMT)	0.01

From the F_1 an additional filter F_2 is calculated (red line in figure 5.13). This filter is obtained in two steps: in the first step the flatted waveform W_{ff} is convolved with a second box car with a width of w_2 time samples that should enclose most of a typical S2 signal (therefore $w_2 > w_1$); after this step the maximum of the F_1 inside this wider box car is subtracted from the obtained convolution. Therefore the F_2 filter is defined by:

$$F_2[i] = \sum_{k=i-(w_2/2)}^{k=i+(w_2/2)} y[k] \quad - \quad \max_{j\in[i-(w_2/2)\,;\,i+(w_2/2)]} F_1[j] \quad , \tag{5.6}$$

where $y[k]$ is the result of the convolution of the flattened waveform W_{ff} with the box car w_2 wide. This filter is designed to react to wide signals (S2-like), where the content in the narrow box car is typically smaller than the content in wider box car. In the ideal case this filter should be zero in the region close to the maximum of an S1 signal, as almost all the energy underneath W_{ff} is already accounted as the amplitude of filter F_1 at its local maximum. However, in many cases it occurs that in the neighbourhood of an S1 pulse another S1 signal or one or more noise peaks, that overcome the threshold for the flattened waveform, are found. Therefore, in such a case the F_2 filter is not strictly zero as it would be expected in the ideal case, and this must be considered in the S1 and S2 classification logic, as will be described later.

A fourth filter is based on the observation that the scintillation light of the Xe is produced by the singlet and triplet state dimers, respectively with lifetimes of $\tau_{\text{S}} = 2.2\,\text{ns}$ and $\tau_{\text{T}} = 27\,\text{ns}$ [126, 291], which are hardly observable with a sampling rate of 100 MHz. Hence, assuming that the S1 time shape is independent on the amount of deposited energy in the interaction with the LXe for a given drift field E_{d}, and that the observed scintillation tail length is primarily determined by the equivalent electronic chain RC constant and by the recombination time (when $E_{\text{d}} = 0$), it is possible in principle to identify the S1 signals by pattern recognition based on their temporal shape.

To this end a χ^2 filter based on a S1 template T has been developed. It is built for each PMT with a few thousand of S1 signals acquired in a dedicated dataset, where the anode electrode was not biased (floating), and thus no electro-luminescence signal from the drifted electrons could be produced. In figure 5.14 are shown the S1 templates for

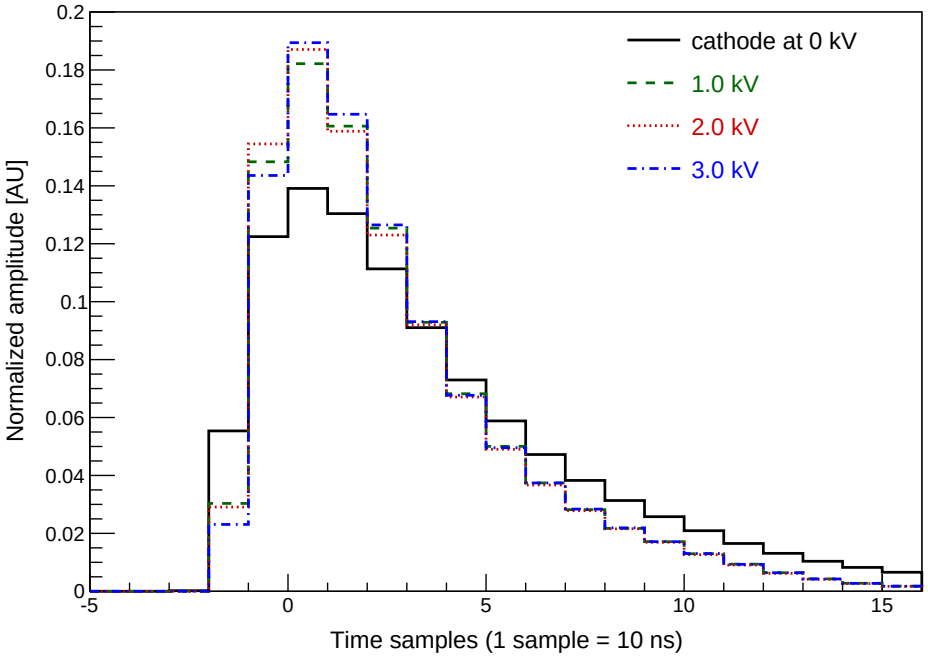

Figure 5.14.: Templates for the S1 signal used in the χ^2 pattern recognition algorithm for different electric fields.

the two PMTs with different drifting field. The S1 template is computed by aligning all the selected signals on the time sample corresponding to the maximum pulse amplitude and normalising each of them by the area computed over a common time interval, in order to remove from them the energy dependence. The template amplitude on each sample is then computed by the median value of all the selected and aligned energy-independent samples. Finally, the template is normalised by its area. In order to build an S1 template with the tail at the right of the maximum bin well determined for at least 100 ns (10 samples), only S1s signals with relatively large amplitude at their maximum (> 20.5 mV) and in temporal coincidence between the two PMTs have been selected. The regions of the waveform W_f more similar to the template T are described by a lower χ^2 value, computed sample by sample as:

$$\chi^2[i] = \sum_{k=-l}^{k=r} \left[T[k] - \widetilde{W}_\mathrm{f}[i+k] \right]^2 , \tag{5.7}$$

where $k = 0$ corresponds to the maximum sample of the template, and $\widetilde{W}_\mathrm{f}[i]$ is the waveform portion overlapped with the template and normalised by its area.

After the filters have been computed, both the $W_{\rm ff}$ and the F_1 filter are convoluted with two Gaussian kernels of unitary area, with a total length l_1 and l_2 and Gaussian width σ_1 and σ_2, respectively:

$$W_{\rm ffs}[i] = \sum_{k=-l_1/2}^{k=l_1/2} G_{\sigma_1}[k] W_{\rm ff}[i+k]; \tag{5.8}$$

$$F_{1\rm s}[i] = \sum_{k=-l_2/2}^{k=l_2/2} G_{\sigma_2}[k] F_1[i+k]\,, \tag{5.9}$$

where the Gaussian kernels are normalised by their area, computed from $-l_i/2$ to $l_i/2$, and the sample $k = 0$ corresponds to their centre. The smoothed versions of the F_1 filter and of the flattened waveform are denoted as $F_{1\rm s}$ and $W_{\rm ffs}$, respectively. They are used for the proper separation of two neighbouring pulses and for the definition of the left and right edges of a specific pulse, as will be detailed in the following.

The first executed module is the *S2 peak finder* that searches for all the S2 signals scanning all the *S2 searching regions*, where one or more S1 or S2 candidates can be found. Because of this they must be isolated by the *S2 pulse separator* module before their classification, starting from the one with the largest peak amplitude (and most likely also the largest area). The algorithm of this module returns a single pulse to be classified by following the F_1 filter on the left and right starting from the local maximum until one of this conditions is verified: I) a local minimum of the $F_{1\rm s}$ is reached; II) the $W_{\rm fs}$ goes below 10^{-3} fraction of its maximum value; III) one edge of the S2 search regions is reached.

An S2 pulse candidate is accepted as a good S2 signal if in correspondence to the time sample k^*, where the F_1 filter has a local maximum (still within the pulse range), the condition $F_1[k^*] < F_2[k^*]$ is verified and the corresponding area, computed from the original waveform, is positive. After this test is passed the similarity test is performed on the S2 candidate. This consists in rejecting the pulse as an S2 signal if the $\chi^2[\hat{i}] < \chi^2_{\rm min}$, where $\hat{i}$ is the sample corresponding to the pulse maximum, and $\chi^2_{\rm min}$ is a minimum threshold (*similarity threshold*), manually optimised for each PMT and loaded from the xml file. In case the χ^2 is found below the similarity threshold over an interval that does not contain the time sample $\hat{i}$, the pulse can still be an S2 signal but it is likely that an S1-like signal is located just few samples in front of the S2 leading edge or just after the S2 tail. Although a missed S1 inside a much larger S2 would bias the area of the latter by a negligible amount, a not identified S1 just before the charge signal, and thus compatible with it, might lead to a wrong reconstruction of the interaction depth in liquid xenon. Hence this S1 signal is separated from the pulse interval by a call to the *S1 pulse separator* module, which is very similar to the algorithm for the S2 separation and will be detailed in the following. Finally, if the S2 candidate is accepted, the corresponding physical and pulse shaping quantities are saved, and the interval corresponding to the pulse is removed from the S2 and S1 search regions by padding to zero the corresponding time samples of the F_1 and F_2 filters. In the opposite case the corresponding interval is removed only from the S2 search regions. Once there are no S2 search regions left in the waveform, the S2 peak finder loop terminates, and the *S1 peak finder* starts to iterate over all the S1 regions to select the S1 signals contained inside. As inside these regions more than one S1 pulse can be found, the *S1 pulse separator* returns a single pulse as an S1 candidate following in this case the $W_{\rm fs}$ filter from the

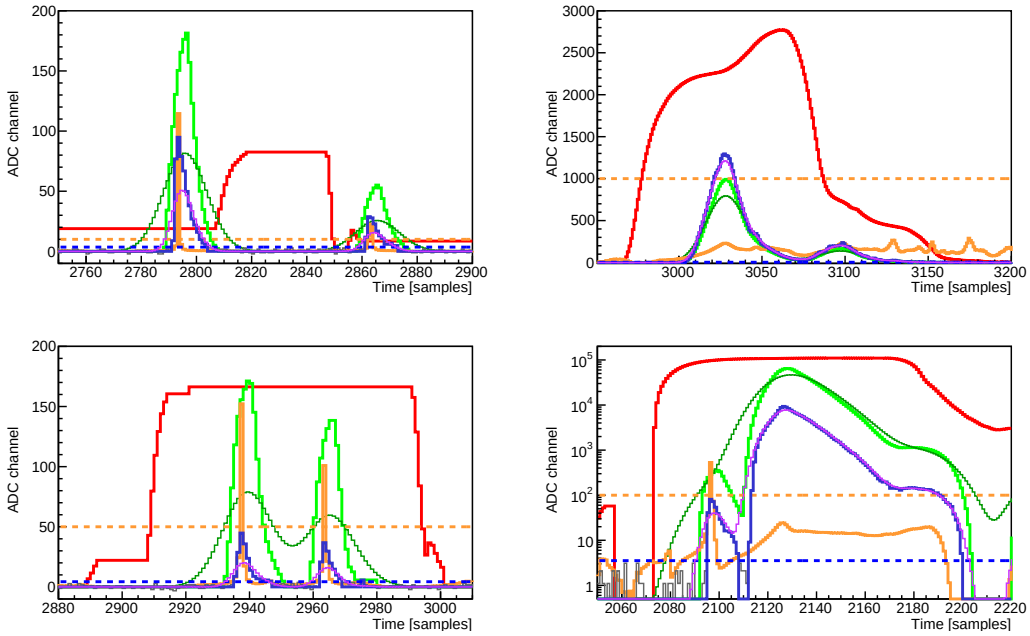

Figure 5.15.: An example of the S1 and S2 search algorithm performance. The top plots are two regions of the waveform displayed in figure 5.12. In the top right diagram the two S1 signals corresponding to two-step de-excitation of ^{83m}Kr decay are identified without the need of the pattern recognition algorithm. On the contrary the bottom left plot is relative to another event where the two decays are closer in time and the second S1 pulse would be misidentified as an S2 signal without the help of the χ^2 filter. In the top right diagram the two S2 signals produced by the ^{83m}Kr decay are separated at the point where the filter F_{1s} (dark green histogram) has a relative minimum. In the bottom right diagram an event from the ^{57}Co calibration is shown where an S1 very close to the main S2 would not be recognised without the pattern recognition algorithm. In this case the waveform interval relative to the S1 signal is removed from the S2 search region using the algorithm for the S1 separation, based on the Gaussian-convoluted version of the flattened waveform (the light violet histogram). This last diagram is shown in logarithmic scale in order to visualise the S1 pulse. In some of the diagrams the red and green filters have been rescaled (by the same factor) visualisation.

maximum to the left and the right. Since the right side of an S1 like signal with respect to its peak is featured by a smooth decreasing tail, on contrary to the left side featured by a sharp rising edge, the conditions to determine the two edges are slightly different. The left edge of the pulse interval is determined by: I) a local minimum of the W_{fs} is found; II) the W_{fs} goes below the 10^{-2} fraction of its maximum value (the value at the start); III) the F_1 is zero (lower edge of the S1 searching region) ; IV) the W_{fs} goes to 0. The right edge of the pulse is given, instead, without the condition (IV) used for the left edge, and by modifying the condition (I) in order to look for a local minimum only if W_f is below the 10 % of its maximum value. Once the interval containing only a single S1 candidate has been obtained, the pulse is accepted if the area computed over the interval using the original waveform is positive. Either the S1 candidate is accepted or not its interval is removed from the S1 search region. The S1 peak finder terminates scanning the waveform when no more S1 search regions are left.

5.4.2 *The processing module for the MPD4 and TAC modules*

This module is executed when the scintillator and/or the TAC module are in-line. The AMP, PSD and TAC signals produced by the respective devices have a square shape with different widths, where all the information is encoded in the amplitudes. For all the three signal types the pulses are taken as the intervals where the flattened waveform W_f is positive. For all of the pulses the maximum amplitude, the area, the beginning and the ending time are saved. In addition, the AMP and PSD signals are checked for time coincidence, which is determined when the intervals of the two pulses overlap with each other.

5.5 LOW-ENERGY ELECTRON RECOIL CALIBRATION WITH A ^{83M}KR SOURCE.

The electronic recoil energy scale of the Xurich II detector is calibrated using the S1 and S2 signals produced in LXe by the ^{83m}Kr decays. This radioactive noble gas is emanated from a ^{83}Rb source embedded inside of ~ 2 mm diameter synthetic zeolite beads (nalsite type from MERK company), featured by a mean porosity of 0.5 nm. The beads are placed inside a vacuum sealed stainless steel chamber, connected to one of the bypasses of the Xurich II gas system, as shown in figure 5.10.The ^{83}Rb source, with an initial activity of 100 kBq, was produced early in 2015 at the Řež cyclotron U-120M of the Nuclear Physics Institute of the Czech Academy of Science.

The source is produced by the ^{nat}Kr (p,xn)^{83}Rb nuclear reactions induced on a pressurised krypton target. The gas is irradiated with $^{-}$H ions with initial energy of 27 MeV degraded down to the $\sim 20 - 25$ MeV energy range after the entrance into the target chamber. Studies of the excitation functions show that for protons in this energy range the production of the ^{84,86}Rb isotopes is minimised, while the ^{83}Rb yield, mostly due to the ^{84}Kr (p,2n)^{83}Rb reaction channel, is around its maximum [292]. After the irradiation, the target chamber is washed with high-purity water, which dilutes the rubidium adsorbed by the metallic surface. The solution is then absorbed by zeolite beads, featured by a mean porosity of 0.5 nm. After the water-rubidium solution is absorbed into the beads, the zeolite is heated to high temperature for several hours letting the water to evaporate out. Some studies showed that this kind of zeolite sieve shows a high chemical retention power for the absorbed rubidium, letting only the ^{83m}Kr to diffuse out of the nanometric sieve structure [289, 293, 294]. This property makes this source particularly suitable for experiments that need low level of contamination from long and medium lived radioactive isotopes. This technique was initially developed to produce a low-energy calibration source for the KATRIN experiment, which attempts to measure the electron neutrino mass by magnetic β spectrometry with ultra low background requirements [295].

The ^{83}Rb decays by electron capture with a half-life $T_{1/2} = 86.2$ d to one of the excited states of the ^{83}Kr . With a probability of $\sim 90\,\%$ the final state of the decay is either the 571 keV or the 562 keV that decay with very short half-life ($\sim$ ps) to the 41.5 keV metastable state of the ^{83m}Kr. The ^{83m}Kr isomer decays with a half life $T_{1/2} = 1.83$ h to the excited state at 9.4 keV by the emission of a γ-ray of 32.15 keV. This state decays with a half-life $T_{1/2} = 156$ ns to the ground level of ^{83}Kr again by γ-emission. However the two γ-rays from nuclear de-excitation are absorbed by the

Table 5.2.: Most prominent decay channels of the 32 keV and 9 keV de-excitations of the ^{83m}Kr sorted by their branching ratio. The CE, A are the conversion electrons and the Auger electrons, respectively, where the sub-shell of origin is indicated. The symbol X stays for the X-ray emission from the atomic relaxation and the subscript indicates the type of transition. This table has been compiled starting from table 2 of [296] and updated with the data of [297], available in the NuDat 2.6 online database [174].

Transition energy	Decay mode	Branching ratio
32.15 keV	$CE_L(30.23\,keV) + A_L(1.5\,keV)$	63.7 %
	$CE_K(17.83\,keV) + X_{K_\alpha}(12.67\,keV) + A_L(1.5\,keV)$	13.8 %
	$CE_M(31.86\,keV)$	10.7%
	$CE_K(17.83\,keV) + A_K(10.8\,keV) + 2A_L(1.5\,keV)$	8.6 %
	γ (32.55 keV)	0.06 %
9.4 keV	$CE_L(7.48\,keV) + A_L(1.5\,keV)$	80.0%
	$CE_M(9.12\,keV)$	12.9 %
	γ (9.4 keV)	5.5 %

atomic electrons with high probability, resulting in emissions of conversion electrons from the K, L, M and N atomic shells, soft X-ras and in particular of the 1.5 keV Auger electron from the L-shell, with a relative intensity of 168%, as summarised in table 5.2. These mechanisms highly suppress the probability of a direct γ-interaction with LXe to a probability of $\sim 0.05\%$ and $\sim 5\%$ for the 32 keV and 9 keV transitions, respectively.

For a noble gas particle detector, designed to be sensitive to low-energy nuclear recoils, the use of the ^{83m}Kr as ER calibration source has some advantages, compared to standard γ-ray sources such as ^{57}Co or ^{137}Cs . The first advantage is due to the low-energy de-excitations, which are located very close to the WIMP search region, and thus address the issue of a proper energy calibration in this energy range. This is possible because the krypton is diffused directly in the LXe target, which addresses the issue of having a uniform calibration free from event localisation systematics. This issue might also be addressed with the ^{131m}Xe ($T_{1/2} = 12$ d) and ^{129m}Xe ($T_{1/2} = 9$ d) isomers, usually produced by neutron activation of ^{nat}Xe in the detector target. The first produces a spectral line at 164 keV while the second de-excites via a fast sequence of γ-emissions at 197 keV and 40 keV ($\Delta t \sim 1$ ns). Because of the typical acquisition rates of the digitisers (100-400 MHz) and the mean de-excitation time of the LXe, it would be very hard to resolve in time the light signals corresponding to the two interactions. All the signals that those two isomers would produce in a LXe detector have, however, the disadvantage of being very far above from the energy region of interest for low-energy nuclear recoils (< 50 keV). In addition, all the three spectral lines are produced with very low branching ratios, which makes impracticable their usage in detectors without low background.

All the issues addressed by the ^{83m}Kr source are particularly important for the a large scale detectors such as XENON1T, for which the calibration of the ERs with external γ-emitter would be a formidable and almost impossible task for at least two reasons. The first is due to the strong attenuation of the γ-radiation in LXe, that implies the use of radioactive sources emitting MeV scale γ-rays (for instance ^{60}Co or

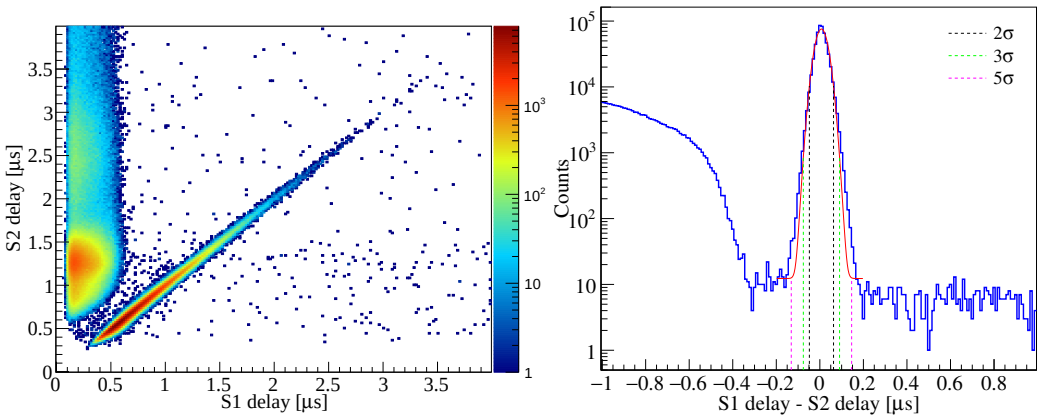

Figure 5.16.: (*Left*) Distribution of the events from a ^{83m}Kr calibration in the (Δt_{S2},Δt_{S1}) parameter space. The events corresponding to the ^{83m}Kr decay are clearly clustered around the $\Delta t_{S2} = \Delta t_{S1}$ line. The population accumulated in the region $\Delta t_{S1} < 0.5\,\mu$s consists of events where the second S1 signal either is a noise peak, an after pulse or a accidental pile-up event not properly rejected by the selection cuts. (*Right*) 1D distribution of the same events on the $\Delta t_{S2} = -\Delta t_{S1}$ axis. The fit is performed with a Gaussian summed with a constant. The black, green and magenta dashed vertical lines define the boundaries of the 2, 3 and 5σ regions of the Gaussian fit, respectively. These regions are used to develop the selections at different purity levels for the class of ^{83m}Kr events which have a double S1 and double S2.

^{228}Th sources) able to penetrate inside the active volume, which would produce signals very far from the relevant energy range. On the other hand the use of γ-emitters with lower de-excitation line, such as the widely used ^{57}Co , would produce energy deposits localised at the edges of the detector and thus not effective for the calibration of a large scale LXe chamber. Hence, after the first successful tests in the small LXe chamber Xurich [289, 290], developed for studies of low-energy Compton scattering interactions in LXe [290], the ^{83m}Kr is now the standard calibration source of many dark matter detectors based on liquid noble gases.

However, the same is true also for small scale R&D detectors like Xurich II , where the horizontal coordinates $(x - y)$ of the interaction vertex are not available and a uniform calibration of the low-energy region the chamber can highly reduce the position dependent systematics. The analysis, that will be shown in the next sections, refers to the calibrations with the ^{83m}Kr source, that where performed during the commissioning of the detector between May and June 2016, prior to the first exposure to the neutron beam. These calibrations were performed at several electric field settings, ranging from $\sim 0.2\,$kV/cm to $\sim 1.1\,$kV/cm.

5.5.1 *Selection of the ^{83m}Kr events*

A set of minimal event selections, tailored to reject those events not fitting the general pattern of a physical energy deposition within the detector volume, are applied for any analysis. The most important of these is the requirement that the main S2 signal should be present in both PMTs and in time coincidence.

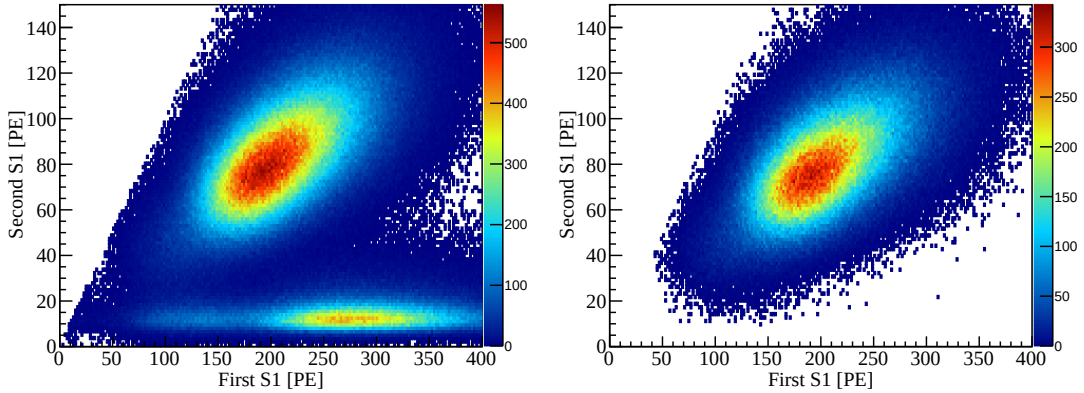

Figure 5.17.: Distribution of the first and the second largest S1 signals before (left) and after (right) the selection criteria defined in figure 5.16 was applied.

Since the two ^{83m}Kr de-excitations are delayed by a mean time of ~ 225 ns, there are two classes of events that can be used. The first class consists of those events where both the S1 and S2 signals are well resolved in time by the peak search algorithm. This class of events is selected by the study of the time delay of the two signals, as shown in figure 5.16, and by observing the high density population around the region defined by Δt_{S2}=Δt_{S1}. Since this population of events is selected based on a feature concerning the decay property of the ^{83m}Kr, it is expected to have a negligible contamination of accidental interactions or of noise events misidentified as an S1 or S2 signal. Hence the events of this class are used to study the light and charge yields for the 9.4 keV and 32.2 keV separately. However, there is a drawback in using this class of events, since the typical width of the charge signals is in the μs range that defines the minimum observable time delay between the two de-excitations. Therefore, for this kind of studies only events in the upper tail of the exponential distribution with $\Delta t_{S1} \geq 1\,\mu$s, corresponding to a fraction 1 %, have been selected. In addition, interactions at the bottom of the TPC are featured by wider S2 signals than those occurred closer to the gate mesh. This effect is induced by the diffusion experienced by the electrons during their drift. Therefore, electron clouds that drifted for longer time in LXe will arrive at the liquid-gas interface with larger the longitudinal dispersions. Hence the selection acceptance of this class of events is expected to decrease with the drift time, as shown in figure 5.19. In order to verify that with these conditions the ^{83m}Kr events are effectively selected, in figure 5.18 is reported the distribution of the delay time between the largest and second largest S1s selected within the $\pm 2\sigma$ region of their distribution (figure 5.16 right). The half-life of the 9.4 keV level is measured by fitting the distribution with a function consisting of an exponential summed with a constant $f(t) = A \cdot \exp(-t/\tau) + C$. The result is $T_{1/2} = (155 \pm 1)$ ns, consistent with the literature value of (156.8 ± 0.5) ns [297].

The second class consists of events corresponding to ^{83m}Kr de-excitation with such a small time delay, that two S1 signals are not time-resolved by the processor, and thus the corresponding S1 and S2 signals correspond to the entire 41.5 keV energy release (hereafter 41 keV signal). The advantage of this class of events is that it is expected to be much more populated than the first class, they are expected to be uniformly distributed along the z coordinate (or in drift time). However, this population is expected to be more contaminated by double scattering interactions or by *pile-up* events. The first

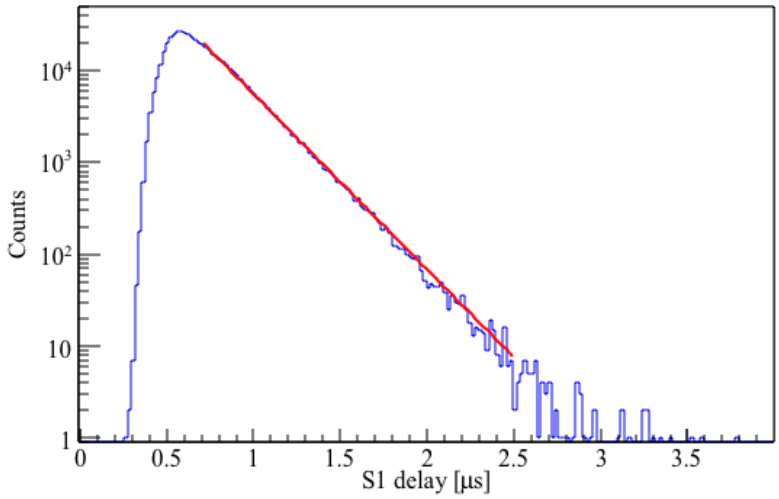

Figure 5.18.: Distribution of the time delay of the prompt scintillation signals from the ^{83m}Kr de-excitations. The half-life of the 9.4 keV level, calculated with an exponential decay summed with a constant background, is $T_{1/2} = (155 \pm 1)$ ns. The range of the fit is taken in order to exclude the region with a lower delays between the S1s, where the roll-off of the efficiency for the S2 time separation would artificially shift the resulting half-life.

kind of events are usually featured by more than one S2 signal compatible with the main S1, and can be rejected by requiring that the second largest S2 is smaller than a threshold in order that only S2 relative to photoionisation of impurities survive as second largest S2. The second kind of events are featured by two or more S1 signals that can correspond to the main S2. The rejection of pile-up events would ideally be performed by requiring that no more an S1 signal is present before the main S2 signal, in a time interval required by an electron to go across the entire interaction chamber. However, this requirement also has some drawback since after the main S1 an *after-pulse*, produced by positively ionised impurities inside the PMTs that drift toward the photocathode, might mimic the S1 of a real interaction. In such a case a genuine single scatter event might be rejected because it is misidentified as a pile-up event, that can lead to a drift-time dependent rejection efficiency.

5.5.2 *S2 corrections and LXe purity*

The ionised atoms, produced by particle interaction with LXe, during their drift travel toward the gate and anode electrodes can be reduced in number by their attachment to electronegative impurities dissolved in liquid. Hence the resulting effect is an S2 signal dependent on the drift time of the electrons, which is undesirable and requires proper corrections. For each electronegative species s dissolved in liquid xenon there are two quantities that influence the surviving probability of an electron cloud: the density ρ_s and the capture rate k_s. Hence the time variation of the electron concentration n_e is given by:

$$\frac{\mathrm{d}\, n_\mathrm{e}}{\mathrm{d}\, t} = -n_\mathrm{e} \sum_s \rho_s k_s = -n_e/\tau_e \,, \tag{5.10}$$

where the index s runs over the chemical species dissolved in LXe and τ_e is the mean electron lifetime in the liquid. Therefore, considering that a number $N_i(0)$ of electrons were initially drifted away from the interaction site, after a time t the number of electrons that survived the capture by electronegative impurities will be:

$$N_{\mathrm{i}}(t) = N_{\mathrm{i}}(0)e^{-t/\tau_{\mathrm{e}}}\,. \tag{5.11}$$

Strictly speaking, the recombination rate $-n_e k_{\mathrm{r}} \rho_{\mathrm{Xe}^+}$ and the neutralisation rate $-n_e k_{\mathrm{n}}$ should also enter in the computation of the electron lifetime [298]. However, since the recombination term takes place only over times 20 ns (depending on the electric field), while the electron drift times for the TPC range from $\sim 1\,\mu$s to $\sim 20\,\mu$s, the method used here for determining the electron life time is not sensitive to the electron recombination. It was observed that the electron neutralisation rate contributes over very short time scales, with the constant k_{n} several order of magnitude lower than the capture rates from the impurity [298].

The most common electronegative impurities that can be dissolved in a LXe detector such as Xurich II are oxygen, water and N_2O.Out of these three species only O_2 and H_2O have been observed with RGA mass spectrometry, always performed before and after the baking of the cryostat prior to filling with liquid xenon. These molecules can be absorbed by the materials during their exposure to air, and then emanated during the operations. Because of the relatively high affinity of LXe with polar molecules,

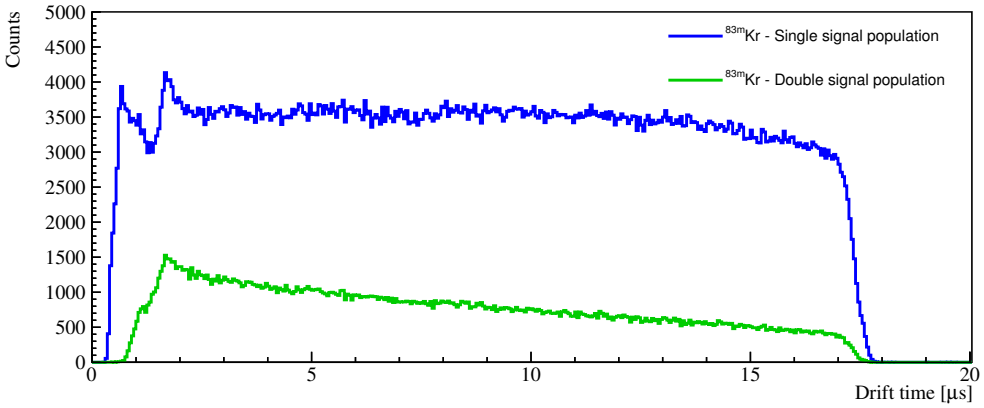

Figure 5.19.: Drift time distribution of events corresponding to the single and double signal population. The negative slope is the effect induced by the lower efficiency of the selection cuts for events coming from the bottom of the TPC. Since during the electron drift the diffusion process takes place, the S2 signals are wider for events with longer drift time. Hence the efficiency of the processor in resolving two charge signals very close in time, as for the case of two-step $^{83\mathrm{m}}$Kr de-excitation, decreases with the drift time. Another feature that can be observed in both the distributions is a peak at a drift time $t_d \sim 1.6\,\mu$s. This most likely corresponds to interactions happening in the proximity of the gate mesh. In this ~ 1 mm region the electric field simulations show a significative deviation from the average field inside the TPC, mostly due to leakage of the electric field from the anode mesh. Events with $t_d < 1\,\mu$s, present only in the single pulse population are relative to interactions happened in the LXe region above the gate. Because of the small drift time, the S1 signal of the 9.4 keV emission is usually hidden inside the main S2 peak, therefore these events are not observed in the double pulse population.

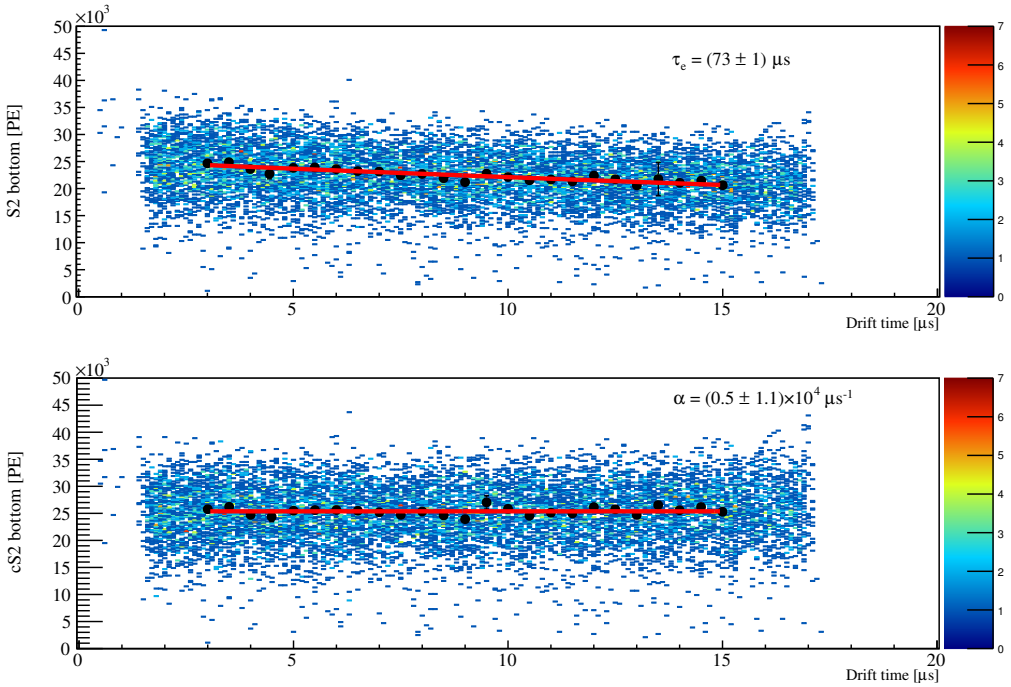

Figure 5.20.: (*Top*) Dependency on the drift time of the charge signal of the 32.1 keV energy emission from ^{83m}Kr decay. This example is relative to a dataset acquired with cathode at 4.0 kV corresponding to a drift field $E_{\mathrm{d}} = (1.26 \pm 0.03)\,\mathrm{kV/cm}$. The x position of the black solid points is determined by dividing in 25 parts an optimal t_d range, which is determined for each cathode voltage setting (in this case from 3 μs to 15 μs) in order to exclude the zones close to the gate and the cathode, where the field significantly deviates from the mean value. For each of the points the mean S2 is determined by a Gaussian fit performed within the ±50 ns around the x position of the data point. Then the electron lifetime is determined by fitting an exponential function to the 25 data points. (*Bottom*) The S2 signal after the correction for the electron lifetime, where the superimposed data points are determined with the same procedure as for the plot before the correction. In order to verify that the correction is properly applied, the data points are fitted employing a function $f(t) = A\exp(-\alpha t)$. The correction is accepted if the obtained value of α is consistent within the uncertainty with the ideal value of 0.

their emanation can be significantly enhanced in the material surfaces in touch with the LXe. However also the components of the gas system can be a significant source of the emanation of electronegative molecules.

Studies of the S2 signal as a function of time were performed by the use of the 32.1 keV and 41.5 keV signals from the ^{83m}Kr decay. In figure 5.20 the dependence of the S2 signal on the drift time is shown for the 32 keV signal. An exponential fit is performed to determine the electron lifetime which is used to compute the corrected charge signal cS2, defined as the S2 signal size if no electron trapping occurred:

$$\mathrm{cS2} = \mathrm{S2}e^{t_d/\tau_e}\,, \tag{5.12}$$

where t_d is the drift time of the event. This correction is applied event by event in analysis stage and is used for the calibration of the energy scales (sections 5.5.5).

The evolution of the electron lifetime over the period of time from May to June 2016 is shown in figure 5.21. An increasing lifetime over the time can be observed as a

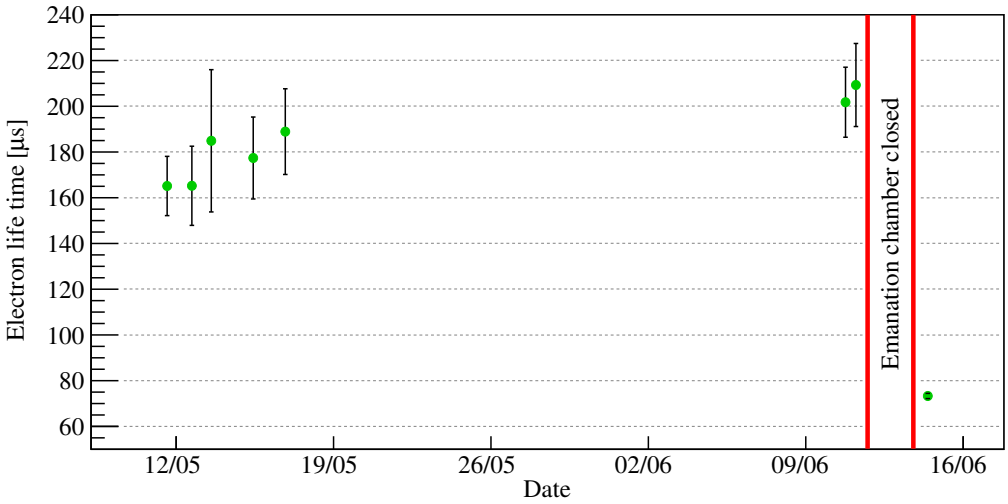

Figure 5.21.: Evolution of the electron life time, during the ^{83m}Kr calibrations of the Xurich II detector during the detector commissioning. The large gap with no data points corresponds to a period of time where no calibration had been performed, but the LXe purification loop was kept active.

result of the continuous purification on this period, when the ^{83m}Kr emanation chamber was always kept open. The electron lifetime measured during this calibration session ranges from $\sim 160\,\mu$s to $\sim 200\,\mu$s, that corresponds to an equivalent O_2 concentration in LXe ranging from $\sim 10^{-9}$ g/g to 8×10^{-10} g/g of O_2 in LXe, where it is assumed an average $k_{O_2} = 0.7\,\text{liter}\,\text{mol}^{-1}\text{s}^{-1}$ (it mildly depends on the field strength) and a LXe density at 184 K of $2.8\,\text{g}\,\text{cm}^{-3}$. Hence the maximum charge attenuation for interactions at the bottom of the drift chamber (drift time $t_\text{d} \sim 15 - 20\,\mu$s) is $\sim 8.5 - 10.5\,\%$. The observed increasing trend of the electron lifetime during this calibration is the consequence of the continuous xenon purification. The last two data points before the vertical red line indicate that the system is close to a steady state, where the rate of purification equals the rate of impurity emanation. The last data point correspond to a dataset acquired with electric field at $\sim 1.2\,\text{kV/cm}$ (cathode biased at -4kV), after that the ^{83}Rb chamber was closed for about a day for a short maintenance operation. The substantial drop of the LXe purity down to $\sim 2 \times 10^{-9}$ g/g O_2 equivalent, is the consequence of the accumulation of the electronegative molecules emanated from the chamber walls and probably water from the zeolite beads.

5.5.3 *Electron drift velocity and position reconstruction*

The z coordinate of an interaction is determined by the product of the drift time and the electron drift velocity. Since this quantity depends both on the electric field and on the LXe temperature, it was measured for Xurich II at the operational temperature of 184 K for drift field values ranging from 0.22 kV/cm to 1.26 kV/cm. The only experimental systematic studies performed in LXe at several available in literature have been performed near the triple point of xenon at $T \sim 163 - 165\,\text{K}$ [299–302]. Since the detector was operated at a temperature $\simeq 184\,\text{K}$, the actual electron velocity in Xurich II might be significantly different from the values present in literature.

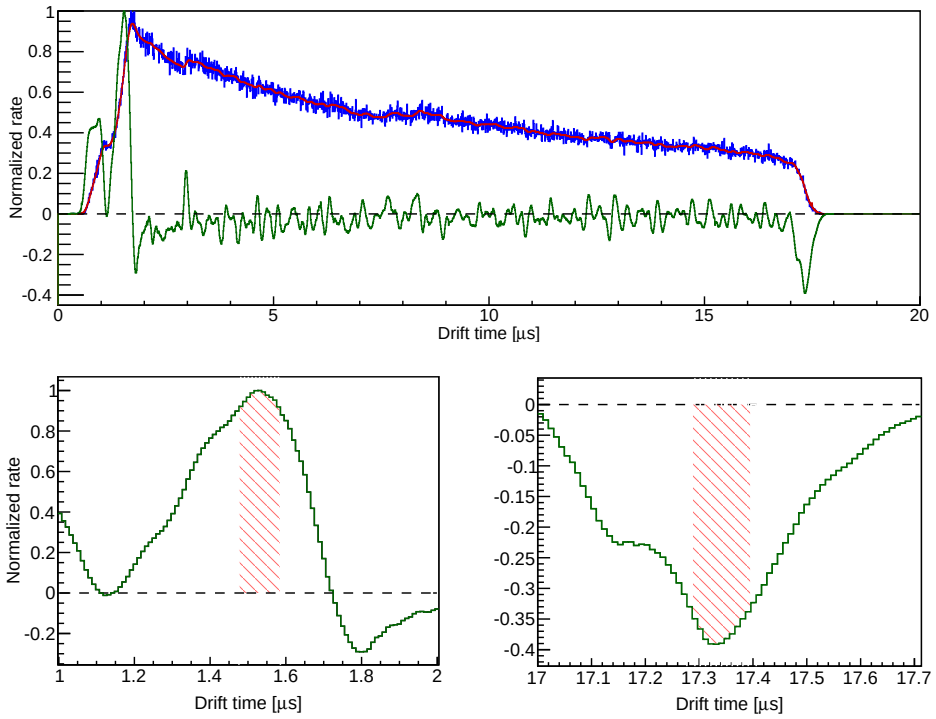

Figure 5.22.: (*Top*) Drift time distribution of the 32 keV signal (blue line) from the double pulse population used to determine the positions of the gate and the cathode meshes. Before the derivative (green line) is computed, the original histogram is convoluted with a Gaussian kernel (red line superimposed to the blue). Both the drift time distribution histogram and the derivative histogram are normalized by their respective maximum absolute values. (*Bottom*) Details of the drift time regions containing the events close to the gate region (left diagram), where the derivative is maximally positive, and the events close to the cathode (right diagram). The gate and the cathode drift times are taken as the drift times corresponding to the maximum and minimum of the derivative, respectively. The uncertainty on meshes position is assumed as half of the shaded regions, that are defined as the regions where the absolute values of the derivatives are above the 90% of the absolute maximum value in the considered region.

The electron drift velocity is determined by selecting the events produced at known positions, namely in the proximity of the cathode and gate electrodes, and by the accurate knowledge of their separation length ($l_d = (31.0 \pm 0.2)$ mm). The drift time corresponding to the cathode mesh is expected to be observed close to the end cut-off of the drift time distribution, where the electric field changes its direction. The same consideration is valid also for interactions in the proximity of the gate mesh, where a sharp rising of the spectrum (or a cut-off going toward smaller drift times) is observed. In figure 5.22 the method used to determine the drift times is shown. Namely the drift time corresponding to the gate is selected as the time where the derivative has the maximum value (positive), while for the cathode the minimum (negative) is chosen. In addition, for each cathode voltage the measurement of the positions of the two meshes is independently performed on the single and double pulse population. This allows for the evaluation of eventual systematics by using two set of events with no elements in common,

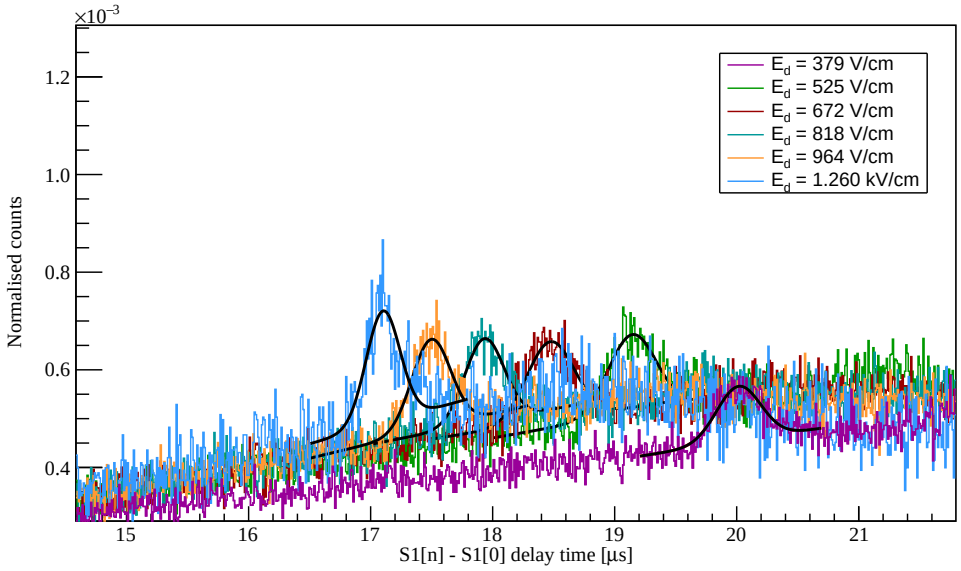

Figure 5.23.: Distributions of the delay times of small signals identified in addition to the main S1 signal for several values of the drift field. Although identified as S1s, many of these signals are actually S2s due to one or a few electrons produced by the S1-induced photo-ionisation of the impurities dissolved in LXe and of the exposed metallic components. In particular on the electrode it is possible to observe those produced on the cathode mesh, which are featured by a well defined drift time (here called delay time), that decreases for higher drift field values. The peak positions are taken from the mean value of the Gaussian function that models the peak. The background, modelled by a first order polynomial, is the effect of requiring that the small signals come after the main S2 signal.

A second method, employed for the consistency control, takes advantage of the electrons produced by the photo-ionisation of the metallic meshes, caused by the main S1 and S2 signals. These photoelectrons will drift, under the action of the electric field, to the gas phase where they will produce the electro-luminescence signal. In figure 5.23 the spectra of the time elapsed from the main S1 and small signals coming after the main S2 are shown for different electric fields. For all the electric fields used for these calibrations, a peak at a particular delay time emerges identifying thus the drift time corresponding to the cathode electrode. The drift time values are obtained by fitting a Gaussian function summed to a linear function, which describes the background. The results, reported in table 5.3, are in excellent agreement with those obtained with the "cut-off method". For the datasets corresponding to low field values, $E_\mathrm{d} = 220\,\mathrm{V/cm}$ and $E_\mathrm{d} = 260\,\mathrm{V/cm}$, the cathode photoelectrons are not observable.

Photoelectrons from the gate electrode are identified with higher order S2 signals and their delay time distribution is shown in figure 5.24. In this case the drift time corresponding to the gate are much smaller compared to those obtained by the former method. This can be explained by observing that gate drift times of $\gtrsim 1.5\,\mu\mathrm{s}$, as obtained by the "cut-off method", would correspond to drift lengths $l_\mathrm{d} > 4\,\mathrm{mm}$, if in the liquid region above the gate, a drift velocity $v_\mathrm{d} > 2.65\,\mathrm{mm}/\mu\mathrm{s}$ is assumed [157, 299, 301] for an electric field $E_\mathrm{d} > 5\,\mathrm{kV/cm}$, as predicted from electric field simulations. Since the gate and the anode grids are separated by 4.0 mm the drift lengths obtained with the "cut-off method" would imply a liquid level above the gate electrode, which

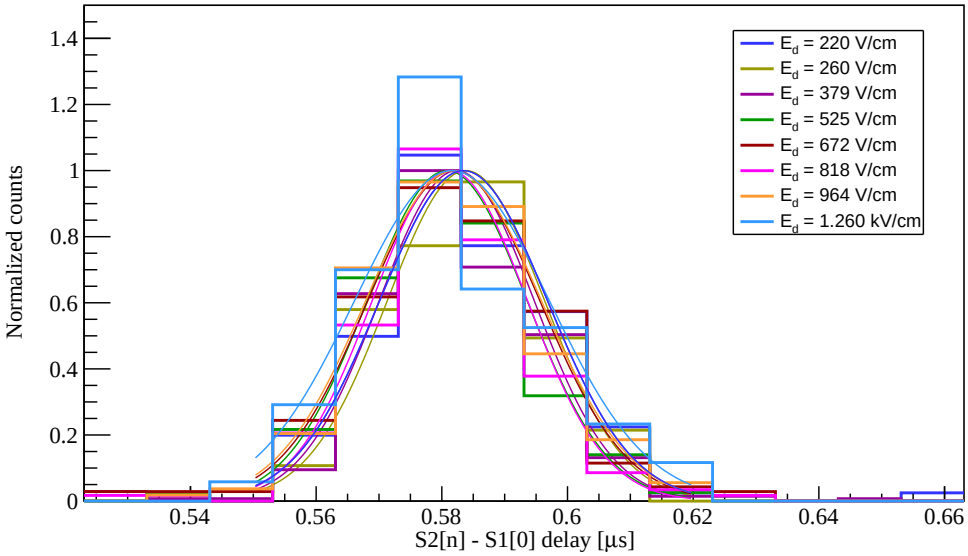

Figure 5.24.: Distribution of the delay time of secondary S2 signals with respect to the main S1. Histograms of different voltages are independently fitted with a Gaussian function, in order to determine the drift time corresponding to the gate mesh. For visualisation purposes the histograms have been normalised by their maximum height inside the fitting interval.

is incompatible with the liquid level measured by the levelmeters and also with the presence of electroluminescence signals. Reversing the argument if a liquid level of 2 mm above the gate is assumed the inferred gate drift time would imply a drift velocity $< 1.3\,\mathrm{mm}/\mu\mathrm{s}$, which also is incompatible with the known values coming from other measurements present at fields $> 5\,\mathrm{kV/cm}$ [157, 299, 301]. From similar arguments the drift time determined by using the gate photoelectrons, implies a liquid level $\gtrsim 1.5\,\mathrm{mm}$, that would be compatible with the operational conditions and would only imply a bias on the level meter readout of $\lesssim 1\,\mathrm{mm}$. These arguments strongly support using this second method for the drift time corresponding to the gate. Additionally, as can be observed in figure 5.24, the gate timing is independent of the electric field in the drifting chamber, which agrees with the expectations as the field above the gate is only determined by the anode voltage.

Table 5.3.: Comparison of the electron velocities obtained with the "cut-off method" and with by using of the photoionisation electrons from the two electrode meshes electrodes. The 1σ spread of the gate and cathode drift times, obtained with the latter method, is assumed as the systematic uncertainty on the measure. The drift velocity is computed assuming a drift length of (31.0 ± 0.2) mm, where the uncertainty is estimated by combining together the components machining tolerances. The uncertainty on the drift velocity is computed by adding in quadrature the uncertainties on the drift times and on the drift length.

Electric field [V/cm]	**Cut-off method**			**Photoionisation electrons**		
	Gate time [μs]	**Cathode time** [μs]	**Drift velocity** [mm/μs]	**Gate time** [μs]	**Cathode time** [μs]	**Drift velocity** [mm/μs]
220 ± 30	1.8 ± 0.1	20.85 ± 0.03	1.63 ± 0.01	0.58 ± 0.01	NA	1.53 ± 0.01
260 ± 30	1.8 ± 0.1	20.64 ± 0.05	1.64 ± 0.01	0.58 ± 0.01	NA	1.55 ± 0.01
380 ± 30	1.7 ± 0.1	19.91 ± 0.05	1.70 ± 0.01	0.58 ± 0.01	20.0 ± 0.2	1.60 ± 0.02
530 ± 30	1.6 ± 0.1	18.96 ± 0.05	1.79 ± 0.02	0.58 ± 0.01	19.1 ± 0.2	1.67 ± 0.02
670 ± 20	1.6 ± 0.1	18.35 ± 0.05	1.85 ± 0.01	0.58 ± 0.01	18.5 ± 0.2	1.73 ± 0.02
820 ± 20	1.6 ± 0.1	17.79 ± 0.07	1.91 ± 0.02	0.58 ± 0.01	17.9 ± 0.2	1.79 ± 0.02
960 ± 30	1.5 ± 0.1	17.34 ± 0.05	1.96 ± 0.02	0.58 ± 0.01	17.5 ± 0.2	1.83 ± 0.02
1260 ± 30	1.5 ± 0.1	16.98 ± 0.09	2.00 ± 0.02	0.58 ± 0.02	17.1 ± 0.1	1.88 ± 0.02

The results of the electron drift velocities are shown in figure 5.25 as function of the drift field in the TPC, and are compared with those present in literature at different temperatures. The comparison of the electron drift velocity with the earliest measurements performed by Miller *et al.* [299] at 163 K and Gushichin *et al.* [301] at 165 K show substantial agreement about the electron velocity dependency on the drift field, that can be well approximated by a power law $v_d \propto {E_d}^{\alpha}$. The systematic lower value of the electron velocity values measured in Xurich II with respect to the measurements performed near the triple point, can be explained by reduction of drifted electrons mean free path induced by the higher temperature [140, 303]. Substantial agreement is also found with the recent measurements of the other LXe TPCs [273, 302, 304], that are all operated at lower temperatures than Xurich II, and thus an higher electron velocity is observed. A remarkable agreement is found with the measurement of the XENON100 experiment [305] which was operated at a temperature just 2 K lower than Xurich II. The behaviour of the measurement at 200 K below 0.1 kV/cm shows an evident turning point and is not with the Xurich II measurements at low field (the lower two data points). At electric fields higher than 350 kV/cm an agreement on the field dependency of the velocity is observed, although at 200 K it was expected to be lower than in Xurich II. However, the electron drift velocity at high fields is also dependent on the concentration of impurities that can modify the momentum transfer and energy transfer mean-free length of the electrons, due to additional scattering centres in the LXe [300]. Hence, a better understanding of the observed discrepancies between the Xurich II and the Gushichin's measurement, requires a full knowledge of the impurities species and their concentration, which are not available in both the cases.

5.5.4 *S1 corrections and light collection efficiency studies*

The size of the prompt scintillation signal S1 is influenced by the TPC internal geometry, the reflection and refraction of light at the boundaries of the LXe with other materials, as well as the light absorption properties; therefore it will be dependent on the interaction position inside the drift volume. Hence, the light collection efficiency (hereafter LCE), defined as the fraction of the primary photons reaching one of the PMT photocathodes, is not uniform across the TPC and must be studied in order to properly correct and reduce the spread of the S1 signals. Since the Xurich II detector is sensitive only to the depth of the interaction vertex, the correction map consists of a function of the single variable z. In order to reduce the spread of the S1 signal for a given interaction, a more suitable quantity, the relative S1 collection efficiency $f(z)$ has been obtained from the data. This position dependent quantity is defined as the ratio between the S1 size at a given z by the averaged S1 over the predefined analysis volume, that in the case of these calibrations is defined by the upper and lower boundaries $z_1 = -5$ mm and $z_2 = -25$ mm, where $z = 0$ corresponds to the gate mesh. Hence the corrected light signals cS1 is defined as:

$$\mathrm{cS1} = \frac{\mathrm{S1}}{f(z)} = \mathrm{S1} \cdot \left[\frac{(z_2 - z_1)\widehat{\mathrm{S1}}(z)}{\int_{z_1}^{z_2} \widehat{\mathrm{S1}}(z')\,\mathrm{d}\,z'} \right]^{-1}, \tag{5.13}$$

where $\widehat{\mathrm{S1}}$ is the size of the prompt scintillation corresponding to a signal with well defined energy within the analysis volume. The fiducial volume has been chosen based

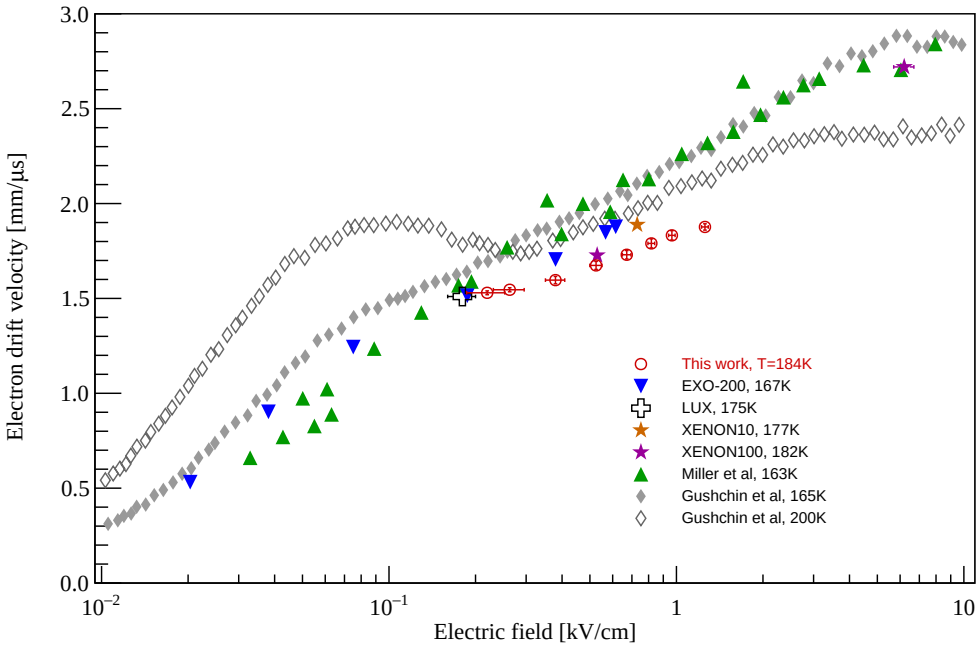

Figure 5.25.: Electron drift velocity measured with the Xurich II TPC as a function of electric field (red open circles). The measurements are compared with data from other authors: Miller *et al.* [299] (green solid triangles), Guschchin *et al.* [301] (solid and open grey diamonds), the EXO-200 experiment [302] (downward solid blue triangles), the XENON10 experiment [304] (solid orange star), the XENON100 experiment [157, 305] (solid magenta star), and the LUX experiment [273] (open black cross).

on the drift field uniformity, that according to the field simulations is $\Delta E_\mathrm{d}/\overline{E_\mathrm{d}} < 1\,\%$ for cathode voltages $\gtrsim 1.0\,\mathrm{kV}$.

The signal correction function has been obtained with the three $^{83\mathrm{m}}$Kr signals: the 32 keV and the 9 keV signals from the high-purity double-pulse population, and the 41 keV from the single pulse population. In figure 5.26 the S1 signal as a function of the depth $(-z)$ before and after the corrections is shown for the 32 keV line with the cathode biased at $-3.0\,\mathrm{kV}$, corresponding to the drift field $E_\mathrm{d} = (960 \pm 30)\,\mathrm{V/cm}$. A Gaussian fit is performed on the S1 distribution in each z slice ($\pm 0.5\,\mathrm{mm}$ around the z point). Its mean value is taken as the S1 mean value at the specific z, and the uncertainty is the statistical uncertainty on the fit parameter. The data points representing the approximation of the function $\widehat{\mathrm{S1}}(z)$ is fitted between the upper and lower boundaries of the analysis volume with a second order polynomial $p(z) = a_0 + a_1 z + a_2 z^2$, which as shown provides an accurate description of the S1 dependence on the interaction depth also outside the z_1 and z_2 volume boundaries. With this parametrisation the mean S1 can be analytically obtained as:

$$\overline{\mathrm{S1}} = a_0 + a_1 \frac{(z_1 + z_2)}{2} + a_2 \frac{z_1^2 + z_1 z_2 + z_2^2}{3}\,. \tag{5.14}$$

Therefore the relative light collection efficiency, shown in figure 5.26, is parametrized by a second order polynomial as well, with coefficients $b_i = a_i/\overline{\mathrm{S1}}$.

Monte Carlo simulations have been performed with the GEANT4 simulation toolkit [202] in order to estimate the position-dependent LCE for the S1 signals across the target

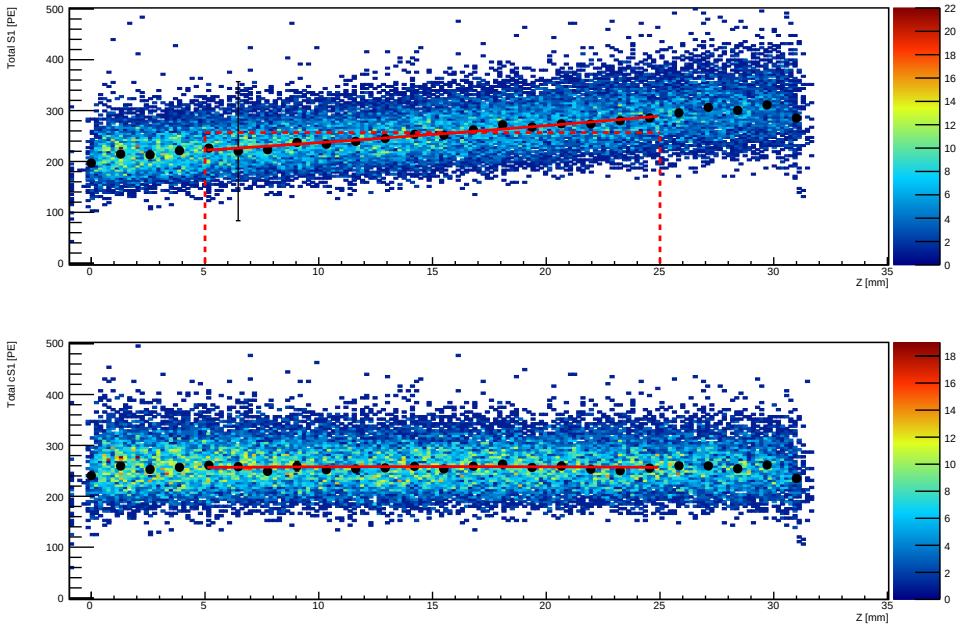

Figure 5.26.: The S1 correction function obtained from the 32 keV line from ^{83m}Kr decay selected from the double-signal population. The black data points are determined by the Gaussian mean after the fit on a slice around the corresponding interaction depth z. The red solid line represents the second order polynomial approximation of S1(z), obtained by fitting the data points. The two vertical dashed lines indicate the z limits where the S1 correction function is estimated and the analysis performed. The red horizontal dashed line represents the mean value of the S1 signal within the analysis range as estimated from the polynomial parametrisation.

volume. The light signals are modelled by generating 1000 photons from 1000000 interaction vertices with $\lambda = 175$ nm. From each primary vertex the photons have been isotropically emitted with random polarisation.

The physical processes, such as light absorption, Rayleigh scattering, reflection and refraction at the surface boundaries, are taken into account in Geant4 for the transportation of optical photons. Each of these processes is encoded in a dedicated class that allows the user to plug the optical parameters for each material of the detector, and thus to tune the outcome of the optical simulations. The assumed parameters for the Xurich II simulations for 178 nm photons are reported in table 5.4.

The LXe refractive index assumed in the simulations is the average value between the two most recent measurements: 1.565 ± 0.008 from [306] and 1.69 ± 0.02 from [307]. The light absorption coefficient in LXe depends on the concentration of the O_2 and H_2O molecules dissolved in the liquid phase, and thus on the efficiency of the gas purification system. As reference for the absorption length, the measurement of 1 m with a 10^{-7} g/g water concentration is considered [308], and an inverse proportionality is assumed for similar or lower LXe purities. For the optical simulations in Xurich II it is conservatively assumed that the O_2 equivalent concentration of $\sim 2.5 \times 10^{-10}$ mol/mol (in section 5.5.2 is given as $\sim 10^{-9}$ g/g), determined by the electron life time measurements, is entirely due to water contamination. Hence, the resulting water concentration would be $\sim 2 \times 10^{-9}$ g/g and thus the assumed absorption length at 178 nm is 50 m. The photon mean free path of 30 cm for the Rayleigh scattering in LXe is taken from the theoretical value calculated in [309], consistent with the measurements reported in [307, 310, 311].

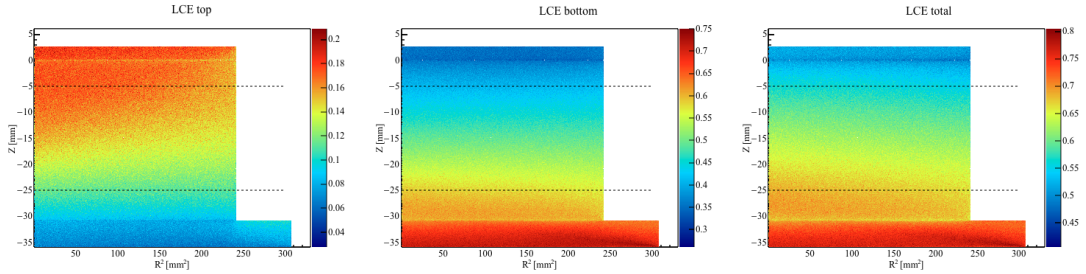

Figure 5.27.: Unbinned light collection efficiency maps for the top (left) and bottom (centre) PMTs, and for their sum (right). The horizontal dashed black lines represent the limits of the analysis volume. The LCE value normalised to 1 is represented by the colour palettes.

The PTFE is the second most important material for the optical simulation as the entire TPC is made entirely of this material and, apart from the optical windows of the PMTs and little cuts for the three electrode meshes no other components are exposed to the scintillation light emitted inside the chamber. This material features a very high reflectivity to VUV light [312], however the reflection properties largely depend on the surface properties after the machining of the components and can range from $\sim 90\,\%$ up to $\sim 99\,\%$. In the Xurich II model for light propagation a reflectivity of $95\,\%$ is assumed, and both the diffusive and specular lobe reflection of the PTFE surfaces are implemented based on the measurements reported in [313].

For the synthetic silica windows of the PMTs only the refractive index is considered, and the value is taken according to measurements reported in [314, 315]. The photocathode is encoded as an aluminium 0.1 mm thick layer on the internal side of the quartz window. In order to simulate a unitary QE the coded photocathode absorption length is much smaller than its thickness (1 nm), and thus it is completely opaque to the photon propagation.

The three electrode meshes are encoded as 0.1 mm thick steel disks, with the optical properties tailored to match the geometrical transparency and to avoid refraction effects. The first task is achieved by setting an absorption length of 1.38 mm that ensures a photon absorption probability of $7\,\%$ along the meshes thickness. The second feature is simply achieved by matching the refractive index of the meshes to that of the surrounding material, namely the GXe refractive index for the anode mesh and the LXe for the gate and the cathode.

In GEANT4 the absorption of a particle (in this case an optical photon) is encoded as a physical process that removes the track corresponding to the particle and releases the energy inside the specific component. Each time a particle[3] is absorbed in one of the two photocathodes the event is recorded together with the information of the PMT where the absorption took place, and will thus contribute to the LCE.

The LCE maps for primary scintillation light, are shown in figure 5.27, where the photons have been uniformly generated in the entire LXe volume using cylindrical coordinates, in agreement with the internal geometry of the drift chamber. From this study it is quite evident that most of the S1 light is collected by the bottom PMT. This is to the internal reflection of light, that occurs at the surface boundary between LXe

3 In GEANT4 each particle is actually called track that contains the dynamic properties of the tracked particle, and what is called particle is actually static collection of the particle properties (eg. mass, charge, etc.).

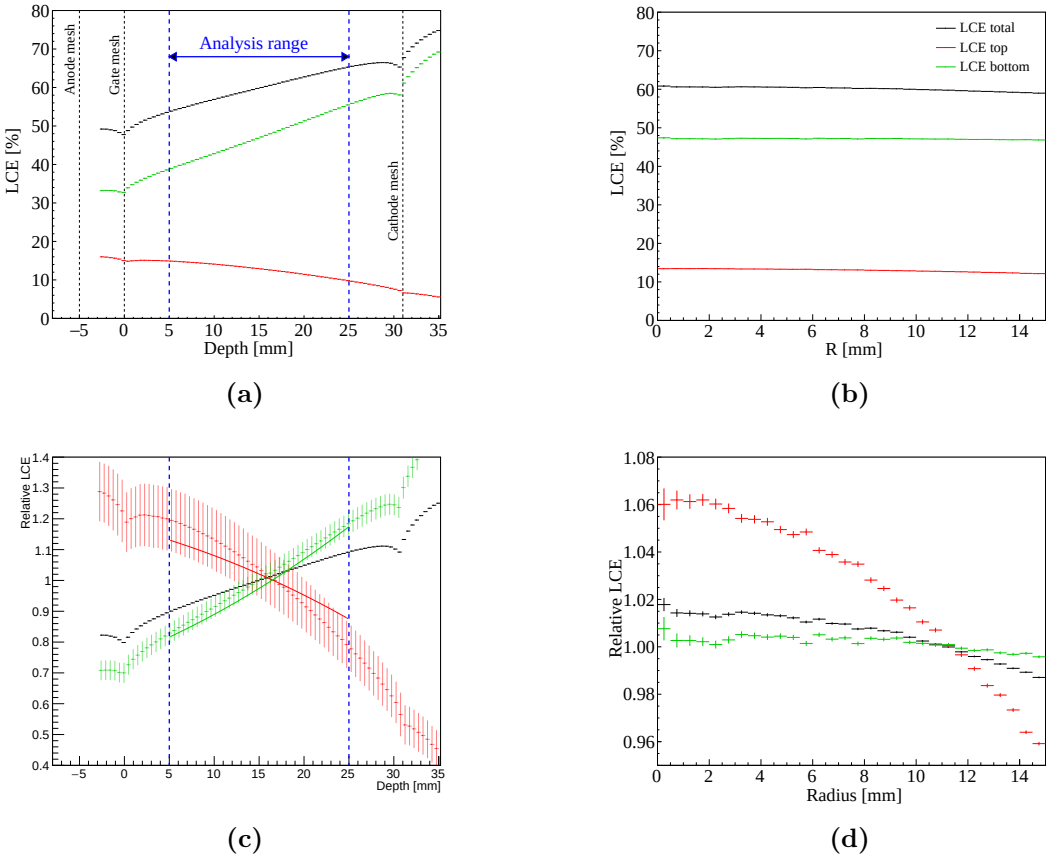

Figure 5.28.: Studies of the mean LCE (a and b) and of mean LCE relative to the volume average value (c and d), as function of the depth below the gate electrode (a and c) and as function of the radial coordinate (b and d). The radial plots have been obtained for the events inside the analysis range with radial slices (the histogram bins) 0.5 mm thick, and the depth-dependent plots have been obtained with z slices 0.5 mm thick. The mean LCE used to produce the relative LCE plots is obtained from the $r - z$ distribution of the LCE (in figure 5.27), considering only events generated in the analysis volume. The vertical bars in each bin represent the standard error on the mean value of the points in the specific z slice. In the bottom right plot the calculation of the mean LCE as a function of depth for the top, bottom PMT, and for the combination of the two. For the relative LCE of the singular PMTs the vertical bars represent the estimation of the relative LCE standard deviation σ for each z slice. These predictions are compared to the $f(z)$ functions for the top and bottom PMTs, as defined in equation 5.13. These functions come from the fits performed on the data, as shown in figure 5.26, and are those used for the S1 corrections. The black histogram represents the prediction of the relative combined LCE, where the vertical bars represent the standard error on the mean for each bin as in the case of the other three plots.

Table 5.4.: List of the most relevant optical parameters encoded in the Geant4 TPC model, used for the simulations of the S1 light propagation and LCE predictions.

Parameter	**Value**
LXe refractive index	1.63
LXe Rayleigh scattering length	30 cm
LXe absorption length	50 m
LXe level above gate mesh	2 mm
Gas Xe refractive index	1.0
Gas Xe Rayleigh scattering length	100 m
Gas Xe absorption length	100 m
PTFE refractive index	1.58
PTFE reflectivity	0.95
Synthetic silica refractive index	1.60
Synthetic silica absorption length	30 m
Photocathode refractive index	1.60
Photocathode absorption length	1 nm
Electrode meshes absorption length	1.38 mm

and GXe as consequence of the higher refractive index of the first medium. This can also be observed in figure 5.28, considering the LCE profile along the z coordinate and the radial coordinate.

The mean LCE values for the top, bottom and the combination of the PMTs are respectively $(12.5 \pm 0.1)\,\%$, $(47.0 \pm 0.1)\,\%$ and $(59.8 \pm 0.1)\,\%$, obtained by fitting a constant function to the unbinned spatial LCE distributions shown in figure 5.27. The uniformity that emerges from the study of the mean LCE dependence on the radial coordinate is remarkable, indicating a variation relative to the mean LCE (decreasing with the radius) of $\sim \pm 5\,\%$ for the top PMT, $\sim \pm 0.5\,\%$ for the bottom PMT, and $\sim \pm 1.5\,\%$ combining the two.

This hypothesis is supported by In figure 5.29, the distribution of the absorbed photon incident angle θ on the photocathodes of each PMT is shown, where the simulations has been performed for different PTFE reflectivity values: 90 %, 95 %, and 99 %. Also from this study it is clear the impact of the internal reflections. For the bottom PMT an increasing quasi-exponential distribution function in $\cos(\theta)$ is observed, which suggests a rather diffused distribution of the photons arriving at the photocathode, that is likely induced by multiple internal reflections. On the contrary the angular distribution of the absorbed photons by the top PMT is more concentrated toward the normal to the photocathode compared to the bottom PMT. The distribution has a sharp drop in correspondence to the critical angle for the total internal reflection from LXe to GXe:

$$\cos(\theta_c) = \sqrt{1 - (\eta_G/\eta_L)^2} \simeq 0.79\,. \tag{5.15}$$

Hence, it is likely that most of the photons reaching the photocathode of the top PMT had no prior reflections on the separation boundary, and unlike for the bottom PMT those photons suffer less from a “memory loss” of the position they originally came

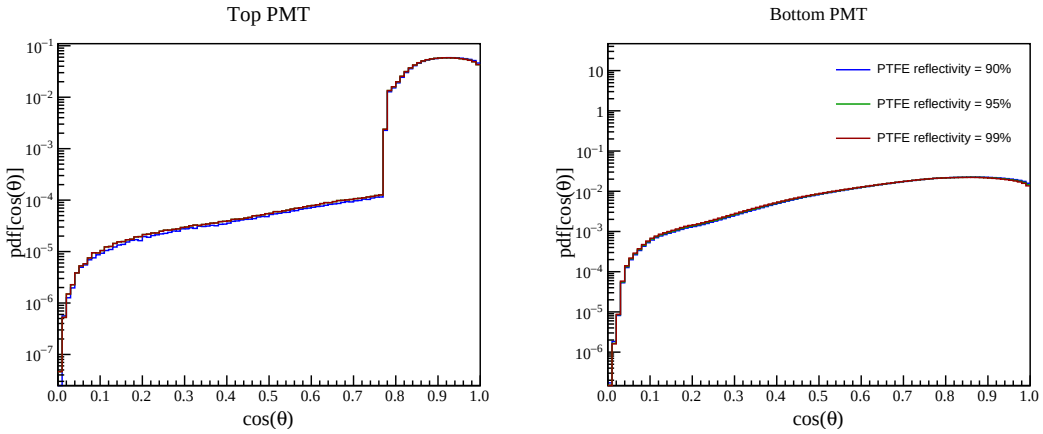

Figure 5.29.: Simulated probability density functions of the photon incidence angle θ when absorbed in each of the two PMTs photocathodes, expressed as a function of the cosine of the angle. The simulations of the pdf have been performed for three different PTFE reflectivity values, which result in three almost perfectly overlapped histograms. The plotted histograms have been obtained selecting events inside the analysis region defined in the text and shown in figure 5.28.

from. The very small fraction of photons with larger incident angle might be explained by the diffusive reflection of photons on the exposed PTFE surfaces in the gas phase. This might also explain the different behaviour of the top and bottom relative LCE as a function of the radial coordinate, observed in the bottom left panel of figure 5.28.

The simulated radial dependence of the relative LCE allows to estimate the uncertainty on the prompt scintillation signals, that comes from the missing radial S1 corrections. If only the bottom PMT is used, the uncertainty should not be worse than $\sim 1\,\%$ of the z corrected signal, while if signals in both the PMTs are used this should increase to $\sim 2\,\%$. This uncertainty can become relatively large, $\sim 10\,\%$ if the light is read by employing only the top PMT, that however is never the case.

The predictions of the relative mean LCE as a function of depth are compared to the fits performed on the data, as shown in bottom right plot of figure 5.28. Within the analysis volume a remarkable agreement can be observed for the predictions of the relative LCE for the bottom PMT, although from the simulations a slight systematic overestimation of this quantity is predicted. Such an agreement provides a further control of the accuracy of the electron drift velocity measurement and of the reconstruction of the z coordinate of an interaction. An agreement is found for the top PMT between the $f(z)$ functions within the $\pm 1\sigma$ of the predictions. However, the latter show a clear steeper decrease of the relative LCE with the depth compared to the fits to the data. The peculiar distribution of the incident angle of the photons absorbed in the top PMT might again explain the observed discrepancy between the data and simulations. A better agreement might be achieved considering the relative quantum efficiency of the PMTs as a function of the photon incident angle in order to correct the simulated relative LCE. As already proved for the XeCube detector [316], taking into account the angular response of the PMTs, typically much higher for smaller incidence angles, can strongly change the predictions of the LCE as a function of the scintillation position. Nevertheless it might also be that some optical details of the components near the top PMT, such as the gate and anode meshes, might play a role, which is not well captured by the way these details are implemented in the Geant4 model of the detector.

5.5.5 *Simultaneous light and charge yields*

The three signals from the ^{83m}Kr de-excitations in LXe feature specific light and charge signal sizes, and the corresponding events can be well-recognised in the S2 versus S1 parameter space. In figure 5.30 the distributions of the energy signals are shown at three different drift fields, where it is possible to observe an almost ellipsoidal distribution of events with a strong anticorrelation between prompt scintillation and ionisation. This is induced by the fluctuations in the electron-ion recombination process and represents a large contribution to the spread of the S1 or the S2 signals. As these fluctuations do not have any effect on the sum of the light and charge quanta $n_{\rm q} = n_{\rm ph} + n_{\rm e} = E/W$, it is possible to define the combined energy scale (CES) which is recombination-independent and will result in a superior energy resolution than using the S1 or S2 signals alone.

The mean S1, and S2 signals corresponding to each energy line are obtained by fitting two-dimensional Gaussian functions to their distributions. The same fits are also employed to obtain other important parameters, such as the 1σ spreads of the S1, S2 and CES energy reconstruction. This is accomplished by repeating the fit of the same peak twice, using the same Gaussian function with two different parametrisations:

$$\begin{aligned} G(x,y) \propto \exp\Bigg[& -\frac{(x-\mu_x)^2}{2}\left(\frac{\cos^2(\theta)}{\sigma_1^2}+\frac{\sin^2(\theta)}{\sigma_2^2}\right) \\ & +\frac{(x-\mu_x)\,(y-\mu_y)\sin(2\theta)}{2}\left(\frac{1}{\sigma_1^2}-\frac{1}{\sigma_2^2}\right) \\ & -\frac{(y-\mu_y)^2}{2}\left(\frac{\cos^2(\theta)}{\sigma_2^2}+\frac{\sin^2(\theta)}{\sigma_1^2}\right)\Bigg], \end{aligned} \tag{5.16}$$

and

$$G(x,y) \propto \exp\left[-\frac{(x-\mu_x)^2}{2\,(1-r^2)\,\sigma_x^2} + \frac{r\,(x-\mu_x)\,(y-\mu_y)}{(1-r^2)\sigma_x\sigma_y} - \frac{(y-\mu_y)^2}{2\,(1-r^2)\,\sigma_y^2}\right], \tag{5.17}$$

where x and y represent the S1 and S2 signals, respectively, and μ represent their mean values. The first of the two parametrisations provides a direct determination of the anti-correlation angle θ, and a direct determination of the major (σ_1) and minor (σ_2) widths, where the latter determines the CES resolution. In the second parametrization of the quadratic form, σ_x and σ_y inside the exponential function are explicit and represent the widths (in PE units) of the S1 and S2 signals, respectively. The parameter $r \in (-1, 1)$ is the correlation factor featuring the combined S2-S1 fluctuations, and assumes the extreme values of ± 1 when all the points fall on the same line, while takes the value 0 when no correlation between the two quantities exists. Since the parameters of the two representations of the fitting function are connected by non-linear functions, this method avoids propagation of uncertainties from one parametrisation to another, which might result in a potential loss of precision. The CES consists, therefore, in the rotation of the S2-S1 parameter space by the angle θ, determined by the diagonalisation of the covariance matrix, and by rescaling of the axis corresponding to the direction of the minor ellipses axis by a factor ν for the conversion from PE to keV units:

$$\mathrm{CES}[keV] = \frac{-\sin(\theta)\mathrm{S1} + \cos(\theta)\mathrm{S2}}{\nu}, \tag{5.18}$$

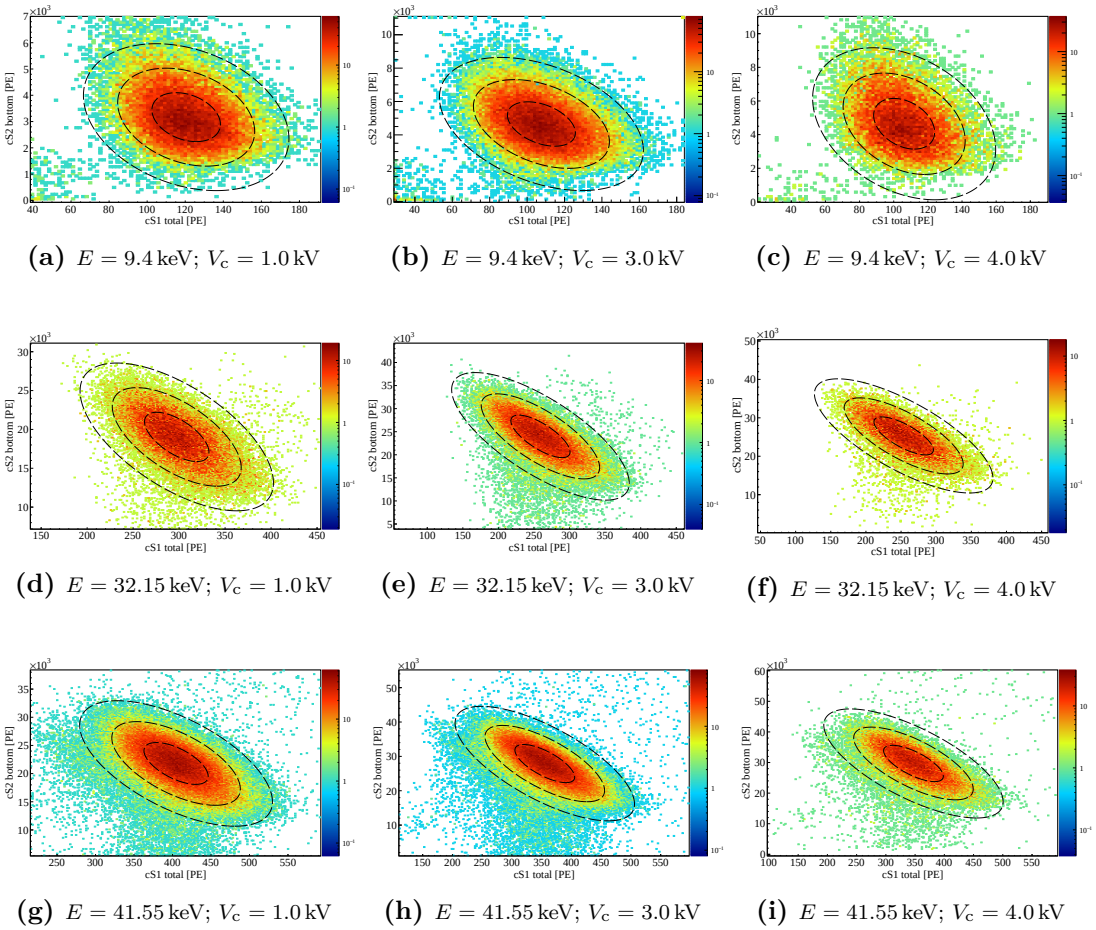

(a) $E = 9.4\,\text{keV}$; $V_c = 1.0\,\text{kV}$ **(b)** $E = 9.4\,\text{keV}$; $V_c = 3.0\,\text{kV}$ **(c)** $E = 9.4\,\text{keV}$; $V_c = 4.0\,\text{kV}$

(d) $E = 32.15\,\text{keV}$; $V_c = 1.0\,\text{kV}$ **(e)** $E = 32.15\,\text{keV}$; $V_c = 3.0\,\text{kV}$ **(f)** $E = 32.15\,\text{keV}$; $V_c = 4.0\,\text{kV}$

(g) $E = 41.55\,\text{keV}$; $V_c = 1.0\,\text{kV}$ **(h)** $E = 41.55\,\text{keV}$; $V_c = 3.0\,\text{kV}$ **(i)** $E = 41.55\,\text{keV}$; $V_c = 4.0\,\text{kV}$

Figure 5.30.: Two-dimensional charge and light distribution of the peaks corresponding to the 9 keV (first raw), 32 keV (second raw), and 41 keV (third raw) signals from the ^{83m}Kr decays in LXe, taken with the drift field at (380 ± 30) V/cm (first column), at (960 ± 30) V/cm (second column), and at (1260 ± 30) V/cm (third column). For each of the peaks the fits are performed with a two-dimensional Gaussian. The background underneath the peaks is modelled by an additive positive constant. The black dashed contours overlapped to the peak distributions are the 1σ, 2σ and 3σ levels of the Gaussian functions.

where the S1 and S2 are the coordinates of the centroid taken from the fit $(\mu_{x,y})$.

The S1 and S2 yields at all drift field settings are plotted in figure 5.31. As expected, the data points fall on a straight line that defines the direction of the recombination process, given by:

$$\frac{1}{W} = \frac{\text{S1}/E}{g1} + \frac{\text{S2}/E}{g2}\,, \tag{5.19}$$

where E is the energy released as an electronic recoil in LXe. The g_1 and g_2 are the conversion factors that give the number of photoelectrons per recombination photon[4] and drifted electron, respectively. These factors are also called amplification factors, and contain the gains of the photosensors, their QE, and the LCE for the S1 and

4 Since the $g_{1,2}$ are built changing the recombination rate by changing the electric drift field, the variation of the S1 signal is actually due to the variation of the number of recombined electrons. Along the rest of the section it is assumed that each recombined electron produces an excited Xe_2^* dimer and that each dimer yields a 175 nm photon.

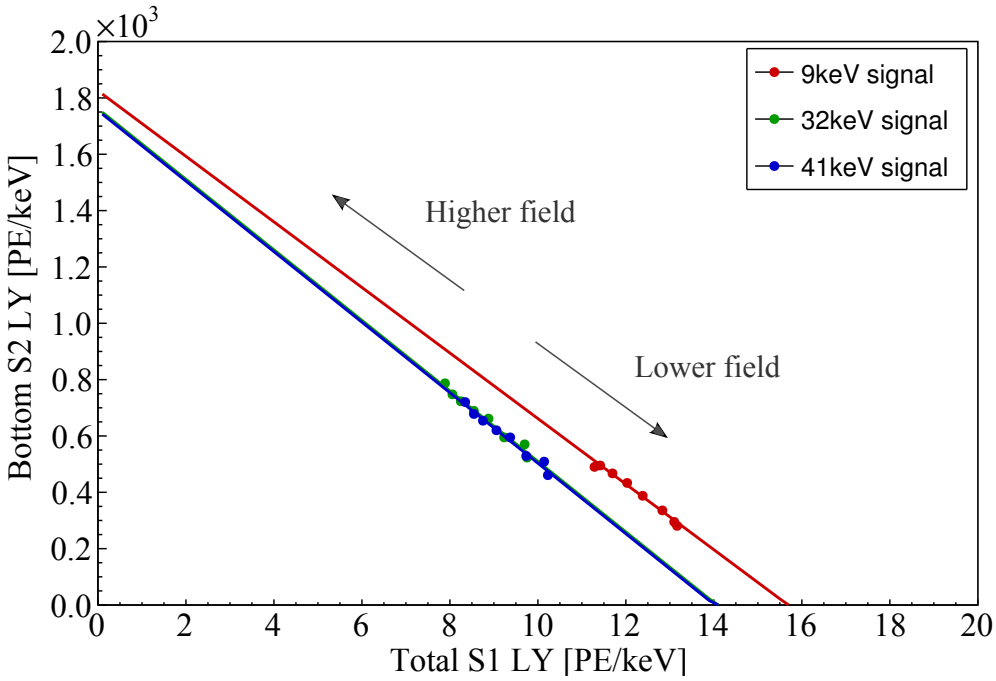

Figure 5.31.: Light yield of the S1 and S2 signals from ^{83m}Kr decay events, at drift fields from 220 V/cm to 1260 V/cm. For each of the energy signals the fit has been independently performed. The x and y intercepts represent the g_1/W and g_2/W values, respectively. Those intercepts values are used for the absolute calibration of the detector by adopting the work function $W = (13.7 \pm 0.2)$ eV reported in [142]. For each datapoint the uncertainties on the S1 light yield are obtained summing in quadrature the statistical uncertainty coming from the fits performed on the peaks and a systematic error on the value coming from the S1 corrections as discussed in section 5.5.4. For the S2 signals the light yield only statistical uncertainties are considered. For both quantities the reported uncertainties are within the data points in this axes ranges.

S2 signals, as well as the electron extraction efficiency and the secondary scintillation photon yield per extracted electron.

The linear fits have been independently performed for each of the three energy signals. The data points for the 32 keV and 41 keV signals fall on the same line with a remarkable agreement, and the fitted lines on the respective data points overlap with each other. This is an expected behaviour as for ERs the number of quanta is known to be proportional to the deposited energy. As the 32 keV and 41 keV events are selected from two non-overlapping populations of events, using cuts based on different criteria (discussion in section 5.5.1), this high agreement also provides a confirmation of substantial absence of systematic errors coming from data treatments. In contrast, for the 9 keV signal this agreement is not observed, resulting in a higher yield of quanta (the distance of the fitted line from the origin of the axis) and in a different slope of the fitted axis.

As the 41 keV signal is composed by the sum of both the ^{83m}Kr de-excitations, it is very unlikely that the observed discrepancy can be explained by a real increase of the quanta yield at 9 keV. Such an effect would also be in contrast with the linear dependence of the total number of quanta with the energy deposited as ERs, verified with increasing accuracy by several experiments performed in the last 4 decades. In

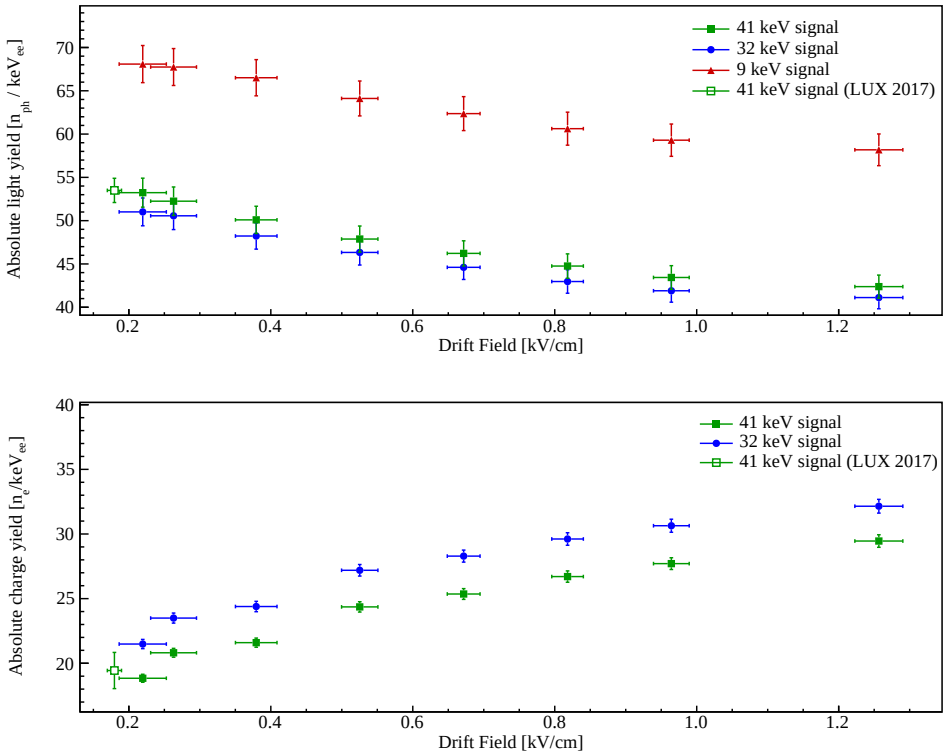

Figure 5.32.: Absolute light (*top*) and charge (*bottom*) yields of the three ^{83m}Kr signals as a function of the drift field. Both yields are compared with the recent data from the LUX experiment at 180 V/cm [317], represented by the open markers. Because of the systematic upshift effect on the S2s of the 9 keV signal detailed in the text, the charge yield for this energy signal is not reported in the bottom plot.

addition, the slope of the axis is dependent only on the detector LCE properties and on the PMTs QE, both included in the $g_{1,2}$ factors. Hence, the only explanation of the observed discrepancy is the presence of a significant systematic effect that artificially upshifts either one of the light or charge signal, or both. The only recognised origin of an artificial S1 upshift is the roll-off of the detection efficiency, which would produce a stronger attenuation of the lower energy tail of the S1 peak distribution, and thus an artificial upshift of the peak centroid. However, the effect of the efficiency roll-off is usually present at the level of a few PE (depending also on electronic noise conditions), and thus it is very unlikely that it can play any role for the 9 keV S1s, corresponding to $\sim$ 100 PEs signals. Hence, the corresponding S1s might still be considered a valid standard candle for the calibration of the Xurich II prompt light response, and the observed systematic effect is most likely coming from a systematic upshift of the S2 signal. The origin of this has been identified in the contamination of the 9 keV S2s caused by two effects: the presence of the trailing tail of the 32 keV S2 pulse underneath the following S2 signal, and the contamination from spurious extracted electrons, originated from photoionisation of the gate electrode and of the LXe impurities following the strong 32 keV proportional scintillation.

Given the high accuracy of the S2 versus S1 light yields for the 32 keV and 41 keV energy signals, their data points have been merged and fitted all together with a linear function in order to obtain the $g_{1,2}$ factors. Assuming a mean work function

$W = (13.7 \pm 0.2)$ eV [142], the obtained values for the amplification factors are $g_1 = (0.191 \pm 0.006)\,\mathrm{PE/n_{ph}}$ and $g_2 = (24.4 \pm 0.4)\,\mathrm{PE/n_e}$. This allows to perform a calibration of the prompt and proportional scintillation signals in absolute number of quanta $[n]$[5]. The absolute light and charge yields as a function of the drift field are shown in figure 5.32. The evaluation of the uncertainty on each of the quantities has been performed by summing in quadrature the statistical uncertainties (from the fits) with the linear propagation of the W uncertainty (from literature). Both the absolute yields for the 41 keV energy signal are found to be in good agreement with the same measurements performed at 180 V/cm by the LUX experiment [317].

It is important to note that the direction ϕ the recombination process is determined by:

$$\tan(\phi) = -g_2/g_1\,, \tag{5.20}$$

that is relatively close to the direction of the ellipse major axis θ defined by:

$$\tan(2\theta) = \frac{2\mathrm{Cov}(\sigma_{S1}, \sigma_{S2})}{(\sigma^2_{S2} - \sigma^2_{S1})}\,, \tag{5.21}$$

and directly obtained from the fits of the energy peaks in the (S1,S2) space, using the parametrisation defined in equation 5.16. This is shown in figure 5.33, where at each field the ellipses major axis is significantly steeper than the axis slope determined by the g_1 and g_2 factors. This feature can be explained by observing that the direction θ is defined by widths of the fluctuations around the mean values $\langle S1\rangle$ and $\langle S2\rangle$. Hence the direction depends both on the fluctuations produced by the recombination process and on those dependent on the response properties of detector and of the photosensors. On the other hand the direction ϕ is determined only by $\langle S1\rangle$ and $\langle S2\rangle$ values at different drift fields, which depend only on the recombination rates and not on the event by event fluctuations.

The macroscopic anticorrelation of light and charge signals for the three ER signals from ^{83m}Kr de-excitations is shown in figure 5.34, where the y axis is in relative units that allow, independently from the actual W value and from the $g_{1,2}$ factors, for the study of the recombination process as a function of the drift field and for the comparison with studies performed with other detectors. In the same plot the data has been compared with that from Manalaysay *et al.* [289], performed with the Xurich I detector, and a very good agreement can be observed for the normalised charge yield of the 41 keV signal. For the scintillation signals at 9 keV and 32 keV a systematically higher scintillation yield is observed with respect to the cited work. Since no zero field measurements have been performed for this set of ^{83m}Kr calibrations of the Xurich II detector, the relative light yield from Manalaysay [289] had to be converted to the light yield normalised to the maximum theoretical light yield (or total number of quanta). In the cited publication the reported LYs at zero field for the 9 keV and 32 keV signals are (6.76 ± 0.06) PE/keV and (6.43 ± 0.06) PE/keV, respectively. However no values for the I_{S1} quantity were reported (the maximum theoretical S1 signal if all the electrons recombined with the ions). Since this quantity was necessary for the comparison with

5 Since it is assumed that each recombined electron produces a photon, $[n_{ph}]$ and $[n_e]$ are equivalent units, and only one unit $[n]$ can be assumed.

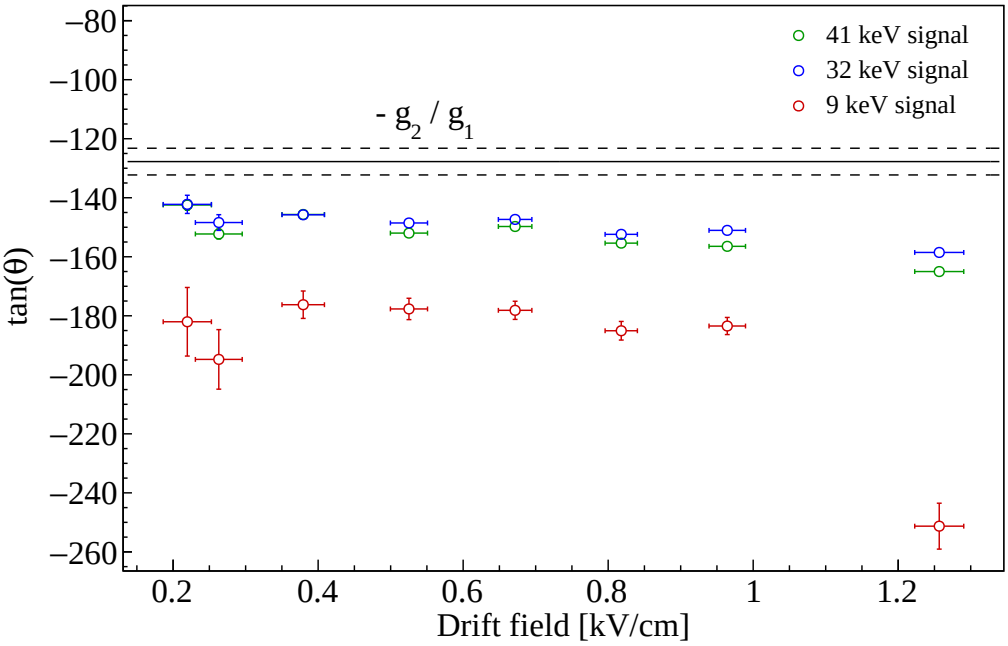

Figure 5.33.: Comparison of the directions of the anticorrelation of the S1 and S2 signals, for all the signals from the ^{83m}Kr decays and at all the fields used in this study. The values are obtained from the fits of the energy peaks in the (S1,S2 space). The black solid line is the direction determined by the g_1 and g_2 calibration factors, which defines the direction of the S1 and S2 variations determined by the recombination process alone.

the Xurich II data of figure 5.34, it was obtained by a fit on the data points of figure 8 of [289]. From this limited re-analysis it was possible to estimate $I_{S1} = (336 \pm 6)$ PE, and thus a $\mathrm{LY}^{(\max)} = (8.1 \pm 0.1)$ PE/keV (calculated for the 41 keV energy signal). With the estimation of the maximum theoretical light yield, the relative light yields in figure 7 of [289] have been multiplied by the ratio $\mathrm{LY}^{(0)}/\mathrm{LY}^{(\max)}$. On the contrary, the transformation of the charge yield to the units used in figure 5.34 was much easier as $n_\mathrm{e}/(n_\mathrm{e}+n_\mathrm{ph}) = Q(E_\mathrm{d}/Q_0)/(1+\beta)$, where Q_0 is the maximum collectable charge and $\beta = 0.06$ as for the measurements of this work. Hence, the discrepancy of the normalised light yields might originate from an unrecognised systematic in the re-analysis of the data published by Manalaysay *et al.* with the Xurich I detector.

The normalised light and charge yields of each line are well described by the Thomas-Imel recombination model [318]:

$$n_e(E_\mathrm{d}) = N_\mathrm{i}\,(1-r) = N_\mathrm{i}\frac{\ln(1+\xi)}{\xi}\,, \tag{5.22}$$

where r is the fraction of electrons that recombine with the ions, $\xi = N_\mathrm{i}\alpha a^{-2}/4v$, α is the volume recombination rate in the Langevin model, a is the spatial dimension of the box where the recombination takes place, and v is the electron velocity inside the box. As will be detailed in the next section, the fits to these data were performed based on Dahl's studies of the electron-ion recombination process at low energies [142].

The resolutions of the S1, S2 and CES are shown in figure 5.35 for all the three energy signals at 960 V/cm. In figure 5.36 the resolutions from the three channels are shown

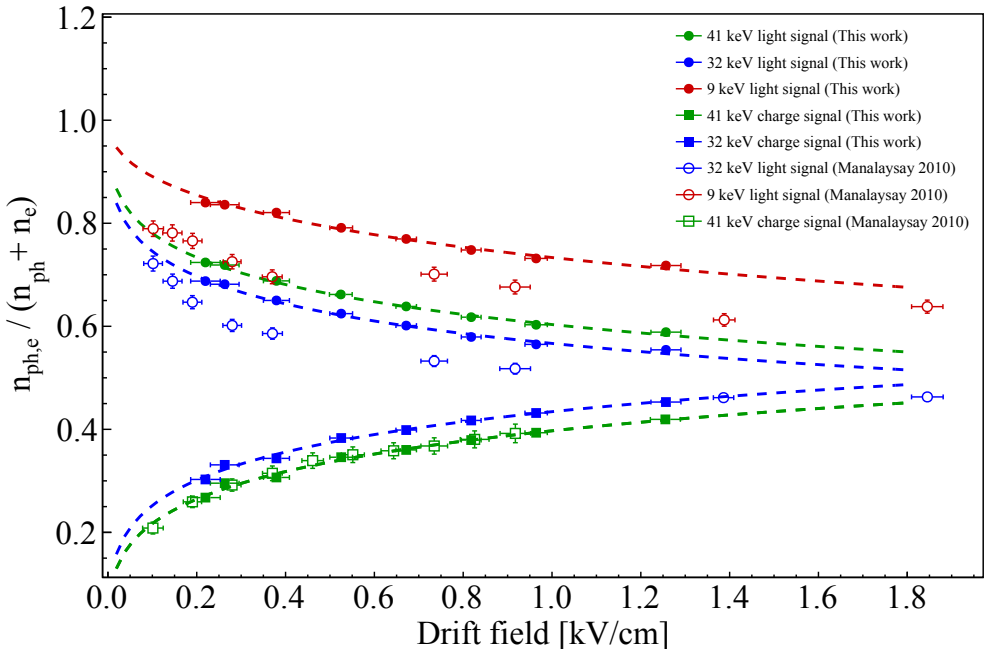

Figure 5.34.: Macroscopic anticorrelation for the light (circles) and charge signals (boxes) of the 41.5 keV (green) and 32.15 keV (blue) energy releases from ^{83m}Kr decay. For the 9.4 keV (dark red) energy release only the light yield dependence is shown. The hollow symbols are data points of the ^{83m}Kr calibrations of the Xurich I detector extracted from the digitisation of the figures 7 and 8 of [289]. Since the light yields where reported relative to the zero-field conditions ($S_r(E)/S_{r0}$) and the charge yields relative to the quantity n_e/N_i, assuming $\beta = 0.06$, a rescaling of these quantities (detailed in the text) was necessary in order to express them relative to the total number of quanta $n_e + n_{ph}$. The uncertainties on these quantities might be larger than the original values. This is because they had to be re-estimated from the figure 7 of the paper and from a new fit of the data points in figure 8 (analogous to figure 5.31 above), performed in order to get the $I_{S1,2}$ values (the intercepts with the x and y axis), not reported in the text. As the error bars of many of the data points are smaller than the marker, half of the marker size was conservatively assumed as uncertainty of the digitised point.

as function of the drift field, where the resolution improvement in using the CES is evident.

For the two largest energy signals a slight degradation of the S1 and S2 resolutions is observed with the increase of the drift field, while for the 9 keV signal the dependence is rather flat, especially for the S1 channel, which should not be affected by systematics. The relatively large fluctuations of the S2 resolutions for the 32 keV signal are associated to the data points featured by higher uncertainty. However, the same behaviour is not observed for the 41 keV signal, which shows smaller fluctuations and smaller uncertainties. The smaller statistics of the data sets corresponding to the data points with highest fluctuations, might provide an explanation of the higher uncertainty that was observed. However, this would hardly explain why these data points show larger fluctuations of S2 resolution, always towards smaller values. As expected from theoretical considerations, the resolution of the CES is not only much better than for the S1 and S2 alone, but is also independent from the drift field.

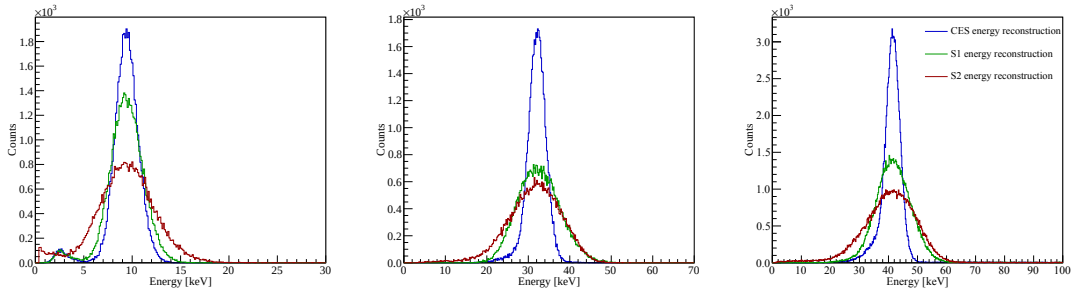

(a) 9.4 keV signal **(b)** 32.15 keV signal **(c)** 41.55 keV signal

Figure 5.35.: Light, charge and combined, energy spectra of the three ^{83m}Kr energy signals at electric field 960 V/cm.

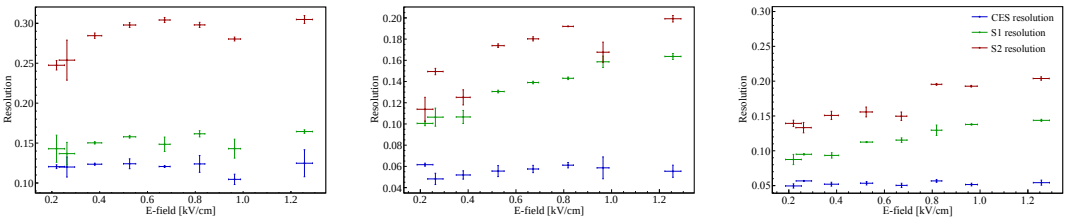

(a) 9.4 keV signal **(b)** 32.15 keV signal **(c)** 41.55 keV signal

Figure 5.36.: Field dependence of the energy resolution of the light, charge and combined signals from the ^{83m}Kr decay events. The resolution is defined here as the ratio of the σ to the mean as obtained from the fits performed on the two dimensional distribution of the energy peaks.

From a first glance to the S1, S2 and CES spectra for the three energy signals, it is possible to observe that spectra of the light and charge channels are not only much broader than the CES, but they result also in a strongly non-Gaussian shape. Although the causes for this behaviour are not yet entirely clear, it is likely that the distribution and the spread of the S1 and S2 signals are not due to only the recombination fluctuations projected on the respective axis, but also to the effect of the event-by-event fluctuations of other quantities, such as the S1 and S2 LCEs variation on the coordinates of the event interaction, and on the PMT gains. In addition to these "instrumental" effects, the PMT QE, the LCEs, the electron extraction efficiency, and the proportional scintillation yield, all determine a sequence of statistical fluctuations that contribute to the final shape and width of the S1 and S2 spectra.

In figure 5.37 the covariance of the light and charge signals as a function of the recombination is shown on the top panel for the 32 keV and 41 keV energy signals. As it is a negative quantity, its sign has been inverted in order to emphasise the magnitude, which has been normalised by the total number of quanta to make an energy independent study, as will be shown in the next section. In the bottom panel of same figure the correlation factor between $n_{\rm ph}$ and $n_{\rm e}$ for the same energy signals, is plotted as a function of the applied drift field. The ordinate of each data point is obtained by the parameters determined by the fits performed on the energy peaks in S2-S1 space:

$$-\mathrm{Cov}(n_{\rm ph}, n_{\rm e}) = \frac{1}{2}\left[\mathrm{Var}(n_{\rm ph}) + \mathrm{Var}(n_{\rm e}) - \mathrm{Var}(n_{\rm ph} + n_{\rm e})\right] , \tag{5.23}$$

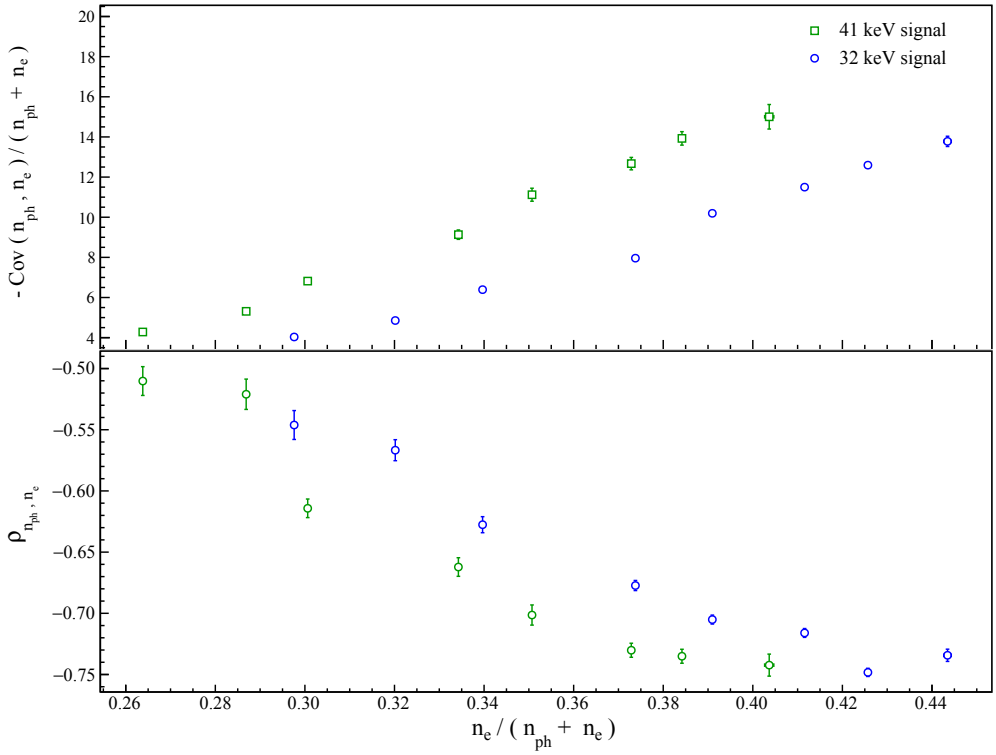

Figure 5.37.: (*Top*) Event by event covariance absolute value of the light and charge signals expressed in quanta units and normalised by the total number of quanta. The covariance has been obtained with the equation 5.23. (*Bottom*) Event by event correlation of the light and charge signals as obtained by the 2D fits using the parametrisation of equation 5.17.

where all the quantities have been converted in quanta units. As already observed in the plots of figure 5.32, the presence of the 9 keV de-excitation within the 41 keV signal determines the shift of the data points for this energy signal towards higher recombination rates (the left direction) with respect to the data points relative to the 32 keV line. In addition, for the same recombination rate the covariance relative to the 41 keV signal results ~ 1.5 times higher than that of the 32 keV signal. The reason for this behaviour must again be identified in the composite nature of the 41 keV signal.

5.5.6 *Discussion*

The data analysis presented in the previous sections provided full characterisation of the Xurich II TPC response down to a few keV energy deposits. In particular, the features offered by the ^{83m}Kr source allowed for a thorough study of the most fundamental parameters of the detector with an excellent control of the systematic effects.

The main achievement was to develop a detector with a LY high enough to detect the luminescence of nuclear recoils with energies < 5 keV. The sensitivity to the prompt scintillation, featured by the Xurich II detector, is only about 2 times lower than the single phase LXe detector developed by Plante *et al.* at Columbia University, which provided one of the first high-accuracy studies of the L_{eff} parameter for nuclear recoils with energies down to 3 keV [268,316]. Hence, the Xurich II detector improves the light

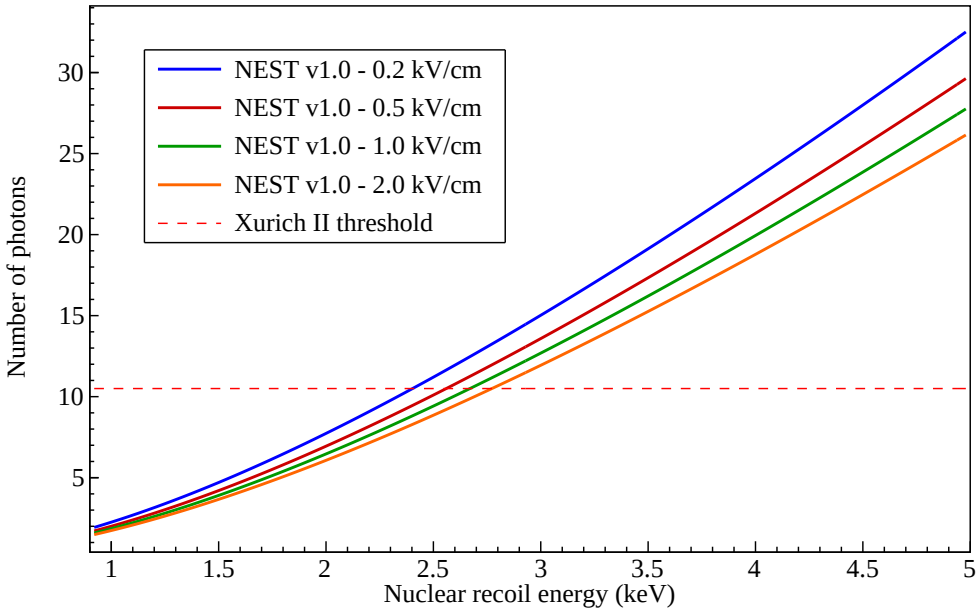

Figure 5.38.: Estimation of the Xurich II energy threshold to NRs corresponding to a typical analysis threshold of 2 PE. This threshold, converted to the absolute number of primary scintillation photons, is represented by the red dashed line. The four curves are represent the energy dependence of the average number of emitted photons, for some selected drift fields, as predicted by the NEST code [281, 319]. The intercept between this function and the Xurich II analysis threshold roughly corresponds to the energy threshold for NRs.

yield with respect to its predecessor Xurich I [289], designed for the study of low-energy Compton scatterings [290], roughly by a factor 12.

The absolute calibration of Xurich II can be exploited to obtain a preliminary prediction of the potential of this detector for the detection of low-energy NRs. The energy threshold can be roughly estimated using the predictions of the NEST model, that provides a description of absolute light and charge yield for both ERs and NRs [281, 319]. A typical S1 analysis threshold is ~ 2 PE, that for the Xurich II TPC corresponds to a mean number of ~ 10.5 primary photons. In figure 5.38 the predictions of the number of luminescence photons emitted in LXe by a NR interaction are shown for selected fields. Hence, the minimum number of detectable photons translates to an energy threshold for NRs varying between ~ 2 and ~ 3 keV, depending on the drift field. However, because of the event-by-event fluctuations originating from the recombination process, the photon yield has a natural spread that should be properly considered for an accurate threshold determination.

The electron-ion recombination process for ERs with energies $\lesssim 20$ keV is well described by Thomas and Imel model [318], while above this energy a better description is provided by the Birk's model modified by Doke [136]. Both models are based on the same physics, however the former assumes that the recombination takes place in a boxed region, while the latter considers an extended column of electron-ion pairs. As shown in table 5.2, both ^{83m}Kr de-excitations produce a mixture of conversion electrons, Auger electrons and low-energy X-rays, which are all in the Thomas-Imel region. A thorough study of the electron-ion recombination processes, based on simu-

lations of low-energy ER tracks using the PENELOPE code [320], was performed by Dahl [142]. It was observed that the scaling of best fitting box dimension is given by $a \propto E_{\mathrm{d}}^{-\gamma}$, with $\gamma \simeq 0.5$, corresponding to the typical scaling of an electrostatic length. In addition, the magnitude of the parameter a was found between the Onsager radius, $r_c = e^2/4\pi\epsilon(K_{\mathrm{B}}T)$, inside which the ion field is dominant and the electron undergoes recombination, and $R_F = \sqrt{e/4\pi\epsilon E_{\mathrm{d}}}$, beyond which the drift field is stronger than the ion field. The difference between the original box model and its modification by Dahl is the interpretation of these two parameters. Thomas and Imel consider the entire ionisation and recombination process happening inside a box with linear dimension $2a$, where the electrons are drifted away with a velocity $v = v_d = \mu_{e^-} E_{\mathrm{d}}$, where μ_{e^-} is the linear electron mobility. Hence, the field dependence of the recombination is given by the scaling law $\xi \propto E^{-1}$, which was assumed in [289]. Those two arguments lead to reinterpret a as an effective field-dependent linear size of the recombination volume, inside which the electron motion is predominantly diffusive. Hence, v is reinterpreted as an effective diffusion velocity, that determines the typical time that the e^- spend in the recombination region.

Motivated by the Dahl's reinterpretation of the Thomas-Imel model, the fits of the macroscopic anticorrelation have been performed using the parametrisation $\xi = a_0 E_{\mathrm{d}}^{-\gamma}$, leading to:

$$\frac{n_{\mathrm{e}}}{n_{\mathrm{ph}} + n_{\mathrm{e}}}(E_{\mathrm{d}}) = \frac{N_{\mathrm{i}}}{N_{\mathrm{ex}} + N_{\mathrm{i}}}(1 - r) = \frac{1}{1+\beta}\left(\frac{\ln(1+\xi)}{\xi}\right), \tag{5.24}$$

$$\frac{n_{\mathrm{ph}}}{n_{\mathrm{ph}} + n_{\mathrm{e}}}(E_{\mathrm{d}}) = \frac{N_{\mathrm{ex}} + rN_{\mathrm{i}}}{N_{\mathrm{ex}} + N_{\mathrm{i}}} = \frac{\beta}{1+\beta}\left[1 + \frac{1}{\beta}\left(1 - \frac{\ln(1+\xi)}{\xi}\right)\right], \tag{5.25}$$

where the electric field is expressed in kV/cm units. The free parameters of the fit are a_0, which contains the energy dependence of the model, and the exponent γ, that allows for a general power law dependence of the recombination fraction on the drift field. The parameter $\beta = N_{\mathrm{ex}}/N_{\mathrm{i}}$ is the ratio of direct excitons number to the ion-electrons number, and is fixed to 0.06 according to theoretical predictions [143]. The fits have been independently performed on each signal energy and signal type, and the results are presented in table 5.5. For the ER energies produced by the $^{83\mathrm{m}}$Kr decays the scaling of ξ is consistent with $1/\sqrt{E_{\mathrm{d}}}$, in contrast with the original Thomas-Imel model that predicts a dependence $\xi \propto E_{\mathrm{d}}^{-1}$. It should be noted that the observed behaviour could be also expected by using the original Thomas-Imel model, considering the drift velocity $v_d = \propto E_{\mathrm{d}}^{0.5}$. This would be consistent with the measurements of the drift velocity presented in section 5.5.3 that are found in good agreement with the measurements present in literature, and thus with the Cohen-Lekner model of electron transport, valid for the electric field range used in these calibrations [140]. Hence, this would explain the observed scaling of the ξ parameter within the context of the non-modified Thomas-Imel model, without the need of a reinterpretation of the the electron velocity inside the box. If this is the case, it should be possible to observe a flattening of ξ for electric fields above $\sim 10\,\mathrm{kV/cm}$, where the drift velocity saturates to a maximum value.

An additional feature that can be observed from the fit is an increase of the γ value for lower energy signals. However, due to relatively strong positive correlation between the two free parameters, this dependence might be only due to the chosen parametrisation of the fits.

The model used for the description of the recombination allows in principle to determine through the fit also the ratio β of excitons to ions, that so far is assumed constant for ERs on the base of theoretical considerations [143, 321]. Experimental attempts to determine this ratio resulted $\sim$ 2-3 times higher than the theoretical value and with the rather large uncertainty of $\sim 50\,\%$. Attempts to determine the β ratio were performed by fitting the macroscopic anti-correlation measurements for the 32 keV and 41 keV energy signals with this ratio as a third free parameter. However, in all the three cases the best fit for the β ratio resulted completely correlated with the a_0 parameter, with a unitary correlation coefficient. This issue most likely originates from the predictability limit of such a simple model for the electron recombination process.

A final result of the recombination study consists in a confirmation that the modified Thomas-Imel model is able to correctly predict the drop of light yield for X-rays below $\sim$ 15 keV, reported by Obodovskii and Ospanov [322] and by Baudis et al. [290] for much smaller ER energies produced by the Compton scattering of the 662 keV γ-rays from Cs sourcee. However, this is in tension with the measurements of Xurich II , where the light yield for the 9 keV de-excitation is found to be significantly higher with respect to the 32 keV de-excitation. The same was observed by Manalasay *et al.* [289], who explained this behaviour assuming a higher stopping power ($-\,\mathrm{d}\,E/\mathrm{d}x$) for lower energy ERs that would produce higher ionisation density and thus also recombination rate, at constant field. However, this explanation would imply that the recombination at low-energies follows the Birk's law and not the Thomas-Imel model, which is not the case. Since it is a well consolidated fact that the recombination process for ^{83m}Kr -induced ERs is governed by the Thomas-Imel model, the origin of the observed contradiction should be searched in the nature of the radiation emitted by the ^{83m}Kr de-excitations, as reported in table 5.2. Although there is not yet a complete understanding of this effect, it is interesting to note that the relative intensity for the emission of the 1.5 keV Auger electron from the Kr L shell is 0.947 and 0.8 for the 32 keV and 9.4 keV transitions, respectively. Considering all the other conversion electrons from the γ self-absorption, it is clear that the two ^{83m}Kr de-excitations actually probe the LXe light response at ER energies significantly lower than the energy of the nuclear transitions. Hence, the observed lower light output of the 32 keV transition than that produced by the 9.4 keV, should imply that the former explores the recombination regime at significantly lower energy than the latter. However, a proper understanding whether this hypothesis is correct would require to compute the proper weighted mean of the LY for each of the emitted electrons, including the absorption of the 12.67 keV K_α X-ray and of the low probability 9.4 keV γ-ray from LXe, that at this stage is not yet feasible. In addition, this scheme can be complicated by the fact that for most of the ^{83m}Kr decay channels the conversion electrons, the Auger electrons, and the X-rays are almost simultaneously emitted, and thus can interfere with each other. A similar feature was already noted by Baudis *et al.* [290], where the light yield of the 9.4 energy signal was observed to depend on the time delay from the 32 keV emission up to $\sim$ 500 ns, suggesting that an interference in the recombination process between almost simultaneous energy recoils produced in some of the de-excitation channels of the ^{83m}Kr emissions is highly probable.

The combined fluctuations of the charge and light signals are closely related to the LXe ionisation-recombination properties and to the detector and light sensors properties. Hence, a simplified probability model has been developed in order to be able to discuss

Table 5.5.: Best fit parameters for the field-dependent normalised light and charge yields, shown in figure 5.31. The last column reports the linear correlation factor, obtained from the covariance matrix of the fit. The fits have been independently performed for each line of the table.

Signal energy	Signal type	a_0	γ	Correlation
41.55 keV	Light	3.66 ± 0.03	0.46 ± 0.02	0.447
	Charge	3.65 ± 0.02	0.47 ± 0.02	0.454
32.15 keV	Light	3.04 ± 0.02	0.43 ± 0.01	0.498
	Charge	3.02 ± 0.03	0.44 ± 0.02	0.530
9.4 keV	Light	7.63 ± 0.03	0.58 ± 0.03	0.488

the observed S1 and S2 fluctuations and their correlations, that were presented in the previous section.

The starting point is to consider the charge readout at the anode of the light sensors as S1 and S2 signals corresponding to n_{ph} primary photons and to n_{e} electrons escaped from the recombination:

$$q_{\mathrm{S1}} = g \cdot \varepsilon_{qe} \cdot \alpha_1 \cdot n_{\mathrm{ph}} \,, \tag{5.26}$$

$$q_{\mathrm{S2}} = g \cdot \varepsilon_{qe} \cdot \alpha_2 \cdot \lambda_2 \cdot \varepsilon_{\mathrm{ex}} \cdot n_{\mathrm{e}} \,, \tag{5.27}$$

where g is the gain of the light sensors and ε_{qe} their QE; $\alpha_{1,2}$ the detector LCEs of the primary and secondary scintillations, respectively; finally the quantities λ_2 and $\varepsilon_{\mathrm{ex}}$ are respectively the photons gain per extracted electron and the extraction efficiency per drifted electron. A complete description of the fluctuations requires the knowledge of the joint probability function of all the variables together:

$$P(q_{\mathrm{S1}}) = \int \mathrm{d}\, g\, \mathrm{d}\, \alpha_1 \sum_{n_{\mathrm{phe}}, n_{\mathrm{ph}}} P(q_{\mathrm{S1}} | g, \varepsilon_{\mathrm{qe}}, \alpha_1, n_{\mathrm{ph}}) \cdot P(g, \varepsilon_{\mathrm{qe}}, \alpha_1, n_{\mathrm{ph}}) \,, \tag{5.28}$$

$$P(q_{\mathrm{S2}}) = \int \mathrm{d}\, g\, \mathrm{d}\, \alpha_2 \sum_{\substack{n_{\mathrm{phe}}, n'_{\mathrm{ph}} \\ n'_{\mathrm{e}}, n_{\mathrm{e}}}} P(q_{\mathrm{S2}} | g, \varepsilon_{\mathrm{qe}}, \alpha_2, \lambda_2, \varepsilon_{\mathrm{ex}}, n_{\mathrm{e}}) \cdot P(g, \varepsilon_{\mathrm{qe}}, \alpha_2, \lambda_2, \varepsilon_{\mathrm{ex}}, n_{\mathrm{e}}) \,, \tag{5.29}$$

where n_{phe}, n'_{ph} and n'_{e} are, respectively, the number of produced photoelectrons, the number of secondary photons, and the number of extracted electrons. Such a model can be easily implemented in a Monte Carlo simulation, and the parameters can be tuned in order to match the data. However, an analytical approach might help in understanding of the role played by each parameter in the fluctuations of the measured signals. The only drawback of this approach is that, differently from a Monte Carlo approach, the analytic study of the equations 5.28 and 5.29 would result in a formidable task and

some simplifications are necessary. To this end it is useful to define the inferred absolute numbers of photons and drifted electrons, $\widetilde{n}_{\rm ph}$ and $\widetilde{n}_{\rm e}$ as:

$$\widetilde{n}_{\rm ph} = \frac{q_{\rm S1}}{\widehat{g}\,\widehat{g}_1} = f_1 n_{\rm ph}\,, \tag{5.30}$$

$$\widetilde{n}_{\rm e} = \frac{q_{\rm S2}}{\widehat{g}\,\widehat{g}_2} = f_2 n_{\rm e}\,, \tag{5.31}$$

where $\widehat{g}$ is the gain of the PMTs determined by the dedicated calibrations, and $\widehat{g}_{1,2}$ are the amplification factors as determined from the fit shown in figure 5.31. Since these two quantities enter here as rescaling factors, they should not be considered as random variables and therefore do not contribute to the fluctuations. Before continuing with the description of the model it must be stressed that a change of notation, with respect to the previous part of this section, has been made: the quantities $n_{\rm ph,e}$ now represent, respectively, the actual number of produced photons and of escaped (drifted) electrons, both subject to the fluctuations induced by the recombination and by the initial energy deposit. Hence, the quantities reported as $n_{\rm ph,e}$ in the former part of this section should be compared here to $\widetilde{n}_{\rm ph,e}$, which are the observed numbers of the respective quanta after the absolute calibrations of the S1 and S2 signals are applied.

The first simplification, most likely the strongest, of the model consists in assuming statistical independence between the factors $f_{1,2}$ and $n_{\rm ph,e}$. Hence, the consistency condition $\langle\widetilde{n}_{\rm ph,e}\rangle = \langle n_{\rm ph,e}\rangle$ implies that $\langle f_{1,2}\rangle = 1$. With this simplification the probability distribution function of the normalised charges can be written as:

$$P(\widetilde{n}_{\rm ph}) = \int \mathrm{d}\, f_1 \sum_{n_{\rm ph}} P(\widetilde{n}_{\rm ph}|f_1, n_{\rm ph}) P(f_1) P(n_{\rm ph})\,, \tag{5.32}$$

$$P(\widetilde{n}_{\rm e}) = \int \mathrm{d}\, f_2 \sum_{n_{\rm e}} P(\widetilde{n}_{\rm e}|f_2, n_{\rm e}) P(f_2) P(n_{\rm ph})\,, \tag{5.33}$$

where the integrals over $f_{1,2}$ hold only symbolically, and their expansion consists in a composition of sums and integrals on discrete and continuos variables, respectively. The conditional probabilities on the variable $\widetilde{n}_{\rm ph,e}$ are actually delta functions that constrain the respective quantities:

$$P(\widetilde{n}_{\rm ph,e}|f_{1,2}, n_{\rm ph,e}) = \delta\left[\widetilde{n}_{\rm ph,e} - f_{1,2}\cdot n_{\rm ph,e}\right]\,. \tag{5.34}$$

In this model the joint distribution function of the number of emitted photons and drifted electrons is:

$$\begin{aligned} P(n_{\rm ph}, n_{\rm e}) &= \sum_{N_{\rm ex}, N_{\rm ex}} P(N_{\rm ex}) P(N_{\rm i}) P(n_{\rm ph}, n_{\rm e}|N_{\rm ex}, N_{\rm i}) \\ &= \sum_{N_{\rm ex}, N_{\rm ex}} P(N_{\rm ex}) P(N_{\rm i}) P(n_{\rm ph}|n_{\rm e}, N_{\rm ex}, N_{\rm i}) \mathcal{B}(n_e|N_{\rm i}, (1-r)) \\ &= \sum_{N_{\rm ex}, N_{\rm ex}} P(N_{\rm ex}) P(N_{\rm i}) \delta[n_{\rm ph} + n_{\rm e} - (N_{\rm ex} + N_{\rm i})] \mathcal{B}(n_e|N_{\rm i}, (1-r))\,, \end{aligned} \tag{5.35}$$

where $\mathcal{B}(n|N,p)$ is the binomial distribution of the variable n, given N trials and success probability p. At this step a second approximation has been introduced, which consists in neglecting the anti-correlation between the two random variables $N_{\rm ex}$ and

N_i. However, the statistical dependence between these two quantities is preserved by fixing their expectation:

$$\begin{aligned}\langle N_\mathrm{ex}\rangle &= \frac{\beta E}{W\,(1+\beta)}\,,\\ \langle N_\mathrm{i}\rangle &= \frac{E}{W\,(1+\beta)}\,.\end{aligned} \tag{5.36}$$

With these simplifications the fluctuations are given by:

$$\begin{aligned}\mathrm{Var}(\widetilde{n}_\mathrm{ph}) = \mathrm{Var}(f_1)\,\Big[&\mathrm{Var}(N_\mathrm{ex}) + r^2\mathrm{Var}(N_\mathrm{i}) + \langle N_\mathrm{ex}\rangle^2 + \\ &+ 2r\langle N_\mathrm{ex}\rangle\langle N_\mathrm{i}\rangle + r^2\langle N_\mathrm{i}\rangle^2 + r\,(1-r)\,\langle N_\mathrm{i}\rangle\Big] + \\ &+ \mathrm{Var}(N_\mathrm{ex}) + r^2\mathrm{Var}(N_\mathrm{i}) + r\,(1-r)\,\langle N_\mathrm{i}\rangle\end{aligned} \tag{5.37}$$

$$\begin{aligned}\mathrm{Var}(\widetilde{n}_\mathrm{e}) = \mathrm{Var}(f_2)\,\Big[&(1-r)^2\,\mathrm{Var}(N_\mathrm{i}) + (1-r)^2\,\langle N_\mathrm{i}\rangle^2 + \\ &+ r\,(1-r)\,\langle N_\mathrm{i}\rangle\Big] + (1-r)^2\,\mathrm{Var}(N_\mathrm{i}) + r\,(1-r)\,\langle N_\mathrm{i}\rangle\end{aligned} \tag{5.38}$$

$$\mathrm{Cov}(\widetilde{n}_\mathrm{ph},\widetilde{n}_\mathrm{e}) = -\,r\,(1-r)\,\Big[\langle N_\mathrm{i}\rangle - \mathrm{Var}(N_\mathrm{i})\Big]\,. \tag{5.39}$$

Already in this strong simplification of the problem it is evident how the propagation, detection, and amplification processes contribute to the S1 and S2 fluctuations together with the recombination process in a non separable combination. However, as expected from the first assumption, the covariance between the two signals depends only on the binomial recombination process, with a predicted maximum (in magnitude) for $r = 0.5$. Although the spread of the number of initial ions contributes to the covariance by reducing its magnitude, its contribution is expected to be negligible because of the small Fano-factor $F \sim 10^{-2}$ [323].

Both the 32 keV and 41 keV energy signals are $\sim 50-60$ times higher than the maximum possible value of $0.25/(1+\beta)$, predicted with the simplified model developed above. A similar discrepancy was also observed by Dahl [142], where the model for the description of the fluctuations was based on different assumptions but predicted the same functional form for the covariance. In the studies from Dahl a maximum of the covariance[6] was observed at $r \simeq 0.5$, for the absorption of the 122 keV ^{57}Co line in LXe. However, also for those measurements the maximum was observed more than 100 times higher (in magnitude) than the predictions by the employed model. Hence, it is possible that the recombination process alone contributes only a smaller part of the observed covariance, while it is already able to explain the observed shape, or at least where the maximum of the covariance is expected.

The model presented here can be immediately extended by dropping the second approximation and introducing the correlation $\mathrm{Cov}(N_\mathrm{ex}, N_\mathrm{i})$:

$$\mathrm{Cov}(\widetilde{n}_\mathrm{ph},\widetilde{n}_\mathrm{e}) = -r\,(1-r)\left[\langle N_\mathrm{i}\rangle - \mathrm{Var}(N_\mathrm{i}) - \frac{\mathrm{Cov}(N_\mathrm{ex}, N_\mathrm{i})}{r}\right]\,, \tag{5.40}$$

where $\mathrm{Cov}(N_\mathrm{ex}, N_\mathrm{i}) < 0$ as the quantities N_ex and N_i are expected to be anti-correlated,

6 Strictly speaking Dahl does not explicitly talk about covariance between the charge and light signals but about the quantity

$$\sigma_R^2 = \frac{1}{2}\left(\sigma^2_{n_\mathrm{ph}} + \sigma^2_{n_\mathrm{e}} - \frac{\sigma^2_\mathrm{E}}{W^2}\right),$$

that corresponds to the equation 5.23.

and thus a larger magnitude for $\mathrm{Cov}(\widetilde{n}_{\mathrm{ph}}, \widetilde{n}_{\mathrm{e}})$ can be obtained with a minimally modified shape. The data of figure 5.37 required a covariance $\mathrm{Cov}(N_{\mathrm{ex}}, N_{\mathrm{i}})$ ranging from $-2.5 \times 10^4\,[n]^2$ to $-6.5 \times 10^4\,[n]^2$ for the 32 keV signal, and from $-4.5 \times 10^4\,[n]^2$ to $-1 \times 10^5\,[n]^2$ for the 41 keV signal, where $\beta = 0.06$ is assumed. However, since $\mathrm{Cov}(N_{\mathrm{ex}}, N_{\mathrm{i}}) = \rho \times \mathrm{Var}(N_{\mathrm{ex}}) \times \mathrm{Var}(N_{\mathrm{i}})$ and since Fano-factor magnitude is small, even if N_{ex} and N_{i} were maximally anticorrelated quantities ($\rho = -1$), the estimated values from data would imply $\mathrm{Var}(N_{\mathrm{ex}}) \sim (\langle N_{\mathrm{ex}} \rangle + \langle N_{\mathrm{i}} \rangle)$, which seems to be quite large. Hence, the observed covariance between the measured light and charge signals might be dependent not only on the microphysics phenomena, but also on the detector and instrumental properties.

Although within the scope of this work other assumptions for the probability model will not be explored, an improvement can be made by considering the effects of the propagation and detection of the photons, as well as the charge extraction from the liquid phase and the proportional scintillation processes. All these processes might produce an amplification effect on the covariance, without significantly changing the functional form, and since they are all governed by binomial or Poisson probabilities it would be possible to treat them analytically.

6

CONCLUSIONS

The XENON1T experiment is currently searching for signals from WIMP-nucleus interactions using a LXe target mass of $\sim 2000\,\mathrm{kg}$. At the moment of writing the results of the first scientific run have just been submitted for publication and are available at [114]. The differential ER background rate in the $(1.042 \pm 0.012) \times 10^3\,\mathrm{kg}$ fiducial volume and in the $[5, 40]\,\mathrm{keV_{nr}}$ energy range, interesting for WIMP searches, is $(1.93 \pm 0.25) \times 10^{-4}\,\mathrm{events\,kg^{-1}\,day^{-1}\,keV_{ee}^{-1}}$. No dark matter signal has been detected, and a profile likelihood analysis of the 34.2 live days of data derived the most stringent upper limit on the spin independent WIMP nucleon cross section to date for particle mass $> 10\,\mathrm{GeV/c^2}$, with a minimum of $7.7 \times 10^{-47}\,\mathrm{cm^2}$ (90 % CL) for a mass of $35\,\mathrm{GeV/c^2}$.

The low background rate observed in the dark matter data of XENON1T is the lowest background ever achieved in a dark matter detector, and is fully compatible with the predictions of $(2.3 \pm 0.2) \times 10^{-4}\,\mathrm{events\,kg^{-1}\,day^{-1}\,keV_{ee}^{-1}}$, where the ^{222}Rn provides the largest contribution. For this achievement, the selection of radio-pure component materials was one of the most crucial ingredients. As shown in this thesis, this was possible thanks to the large potential of our HP-Ge spectrometers to detect radioactive contamination in materials with very high sensitivity, at the level of $\sim 10^{-17}\,\mathrm{g/g}$ and $\sim 10^{-10}\,\mathrm{g/g}$ for radionucleides belonging to the ^{238}U and ^{232}Th decay chains, respectively. Within the XENON1T screening program several ultra-pure materials suitable for building the detector have been identified and a complete overview of the results has been submitted for publication and is available at [163]. One of the most challenging objectives of the material screening campaign has been to developed light sensors with higher radiopurity compared to those used in previous dark matter experiments, in order to fulfil the background requirements of the XENON1T. The efforts resulted in the development of the Hamamatsu R11410-21 PMTs, which to date are the light sensors with the lowest ratio between radioactive contamination and photosensitive area [213].

The material radioassay and screening program for the XENON program is continuing for the upcoming XENONnT detector, which aims to probe the SI WIMP-nucleon cross section down to $2 \times 10^{-48}\,\mathrm{cm^2}$, with a LXe target mass of $\sim 6.5\,\mathrm{t}$ and a FV of $5\,\mathrm{t}$ [181]. For this new campaign, the Gator HP-Ge spectrometer will be upgraded in order to further reduce its background from ^{222}Rn and increase its detection sensitivity to weaker γ-emitters such as those belonging to the upper ^{238}U chain. In addition, an increase of detection sensitivity with the detector has already been achieved by the development of a statistical tool tailored to extract more information from the very low count spectra resulting from the measurement of the most radio pure samples.

The first dedicated experimental study of the cosmogenic activation of natural xenon has been performed and the results published in [220]. The main goal of the study

consisted in understanding the maximum tolerable exposure of xenon to cosmic radiation in view of next generation, multi-tonne scale LXe dark matter detectors, where the requirements on the radiopurity of the detection medium are much more stringent compared to the current class of dark matter detectors. The activation of the xenon took place at the High Altitude Research Station Jungfraujoch at an altitude of 3450 m above sea level, where the sample was exposed for about one year. The cosmogenic production rate of radioactive products was inferred by γ-spectrometry using the Gator HP-Ge spectrometer. For the analysis of the spectrum of the activated xenon a Bayesian approach, based on the Monte Carlo Markov Chain method, has been developed. As shown, this method is highly sensitive to the small amount of information contained in the spectra of the activated samples, allowing thus to reach a higher sensitivity, compared to the traditional frequentist methods, to the γ-emitters produced by the interaction of high-energy cosmic rays with the xenon nuclei. As a benchmark, an oxygen-free, high-conductivity copper sample has been exposed to the cosmic radiation together with the xenon, as for this material the existing codes [223, 224] are well validated and provide reliable predictions. The measured cosmogenic activation in copper was found to be in good agreement with the predictions from the Activia [223] and Cosmo [224] codes and with the only existing measurement of copper activation by cosmic rays [206]. As expected from previous studies [154], the measured activation in xenon resulted in disagreement with the numerical predictions, which strongly underestimate the production rates of many of the detected cosmogenic products. This was attributed to the lack of knowledge of the production cross sections, which are calculated based on the Silberberg and Tsao [225–227] semi-empirical models, that seem more reliable for nuclei lighter than xenon.

The largest contribution to the uncertainties on the analysis of dark matter data come from the uncertainties on the nuclear quenching of the scintillation and charge yield for low-energy nuclear recoils $E_{\mathrm{nr}} \lesssim 5\,\mathrm{keV}$, where most of the WIMP signal is expected. To elucidate this problem, a small dual phase (liquid-gas) xenon time projection chamber, Xurich II, has been developed at the University of Zurich with the aim of measuring the LXe response to low-energy neutron-induced nuclear recoils. As detailed in this thesis, the experimental setup, the design, the geometry and component of the time projection chamber have been carefully optimised and selected in order to reduce as much as possible the sources of systematics, identified in previous similar experiments, that can compromise the measurement accuracy of the light and charge yield of low-energy nuclear recoils. An important part concerning the development of the Xurich II experiment consists in the development of the software for the processing of the raw waveforms coming from the photosensors, with the aim of identify scintillation signals down to the limit imposed by the single photoelectron response of the photosensors. This is mainly achieved by using a pattern recognition software that is able to discriminate with large efficiency light signals from noise or other kind of signals, such as those from the electroluminescence of the accelerated electrons in the xenon gas phase.

In this thesis the outcome of Xurich II detector commissioning phase is reported. The internal $^{83\mathrm{m}}$Kr radioactive source have been used to perform the calibrations of the light and charge response to low-energy electronic recoils in liquid xenon. The employed calibration source is not only optimal for the uniform calibration of the liquid xenon chamber, but thanks to the nature of its de-excitation mechanism, it allowed also for the identification of eventual systematics, coming from the data se-

lection criteria used for the analysis, that can affect the energy reconstruction of the interaction events. From the analysis of the ^{83m}Kr calibrations the detector showed excellent performances: for a 32.15 keV electron recoils and with an electric field of $\sim 1\,\mathrm{kV/cm}$, a light of $\sim 9\,\mathrm{PE/keV}$ and a charge yield of $\sim 750\,\mathrm{PE/keV}$ was obtained. Considering the light and charge yield at different electric fields, it was possible to determine the absolute detector response to liquid xenon scintillation light, given by $g_1 = (0.191 \pm 0.006)\,\mathrm{PE/photons}$, and the absolute response to the extracted charge, given by $g_2 = (24.4 \pm 0.4)\,\mathrm{PE/electron}$. The former of the two quantities is the factor that determines the energy threshold of the detector, which for nuclear recoils is estimated to be $\sim 2.5\,\mathrm{keV}$ at an electric field of $\sim 1\,\mathrm{kV/cm}$.

It was shown that the electric field dependent light and charge yield of the ^{83m}Kr-induced electron recoils are very well described by the Thomas-Imel recombination model [318], and are in agreement with the recent measurements performed in the LUX experiment [317] using an electric field of $\sim 180\,\mathrm{V/cm}$. However, it was discussed that despite of the fact that the recombination model is able to provide an accurate description of the light and charge yield as function of the electric field, it is not sensitive to quantities such as the exciton-to-ion ratio $N_{\mathrm{ex}}/N_{\mathrm{i}}$ and the Fano factor for the ionisation process [324–326]. Both these quantities are fundamental for the understanding of the recombination-induced fluctuations of the charge and light signals, and their measured values are in conflict with the predictions of the theoretical models [143]. As the event-by-event fluctuation of the measured light and charge yield are strictly connected to the recombination process and to the exciton-to-ion ratio, a probabilistic model has been developed in order to describe these fluctuations and to disentangle the contributions coming from the recombination process from those coming from the detector and instrumental effects. With this model an analytic, distribution-free description of variances and covariances of the measured light and charge signals as function of the recombination probability, of the exciton-to-ion ratio and of the detector response fluctuations has been derived. The derivation is based on the approximation that the detector and instrumental effects, taken as a whole, are statistically uncorrelated with the fluctuations induced by the recombination process. Within this thesis only this simplified model has been investigated, and it was found that it can already explain the reason why the observed anticorrelation direction of the electron recoil events in the S2-S1 (charge-light) parameter space for the 32.15 keV and 41.55 keV energy peaks is not the same as the anticorrelation direction used for the absolute calibration of the detector response. Although the analytical model derived and discussed in this thesis does not provide a quantitative explanation of the data, it can be extend in order to take into account also the fluctuation induced from the light collection efficiency, from the electron extraction efficiency, from the production of the electroluminescence light, from the PMTs quantum efficiency and from the PMTs gain fluctuations. Once these key parameters are well understood, the developed formalism can be easily implemented in a Monte Carlo simulation code, in order to reproduce and to predict the joint distribution of the light and charge signals for a specific energy and a specific electric field by directly using the probability distribution functions related to each of the processes occurring during in the signal formation.

A

TABLES OF MATERIAL RADIOASSAY RESULTS

Table A.1.: Radioassay results of several copper samples for primordial radionuclides and for the anthropogenic ^{137}Cs.

Sample	Material	Use	Facility	Mass [kg]	Time [d]	Specific activity [mBq/kg]						
						^{235}U	^{238}U	^{226}Ra	^{232}Th	^{228}Th	^{40}K	^{137}Cs
1	OFE-Cu	Field shaping rings	GeMPI II	58.0	24.8	< 180	< 1000	< 35	< 33	< 26	400(100)	< 33
			ICP-MS	-	-		29.4(6)		< 8			
2	OFHC-Cu	PMT arrays	GeMPI I	8.84	37.2	< 120	< 1900	< 130	90(40)	90(40)	500(200)	< 78
			ICP-MS	-	-		< 25		< 8			
3	OFHC-Cu	PMT arrays	GeMPI II	23.3	23.5	< 120	< 1200	< 33	< 43	< 34	< 280	< 16
			ICP-MS	-	-		< 25		< 8			
4	OFHC-Cu	TPC bottom plate	GeMPI I	31.3	4.2	< 150	< 2400	< 73	100(4)	160(40)	< 340	< 33
5	Au plated OFHC-Cu	Not used	Gator	2.35	28	< 940	< 32000	< 1100	< 1600	< 1100	$1.4(2) \cdot 10^5$	< 0.30

Table A.2.: Radioassay results of several copper samples for cosmogenic radionuclides.

Sample	Material	Use	Facility	Mass [kg]	Time [d]	Specific activity [mBq/kg]							
						^{56}Co	^{57}Co	^{58}Co	^{60}Co	^{54}Mn	^{46}Sc	Other	
1	OFE-Cu	Field shaping rings	GeMPI II	58.0	24.8	60(20)	200(100)	360(40)	< 19	< 27	NA	-	
2	OFHC-Cu	PMT arrays	GeMPI I	8.84	37.2	310(30)	400(100)	$1.78(16) \cdot 10^3$	70(10)	220(30)	80(20)	^{48}V: ^{51}Cr: ^{52}Mn: ^{59}Fe:	200(20) 900(300) 362(31) 120(20)
3	OFHC-Cu	PMT arrays	GeMPI II	23.3	23.5	40(10)	400(100)	350(40)	100(10)	150(20)	NA	-	
4	OFHC-Cu	TPC bottom plate	GeMPI I	31.3	4.2	150(20)	740(150)	$1.1(1) \cdot 10^3$	210(20)	350(40)	40(10)	^{59}Fe:	90(20)
5	Au plated OFHC-Cu*	Not used	Gator	2.35	28								

Table A.3.: Radioassay results of several stainless steel samples for primordial and anthropogenic radionuclides.

Sample	Material	Use	Facility	Mass [kg]	Time [d]	Specific activity [mBq/kg]						
						^{235}U	^{238}U	^{226}Ra	^{232}Th	^{228}Th	^{40}K	^{137}Cs
1	AISI 316Ti	Cryostat flanges	Gator	10.8	7.3	< 3.9	< 150	< 4.0	< 4.8	4.5(6)	< 5.6	< 1.5
			ICP-MS	-	-		1.5(5)		0.21(6)			
2	AISI 304L	Cryostat shells	GeMPI II	10.1	6.7	< 2.0	< 40	< 0.64	< 0.81	< 0.36	< 2.7	< 0.64
			ICP-MS	-	-		2.5(7)		0.21			
3	AISI 304	Bell, field cage	GeMPI II	10.3	5.9	< 1.4	< 37	1.2(3)	2.1(7)	2.0(4)	< 1.3	< 0.58
			ICP-MS	-	-		11(3)		1.2(4)			
4	AISI 316L	Cryostat pipe	Gator	4.5	8.2	< 1.7	< 38	< 2.7	< 5.5	4.3(6)	< 6.8	< 0.65
5	AISI 304	Cathode high voltage feedthrough	Gator	5.8	19.0	1.4(4)	30.4(9)	1.39(44)	< 2.8	5.9(5)	< 4.9	< 0.66
6	AISI 304L	Support structure	GeMPI I	5.9	50.0	< 3.6	< 59.0	< 5.0	3.0(1)	27(2)	< 7.8	< 0.43
7	AISI 316L	Not used	Gator	10.3	11.0	< 2.7	< 83	4.3(4)	4(1)	7.0(6)	< 3.8	< 0.73
8	AISI 304L	Not used	GeMPI I	17.9	4.0	< 25	< 94	3.1(6)	3(1)	6(1)	< 1.6	< 1.1
9	AISI 316L	Not used	GeMPI II	10.4	7.9	< 4.9	< 140	2.3(7)	< 4.4	14(1)	4(2)	< 1.2
10	AISI 316L	Not used	GeMPI I	18.0	8.9	< 1.6	< 61	2.4(3)	1.7(7)	2.1(3)	< 2.9	< 0.64
11	AISI 304	Not used	GeMPI I	10.2	8.9	< 2.1	< 70	2.8(6)	< 2.1	< 0.75	6(2)	< 0.68
12	AISI 304L	Not used	GeMPI II	9.8	3.9	< 3.5	100(50)	< 1.9	4.00(10)	30.20(24)	< 4.1	< 0.49
13	AISI 316Ti	Not used	GeMPI II	9.9	6.8	< 2.7	< 120	< 1.0	< 2.7	< 0.89	< 4.2	< 1.1
			ICP-MS	-	-		3.1(9)		0.7(2)			
14	AISI 316Ti	Not used	GeMPI II	8.0	4.9	< 4.0	< 120	< 1.2	< 3.7	< 1.8	< 6.8	< 1.4

Sample	Material	Use	Facility	Mass [kg]	Time [d]	Specific activity [mBq/kg]						
						^{235}U	^{238}U	^{226}Ra	^{232}Th	^{228}Th	^{40}K	^{137}Cs
15	ASME 304L	Not used	GeMPI I	10.2	8.8	< 2.1	< 54	0.6(3)	< 1.2	0.8(3)	< 2.9	< 0.43
			ICP-MS	-	-		2.5(7)		0.14(4)			
16	AISI 316	Not used	GeMPI I	10.0	10.8	< 1.8	< 29	< 0.55	< 0.97	< 0.5	< 3.0	< 0.46
			ICP-MS	-	-		4(1)		1.2(3)			
17	ASME 304L	Not used	Gator	13.9	7.5	< 4.22	< 109	6.11(56)	6.1(1.1)	11.98(84)	< 4.95	< 0.94
			ICP-MS	-	-		5(1)		9(3)			
18	AISI 316Ti	Not used	GeMPI I	10.0	6.9	< 2.9	< 200	< 0.54	< 5.5	< 3.8	3.4(1.7)	< 1.8
19	AISI 304	Not used	GeMPI II	20.2	7.1	< 1.2	27(14)	2.2(3)	1.6(4)	2.0(3)	1.6(4)	0.30(14)

Table A.4.: Radioassay results of several stainless steel samples for cosmogenic radionuclides.

Sample	Material	Use	Facility	Mass [kg]	Time [d]	Specific activity [mBq/kg]		
						^{60}Co	^{58}Co	^{54}Mn
1	AISI 316Ti	Cryostat flanges	Gator	10.8	7.3	37.3(9)		
2	AISI 304L	Cryostat shells	GeMPI II	10.1	6.7	9.7(8)	< 0.60	0.5(2)
3	AISI 304	Bell, field cage	GeMPI II	10.3	5.9	5.5(5)	NA	1.1(3)
4	AISI 316L	Cryostat pipe	Gator	4.5	8.2	15(1)		1.4(3)
5	AISI 304	Cathode high voltage feedthrough	Gator	5.8	19.0	3.2(3)		2.5(4)
6	AISI 304L	Support structure	GeMPI I	5.9	50.0	4.0(6)	NA	NA
7	AISI 316L	Not used	Gator	10.3	11.0	29(2)		1.4(3)
8	AISI 304L	Not used	GeMPI I	17.9	4.0	36.2(2.6)	< 1.4	2.5(5)
9	AISI 316L	Not used	GeMPI II	10.4	7.9	142(9)	1.5(6)	2.0(6)
10	AISI 316L	Not used	GeMPI I	18.0	8.9	20.5(1.5)	NA	NA
11	AISI 304	Not used	GeMPI I	10.2	8.9	25.3(1.9)	< 1.0	2.3(5)
12	AISI 304L	Not used	GeMPI II	9.8	3.9	14.6(1.3)	NA	NA
13	AISI 316Ti	Not used	GeMPI II	9.9	6.8	17.3(1.4)	NA	NA
14	AISI 316Ti	Not used	GeMPI II	8.0	4.9	113(8)	NA	< 1.5
15	ASME 304L	Not used	GeMPI I	10.2	8.8	14.7(1.1)	< 0.61	1.3(3)
16	AISI 316	Not used	GeMPI I	10.0	10.8	10.7(8)	NA	1.4(8)
17	ASME 304L	Not used	Gator	13.9	7.5	3.99(28)		6.11(56)
18	AISI 316Ti	Not used	GeMPI I	10.0	6.9	86.0(6.0)	NA	< 2.0
19	AISI 304	Not used	GeMPI II	20.2	7.1	11.4(9)	NA	1.5(0.9)

Table A.5.: Radioassay results of several titanium samples for primordial, anthropogenic, and cosmogenic radionuclides.

Sample	Material	Facility	Mass [kg]	Time [d]	Specific activity [mBq/kg]								
					^{235}U	^{238}U	^{226}Ra	^{232}Th	^{228}Th	^{40}K	^{137}Cs	^{60}Co	^{46}Sc
1	Grade 1 Ti	Gator	14.0	6.0	2.4(4)	70(20)	< 1.3	< 1.4	< 1.7	< 3.6	< 0.54	< 0.30	2.15(3)
2	Grade 1 Ti	Gator	28.3	13.0	1.4(3)	27(6)	< 0.58	< 0.81	0.7(3)	< 1.5	< 0.24	< 0.17	1.9(2)
3	Grade 4 Ti	Gator	11.3	13.5	< 2.2	< 42	< 1.2	2.1(6)	9(1)	< 2.9	< 0.36	< 0.19	1.9(2)
4	Grade 2 Ti	Gator	10.8	17	1.4(4)	40(10)	< 0.81	1.9(6)	3.1(3)	< 2.9	< 0.46	< 0.25	2.7(3)
5	Grade 1 Ti	Gator	10.5	27.6	1.3(3)	30(10)	1.1(4)	< 1.1	< 0.71	< 2.8	< 0.19	< 0.18	1.8(2)
		ICP-MS	-	-		25(4)		< 8.1					

Table A.6.: Radioassay results of several plastic samples for primordial and anthropogenic radionuclides.

Sample	Material	Use	Facility	Mass [kg]	Time [d]	Specific activity [mBq/kg]						
						^{235}U	^{238}U	^{226}Ra	^{232}Th	^{228}Th	^{40}K	^{137}Cs
1	PTFE	TPC reflectors	Gator	44.0	58.0	< 0.087	< 1.9	< 0.12	< 0.11	< 0.065	< 0.34	0.17(3)
			ICP-MS	-	-		< 0.19		< 0.041			
2	PTFE	PMT array	GeMPI II	13.1	58.1	< 0.055	< 1.2	0.073(16)	< 0.071	0.057(21)	5.2(6)	< 0.024
			ICP-MS	-	-		0.09(1)		0.049(8)			
3	PTFE	TPC parts	GeMPI I	16.7	26.4	< 0.08	< 1.7	< 0.053	< 0.060	< 0.063	< 0.37	< 0.024
			ICP-MS	-	-		< 0.12		< 0.041			
4	PTFE	Cathode insulation	ICP-MS	-	-		< 0.12		< 0.041			
5	PTFE	TPC parts	ICP-MS	-	-		< 0.12		< 0.041			
6	Torlon 4203L	TPC parts	GeMPI I	0.75	21.6	2.9(8)	< 41?	2.0(5)	2.9(8)	2.4(6)	22(5)	< 0.46
7	Torlon 4203L	TPC parts	Gator	1.2	20	< 26	< 33	< 2.6	< 5.5	3(1)	11.5(1)	< 1.0
			ICP-MS	-	-		0.49(4)		4.9(4)			

Table A.7.: Radioassay results of the bulk materials used for the construction of the XENON1T photomultipliers. Values for primordial decay series only.

Sample	Facility	Time [d]	Specific activity [mBq/PMT]				
			^{235}U	^{238}U	^{226}Ra	^{232}Th - ^{228}Ra	^{228}Th
1	GeMPI I	29.1	$< 1.1 \times 10^{-2}$	$< 3.3 \times 10^{-1}$	$3.6(6) \times 10^{-2}$	$< 1.2 \times 10^{-2}$	$< 1.1 \times 10^{-2}$
	GD-MS	-		< 1.8		$< 6.3 \times 10^{-1}$	
2	GeMPI I	17.8	$< 5.5 \times 10^{-4}$	$< 2.8 \times 10^{-2}$	$< 7.2 \times 10^{-4}$	$< 6.6 \times 10^{-4}$	$6.6(3) \times 10^{-4}$
	GD-MS	-		$< 1.5 \times 10^{-3}$		$< 2.5 \times 10^{-4}$	
3	Gator	11.1	$< 1.7 \times 10^{-1}$	< 9.2	$< 2.6 \times 10^{-1}$	$< 3.6 \times 10^{-1}$	$< 3.4 \times 10^{-1}$
	GD-MS	-		$< 9.5 \times 10^{-2}$		$< 3.2 \times 10^{-3}$	
4	Gator	25.5	$< 1.9 \times 10^{-2}$	$< 9.0 \times 10^{-1}$	$< 2.5 \times 10^{-2}$	$< 4.3 \times 10^{-2}$	$< 3.3 \times 10^{-2}$
	GD-MS	-		5.0×10^{-2}		6.8×10^{-3}	
5	GeMPI I	54.0	$< 1.1 \times 10^{-2}$	$< 5.3 \times 10^{-1}$	$2.7(6) \times 10^{-2}$	$< 9.4 \times 10^{-3}$	$< 9.4 \times 10^{-3}$
	GD-MS	-		$< 1.7 \times 10^{-1}$		$< 1.5 \times 10^{-2}$	
6	GeMPI I	13.7	$< 5.2 \times 10^{-2}$	$< 3.7 \times 10^{-1}$	$1.3(2) \times 10^{-2}$	$8(4) \times 10^{-3}$	$8(4) \times 10^{-3}$
	GD-MS	-		$< 3.4 \times 10^{-2}$		$< 1.7 \times 10^{-2}$	
7	GeMPI I	34.1	$< 6 \times 10^{-3}$	$< 2 \times 10^{-1}$	$2.9(3) \times 10^{-2}$	$< 1.1 \times 10^{-2}$	$< 7.0 \times 10^{-3}$
	GD-MS	-		$< 8.8 \times 10^{-1}$		$< 3.0 \times 10^{-1}$	
8	GeMPI II	27.6	$< 1.8 \times 10^{-2}$	$< 7.9 \times 10^{-1}$	$3.7(7) \times 10^{-2}$	$< 1.8 \times 10^{-2}$	$< 1.8 \times 10^{-2}$
	GD-MS	-		4.4×10^{-2}		9.8×10^{-3}	
9	Gator	12.5	$1.1(2) \times 10^{-1}$	2.4(4)	$2.6(2) \times 10^{-1}$	$2.3(3) \times 10^{-1}$	$1.1(2) \times 10^{-1}$
	GeMPI I	11.8	$1.1(3) \times 10^{-1}$	3(1)	$3.0(3) \times 10^{-1}$	$2.1(3) \times 10^{-1}$	$1.1(2) \times 10^{-1}$
10	GeMPI II	14.8	$< 1.7 \times 10^{-2}$	$< 6.5 \times 10^{-1}$	$< 8.3 \times 10^{-3}$	$< 3.0 \times 10^{-2}$	$< 7.5 \times 10^{-3}$
	GD-MS	-		$< 1.7 \times 10^{-2}$		$< 6.0 \times 10^{-3}$	
11	GeDSG (LNGS)	39.3	$1.8(3) \times 10^{-2}$	$< 7.0 \times 10^{-1}$	$3.5(4) \times 10^{-2}$	$< 2.0 \times 10^{-2}$	$< 2.9 \times 10^{-2}$

Table A.8.: Radioassay results of the bulk materials used for the construction of the XENON1T photomultipliers. Values for the primordial ^{40}K and the anthropogenic ^{137}Cs. The only significant cosmogenic radionuclide observed is the ^{60}Co.

Sample	Facility	Time [d]	Specific activity [mBq/PMT]		
			^{40}K	^{60}Co	^{137}Cs
1	GeMPI I	29.1	$< 8.1 \times 10^{-2}$	$< 4.5 \times 10^{-3}$	$< 4.8 \times 10^{-3}$
2	GeMPI I	17.8	$< 5.7 \times 10^{-3}$	$< 1.2 \times 10^{-4}$	$< 2.3 \times 10^{-4}$
3	Gator	11.1	$< 9.9 \times 10^{-1}$	$7(2) \times 10^{-2}$	$< 1.0 \times 10^{-1}$
4	Gator	25.5	$< 6.4 \times 10^{-2}$	$< 7.2(6) \times 10^{-2}$	$< 8.0 \times 10^{-3}$
5	GeMPI I	54.0	$6(3) \times 10^{-2}$	$6(3) \times 10^{-3}$	$< 7.9 \times 10^{-3}$
6	GeMPI I	13.7	$< 3.2 \times 10^{-2}$	$2(1) \times 10^{-3}$	$< 2.6 \times 10^{-3}$
7	GeMPI I	34.1	$7(3) \times 10^{-2}$	$< 2.3 \times 10^{-3}$	$< 1.6 \times 10^{-3}$
8	GeMPI II	27.6	$7(4) \times 10^{-2}$	$2.6(2) \times 10^{-1}$	$9(4) \times 10^{-3}$
9	Gator	12.5	1.1(2)	$< 2.0 \times 10^{-2}$	$< 2.0 \times 10^{-2}$
	GeMPI I	11.8	1.6(2)	$< 1.6 \times 10^{-2}$	$< 1.2 \times 10^{-2}$
10	GeMPI II	14.8	$7(4) \times 10^{-2}$	$2.2(2) \times 10^{-1}$	$1.3(6) \times 10^{-2}$
11	GeDSG (LNGS)	39.3	$8(3) \times 10^{-2}$	$< 4.2 \times 10^{-3}$	$< 4.2 \times 10^{-3}$

Table A.9.: Radioassay results of the PMTs used in the XENON1T experiment, measured in batches of maximum 16 elements in the Gator spectrometer. Values for primordial decays only. The smaller PMT batches, measured with the GeMPI II spectrometer for consistency check, are always in number of 4, and they are considered representative of the entire batch measured previously with Gator.

Batch	Facility	Number of units	Time [d]	Specific activity [mBq/PMT]				
				^{235}U	^{238}U	^{226}Ra	^{228}Ra	^{228}Th
0	Gator	10	15	$< 7.9 \times 10^{-1}$	$< 1.8 \times 10^{1}$	$< 8.2 \times 10^{-1}$	$9(3) \times 10^{-1}$	$9(2) \times 10^{-1}$
1	Gator	10	25.5	$5(1) \times 10^{-1}$	$< 1.8 \times 10^{1}$	$4(1) \times 10^{-1}$	< 1.1	$4(1) \times 10^{-1}$
2	Gator	16	15	$2.9(9) \times 10^{-1}$	$< 1.6 \times 10^{1}$	$5(1) \times 10^{-1}$	$< 8.5 \times 10^{1}$	$< 6.1 \times 10^{-1}$
	GeMPI II	4	5.9	$< 8.1 \times 10^{-1}$	$< 1.4 \times 10^{1}$	$7(2) \times 10^{-1}$	$< 6.7 \times 10^{1}$	$3(1) \times 10^{-1}$
3	Gator	15	11.3	$< 5.2 \times 10^{-1}$	$< 2.0 \times 10^{1}$	$< 8.2 \times 10^{-1}$	< 1.1	$5(2) \times 10^{-1}$
4	Gator	15	21.5	$3.5(9) \times 10^{-1}$	$< 1.3 \times 10^{1}$	$5(1) \times 10^{-1}$	$4(1) \times 10^{-1}$	$4(1) \times 10^{-1}$
5	Gator	15	16	$< 5.7 \times 10^{-1}$	$< 1.7 \times 10^{1}$	$6(1) \times 10^{-1}$	$< 9.3 \times 10^{-1}$	$< 6.2 \times 10^{-1}$
6	Gator	11	22.7	$< 5.5 \times 10^{-1}$	$< 1.5 \times 10^{1}$	$6(1) \times 10^{-1}$	$< 7.7 \times 10^{-1}$	$7(1) \times 10^{-1}$
	GeMPI II	4	38.7	$< 2.3 \times 10^{-1}$	< 8.5	$5(1) \times 10^{-1}$	$2(1) \times 10^{-1}$	$2(1) \times 10^{-1}$
7	Gator	11	23	$4(1) \times 10^{-1}$	$< 1.9 \times 10^{1}$	1.0(1)	$< 7.7 \times 10^{-1}$	$7(1) \times 10^{-1}$
8	Gator	15	13.6	$< 6.3 \times 10^{-1}$	$< 1.5 \times 10^{1}$	$7(2) \times 10^{-1}$	$5(2) \times 10^{-1}$	$7(1) \times 10^{-1}$
	GeMPI II	4	35.5	$< 2.8 \times 10^{-1}$	< 6.2	$6(1) \times 10^{-1}$	$3(1) \times 10^{-1}$	$2(1) \times 10^{-1}$
9	Gator	15	19.6	$< 4.4 \times 10^{-1}$	$< 1.4 \times 10^{1}$	$5.7(9) \times 10^{-1}$	$< 7.9 \times 10^{-1}$	$5(1) \times 10^{-1}$
10	Gator	15	25.5	$< 4.4 \times 10^{-1}$	$< 1.5 \times 10^{1}$	$4.5(7) \times 10^{-1}$	$5(1) \times 10^{-1}$	$4.5(8) \times 10^{-1}$
11	Gator	15	12	$< 4.7 \times 10^{-1}$	$< 1.0 \times 10^{1}$	$5(2) \times 10^{-1}$	< 1.2	$6(1) \times 10^{-1}$

Batch	Facility	Number of units	Time [d]	Specific activity [mBq/PMT]				
				^{235}U	^{238}U	^{226}Ra	^{228}Ra	^{228}Th
12	Gator	15	18	$< 4.5 \times 10^{-1}$	$< 1.0 \times 10^{1}$	$< 7.1 \times 10^{-1}$	$7(2) \times 10^{-1}$	$7(1) \times 10^{-1}$
13	Gator	15	34	$3.8(8) \times 10^{-1}$	$< 1.0 \times 10^{1}$	$5.0(6) \times 10^{-1}$	$6(1) \times 10^{-1}$	$5.0(7) \times 10^{-1}$
14	Gator	15	21	$< 4.1 \times 10^{-1}$	$< 1.6 \times 10^{1}$	$5.3(8) \times 10^{-1}$	$< 8.2 \times 10^{-1}$	$5(1) \times 10^{-1}$
15	Gator	15	17	$< 5.0 \times 10^{-1}$	$< 1.5 \times 10^{1}$	$5.4(9) \times 10^{-1}$	$< 7.4 \times 10^{-1}$	$6(1) \times 10^{-1}$
16	Gator	15	19	$< 3.8 \times 10^{-1}$	$< 1.0 \times 10^{1}$	$5.5(9) \times 10^{-1}$	$8(2) \times 10^{-1}$	$5(1) \times 10^{-1}$
17	Gator	12	10.5	$< 6.3 \times 10^{-1}$	$< 1.7 \times 10^{1}$	$6(2) \times 10^{-1}$	< 1.1	$7(2) \times 10^{-1}$
18	Gator	14	10.5	$< 5.2 \times 10^{-1}$	$< 1.9 \times 10^{1}$	$6(1) \times 10^{-1}$	< 1.2	$7(1) \times 10^{-1}$
19	Gator	14	13.2	$< 5.9 \times 10^{-1}$	$< 1.6 \times 10^{1}$	$5(1) \times 10^{-1}$	$6(2) \times 10^{-1}$	$6(1) \times 10^{-1}$
20	Gator	14	12	$< 4.6 \times 10^{-1}$	$< 1.4 \times 10^{1}$	$6(1) \times 10^{-1}$	< 1.1	$6(1) \times 10^{-1}$
21	Gator	13	17.7	$< 4.7 \times 10^{-1}$	$< 1.6 \times 10^{1}$	$5(1) \times 10^{-1}$	$6(1) \times 10^{-1}$	$6(1) \times 10^{-1}$
22	Gator	15	17.5	$< 4.4 \times 10^{-1}$	$< 1.4 \times 10^{1}$	$7(1) \times 10^{-1}$	$8(3) \times 10^{-1}$	$5.9(9) \times 10^{-1}$

Table A.10.: Radioassay results of the PMTs used in the XENON1T experiment, measured in batches of maximum 16 elements in the Gator spectrometer. Values for primordial ^{40}K, for the observed cosmogenic radionuclides, for the common anthropogenic ^{137}Cs and for the unexpected ^{110m}Ag. The smaller PMT batches, measured with the GeMPI II spectrometer for consistency check, are always in number of 4, and they are considered representative of the entire batch measured previously with Gator.

Batch	Facility	Number of units	Time [d]	Specific activity [mBq/PMT]				
				^{40}K	^{60}Co	^{54}Mn	^{137}Cs	^{110m}Ag
$0^{(1)}$	Gator	10	15	$1.2(2) \times 10^{1}$	1.3(2)	$2.4(7) \times 10^{-1}$	$< 2.6 \times 10^{-1}$	$9(3) \times 10^{-1}$
1	Gator	10	25.5	$1.2(2) \times 10^{1}$	$7(1) \times 10^{-1}$	$2.7(6) \times 10^{-1}$	$< 2.7 \times 10^{-1}$	$9(1) \times 10^{-1}$
2	Gator	16	15	$1.3(2) \times 10^{1}$	$7.9(8) \times 10^{-1}$	$2.0(5) \times 10^{-1}$	$< 3.2 \times 10^{-1}$	$8.7(9) \times 10^{-1}$
	GeMPI II	4	5.9	$1.1(3) \times 10^{1}$	$6(2) \times 10^{-1}$	$5(2) \times 10^{-1}$	$< 1.2 \times 10^{-1}$	$8(2) \times 10^{-1}$
3	Gator	15	11.3	$1.3(2) \times 10^{1}$	$7.3(9) \times 10^{-1}$	$2.2(6) \times 10^{-1}$	$< 3.2 \times 10^{-1}$	$5.0(7) \times 10^{-1}$
4	Gator	15	21.5	$1.2(2) \times 10^{1}$	$7.3(9) \times 10^{-1}$	$2.3(5) \times 10^{-1}$	$< 1.9 \times 10^{-1}$	$2.1(3) \times 10^{-1}$
5	Gator	15	16	$1.4(2) \times 10^{1}$	$6.3(7) \times 10^{-1}$	$< 2.5 \times 10^{-1}$	$< 2.2 \times 10^{-1}$	$2.8(6) \times 10^{-1}$
6	Gator	11	22.7	$1.4(2) \times 10^{1}$	$7.1(7) \times 10^{-1}$	$2.4(5) \times 10^{-1}$	$< 1.8 \times 10^{-1}$	$2.3(4) \times 10^{-1}$
	GeMPI II	4	38.7	5(1)	$8(1) \times 10^{-1}$	$2.2(7) \times 10^{-1}$	$< 1.1 \times 10^{-1}$	$2.2(4) \times 10^{-1}$
7	Gator	11	23	$1.5(2) \times 10^{1}$	1.0(1)	$2.6(6) \times 10^{-1}$	$< 4.9 \times 10^{-1}$	$1.9(7) \times 10^{-1}$
8	Gator	15	13.6	$1.4(2) \times 10^{1}$	1.2(1)	$2.0(5) \times 10^{-1}$	$< 3.5 \times 10^{-1}$	$< 2.3 \times 10^{-1}$
	GeMPI II	4	35.5	7(1)	1.2(1)	$2(1) \times 10^{-1}$	$< 1.1 \times 10^{-1}$	$1.6(4) \times 10^{-1}$
9	Gator	15	19.6	$1.3(2) \times 10^{1}$	$8.1(8) \times 10^{-1}$	$2.2(5) \times 10^{-1}$	$< 3.6 \times 10^{-1}$	$5.3(6) \times 10^{-1}$
10	Gator	15	25.5	$1.3(2) \times 10^{1}$	$8.7(8) \times 10^{-1}$	$< 1.4 \times 10^{-1}$	$< 2.3 \times 10^{-1}$	$5.4(7) \times 10^{-1}$

Batch	Facility	Number of units	Time [d]	Specific activity [mBq/PMT]				
				^{40}K	^{60}Co	^{54}Mn	^{137}Cs	^{110m}Ag
11	Gator	15	12	$1.2(2) \times 10^{1}$	$7.7(9) \times 10^{-1}$	$1.9(5) \times 10^{-1}$	$< 4.4 \times 10^{-1}$	$5.5(9) \times 10^{-1}$
12	Gator	15	18	$1.1(2) \times 10^{1}$	$7.8(8) \times 10^{-1}$	$1.3(4) \times 10^{-1}$	$< 3.7 \times 10^{-1}$	$7.3(9) \times 10^{-1}$
13	Gator	15	34	$1.2(1) \times 10^{1}$	$8.2(7) \times 10^{-1}$	$1.8(4) \times 10^{-1}$	$< 2.4 \times 10^{-1}$	$6(1) \times 10^{-1}$
14	Gator	15	21	$1.4(2) \times 10^{1}$	$8.1(8) \times 10^{-1}$	$1.8(4) \times 10^{-1}$	$< 3.2 \times 10^{-1}$	$< 8.2 \times 10^{-1}$
15	Gator	15	17	$1.2(2) \times 10^{1}$	$8.1(8) \times 10^{-1}$	$2.8(6) \times 10^{-1}$	$< 3.7 \times 10^{-1}$	$< 7.4 \times 10^{-1}$
16	Gator	15	19	$1.0(1) \times 10^{1}$	$7.8(8) \times 10^{-1}$	$2.0(5) \times 10^{-1}$	$< 3.2 \times 10^{-1}$	$4.4(7) \times 10^{-1}$
17	Gator	12	10.5	$1.1(2) \times 10^{1}$	$8(1) \times 10^{-1}$	$2.1(6) \times 10^{-1}$	$< 2.8 \times 10^{-1}$	$6(1) \times 10^{-1}$
18	Gator	14	10.5	$1.0(2) \times 10^{1}$	$7.6(9) \times 10^{-1}$	$1.9(6) \times 10^{-1}$	$< 2.2 \times 10^{-1}$	$5(1) \times 10^{-1}$
19	Gator	14	13.2	$1.1(2) \times 10^{1}$	$8.5(9) \times 10^{-1}$	$2.3(6) \times 10^{-1}$	$< 2.1 \times 10^{-1}$	$6.1(9) \times 10^{-1}$
20	Gator	14	12	$1.2(2) \times 10^{1}$	$7.5(9) \times 10^{-1}$	$2.7(7) \times 10^{-1}$	$< 2.0 \times 10^{-1}$	$5(1) \times 10^{-1}$
21	Gator	13	17.7	$1.0(2) \times 10^{1}$	$8.4(8) \times 10^{-1}$	$2.1(5) \times 10^{-1}$	$< 1.5 \times 10^{-1}$	$4.4(8) \times 10^{-1}$
22	Gator	15	17.5	$1.0(1) \times 10^{1}$	1.2(1)	$3.0(6) \times 10^{-1}$	$< 1.7 \times 10^{-1}$	$2.9(7) \times 10^{-1}$

BIBLIOGRAPHY

[1] Kelvin KS Wu, Ofer Lahav, and Martin J Rees. The large-scale smoothness of the universe. *Nature*, 397(6716):225–230, 1999.

[2] Jaswant Yadav, Somnath Bharadwaj, Biswajit Pandey, and TR Seshadri. Testing homogeneity on large scales in the sloan digital sky survey data release one. *Monthly Notices of the Royal Astronomical Society*, 364(2):601–606, 2005.

[3] R. Adam, P. A. R. Ade, N. Aghanim, M. Arnaud, M. Ashdown, J. Aumont, C. Baccigalupi, A. J. Banday, R. B. Barreiro, J. G. Bartlett, et al. Planck 2015 results-ix. diffuse component separation: Cmb maps. *Astron. Astrophys.*, 594:A9, 2016.

[4] P. A. R. Ade, N. Aghanim, M. Arnaud, M. Ashdown, J. Aumont, C. Baccigalupi, A. J. Banday, R. B. Barreiro, J. G. Bartlett, N. Bartolo, et al. Planck 2015 results-XIII. Cosmological parameters. *Astron. Astrophys.*, 594:A13, 2016.

[5] C. L. Bennett, A. J. Banday, K. M. Górski, G. Hinshaw, P. Jackson, P. Keegstra, A. Kogut, G. F. Smoot, D. T. Wilkinson, and E. L. Wright. Four-Year COBE DMR Cosmic Microwave Background Observations: Maps and Basic Results. *Astrophys. J. Lett.*, 464:L1, 1996.

[6] C. L. Bennett, D. Larson, J. L. Weiland, N. Jarosik, G. Hinshaw, N. Odegard, K. M. Smith, R. S. Hill, B. Gold, M. Halpern, E. Komatsu, M. R. Nolta, L. Page, D. N. Spergel, E. Wollack, J. Dunkley, A. Kogut, M. Limon, S. S. Meyer, G. S. Tucker, and E. L. Wright. Nine-year Wilkinson Microwave Anisotropy Probe (WMAP) Observations: Final Maps and Results. *Astrophys. J. Suppl. Ser.*, 208:20, 2013.

[7] R. Adam, P. A. R. Ade, N. Aghanim, Y. Akrami, M. I. R. Alves, F. Argüeso, M. Arnaud, F. Arroja, M. Ashdown, J. Aumont, et al. Planck 2015 results-i. overview of products and scientific results. *Astron. Astrophys.*, 594:A1, 2016.

[8] E. Kolb and M. Turner. *The Early Universe*. Frontiers in physics. Avalon Publishing, 1994.

[9] Jeremy Bernstein. *Kinetic theory in the expanding universe*. Cambridge University Press, 2004.

[10] Horace W Babcock. The rotation of the andromeda nebula. *Lick Observatory Bulletin*, 19:41–51, 1939.

[11] Arthur B Wyse and NU Mayall. Distribution of mass in the spiral nebulae messier 31 and messier 33. *Astrophys. J.*, 95:24, 1942.

[12] Martin Schwarzschild. Mass distribution and mass-luminosity ratio in galaxies. *The Astronomical Journal*, 59:273, 1954.

[13] HC Van de Hulst, E Raimond, and H Van Woerden. Rotation and density distribution of the andromeda nebula derived from observations of the 21-cm line. *Bulletin of the Astronomical Institutes of the Netherlands*, 14:1, 1957.

[14] LMJS Volders. Neutral hydrogen in m 33 and m 101. *Bulletin of the Astronomical Institutes of the Netherlands*, 14:323, 1959.

[15] E Margaret Burbidge, GR Burbidge, and KH Prendergast. Motions in barred spiral galaxies. ii the rotation of ngc 7479. *Astrophys. J.*, 132:654, 1960.

[16] Edward Argyle. A spectrometer survey of atomic hydrogen in the andromeda nebula. *Astrophys. J.*, 141:750, 1965.

[17] Vera C Rubin and W Kent Ford Jr. Rotation of the andromeda nebula from a spectroscopic survey of emission regions. *Astrophys. J.*, 159:379, 1970.

[18] DH Rogstad and GS Shostak. Gross properties of five scd galaxies as determined from 21-centimeter observations. *Astrophys. J.*, 176:315, 1972.

[19] Vera C Rubin, N Thonnard, and WK Ford Jr. Extended rotation curves of high-luminosity spiral galaxies. iv-systematic dynamical properties, sa through sc. *Astrophys. J.*, 225:L107–L111, 1978.

[20] Astrori Bosma. 21-cm line studies of spiral galaxies. ii. the distribution and kinematics of neutral hydrogen in spiral galaxies of various morphological types. *The Astronomical Journal*, 86:1825–1846, 1981.

[21] Astron Bosma. 21-cm line studies of spiral galaxies. i-observations of the galaxies ngc 5033, 3198, 5055, 2841, and 7331. ii-the distribution and kinematics of neutral hydrogen in spiral galaxies of various morphological types. *The Astronomical Journal*, 86:1791–1846, 1981.

[22] Vera C Rubin, David Burstein, W Kent Ford Jr, and Norbert Thonnard. Rotation velocities of 16 sa galaxies and a comparison of sa, sb, and sc rotation properties. *Astrophys. J.*, 289:81–98, 1985.

[23] TS-Van Albada et al. Distribution of dark matter in the spiral galaxy ngc 3198. *Astrophys. J.*, 295:305–313, 1985.

[24] KG Begeman. Hi rotation curves of spiral galaxies. i-ngc 3198. *Astronomy and Astrophysics*, 223:47–60, 1989.

[25] WJG De Blok, Stacy S McGaugh, and Vera C Rubin. High-resolution rotation curves of low surface brightness galaxies. ii. mass models. *The Astronomical Journal*, 122(5):2396, 2001.

[26] Fritz Zwicky. Die rotverschiebung von extragalaktischen nebeln. *Helvetica Physica Acta*, 6:110–127, 1933.

[27] Sinclair Smith. The mass of the virgo cluster. *Astrophys. J.*, 83:23, 1936.

[28] George O Abell. The distribution of rich clusters of galaxies. *Astrophys. J. Suppl. Ser.*, 3:211, 1958.

[29] F Zwicky and ML Humason. Spectra and other characteristics of interconnected galaxies and of galaxies in groups and in clusters. iii. *Astrophys. J.*, 139:269, 1964.

[30] Herbert J Rood et al. Empirical properties of the mass discrepancy in groups and clusters of galaxies. *Astrophys. J.*, 188:451–462, 1974.

[31] E. T. Byram, T. A. Chubb, and H. Friedman. Cosmic x-ray sources, galactic and extragalactic. *Science*, 152(3718):66–71, 1966.

[32] John F Meekins, Gilbert Fritz, Talbot A Chubb, H Friedman, and RICHARD C HENRY. Physical sciences: X-rays from the coma cluster of galaxies. *Nature*, 231:107, 1971.

[33] Gilbert Fritz, Arthur Davidsen, John F Meekins, and H Friedman. Discovery of an x-ray source in perseus. *Astrophys. J.*, 164:L81, 1971.

[34] R Giacconi, E Kellogg, P Gorenstein, H Gursky, and H Tananbaum. An x-ray scan of the galactic plane from uhuru. *Astrophys. J.*, 165:L27, 1971.

[35] R Rothschild, E Boldt, S Holt, P Serlemitsos, G Garmire, P Agrawal, G Riegler, S Bowyer, and M Lampton. The cosmic x-ray experiment aboard heao-1. *Space Science Instrumentation*, 4:269–301, 1979.

[36] JD McKee, RF Mushotzky, EA Boldt, SS Holt, FE Marshall, SH Pravdo, and PJ Serlemitsos. The heao a-2 survey of abell clusters and the x-ray luminosity function. *Astrophys. J.*, 242:843–856, 1980.

[37] MW Johnson, RG Cruddace, KS Wood, MP Ulmer, and MP Kowalski. A survey by heao 1 of clusters of galaxies. iii-the complete abell catalog. *Astrophys. J.*, 266:425–445, 1983.

[38] MP Kowalski, MP Ulmer, RG Cruddace, and KS Wood. An x-ray survey of clusters of galaxies. iv-a survey of southern clusters and a compilation of upper limits for both abell and southern clusters. *Astrophys. J. Suppl. Ser.*, 56:403–506, 1984.

[39] R Giacconi, G Branduardi, U Briel, A Epstein, D Fabricant, E Feigelson, W Forman, P Gorenstein, J Grindlay, H Gursky, et al. The einstein/heao 2/x-ray observatory. *Astrophys. J.*, 230:540–550, 1979.

[40] FRANK Abramopoulos and WH-M Ku. X-ray survey of clusters of galaxies with the einstein observatory. *Astrophys. J.*, 271:446–460, 1983.

[41] Christine Jones and W Forman. The structure of clusters of galaxies observed with einstein. *Astrophys. J.*, 276:38–55, 1984.

[42] Martin C Weisskopf, Harvey D Tananbaum, Leon P Van Speybroeck, and Stephen L O'Dell. Chandra x-ray observatory (cxo): overview. In *Astronomical Telescopes and Instrumentation*, pages 2–16. International Society for Optics and Photonics, 2000.

[43] F Jansen, D Lumb, B Altieri, J Clavel, M Ehle, C Erd, C Gabriel, M Guainazzi, P Gondoin, R Much, et al. Xmm-newton observatory-i. the spacecraft and operations. *Astron. Astrophys.*, 365(1):L1–L6, 2001.

[44] SW Allen, RW Schmidt, and AC Fabian. Cosmological constraints from the x-ray gas mass fraction in relaxed lensing clusters observed with chandra. *Monthly Notices of the Royal Astronomical Society*, 334(2):L11–L15, 2002.

[45] S Ettori, P Tozzi, and P Rosati. Constraining the cosmological parameters with the gas mass fraction in local and $z > 0.7$ galaxy clusters. *Astron. Astrophys.*, 398(3):879–890, 2003.

[46] Alexey Vikhlinin, A Kravtsov, W Forman, C Jones, M Markevitch, SS Murray, and L Van Speybroeck. Chandra sample of nearby relaxed galaxy clusters: Mass, gas fraction, and mass-temperature relation. *Astrophys. J.*, 640(2):691, 2006.

[47] Y-Y Zhang, A Finoguenov, H Böhringer, J-P Kneib, GP Smith, O Czoske, and G Soucail. Scaling relations and mass calibration of the x-ray luminous galaxy clusters at redshift˜ 0.2: Xmm-newton observations. *Astron. Astrophys.*, 467(2):437–457, 2007.

[48] CS Kochanek, Martin White, J Huchra, L Macri, TH Jarrett, SE Schneider, and J Mader. Clusters of galaxies in the local universe. *Astrophys. J.*, 585(1):161, 2003.

[49] S. D. M. White, J. F. Navarro, A. E. Evrard, and C. S. Frenk. The baryon content of galaxy clusters-a challenge to cosmological orthodoxy. *Nature*, 366:429, 1993.

[50] M Fukugita, CJ Hogan, and PJE Peebles. The cosmic baryon budget. *Astrophys. J.*, 503(2):518, 1998.

[51] Matthias Bartelmann. Gravitational lensing. *Classical and Quantum Gravity*, 27(23):233001, 2010.

[52] Douglas Clowe, Maruša Bradač, Anthony H Gonzalez, Maxim Markevitch, Scott W Randall, Christine Jones, and Dennis Zaritsky. A direct empirical proof of the existence of dark matter. *Astrophys. J. Lett.*, 648(2):L109, 2006.

[53] M. Markevitch, A. H. Gonzalez, D. Clowe, A. Vikhlinin, W. Forman, C. Jones, S. Murray, and W. Tucker. Direct constraints on the dark matter self-interaction cross section from the merging galaxy cluster 1E 0657–56. *Astrophys. J.*, 606:819, 2004.

[54] S. W. Randall, M. Markevitch, D. Clowe, A. H. Gonzalez, et al. Constraints on the Self-Interaction Cross Section of Dark Matter from Numerical Simulations of the Merging Galaxy Cluster 1E 0657–56. *Astrophys. J.*, 679:1173, 2008.

[55] J. Alves, F. Combes, A. Ferrara, T. Forveille, and S. Shore. Planck 2015 results. *Astron. Astrophys.*, 594:E1, 2016.

[56] Erik Aver, Keith A. Olive, R.L. Porter, and Evan D. Skillman. The primordial helium abundance from updated emissivities. *J. Cosmol. Astropart. Phys.*, 2013(11):017, 2013.

[57] Fabio Iocco, Gianpiero Mangano, Gennaro Miele, Ofelia Pisanti, and Pasquale D. Serpico. Primordial nucleosynthesis: From precision cosmology to fundamental physics. *Phys. Rep.*, 472(1–6):1 – 76, 2009.

[58] Ryan J. Cooke, Max Pettini, Regina A. Jorgenson, Michael T. Murphy, and Charles C. Steidel. Precision measures of the primordial abundance of deuterium. *Astrophys. J.*, 781(1):31, 2014.

[59] Jeffrey L Linsky, Alexander Brown, Ken Gayley, Athanassios Diplas, Blair D Savage, Thomas R Ayres, Wayne Landsman, Steven N Shore, and Sara R Heap. Goddard high-resolution spectrograph observations of the local interstellar medium and the deuterium/hydrogen ratio along the line of sight toward capella. *Astrophys. J.*, 402:694–709, 1993.

[60] Jeffrey L Linsky, Athanassios Diplas, Brian E Wood, Alexander Brown, Thomas R Ayres, and Blair D Savage. Deuterium and the local interstellar medium properties for the procyon and capella lines of sight. *Astrophys. J.*, 451:335, 1995.

[61] Keith A Olive. Primordial big bang nucleosynthesis. *arXiv preprint astro-ph/9901231*, 1999.

[62] David Kirkman, David Tytler, Nao Suzuki, John M. O'Meara, and Dan Lubin. The cosmological baryon density from the deuterium-to-hydrogen ratio in qso absorption systems: D/h toward q1243+3047. *Astrophys. J. Suppl. Ser.*, 149(1):1, 2003.

[63] S. Capozziello and M. de Laurentis. Extended theories of gravity. *Phys. Rep.*, 509(4-5):167–321, 2011. cited By 617.

[64] Benoît Famaey and Stacy S. McGaugh. Modified newtonian dynamics (mond): Observational phenomenology and relativistic extensions. *Living Rev. Relativ.*, 15(1):10, 2012.

[65] George F. Chapline and Paul H. Frampton. A new direction for dark matter research: intermediate-mass compact halo objects. *J. Cosmol. Astropart. Phys.*, 2016(11):042, 2016.

[66] Marc Moniez. Microlensing as a probe of the galactic structure: 20 years of microlensing optical depth studies. *Gen. Rel. Gravit.*, 42(9):2047–2074, 2010.

[67] Louis E. Strigari. Galactic searches for dark matter. *Phys. Rep.*, 531(1):1 – 88, 2013. Galactic searches for dark matter.

[68] R. D. Peccei and H. R. Quinn. CP conservation in the presence of pseudoparticles. *Phys. Rev. Lett.*, 38:1440, 1977.

[69] L. J. Rosenberg and K. A. van Bibber. Searches for invisible axions. *Phys. Rep.*, 325:1, 2000.

[70] H. Georgi, D. B. Kaplan, and L. Randall. Manifesting the invisible axion at low energies. *Phys. Lett. B*, 169:73, 1986.

[71] Michael Dine, Willy Fischler, and Mark Srednicki. A simple solution to the strong CP problem with a harmless axion. *Phys. Lett. B*, 104(3):199 – 202, 1981.

[72] M.A. Shifman, A.I. Vainshtein, and V.I. Zakharov. Can confinement ensure natural cp invariance of strong interactions? *Nucl. Phys. B*, 166(3):493 – 506, 1980.

[73] P. Sikivie. Experimental tests of the "invisible" axion. *Phys. Rev. Lett.*, 51:1415, 1983.

[74] Lawrence Krauss, John Moody, Frank Wilczek, and Donald E. Morris. Calculations for cosmic axion detection. *Phys. Rev. Lett.*, 55:1797, 1985.

[75] F. Wilczek. Axions and family symmetry breaking. *Phys. Rev. Lett.*, 49:1549, 1982.

[76] Y. Chikashige, R. N. Mohapatra, and R. D. Peccei. Spontaneously broken lepton number and cosmological constraints on the neutrino mass spectrum. *Phys. Rev. Lett.*, 45:1926, 1980.

[77] Y. Chikashige, R.N. Mohapatra, and R.D. Peccei. Are there real Goldstone bosons associated with broken lepton number? *Phys. Lett. B*, 98:265, 1981.

[78] E. J. Chun, J. E. Kim, and H. P. Nilles. A natural solution of the μ problem with a composite axion in the hidden sector. *Nucl. Phys. B*, 370:105, 1992.

[79] A. E. Nelson and N. Seiberg. R-symmetry breaking versus supersymmetry breaking. *Nucl. Phys. B*, 416:46, 1994.

[80] R. Kappl, H. P. Nilles, S. Ramos-Sánchez, M. Ratz, K. Schmidt-Hoberg, and P. K. S. Vaudrevange. Large Hierarchies from Approximate R Symmetries. *Phys. Rev. Lett.*, 102:121602, 2009.

[81] JE Gunn, BW Lee, I Lerche, DN Schramm, and G Steigman. Some astrophysical consequences of the existence of a heavy stable neutral lepton. *Astrophys. J.*, 223:1015, 1978.

[82] Graciela Gelmini and Gondolo Paolo. "Dark matter production mechanisms", in *Particle Dark Matter*, chapter 7, page 117. Cambridge University Press, 2010.

[83] J. Ellis and K. A. Olive. "Supersymmetric Dark Matter Candidates", in *Particle Dark Matter*, chapter 8, page 138. Cambridge University Press, 2010.

[84] T. Kaluza. Zum unitätsproblem der physik. *Sitzungsber. Preuss. Akad. Wiss. Berlin.(Math. Phys.)*, pages 966–972, 1921.

[85] O. Klein. The atomicity of electricity as a quantum theory law. *Nature*, 118:516, 1926.

[86] Ignatios Antoniadis, Nima Arkani-Hamed, Savas Dimopoulos, and Gia Dvali. New dimensions at a millimeter to a fermi and superstrings at a TeV. *Phys. Lett. B*, 436:257 – 263, 1998.

[87] G. Servant. "Dark Matter at the electroweak scale: non-supersymmetric candidates", in *Particle Dark Matter*, chapter 9, page 160. Cambridge University Press, 2010.

[88] Dan Hooper and Lisa Goodenough. Dark matter annihilation in the Galactic Center as seen by the Fermi Gamma Ray Space Telescope. *Phys. Lett. B*, 697:412 – 428, 2011.

[89] Kevork N. Abazajian, Nicolas Canac, Shunsaku Horiuchi, and Manoj Kaplinghat. Astrophysical and dark matter interpretations of extended gamma-ray emission from the Galactic Center. *Phys. Rev. D*, 90:023526, 2014.

[90] Francesca Calore, Ilias Cholis, and Christoph Weniger. Background model systematics for the Fermi GeV excess. *J. Cosmol. Astropart. Phys.*, 2015(03):038, 2015.

[91] Tansu Daylan, Douglas P. Finkbeiner, Dan Hooper, Tim Linden, Stephen K.N. Portillo, Nicholas L. Rodd, and Tracy R. Slatyer. The characterization of the gamma-ray signal from the central Milky Way: A case for annihilating dark matter. *Phys. Dark Universe*, 12:1 – 23, 2016.

[92] Esra Bulbul, Maxim Markevitch, Adam Foster, Randall K. Smith, Michael Loewenstein, and Scott W. Randall. Detection of an Unidentified Emission Line in the Stacked X-Ray Spectrum of Galaxy Clusters. *Astrophys. J.*, 789(1):13, 2014.

[93] A. Boyarsky, O. Ruchayskiy, D. Iakubovskyi, and J. Franse. Unidentified Line in X-Ray Spectra of the Andromeda Galaxy and Perseus Galaxy Cluster. *Phys. Rev. Lett.*, 113:251301, 2014.

[94] Adriani, O. and others (PAMELA collaboration). An anomalous positron abundance in cosmic rays with energies $1.5 - 100\,\mathrm{GeV}$. *Nature*, 458:607, 2009.

[95] M. Aguilar and others (AMS collaboration). First Result from the Alpha Magnetic Spectrometer on the International Space Station: Precision Measurement of the Positron Fraction in Primary Cosmic Rays of $0.5 - 350\,\mathrm{GeV}$. *Phys. Rev. Lett.*, 110:141102, 2013.

[96] Dan Hooper, Pasquale Blasi, and Pasquale Dario Serpico. Pulsars as the sources of high energy cosmic ray positrons. *J. Cosmol. Astropart. Phys.*, 2009(01):025, 2009.

[97] V. Barger, Y. Gao, W.-Y. Keung, D. Marfatia, and G. Shaughnessy. Dark matter and pulsar signals for fermi lat, pamela, atic, {HESS} and {WMAP} data. *Phys. Lett. B*, 678(3):283 – 292, 2009.

[98] S. Profumo. Dissecting cosmic-ray electron-positron data with Occam's Razor: the role of known Pulsars. *Open Physics*, 10:1, 2012.

[99] CMS collaboration. Search for the production of dark matter in association with top-quark pairs in the single-lepton final state in proton-proton collisions at $\sqrt{s} = 8\,\mathrm{TeV}. J. High Energy Phys., 2015(6) : 121, 2015.$

[100] D. Pinna. *Search for Dark Matter in Association with Top Quarks with the CMS Detector*. PhD thesis, University of Zurich, 2017.

[101] J. I. Read. The local dark matter density. *J. Phys. G*, 41:063101, 2014.

[102] S. E. Koposov, H.-W. Rix, and D. W. Hogg. Constraining the Milky Way Potential with a Six-Dimensional Phase-Space Map of the GD-1 Stellar Stream. *Astrophys. J.*, 712:260, 2010.

[103] T. Piffl, C. Scannapieco, J. Binney, M. Steinmetz, R.-D. Scholz, M. E. K. Williams, R. S. De Jong, G. Kordopatis, G. Matijevič, O. Bienaymé, et al. The RAVE survey: the Galactic escape speed and the mass of the Milky Way. *Astron. Astrophys.*, 562:A91, 2014.

[104] Vernon Barger, Wai-Yee Keung, and Gabe Shaughnessy. Spin dependence of dark matter scattering. *Phys. Rev. D*, 78:056007, 2008.

[105] D.G. Cerdeño and A. Green. "Direct detection of WIMPs", in *Particle Dark Matter*, chapter 17. Cambridge University Press, 2010.

[106] J. D. Lewin and P. F. Smith. Review of mathematics, numerical factors, and corrections for dark matter experiments based on elastic nuclear recoil. *Astropart. Phys.*, 6:87, 1996.

[107] J. Menéndez, D. Gazit, and A. Schwenk. Spin-dependent wimp scattering off nuclei. *Phys. Rev. D*, 86:103511, 2012.

[108] P. Klos, J. Menéndez, D. Gazit, and A. Schwenk. Large-scale nuclear structure calculations for spin-dependent wimp scattering with chiral effective field theory currents. *Phys. Rev. D*, 88:083516, 2013.

[109] L. Baudis. Direct dark matter detection: The next decade. *Phys. Dark Universe*, 1:94, 2012.

[110] E. Aprile and others (XENON collaboration). XENON100 dark matter results from a combination of 477 live days. *Phys. Rev. D*, 94:122001, 2016.

[111] Akerib, D. S. and others (LUX collaboration). Results from a Search for Dark Matter in the Complete LUX Exposure. *Phys. Rev. Lett.*, 118:021303, 2017.

[112] CREST collaboration. Results on low mass wimps using an upgraded cresst-ii detector. *Eur. Phys. J. C*, 74:3184, 2014.

[113] Cao, XiGuang and others (PandaX collaboration). PandaX: a liquid xenon dark matter experiment at CJPL. *Science China Physics, Mechanics & Astronomy*, 57(8):1476–1494, 2014.

[114] Aprile, E. and others (XENON collaboration). First Dark Matter Search Results from the XENON1T Experiment. *Phys. Rev. Lett.*, 119:181301, 2017.

[115] SuperCDMS collaboration. Search for Low-Mass Weakly Interacting Massive Particles with SuperCDMS. *Phys. Rev. Lett.*, 112:241302, 2014.

[116] S. Archambault and others (PICASSO collaboration). Constraints on low-mass WIMP interactions on ^{19}F from PICASSO. *Phys. Lett. B*, 711:153 – 161, 2012.

[117] Behnke, E. and others (COUPP collaboration). First dark matter search results from a 4-kg $CF_3\mathbf{I}$ bubble chamber operated in a deep underground site. *Phys. Rev. D*, 86:052001, 2012.

[118] M Felizardo, T A Girard, T Morlat, A C Fernandes, A R Ramos, and J G Marques. Recent results from the SIMPLE dark matter search. *Journal of Physics: Conference Series*, 375(1):012011, 2012.

[119] L. Baudis and others (DARWIN collaboration). DARWIN: towards the ultimate dark matter detector. *J. Cosmol. Astropart. Phys.*, 017, 2016.

[120] L. E. Strigari. Neutrino coherent scattering rates at direct dark matter detectors. *New J. Phys.*, 11:105011, 2009.

[121] A. Gütlein, C. Ciemniak, F. von Feilitzsch, N. Haag, M. Hofmann, C. Isaila, T. Lachenmaier, J.-C. Lanfranchi, L. Oberauer, S. Pfister, W. Potzel, S. Roth, M. von Sivers, R. Strauss, and A. Zöller. Solar and atmospheric neutrinos: Background sources for the direct dark matter searches. *Astropart. Phys.*, 34(2):90–96, 2010.

[122] A. J. Anderson, J. M. Conrad, E. Figueroa-Feliciano, K. Scholberg, and J. Spitz. Coherent neutrino scattering in dark matter detectors. *Phys. Rev. D*, 84:013008, 2011.

[123] J. Billard, E. Figueroa-Feliciano, and L. Strigari. Implication of neutrino backgrounds on the reach of next generation dark matter direct detection experiments. *Phys. Rev. D*, 89:023524, 2014.

[124] Albert, J. B. and others (EXO collaboration). Improved measurement of the $2\nu\beta\beta$ half-life of ^{136}Xe with the EXO-200 detector. *Phys. Rev. C*, 89:015502, 2014.

[125] Tadayoshi Doke, Kimiaki Masuda, and Eido Shibamura. Estimation of absolute photon yields in liquid argon and xenon for relativistic (1 MeV) electrons. *Nucl. Instr. Meth. Phys. Res. A*, 291(3):617–620, 1990.

[126] Vitaly Chepel and Henrique Araújo. Liquid noble gas detectors for low energy particle physics. *J. Instrum.*, 8(04):R04001, 2013.

[127] S Kubota, A Nakamoto, T Takahashi, S Konno, T Hamada, M Miyajima, A Hitachi, E Shibamura, and T Doke. Evidence of the existence of exciton states in liquid argon and exciton-enhanced ionization from xenon doping. *Phys. Rev. B*, 13(4):1649, 1976.

[128] NIST-ESTAR. http://physics.nist.gov/PhysRefData/Star/Text/.

[129] NIST-ASTAR. http://physics.nist.gov/PhysRefData/Star/Text/ASTAR.html.

[130] NIST-XCOM. http://physics.nist.gov/PhysRefData/Xcom/Text/.

[131] ENSDF. http://www.nndc.bnl.gov/ensdf/.

[132] Keiko Fujii, Yuya Endo, Yui Torigoe, Shogo Nakamura, Tomiyoshi Haruyama, Katsuyu Kasami, Satoshi Mihara, Kiwamu Saito, Shinichi Sasaki, and Hiroko Tawara. High-accuracy measurement of the emission spectrum of liquid xenon in the vacuum ultraviolet region. *Nucl. Instr. Meth. Phys. Res. A*, 795:293 – 297, 2015.

[133] S Kubota, M Hishida, and J Raun. Evidence for a triplet state of the self-trapped exciton states in liquid argon, krypton and xenon. *J. Phys. C: Solid State Physics*, 11(12):2645, 1978.

[134] Shinzou Kubota, Masahiko Hishida, Masayo Suzuki, and Jian zhi Ruan. Liquid and solid argon, krypton and xenon scintillators. *Nucl. Instr. Meth. Phys. Res.*, 196(1):101 – 105, 1982.

[135] Shinzou Kubota, A Nakamoto, Tan Takahashi, T Hamada, Eido Shibamura, Mitsuhiro Miyajima, Kimiaki Masuda, and Tadayoshi Doke. Recombination luminescence in liquid argon and in liquid xenon. *Phys. Rev. B*, 17(6):2762, 1978.

[136] Tadayoshi Doke, Henry J Crawford, Akira Hitachi, Jun Kikuchi, Peter J Lindstrom, Kimiaki Masuda, Eido Shibamura, and Tan Takahashi. LET dependence of scintillation yields in liquid argon. *Nucl. Instr. Meth. Phys. Res. A*, 269(1):291–296, 1988.

[137] Akira Hitachi. Properties of liquid xenon scintillation for dark matter searches. *Astropart. Phys.*, 24(3):247 – 256, 2005.

[138] I. T. Steinberger and U. Asaf. Band-structure parameters of solid and liquid xenon. *Phys. Rev. B*, 8:914, 1973.

[139] W Shockley. Hot electrons in germanium and ohm's law. *Bell System Technical Journal*, 30(4):990–1034, 1951.

[140] Morrel H Cohen and J Lekner. Theory of hot electrons in gases, liquids, and solids. *Phys. Rev.*, 158(2):305, 1967.

[141] Y Sakai, S Nakamura, and H Tagashira. Drift velocity of hot electrons in liquid Ar, Kr, and Xe. *IEEE Transactions on Electrical Insulation*, (2):133–137, 1985.

[142] Carl Eric Dahl. *The physics of background discrimination in liquid xenon, and first results from XENON*10 *in the hunt for WIMP dark matter.* PhD thesis, Princeton University, 2009.

[143] Tan Takahashi, S Konno, T Hamada, Mitsuhiro Miyajima, Shinzou Kubota, A Nakamoto, Akira Hitachi, Eido Shibamura, and Tadayoshi Doke. Average energy expended per ion pair in liquid xenon. *Phys. Rev. A*, 12(5):1771, 1975.

[144] A. Manalaysay. *Response of liquid xenon to low-energy ionizing radiation and its use in the XENON10 dark matter search.* PhD thesis, University of Florida, 2009.

[145] J Lindhard and M Scharff. Energy dissipation by ions in the keV region. *Phys. Rev.*, 124(1):128, 1961.

[146] J. Lindhard, V. Nielsen, M. Scharff, and P.V. Thomsen. Integral equations governing radiation effects. *Mat. Fys. Medd. Dan. Vid. Selsk*, 33(10):1–42, 1963.

[147] C. Chasman, K. W. Jones, H. W. Kraner, and Werner Brandt. Band-Gap Effects in the Stopping of Ge^{72*} Atoms in Germanium. *Phys. Rev. Lett.*, 21:1430, 1968.

[148] K. W. Jones and H. W. Kraner. Energy lost to ionization by 254-eV ^{73}Ge atoms stopping in Ge. *Phys. Rev. A*, 11:1347, 1975.

[149] Y. Messous, B. Chambon, V. Chazal, M. De Jésus, D. Drain, C. Pastor, A. de Bellefon, M. Chapellier, G. Chardin, E. Gaillard-Lecanu, G. Gerbier,

Y. Giraud-Héraud, D. Lhote, J. Mallet, L. Mosca, M.-C. Perillo-Isaac, C. Tao, and D. Yvon. Calibration of a Ge crystal with nuclear recoils for the development of a dark matter detector. *Astropart. Phys.*, 3(4):361 – 366, 1995.

[150] Akerib, D. S. and others (LUX collaboration). Low-energy (0.7-74 keV) nuclear recoil calibration of the LUX dark matter experiment using DD neutron scattering kinematics. *arXiv preprint arXiv:1608.05381*, 2016.

[151] Elena Aprile, CE Dahl, L De Viveiros, RJ Gaitskell, Karl-Ludwig Giboni, J Kwong, P Majewski, K Ni, T Shutt, and M Yamashita. Simultaneous measurement of ionization and scintillation from nuclear recoils in liquid xenon for a dark matter experiment. *Phys. Rev. Lett.*, 97(8):081302, 2006.

[152] E. Aprile and others (XENON collaboration). Dark matter results from 225 live days of XENON100 data. *Phys. Rev. Lett.*, 109:181301, 2012.

[153] E. Aprile and others (XENON collaboration). The XENON100 dark matter experiment. *Astropart. Phys.*, 35:573, 2012.

[154] Alexander Kish. *Dark Matter Search with the XENON*100 *Experiment.* PhD thesis, University of Zurich, 2011.

[155] EM Gushchin, AA Kruglov, and IM Obodovskii. Emission of "hot" electrons from liquid and solid argon and xenon. *Sov. Phys. JETP*, 55(5):860–862, 1982.

[156] E. Aprile, K. L. Giboni, P. Majewski, K. Ni, and M. Yamashita. Proportional light in a dual-phase xenon chamber. *IEEE Transactions on nuclear science*, 51(5):1986–1990, 2004.

[157] E. Aprile and others (XENON collaboration). Observation and applications of single-electron charge signals in the XENON100 experiment. *J. Phys. G*, 41:035201, 2014.

[158] Armando JPL Policarpo. Light production and gaseous detectors. *Phys. Scr.*, 23(4A):539, 1981.

[159] Tetsuhiko Takahashi, Susumu Himi, Masayo Suzuki, Jian zhi Ruan(Gen), and Shinzou Kubota. Emission spectra from ArXe, ArKr, ArN2, ArCH4, ArCO2 and XeN2 gas scintillation proportional counters. *Nucl. Instr. Meth. Phys. Res.*, 205(3):591 – 596, 1983.

[160] C. A. N. Conde, L. R. Ferreira, and M. F. A. Ferreira. The secondary scintillation output of xenon in a uniform field gas proportional scintillation counter. *IEEE Transactions on Nuclear Science*, 24:221, 1977.

[161] S. Belogurov, A. Bolozdynya, D. Churakov, A. Koutchenkov, V. Morgunov, V. Solovov, G. Safronov, G. Smirnov, V. Egorov, and S. Medved. High pressure gas scintillation drift chamber with photomultipliers inside of working medium. In *1995 IEEE Nuclear Science Symposium and Medical Imaging Conference Record*, volume 1, pages 519–523 vol.1, 1995.

[162] P. Barrow, L. Baudis, D. Cichon, M. Danisch, D. Franco, F. Kaether, A. Kish, M. Lindner, T. Marrodán Undagoitia, D. Mayani, L. Rauch, Y. Wei, and J. Wulf. Qualification tests of the R11410-21 photomultiplier tubes for the XENON1T detector. *J. Instrum.*, 12(01):P01024, 2017.

[163] Aprile, E. and others (XENON collaboration). Material radioassay and selection for the XENON1T dark matter experiment. *Eur. Phys. J. C*, 77:890, 2017.

[164] Aprile, E. and others (XENON collaboration). Conceptual design and simulation of a water Cherenkov muon veto for the XENON1T experiment. *J. Instrum.*, 9:P11006, 2014.

[165] E. Aprile and others (XENON collaboration). First dark matter results from the XENON100 experiment. *Phys. Rev. Lett.*, 105:131302, 2010.

[166] E. Aprile and others (XENON collaboration). Dark matter results from 100 live days of XENON100 data. *Phys. Rev. Lett.*, 107(13):131302, 2011.

[167] E. Aprile and others (XENON collaboration). The neutron background of the XENON100 dark matter search experiment. *J. Phys. G*, 40:115201, 2013.

[168] William M Haynes. *CRC handbook of chemistry and physics*. CRC press, 2014.

[169] Norman Neill Greenwood and Alan Earnshaw. *Chemistry of the Elements*. Elsevier, 2012.

[170] Juris Meija, Tyler B Coplen, Michael Berglund, Willi A Brand, Paul De Bièvre, Manfred Gröning, Norman E Holden, Johanna Irrgeher, Robert D Loss, Thomas Walczyk, et al. Isotopic compositions of the elements 2013 (IUPAC Technical Report). *Pure and Applied Chemistry*, 88(3):293–306, 2016.

[171] Joe Hiess, Daniel J. Condon, Noah McLean, and Stephen R. Noble. $^{238}U/^{235}U$ Systematics in Terrestrial Uranium-Bearing Minerals. *Science*, 335(6076):1610–1614, 2012.

[172] Stefan Brünner. Study of radon adsorption on activated carbon for a purification system in xenon1t. Master's thesis, Diplomarbeit Universität Graz, 2013.

[173] Marc Weber. *Gentle neutron signals and noble background in the XENON100 dark matter search experiment*. PhD thesis, Max Planck Institut fur KernPhysik, Heidelberg Germany, 2013.

[174] Nudat 2.6. http://www.nndc.bnl.gov/nudat2/.

[175] Peter G Cook and Andrew L Herczeg. *Environmental tracers in subsurface hydrology*. Springer Science & Business Media, 2012.

[176] J. Bieringer, C. Schlosser, H. Sartorius, and S. Schmid. Trace analysis of aerosol bound particulates and noble gases at the BfS in Germany. *Appl. Radiat. Isot.*, 67(5):672 – 677, 2009. 5th International Conference on Radionuclide Metrology - Low-Level Radioactivity Measurement Techniques ICRM-LLRMT'08.

[177] X Du, R Purtschert, K Bailey, BE Lehmann, R Lorenzo, Z-T Lu, P Mueller, TP O'Connor, NC Sturchio, and L Young. A new method of measuring ^{81}Kr and ^{85}Kr abundances in environmental samples. *Geophysical research letters*, 30(20), 2003.

[178] W. L. McCabe, J. C. Smith, and P. Harriot. *Unit Operation of Chemical Engeneering*. McGraw-Hill, 5 edition, 1993.

[179] K Abe and others (XEMASS collaboration). Distillation of liquid xenon to remove krypton. *Astropart. Phys.*, 31(4):290–296, 2009.

[180] E. Aprile and others (XENON collaboration). Study of the electromagnetic background in the XENON100 experiment. *Phys. Rev. D*, 83:082001, 2011.

[181] Aprile, E. and others (XENON collaboration). Physics reach of the XENON1T dark matter experiment. *J. Cosmol. Astropart. Phys.*, 2016:027, 2016.

[182] S Rosendahl, E Brown, I Cristescu, A Fieguth, C Huhmann, M Murra, and C Weinheimer. A cryogenic distillation column for the XENON1T experiment. In *Journal of Physics: Conference Series*, volume 564, page 012006. IOP Publishing, 2014.

[183] Alexander Fieguth et al. Distillation column for the XENON1T experiment. In *Journal of Physics: Conference Series*, volume 718, page 042020. IOP Publishing, 2016.

[184] Aprile, E. and others (XENON collaboration). Removing krypton from xenon by cryogenic distillation to the ppq level. *Eur. Phys. J. C*, 77:275, 2017.

[185] G Heusser, M Laubenstein, and H Neder. Low-level germanium gamma-ray spectrometry at the μBq/kg level and future developments towards higher sensitivity. *Radioactivity in the Environment*, 8:495–510, 2006.

[186] L. Baudis, A. D. Ferella, A. Askin, J. Angle, E. Aprile, T. Bruch, A. Kish, M. Laubenstein, A. Manalaysay, T. M. Undagoitia, et al. Gator: a low-background counting facility at the Gran Sasso Underground Laboratory. *J. Instrum.*, 6:P08010, 2011.

[187] S Nisi, A Di Vacri, ML Di Vacri, A Stramenga, and M Laubenstein. Comparison of inductively coupled mass spectrometry and ultra low-level gamma-ray spectroscopy for ultra low background material selection. *Appl. Radiat. Isot.*, 67(5):828, 2009.

[188] Evans Analytical Group. http://www.eag.com/gas-chromatography-mass-spectrometry-gc-ms/.

[189] Gerd Heusser. Low-radioactivity background techniques. *Annual Review of Nuclear and Particle Science*, 45(1):543–590, 1995.

[190] Gordon Gilmore. *Practical gamma-ray spectroscopy*. 2011.

[191] RG Helmer and MA Lee. Analytical functions for fitting peaks from Ge semiconductor detectors. *Nuclear Instruments and Methods*, 178(2-3):499–512, 1980.

[192] Gary W Phillips and Keith W Marlow. Automatic analysis of gamma-ray spectra from germanium detectors. *Nuclear Instruments and Methods*, 137(3):525–536, 1976.

[193] J.L. Campbell and J.A. Maxwell. A cautionary note on the use of the Hypermet tailing function in X-ray spectrometry with Si(Li) detectors. *Nucl. Instr. Meth. Phys. Res. B*, 129(2):297–299, 1997.

[194] Nicholas Metropolis and Stanislaw Ulam. The monte carlo method. *Journal of the American statistical association*, 44(247):335–341, 1949.

[195] Nicholas Metropolis, Arianna W Rosenbluth, Marshall N Rosenbluth, Augusta H Teller, and Edward Teller. Equation of state calculations by fast computing machines. *The journal of chemical physics*, 21(6):1087–1092, 1953.

[196] L Moneta and F James. Minuit2 minimization package, 2010.

[197] (Particle Data Group). Mathematical tools or statistics, monte carlo, group theory. *Phys. Lett. B*, 667(1):316–339, 2008.

[198] G Heusser, W Rau, B Freudiger, M Laubenstein, M Balata, and T Kirsten. ^{222}Rn detection at the μBq/m^3 range in nitrogen gas and a new Rn purification technique for liquid nitrogen. *Appl. Radiat. Isot.*, 52(3):691 – 695, 2000.

[199] H. Simgen. Ultrapure gases for GERDA. *Prog. Part. Nucl. Phys.*, 57(1):266 – 268, 2006. International Workshop of Nuclear Physics 27th course: Neutrinos in Cosmology, in Astro, Particle and Nuclear PhysicsEttore Majorana Center for Scientific Culture.

[200] G. Zuzel and H. Simgen. High sensitivity radon emanation measurements. *Appl. Radiat. Isot.*, 67(5):889 – 893, 2009. 5th International Conference on Radionuclide Metrology - Low-Level Radioactivity Measurement Techniques ICRM-LLRMT'08.

[201] I. Antcheva, M. Ballintijn, B. Bellenot, M. Biskup, R. Brun, N. Buncic, Ph. Canal, D. Casadei, O. Couet, V. Fine, L. Franco, G. Ganis, A. Gheata, D. Gonzalez Maline, M. Goto, J. Iwaszkiewicz, A. Kreshuk, D. Marcos Segura, R. Maunder, L. Moneta, A. Naumann, E. Offermann, V. Onuchin, S. Panacek, F. Rademakers, P. Russo, and M. Tadel. ROOT — A C++ framework for petabyte data storage, statistical analysis and visualization. *Comput. Phys. Commun.*, 180(12):2499 – 2512, 2009.

[202] Sea Agostinelli, John Allison, K al Amako, J Apostolakis, H Araujo, P Arce, M Asai, D Axen, S Banerjee, G Barrand, et al. GEANT4—a simulation toolkit. *Nucl. Instr. Meth. Phys. Res. A*, 506(3):250–303, 2003.

[203] Steffen Hauf, Markus Kuster, Matej Batič, Zane W Bell, Dieter HH Hoffmann, Philipp M Lang, Stephan Neff, Maria Grazia Pia, Georg Weidenspointner, and Andreas Zoglauer. Radioactive decays in Geant4. *IEEE Transactions on Nuclear Science*, 60(4):2966–2983, 2013.

[204] Christian Hurtgen, Simon Jerome, and Mike Woods. Revisiting Currie—how low can you go? *Appl. Radiat. Isot.*, 53(1):45–50, 2000.

[205] W. B. et al Wilson. SOURCES-4A, Technical Report. Technical Report LA-13539-MS, Los Alamos, 1999.

[206] M. Laubenstein and G. Heusser. Cosmogenic radionuclides in metals as indicator for sea level exposure history. *Appl. Radiat. Isot.*, 67:750, 2009.

[207] Ulrich Quade. Radiological characterization of steel scrap recycling by melting. *Siempelkamp Nukleartechnik GmbH, Krefeld, Germany*, 2001.

[208] D Neuschütz, D Spirin, U Quade, J Meier-Kortwig, L Holappa, M Hämäläinen, MA Heredia Lozano, and MJ Guio Bonany. Inadvertent melting of radioactive sources in bof or eaf: Distribution of nuclides, monitoring, prevention. *ISIJ international*, 45(2):288–295, 2005.

[209] Matthew J Donachie. *Titanium: a technical guide*. ASM international, 2000.

[210] E. Aprile and others (XENON collaboration). Material screening and selection for XENON100. *Astropart. Phys.*, 35:43, 2011.

[211] Accuglass Inc. https://accuglassproducts.com/home.php.

[212] Akerib, D. S. and others (LUX collaboration). Radiogenic and muon-induced backgrounds in the LUX dark matter detector. *Astropart. Phys.*, 62:33, 2015.

[213] Aprile, E. and others (XENON collaboration). Lowering the radioactivity of the photomultiplier tubes for the XENON1T dark matter experiment. *Eur. Phys. J. C*, 75:1, 2015.

[214] Laura Baudis, Annika Behrens, Alfredo Ferella, Alexander Kish, T Marrodán Undagoitia, Daniel Mayani, and Marc Schumann. Performance of the Hamamatsu R11410 photomultiplier tube in cryogenic xenon environments. *J. Instrum.*, 8(04):P04026, 2013.

[215] Takahiro Watanabe, Noriyoshi Tsuchiya, Yasuji Oura, Mitsuru Ebihara, Chihiro Inoue, Nobuo Hirano, Ryoichi Yamada, Shin-ichi Yamasaki, Atsushi Okamoto, Fukimo Watanabe Nara, et al. Distribution of artificial radionuclides (^{110m}Ag, ^{129m}Te, ^{134}Cs, ^{137}Cs) in surface soils from Miyagi Prefecture, northeast Japan, following the 2011 Fukushima Dai-ichi nuclear power plant accident. *Geochemical Journal*, 46(4):279–285, 2012.

[216] F Perrot, Ph Hubert, Ch Marquet, MS Pravikoff, P Bourquin, H Chiron, P-Y Guernion, and A Nachab. Evidence of ^{131}I and ^{134,137}Cs activities in Bordeaux, France due to the Fukushima nuclear accident. *Journal of environmental radioactivity*, 114:61–65, 2012.

[217] G Le Petit, G Douysset, G Ducros, P Gross, P Achim, M Monfort, P Raymond, Y Pontillon, C Jutier, X Blanchard, et al. Analysis of radionuclide releases from the Fukushima Dai-Ichi nuclear power plant accident Part I. *Pure and Applied Geophysics*, 171(3-5):629–644, 2014.

[218] A. Vargas, A. Camacho, M. Laubenstein, and W. Plastino. Dry deposition velocity of ^{137}Cs and ^{134}Cs in Spain after the Fukushima Dai-Ichi Nuclear Power Plant accident. *Appl. Radiat. Isot.*, 109:441, 2016.

[219] Akerib, D. S. and others (LUX collaboration). An ultra-low background PMT for liquid xenon detectors. *Nucl. Instr. Meth. Phys. Res. A*, 703:1, 2013.

[220] L. Baudis, A. Kish, F. Piastra, and M. Schumann. Cosmogenic activation of xenon and copper. *Eur. Phys. J. C*, 75:1, 2015.

[221] F. Piastra. Measurement of cosmogenic radioactive products in xenon and copper. In *Journal of Physics: Conference Series*, volume 689, page 012021. IOP Publishing, 2016.

[222] D. C. Malling and others (LZ collaboration). After LUX: the LZ program. *arXiv preprint arXiv:1110.0103*, 2011.

[223] J. J. Back and Y. A. Ramachers. ACTIVIA: Calculation of isotope production cross-sections and yields. *Nucl. Instr. Meth. Phys. Res. A*, 586:286, 2008.

[224] C. J. Martoff and P. D. Lewin. COSMO - A program to estimate spallation radioactivity produced in a pure substance by exposure to cosmic radiation on the earth. *Comput. Phys. Commun.*, 72:96, 1992.

[225] R Silberberg and CH Tsao. Partial Cross-Sections in High-Energy Nuclear Reactions, and Astrophysical Applications. I. Targets With Z<= 28. *Astrophys. J. Suppl. Ser.*, 25:315–333, 1973.

[226] R Silberberg and C Ho Tsao. Partial cross-sections in high-energy nuclear reactions, and astrophysical applications. II. Targets heavier than nickel. *Astrophys. J. Suppl. Ser.*, 25:335–367, 1973.

[227] R Silberberg, CH Tsao, and AF Barghouty. Updated partial cross sections of proton-nucleus reactions. *Astrophys. J.*, 501(2):911, 1998.

[228] High Altitude Research Station Jungfraujoch. http://www.ifjungo.ch/jungfraujoch/.

[229] M. Aglietta, B. Alessandro, P. Antonioli, F. Arneodo, L. Bergamasco, M. Bertaina, C. Castagnoli, A. Castellina, A. Chiavassa, G. Cini Castagnoli, B. D'Ettorre Piazzoli, G. Di Sciascio, W. Fulgione, P. Galeotti, P.L. Ghia, M. Iacovacci, G. Mannocchi, C. Morello, G. Navarra, L. Riccati, O. Saavedra, G.C. Trinchero, S. Valchierotti, P. Vallania, S. Vernetto, and C. Vigorito. Measurement of the cosmic ray hadron spectrum up to 30 TeV at mountain altitude: the primary proton spectrum. *Astropart. Phys.*, 19(3):329 – 338, 2003.

[230] H H Mielke, M Foller, J Engler, and J Knapp. Cosmic ray hadron flux at sea level up to 15 TeV. *J. Phys. G*, 20(4):637, 1994.

[231] J. J. Beatty, S. Coutu, S. A. Minnick, A. Bhattacharyya, C. R. Bower, J. A. Musser, S. P. McKee, M. Schubnell, G. Tarlé, A. D. Tomasch, A. W. Labrador, D. Müller, S. P. Swordy, M. A. DuVernois, and S. L. Nutter. New measurement of the altitude dependence of the atmospheric muon intensity. *Phys. Rev. D*, 70:092005, 2004.

[232] Tanja Hagner, R von Hentig, B Heisinger, L Oberauer, S Schönert, F von Feilitzsch, and E Nolte. Muon-induced production of radioactive isotopes in scintillation detectors. *Astropart. Phys.*, 14(1):33–47, 2000.

[233] B. Heisinger, D Lal, A.J.T Jull, P Kubik, S Ivy-Ochs, S Neumaier, K Knie, V Lazarev, and E Nolte. Production of selected cosmogenic radionuclides by muons: 1. fast muons. *Earth and Planetary Science Letters*, 200(3–4):345 – 355, 2002.

[234] U.S. Standard Atmosphere 1976: http://www.pdas.com/atmos.html .

[235] James F Ziegler. Terrestrial cosmic rays. *IBM journal of research and development*, 40(1):19–39, 1996.

[236] Todor Stanev. *High energy cosmic rays*. Springer Science & Business Media, 2010.

[237] IS Diggory, JR Hook, IA Jenkins, and KE Turver. The momentum spectra of nuclear active particles in the cosmic radiation at sea level. i. experimental data. *Journal of Physics A: Mathematical, Nuclear and General*, 7(6):741, 1974.

[238] Peter KF Grieder. *Cosmic rays at Earth*. Elsevier, 2001.

[239] T. W. Armstrong, K. C. Chandler, and J. Barish. Calculations of neutron flux spectra induced in the Earth's atmosphere by galactic cosmic rays. *Journal of Geophysical Research*, 78:2715, 1973.

[240] N. Gehrels. Instrumental background in balloon-borne gamma-ray spectrometers and techniques for its reduction. *Nucl. Instr. Meth. Phys. Res. A*, 239(2):324 – 349, 1985.

[241] T. Francke et al. A new measurement of the atmospheric proton and muon fluxes. In *Proceedings, 26th International Cosmic Ray Conference, August 17-25, 1999, Salt Lake City: Invited, Rapporteur, and Highlight Papers*, pages 80–83, 1999.

[242] M. Merker, E. S. Light, H. J. Verschell, R. B. Mendell, and S. A. Korff. Time dependent worldwide distribution of atmospheric neutrons and of their products: 1. fast neutron observations. *Journal of Geophysical Research*, 78:2727, 1973.

[243] E. S. Light, M. Merker, H. J. Verschell, R. B. Mendell, and S. A. Korff. Time dependent worldwide distribution of atmospheric neutrons and of their products: 2. calculation. *Journal of Geophysical Research*, 78(16):2741–2762, 1973.

[244] Claudio Manfredotti, C. Ongaro, Alba Zanini, M. Cavaioli, and L. Tommasino. Spectrometry of low- and high-energy neutrons by unfolding passive detector responses. volume 2867, pages 619–622, 1997.

[245] A Shukla, PK Raina, and PK Rath. Study of two neutrino $\beta^+\beta^+/\beta^+$ EC/ECEC decay of ^{124,126}Xe and ^{130,132}Ba for $0^+ \to 0^+$ transition in PHFB model. *J. Phys. G*, 34(3):549, 2007.

[246] K. Weise and M. Matzke. A priori distributions from the principle of maximum entropy for the Monte Carlo unfolding of particle energy spectra. *Nucl. Instr. Meth. Phys. Res. A*, 280:103, 1989.

[247] K. Weise and W. Woger. A Bayesian theory of measurement uncertainty. *Meas. Sci. Technol.*, 4:1, 1993.

[248] I. Lira and D. Grientschnig. Bayesian assessment of uncertainty in metrology: a tutorial. *Metrologia*, 47:R1, 2010.

[249] Allen Caldwell, Daniel Kollár, and Kevin Kröninger. {BAT} – The Bayesian analysis toolkit. *Comput. Phys. Commun.*, 180(11):2197 – 2209, 2009.

[250] S. Cebrian, H. Gómez, G. Luzón, J. Morales, A. Tomás, and J. A. Villar. Cosmogenic activation in germanium and copper for rare event searches. *Astropart. Phys.*, 33:316, 2010.

[251] D.-M. Mei, Z.-B. Yin, and S. R. Elliott. Cosmogenic production as a background in searching for rare physics processes. *Astropart. Phys.*, 31:417, 2009.

[252] http://www.talys.eu.

[253] Yu N Shubin, VP Lunev, A Yu Konobeyev, and AI Dityuk. Mendl-2p, proton reaction data library for nuclear activation (medium energy nuclear data library). *IAEANDS-204*, 1998.

[254] L. Baudis, A. Ferella, A. Kish, A. Manalaysay, T. Marrodán Undagoitia, and M. Schumann. Neutrino physics with multi-ton scale liquid xenon detectors. *J. Cosmol. Astropart. Phys.*, 2014(01):044, 2014.

[255] Marc Schumann, Laura Baudis, Lukas Bütikofer, Alexander Kish, and Marco Selvi. Dark matter sensitivity of multi-ton liquid xenon detectors. *J. Cosmol. Astropart. Phys.*, 2015(10):016, 2015.

[256] M Laubenstein. Private communication, 2015.

[257] M. S. Gordon, P. Goldhagen, K. P. Rodbell, T. H. Zabel, H. H. K. Tang, J. M. Clem, and P. Bailey. Measurement of the flux and energy spectrum of cosmic-ray induced neutrons on the ground. *IEEE Transactions on Nuclear Science*, 51:3427, 2004.

[258] T. Doke, H. J. Crawford, C. R. Gruhn, A. Hitachi, J. Kikuchi, K. Masuda, S. Nagamiya, E. Shibamura, and S. Tamada. Scintillation yields by relativistic heavy ions and the relation between ionization and scintillation in liquid argon. *Nucl. Instr. Meth. Phys. Res. A*, 235:136, 1985.

[259] M Tanaka, T Doke, A Hitachi, T Kato, J Kikuchi, K Masuda, T Murakami, F Nishikido, H Okada, K Ozaki, et al. LET dependence of scintillation yields in liquid xenon. *Nucl. Instr. Meth. Phys. Res. A*, 457(3):454–463, 2001.

[260] Tadayoshi Doke, Akira Hitachi, Jun Kikuchi, Kimiaki Masuda, Hiroyuki Okada, and Eido Shibamura. Absolute scintillation yields in liquid argon and xenon for various particles. *Japanese journal of applied physics*, 41(3R):1538, 2002.

[261] F. Arneodo, B. Baiboussinov, A. Badertscher, P. Benetti, E. Bernardini, A. Bettini, A. B. Di Tiogliole, R. Brunetti, A. Bueno, E. Calligarich, et al. Scintillation efficiency of nuclear recoil in liquid xenon. *Nucl. Instr. Meth. Phys. Res. A*, 449:147, 2000.

[262] R Bernabei, P Belli, R Cerulli, F Montecchia, A Incicchitti, D Prosperi, CJ Dai, M Angelone, P Batistoni, and M Pillon. Light response of a pure liquid Xenon scintillator irradiated with 2.5 MeV neutrons. *EPJ direct*, 3(1):1–8, 2001.

[263] D Akimov, A Bewick, D Davidge, J Dawson, AS Howard, I Ivaniouchenkov, WG Jones, J Joshi, VA Kudryavtsev, TB Lawson, et al. Measurements of scintillation efficiency and pulse shape for low energy recoils in liquid xenon. *Phys. Lett. B*, 524(3):245–251, 2002.

[264] E Aprile, KL Giboni, P Majewski, K Ni, M Yamashita, R Hasty, A Manzur, and DN McKinsey. Scintillation response of liquid xenon to low energy nuclear recoils. *Phys. Rev. D*, 72(7):072006, 2005.

[265] E Aprile, L Baudis, B Choi, KL Giboni, K Lim, A Manalaysay, ME Monzani, G Plante, R Santorelli, and M Yamashita. New measurement of the relative scintillation efficiency of xenon nuclear recoils below 10 keV. *Phys. Rev. C*, 79(4):045807, 2009.

[266] V Chepel, V Solovov, F Neves, A Pereira, PJ Mendes, CP Silva, A Lindote, J Pinto da Cunha, MI Lopes, and S Kossionides. Scintillation efficiency of liquid xenon for nuclear recoils with the energy down to 5 keV. *Astropart. Phys.*, 26(1):58–63, 2006.

[267] A Manzur, A Curioni, L Kastens, DN McKinsey, K Ni, and T Wongjirad. Scintillation efficiency and ionization yield of liquid xenon for monoenergetic nuclear recoils down to 4 keV. *Phys. Rev. C*, 81(2):025808, 2010.

[268] Guillaume Plante, E Aprile, R Budnik, B Choi, K-L Giboni, LW Goetzke, RF Lang, KE Lim, and AJ Melgarejo Fernandez. New measurement of the scintillation efficiency of low-energy nuclear recoils in liquid xenon. *Phys. Rev. C*, 84(4):045805, 2011.

[269] P Sorensen, A Manzur, CE Dahl, J Angle, E Aprile, F Arneodo, L Baudis, A Bernstein, A Bolozdynya, LCC Coelho, et al. The scintillation and ionization yield of liquid xenon for nuclear recoils. *Nucl. Instr. Meth. Phys. Res. A*, 601(3):339–346, 2009.

[270] VN Lebedenko, HM Araújo, EJ Barnes, A Bewick, R Cashmore, V Chepel, A Currie, D Davidge, J Dawson, T Durkin, et al. Results from the first science run of the ZEPLIN-III dark matter search experiment. *Phys. Rev. D*, 80(5):052010, 2009.

[271] E. Aprile and others (XENON collaboration). Response of the XENON100 dark matter detector to nuclear recoils. *Phys. Rev. D*, 88:012006, 2013.

[272] E. Aprile and others (XENON collaboration). Likelihood approach to the first dark matter results from XENON100. *Phys. Rev. D*, 84:052003, 2011.

[273] Akerib, D. S. and others (LUX collaboration). First results from the LUX dark matter experiment at the Sanford Underground Research Facility. *Phys. Rev. Lett.*, 112:091303, 2014.

[274] M. Horn, V. A. Belov, D. Y. Akimov, H. M. Araujo, E. J. Barnes, A. A. Burenkov, V. Chepel, A. Currie, B. Edwards, C. Ghag, et al. Nuclear recoil scintillation and ionisation yields in liquid xenon from ZEPLIN-III data. *Phys. Lett. B*, 705:471, 2011.

[275] E. Aprile and others (XENON collaboration). Search for light dark matter in XENON10 data. *Phys. Rev. Lett.*, 107:051301, 2011.

[276] E. Aprile, P. Cushman, K. Ni, and P. Shagin. Detection of liquid xenon scintillation light with a silicon photomultiplier. *Nucl. Instr. Meth. Phys. Res. A*, 556:215, 2006.

[277] T Shutt, Carl E Dahl, J Kwong, A Bolozdynya, and P Brusov. Performance and fundamental processes at low energy in a two-phase liquid xenon dark matter detector. *Nucl. Instr. Meth. Phys. Res. A*, 579(1):451–453, 2007.

[278] E. Aprile, K. L. Giboni, P. Majewski, K. Ni, and M. Yamashita. Observation of anticorrelation between scintillation and ionization for MeV gamma rays in liquid xenon. *Phys. Rev. B*, 76:014115, 2007.

[279] Peter Sorensen and Carl Eric Dahl. Nuclear recoil energy scale in liquid xenon with application to the direct detection of dark matter. *Phys. Rev. D*, 83(6):063501, 2011.

[280] Fedor Bezrukov, Felix Kahlhoefer, and Manfred Lindner. Interplay between scintillation and ionization in liquid xenon Dark Matter searches. *Astropart. Phys.*, 35(3):119–127, 2011.

[281] Matthew Szydagis, Adalyn Fyhrie, Daniel Thorngren, and Mani Tripathi. Enhancement of NEST capabilities for simulating low-energy recoils in liquid xenon. *J. Instrum.*, 8(10):C10003, 2013.

[282] Adrian Aeshcbacher. Simulation of a Neutron Generator's Radiation Shield. Bachelor thesis, 2010.

[283] Dario Biasini. Monte carlo simulation of the liquid xenon detector response Monte Carlo Simulation of the Liquid Xenon Detector Response to Low-Energy Neutrons. Bachelor thesis, 2014.

[284] Hrvoje Dujmović. Characterization and calibration of a liquid xenon time projection chamber. Master's thesis, University of Zurich, 2014.

[285] Horst Klein and Sonja Neumann. Neutron and photon spectrometry with liquid scintillation detectors in mixed fields. *Nucl. Instr. Meth. Phys. Res. A*, 476(1):132–142, 2002.

[286] Andreas Ruben, Timothy E Hoagland, Ron Fox, Phillip L Kerr, Gregor Montermann, and Robert Schneider. A new four channel pulse shape discriminator. In *Nuclear Science Symposium Conference Record, 2007. NSS'07. IEEE*, volume 1, pages 681–684. IEEE, 2007.

[287] Payam Pakarha. Preparations for measurements of the low energy response of liquid xenon. Master's thesis, University of Zurich, 2012.

[288] Daniel Furse, Stefan Groh, Nikolaus Trost, Martin Babutzka, John P Barrett, Jan Behrens, Nicholas Buzinksy, Thomas Corona, Sanshiro Enomoto, Moritz Erhard, et al. Kassiopeia: A modern, extensible c++ particle tracking package. *arXiv preprint arXiv:1612.00262*, 2016.

[289] A Manalaysay, T Marrodán Undagoitia, A Askin, L Baudis, A Behrens, AD Ferella, A Kish, O Lebeda, R Santorelli, D Vénos, et al. Spatially uniform calibration of a liquid xenon detector at low energies using ^{83m}Kr. *Review of Scientific Instruments*, 81(7):073303, 2010.

[290] L. Baudis, H. Dujmovic, C. Geis, A. James, A. Kish, A. Manalaysay, T. M. Undagoitia, and M. Schumann. Response of liquid xenon to Compton electrons down to 1.5 keV. *Phys. Rev. D*, 87:115015, 2013.

[291] Tadayoshi Doke and Kimiaki Masuda. Present status of liquid rare gas scintillation detectors and their new application to gamma-ray calorimeters. *Nucl. Instr. Meth. Phys. Res. A*, 420(1):62–80, 1999.

[292] Z Kovács, F Tárkányi, SM Qaim, and G Stöcklin. Excitation functions for the formation of some radioisotopes of rubidium in proton induced nuclear reactions on ^{nat}Kr, ^{82}Kr and ^{83}Kr with special reference to the production of ^{81}Rb (^{81m}Kr) generator radionuclide. *International Journal of Radiation Applications and Instrumentation. Part A. Appl. Radiat. Isot.*, 42(4):329–335, 1991.

[293] D Vénos, A Špalek, O Lebeda, and M Fišer. ^{83m}Kr radioactive source based on ^{83}Rb trapped in cation-exchange paper or in zeolite. *Appl. Radiat. Isot.*, 63(3):323–327, 2005.

[294] V Hannen, E Aprile, F Arneodo, L Baudis, M Beck, K Bokeloh, AD Ferella, K Giboni, RF Lang, O Lebeda, et al. Limits on the release of Rb isotopes from a zeolite based ^{83m}Kr calibration source for the XENON project. *J. Instrum.*, 6(10):P10013, 2011.

[295] KATRIN collaboration. Katrin design report 2004. *FZKA report*, 7090, 2004.

[296] M Berggren, A Cattai, V Gracco, FL Navarria, HG Fischer, A Algeri, et al. Performance of the HPC Calorimeter in DELPHI. *Nucl. Instr. and Meth*, 225:477, 1984.

[297] EA McCutchan. Nuclear data sheets for A= 83. *Nuclear Data Sheets*, 125:201–394, 2015.

[298] George Bakale, U Sowasa, and WF Schmitd. Effect of an electric field on electron attachment to SF_6, N_2O and O_2 in liquid argon and xenon. *J. Phys. Chem.*, 80(23), 1976.

[299] LS Miller, S Howe, and WE Spear. Charge transport in solid and liquid Ar, Kr, and Xe. *Phys. Rev.*, 166(3):871, 1968.

[300] K Yoshino, U Sowada, and WF Schmidt. Effect of molecular solutes on the electron drift velocity in liquid Ar, Kr, and Xe. *Phys. Rev. A*, 14(1):438, 1976.

[301] EM Gushchin, AA Kruglov, and IM Obodovskif. Electron dynamics in condensed argon and xenon. *Zh, Eksp. Teor. Fiz*, 82:1114–1125, 1982.

[302] JB Albert, PS Barbeau, D Beck, V Belov, M Breidenbach, T Brunner, A Burenkov, GF Cao, WR Cen, C Chambers, et al. Measurement of the Drift Velocity and Transverse Diffusion of Electrons in Liquid Xenon with the EXO-200 Detector. *arXiv preprint arXiv:1609.04467*, 2016.

[303] J. Lekner. Motion of electrons in liquid argon. *Phys. Rev.*, 158:130–137, 1967.

[304] Peter Sorensen. *A position-sensitive liquid xenon time-projection chamber for direct detection of dark matter: The xenon10 experiment.* PhD thesis, Brown University, 2008.

[305] E. Aprile and others (XENON collaboration). Analysis of the XENON100 dark matter search data. *Astropart. Phys.*, 54:11, 2014.

[306] LM Barkov, AA Grebenuk, NM Ryskulov, P Yu Stepanov, and SG Zverev. Measurement of the refractive index of liquid xenon for intrinsic scintillation light. *Nucl. Instr. Meth. Phys. Res. A*, 379(3):482–483, 1996.

[307] VN Solovov, V Chepel, MI Lopes, A Hitachi, R Ferreira Marques, and AJPL Policarpo. Measurement of the refractive index and attenuation length of liquid xenon for its scintillation light. *Nucl. Instr. Meth. Phys. Res. A*, 516(2):462–474, 2004.

[308] A Baldini, C Bemporad, F Cei, T Doke, M Grassi, AA Grebenuk, DN Grigoriev, T Haruyama, K Kasami, J Kikuchi, et al. Absorption of scintillation light in a 100 l liquid xenon γ-ray detector and expected detector performance. *Nucl. Instr. Meth. Phys. Res. A*, 545(3):753–764, 2005.

[309] GM Seidel, RE Lanou, and W Yao. Rayleigh scattering in rare-gas liquids. *Nucl. Instr. Meth. Phys. Res. A*, 489(1):189–194, 2002.

[310] André Braem, A Gonidc, D Schinzel, W Seidl, EF Clayton, G Davies, G Hall, R Payne, S Roe, C Seez, et al. Observation of the UV scintillation light from high energy electron showers in liquid xenon. *Nucl. Instr. Meth. Phys. Res. A*, 320(1):228–237, 1992.

[311] V Yu Chepel, MI Lopes, R Ferreira Marques, and AJPL Policarpo. Purification of liquid xenon and impurity monitoring for a PET detector. *Nucl. Instr. Meth. Phys. Res. A*, 349(2-3):500–505, 1994.

[312] M Yamashita, T Doke, K Kawasaki, J Kikuchi, and S Suzuki. Scintillation response of liquid Xe surrounded by PTFE reflector for gamma rays. *Nucl. Instr. Meth. Phys. Res. A*, 535(3):692–698, 2004.

[313] C Silva, JP da Cunha, A Pereira, V Chepel, MI Lopes, and V Solovov. Reflection of the xenon scintillation light from Polytetrafluoroethylene (PTFE). In *Nuclear Science Symposium Conference Record, 2008. NSS'08. IEEE*, pages 1253–1258. IEEE, 2008.

[314] I. H. Malitson. Interspecimen comparison of the refractive index of fused silica. *Josa*, 55(10):1205–1209, 1965.

[315] R. Kitamura, L. Pilon, and M. Jonasz. Optical constants of silica glass from extreme ultraviolet to far infrared at near room temperature. *Applied optics*, 46:8118, 2007.

[316] Guillaume Plante. *The XENON*100 *Dark Matter Experiment: Design, Construction, Calibration and 2010 Search Results with Improved Measurement of the Scintillation Responce of Liquid Xenon to Low-Energy Nuclear Recoils.* PhD thesis, Columbia University, 2012.

[317] D. S. Akerib and others (LUX collaboration). Signal yields, energy resolution, and recombination fluctuations in liquid xenon. *Phys. Rev. D*, 95:012008, 2017.

[318] J Thomas and DA Imel. Recombination of electron-ion pairs in liquid argon and liquid xenon. *Phys. Rev. A*, 36(2):614, 1987.

[319] M Szydagis, N Barry, K Kazkaz, J Mock, D Stolp, M Sweany, M Tripathi, S Uvarov, N Walsh, and M Woods. NEST: a comprehensive model for scintillation yield in liquid xenon. *J. Instrum.*, 6(10):P10002, 2011.

[320] F. Salvat, J. M. Fernández-Varea, and J. Sempau. PENELOPE-2008: A code system for Monte Carlo Simulation of Electron and Photon Transport. nuclear energy agency. In *Workshop Proceedings, Data Bank NEA/NSC/DOC(2011)5, Barcelona*, 2006.

[321] M Miyajima, T Takahashi, S Konno, T Hamada, S Kubota, H Shibamura, and T Doke. Average energy expended per ion pair in liquid argon. *Phys. Rev. A*, 9(3):1438, 1974.

[322] IM Obodovskii and KT Ospanov. Scintillation output of liquid xenon for low-energy γ-quanta. *Instruments and Experimental Techniques*, 37(1):42–45, 1994.

[323] Tadayoshi Doke, Akira Hitachi, Shinzou Kubota, A Nakamoto, and Tan Takahashi. Estimation of Fano factors in liquid argon, krypton, xenon and xenon-doped liquid argon. *Nuclear Instruments and Methods*, 134(2):353–357, 1976.

[324] H. Ichinose, T. Doke, A. Hitachi, J. Kikuchi, K. Masuda, and E. Shibamura. Energy resolution for gamma-rays and electrons from ^{207}Bi in liquid Xe doped with TEA. *Nucl. Instr. Meth. Phys. Res. A*, 322:216, 1992.

[325] E Conti, R DeVoe, G Gratta, T Koffas, S Waldman, J Wodin, D Akimov, G Bower, M Breidenbach, R Conley, et al. Correlated fluctuations between luminescence and ionization in liquid xenon. *Phys. Rev. B*, 68(5):054201, 2003.

[326] T. Doke. Use of sum signals of ionization and scintillation in liquid rare gases and the Fano factor for the sum signals. *Nucl. Instr. Meth. Phys. Res. B*, 234:203, 2005.